



**UNIVERSITAT POLITÈCNICA DE CATALUNYA**  
**BARCELONATECH**

---

**Departament d'Enginyeria Electrònica**

# CHARACTERIZATION OF ALTERNATIVE CARRIER SELECTIVE MATERIALS AND THEIR APPLICATION TO HETEROJUNCTION SOLAR CELLS

Tesi doctoral presentada per a l'obtenció del títol de Doctor per la Universitat  
Politécnica de Catalunya, dins el Programa de Doctorat en Enginyeria Electrònica

**M. Sc. Luis Guillermo Gerling Sarabia**

**Director:** Joaquim Puigdollers González

**Co-Director:** Cristóbal Voz Sánchez

**Equip de recerca:** Micro i Nano Technologies (MNT)

Barcelona, Julio 2017









## Table of contents

	Page
<b>Resumen</b> .....	iv
<b>Summary</b> .....	vii
<b>Agradecimientos</b> .....	x
<b>Abbreviations</b> .....	xii
<b>1 Introduction</b> .....	1
1.1 Context .....	1
1.1.1 Solar photovoltaic energy.....	2
1.1.2 Crystalline silicon solar cells.....	6
1.2 Thesis motivation .....	9
1.2.1 State-of-the-art .....	12
1.3 Objective and thesis structure .....	13
1.4 References .....	15
<b>2 Theoretical background</b> .....	20
2.1 Solar cell operation principles.....	20
2.1.1 Electrochemical potentials as a driving force .....	20
2.1.2 The diode model.....	21
2.1.3 The p/n junction in c-Si.....	23
2.1.4 Design parameters .....	26
2.2 Recombination .....	29
2.3 Contacts .....	32
2.3.1 Selective contact strategies.....	32
2.3.2 Ohmic contacts .....	35
2.3.3 Definition of selectivity.....	37
2.4 References .....	41
<b>3 Experimental methods</b> .....	44
3.1 Solar cell fabrication .....	44
3.1.1 Cleaning and texturing .....	45
3.1.2 a-SiC <sub>x</sub> :H electron-selective contact.....	46
3.1.3 Carrier-selective contacts .....	48
3.1.4 PEDOT:PSS hole-selective contact/transparent electrode.....	49
3.1.5 ITO transparent conductive electrode .....	50
3.1.6 Active area definition .....	51
3.1.7 Front/rear electrodes.....	51

3.2 Solar cell characterization .....	52
3.2.1 Carrier lifetime .....	52
3.2.2 Current-Voltage.....	53
3.2.3 Quantum efficiency .....	55
3.2.4 Suns- $V_{OC}$ .....	57
3.3 Other characterization techniques .....	58
3.3.1 Contact resistance.....	58
3.3.2 Impedance spectroscopy .....	59
3.3.3 Spectrophotometry .....	60
3.3.4 X-ray photoelectron spectroscopy (XPS).....	61
3.3.5 Electron microscopy.....	62
3.3.6 Time-of-flight secondary ion mass spectrometry (ToF-SIMS).....	63
3.4 References .....	63
<b>4 Materials characterization .....</b>	<b>65</b>
4.1 Transition metal oxides .....	67
4.1.1 Electronic structure .....	69
4.1.2 Optical properties .....	71
4.2 TMO/n-Si characterization.....	74
4.2.1 Electric properties .....	74
4.2.2 Passivation properties.....	78
4.2.2.1 Passivation stability.....	81
4.3 Origin of passivation in TMO/n-Si heterojunctions.....	82
4.3.1 The $SiO_x$ interlayer.....	82
4.3.1.1 ToF-SIMS.....	83
4.3.1.2 XPS.....	87
4.3.2 The inversion layer.....	89
4.4 Alternative $SiO_x$ interlayers .....	93
4.5 PEDOT:PSS .....	97
4.5.1 Solution pre-conditioning.....	97
4.5.2 Optoelectronic properties .....	99
4.5.3 Passivation.....	101
4.6 References .....	103
<b>5 Solar cell results.....</b>	<b>108</b>
5.1 TMO/n-Si solar cells .....	108
5.1.1 Current-voltage characteristics.....	108
5.1.2 Diode analysis .....	111
5.1.3 Impedance spectroscopy (IS) .....	114
5.1.4 External quantum efficiency .....	116
5.1.5 Temperature annealing effects .....	118
5.1.6 Laser damage.....	119
5.1.7 Rear contact optimization.....	120
5.2 PEDOT:PSS/n-Si solar cells performance .....	124
5.2.1 Current-voltage and quantum efficiency .....	124

5.3 References .....	126
<b>6 Conclusions and future outlook .....</b>	<b>128</b>
6.1 Conclusions .....	128
6.1.1 Material characterization .....	128
6.1.2 Heterojunction physics .....	130
6.1.3 c-Si heterojunction solar cells .....	132
6.2 Future work and scientific relevance .....	134
<b>Appendix .....</b>	<b>136</b>
A Cost and environmental assessment of c-Si solar cells .....	136
B Other materials tested .....	140
B.1 NiO and ReO <sub>3</sub> .....	140
B.2 LiF .....	141
B.3 V <sub>2</sub> O <sub>x</sub> ·H <sub>2</sub> O (from solution), DBP, CuSCN and MoO <sub>3</sub> (ALD) .....	142
B.4 TMO/a-SiC <sub>x</sub> :H/n-Si contacts .....	143
B.5 Electrochromism in TMO materials .....	144
C List of scientific contributions .....	145
C.1 Journal publications .....	145
C.2 Conference publications .....	147
C.3 Conference presentations .....	148
Appendix references .....	150

## Resumen

A medida que la demanda energética mundial continúa en ascenso, se pronostica que la participación de la energía solar fotovoltaica en el mercado eléctrico continuará en ascenso, con las celdas solares de silicio cristalino (c-Si) como principal contribuidor dado su coste competitivo y su facilidad de escalamiento. Las celdas solares de c-Si pueden ser consideradas un producto maduro y altamente industrializado cuya tecnología de estado del arte –heterounión con capa delgada de silicio amorfo hidrogenado (HIT)– han alcanzado eficiencias de conversión record de 26.6%, muy cercanas al límite práctico de 29.4% (para una única unión p/n). En consecuencia, la investigación y desarrollo actuales están abordando las limitantes restantes en eficiencia y costes, incluyendo la reducción de (1) la recombinación de portadores en materiales altamente dopados, (2) la absorción parásita debido a energías de banda prohibida ( $E_{gap}$ ) insuficientes y (3) los procesos térmicos (un factor crítico para obleas delgadas de 100 micras o menos, altamente sensibles a la temperatura).

En paralelo, tecnologías de capa delgada (e.g. orgánicos y perovskitas) han introducido un gran número de materiales selectivos a electrones o huecos, libres de dopantes y cuyas propiedades optoelectrónicas son comparables o superiores a las capas dopadas tipo-n o tipo-p usadas de manera estándar en c-Si. La naturaleza química de estos materiales, que abarcan polímeros orgánicos, compuestos alcalinos/alcalinotérreos y óxidos de metales de transición (TMOs), permiten su depósito mediante procesos a baja temperatura (100 °C) y presión ambiente, permitiendo una posible reducción de costes y complejidad del proceso. Es así que esta tesis explora heterouniones novedosas entre c-Si y dichos materiales de contacto selectivos, poniendo especial énfasis en capas delgadas de TMOs cuya energía de band prohibida ( $>3$  eV), pasivación superficial y alta función de trabajo ( $>5$  eV) permiten su utilización como contactos frontales, transparentes, pasivantes y selectivos a huecos en celdas con substrato tipo-n (n-Si).

La idea de dispositivos TMO/n-Si híbridos resultó de manera natural dada la experiencia previa de nuestro grupo de investigación en celdas solares tanto de c-Si como orgánicas, motivados además por el concepto más simple de celdas solar que involucra un material absorbedor (c-Si) y dos contactos adyacentes (tipo-n y tipo-p) para la separación y extracción selectiva de portadores. En este modelo simplificado, la separación de portadores mayoritarios y minoritarios ocurre mediante gradientes de conductividad localizados en cada uno de los contactos, de manera que la eficiencia final es completamente determinada por la resistencia de contacto de

mayoritarios ( $\rho_c$ ) y la corriente de recombinación de minoritarios ( $J_0$ ), siempre y cuando el resto de las variables de diseño hayan sido optimizadas.

Con este propósito, se realizó un estudio comparativo entre tres TMOs evaporados térmicamente ( $V_2O_5$ ,  $MoO_3$  and  $WO_3$ ) que permitió correlacionar su composición química con la conductividad, transmitancia óptica, pasivación y resistencia de contacto de capas delgadas sobre sustratos de n-Si. La variabilidad de estas propiedades con el grosor de las capas, su exposición al aire o a recocidos de alta temperatura también fue estudiada. En general,  $V_2O_x$  tuvo un mejor desempeño que el resto de los óxidos al obtener mayores pseudo-voltajes de circuito abierto (i.e. menores  $J_0$ ) y menores resistencias de contacto ( $\rho_c$ ), traduciéndose en una mayor selectividad. Posibles mejoras mediante intra-capas delgadas pasivantes también fueron exploradas, incluyendo  $SiO_x$  (crecido químicamente) y carburos de silicio amorfo hidrogenado a-SiC<sub>x</sub>:H (depósito químico en fase vapor asistido por plasma a 300 °C).

En seguida, un estudio detallado de la interface TMO/c-Si fue llevado a cabo mediante microscopia de electrones, espectrometría de masas de iones secundarios y espectroscopia fotoelectrónica de rayos-x, identificando dos contribuciones a la pasivación superficial: (1) un componente químico, demostrado por la presencia de una inter-capa de  $SiO_x$  formada mediante reacción química durante el depósito del TMO; y (2) un componente de “efecto de campo”, que es resultado de la fuerte inversión de la superficie ( $p^+/n$ -Si) inducida por la gran disparidad en funciones de trabajo entre ambos materiales. Bajo esta consideración, se propuso un diagrama de bandas para la heterounión TMO/ $SiO_x$ /n-Si que refleja los posibles mecanismos de pasivación y transporte de cargas.

Acto seguido, se implementaron dichas heterouniones como contactos tipo-p frontales en celdas solares finalizadas (tanto en sustratos n-Si pulidos y texturizados), con la estructura Ag/ITO(80 nm)/TMO (15 nm)/n-Si, donde el ITO –óxido de indio y estaño– sirve de capa antirreflejo conductora y la plata (rejilla metálica) como electrodo. Para el contacto tipo-n trasero, capas de a-SiC<sub>x</sub>:H dopado (20 nm) fueron utilizadas en dos configuraciones (dopado puntual por láser y contacto en área completa). El mejor desempeño se obtuvo para las celdas de  $V_2O_x/n$ -Si, caracterizadas por voltajes de circuito abierto ( $V_{OC}$ ) cercanos a 660 mV y una eficiencia máxima de 16.5%, valores relativamente altos si se considera el bajo grosor de la capa de TMO y la simplicidad del proceso de depósito. La caracterización adicional de estos dispositivos reveló factores de idealidad cercanos a 1 y una barrera interna de potencial mayor a 700 mV,

comprobando la buena calidad de la unión p<sup>+</sup>/n-Si inducida. Además, ganancias en fotocorriente de ~1 mA/cm<sup>2</sup> (para el rango de longitudes de onda de 300–550 nm) fueron directamente atribuidas a las diferencias en energías de banda prohibida entre el TMO (>2.5 eV) y la capa referencia de a-SiC<sub>x</sub>:H (~1.7 eV), confirmando el gran potencial de aplicación de este tipo de heterouniones.

Bajo un enfoque secundario, contactos tipo-p basados en soluciones poliméricas de PEDOT:PSS fueron también caracterizados para sus propiedades optoelectrónicas y de pasivación en heterouniones con n-Si, comparando dos productos comerciales (HTL Solar y PH1000). Dado una mayor pasivación y menor resistencia de contacto para HTL Solar, se obtuvo la mejor eficiencia en solo 11.6%, sufriendo grandes pérdidas de  $V_{OC}$  y factor de forma debido al recubrimiento no uniforme de la superficie texturizada. Sin embargo, estos dispositivos no utilizaron la capa de ITO, confirmando la viabilidad de nuevos conceptos que no utilizan este material escaso y costoso (indio).

Finalmente, vale la pena enfatizar el alto grado de innovación en este proyecto de tesis, reportando por primera vez las propiedades de estos materiales de contacto alternativos en el contexto de la fotovoltaica de silicio cristalino, contribuyendo a una comprensión más generalizada del diseño y operación de celdas solares.

## Summary

As the global energy demand continues to grow, the share of solar photovoltaic (PV) energy in the electricity market is projected to rise steadily, with crystalline silicon (c-Si) solar cells as the largest contributor due to its competitive prices and scalability. C-Si solar cells can be considered a highly industrialized and mature product whose state-of-the-art technology, heterojunctions with intrinsic/doped thin films of hydrogenated amorphous silicon (HIT), have achieved a record conversion efficiency of 26.6% that is not far from the practical limit of 29.4% (for single p/n junction devices). Accordingly, current research and development are addressing some remaining efficiency and cost limitations, including the reduction of (1) carrier recombination in highly doped materials, (2) parasitic absorption by narrow band gap films and (3) high temperature energy-intensive processing (critical for wafer thicknesses below 100  $\mu\text{m}$ ).

In parallel, thin-film PV (e.g. organics and perovskites) have introduced a large number of dopant-free, hole- or electron-selective materials with optoelectronic properties that are comparable or superior to standard p- and n-doped layers in c-Si. The chemical nature of these materials, comprising organic polymers, alkali/alkaline earth compounds and transition metal oxides (TMOs), also allows for low-temperature (100  $^{\circ}\text{C}$ ) vacuum-free deposition techniques that could potentially reduce costs and processing complexity. Consequently, this thesis work explores novel heterojunctions between c-Si and these carrier-selective contact materials, putting special emphasis on TMO thin films whose wide energy band gap ( $>3$  eV), surface passivation and large work function ( $>5$  eV) characteristics permit their utilization as transparent/passivating/hole-selective front contacts in n-type c-Si (n-Si) solar cells.

The idea of a hybrid TMO/c-Si device came intuitively given our research group's previous experience in c-Si and organic PV devices, motivated by the simplest solar cell concept that incorporates a photovoltaic absorber (c-Si) and two adjacent contacts (p- and n-type) for selective carrier separation and extraction. In this simplified model, majority/minority carrier separation occurs via conductivity gradients at each selective contact, in a way that the final conversion efficiency is completely determined by the majority carrier contact resistance ( $\rho_c$ ) and the minority carrier recombination current ( $J_0$ ), with all other design parameters being at an optimal value.

To this purpose, a comparative study among three thermally evaporated TMOs ( $\text{V}_2\text{O}_5$ ,  $\text{MoO}_3$  and  $\text{WO}_3$ ) allowed correlating their chemical composition with thin film conductivity, optical

transmittance, passivation potential and contact resistance on n-Si substrates. The variation of these properties with film thickness, air exposure, temperature annealings and sputtered (damaging) overlayers was also studied. Overall,  $V_2O_x$  outperformed the other oxides by obtaining a higher implied open-circuit voltage (i.e. a lower recombination current  $J_0$ ) and a lower contact resistance ( $\rho_c$ ), translating into a higher selectivity. Performance improvements by additional passivation interlayers were also explored, namely  $SiO_x$  ultra-thin films (deposited by low-temperature ambient-pressure chemical methods) and hydrogenated amorphous silicon carbide a- $SiC_x:H$  (deposited by plasma-enhanced chemical vapor deposition at 300 °C).

Next, a thorough study of the TMO/c-Si interface was performed by electron microscopy, secondary ion-mass spectrometry and x-ray photoelectron spectroscopy, identifying two separate contributions to the observed passivation: (1) a chemical component, as evidenced by a thin  $SiO_x$  interlayer naturally-grown by chemical reaction during TMO evaporation; and (2) a “field-effect” component, a result of a strong inversion ( $p^+$ ) of the n-Si surface, induced by the large work function difference between both materials. Considering all this, an energy band diagram for the TMO/ $SiO_x$ /n-Si heterojunction was proposed, reflecting the possible physicochemical mechanisms behind c-Si passivation, heterojunction formation and carrier transport.

Then, the characterized TMO/n-Si heterojunctions were implemented as front hole contacts in complete solar cell devices (planar and randomly-textured front surfaces), using thin TMO films (15 nm) contacted by an indium-tin oxide (ITO) anti-reflection/conductive electrode and a silver finger grid. As rear electron contacts, n-type a- $SiC_x:H$  thin films (20 nm) were used in localized (laser-doped) and full-area configurations, the former contacted by titanium/aluminum while the latter by ITO/silver electrodes. The best performance solar cells were obtained for  $V_2O_x$ /n-Si heterojunctions, characterized by an open-circuit voltage ( $V_{OC}$ ) close to 660 mV and a maximum conversion efficiency of 16.5%, both rather high values considering the thinness of the TMO film and the simplicity of the deposition process. Additional characterization by Suns- $V_{OC}$  and impedance spectroscopy confirmed the good quality of the induced  $p^+$ /n-Si junction, with ideality factors close to 1 and built-in potentials above 700 mV. Moreover, a photocurrent gain of  $\sim 1 \text{ mA/cm}^2$  (300–550 nm wavelength range) was directly attributed to the difference in energy band gaps between TMOs ( $>2.5 \text{ eV}$ ) and the a- $SiC_x:H$  reference ( $\sim 1.7 \text{ eV}$ ), corroborating the large application potential for this kind of heterojunctions.

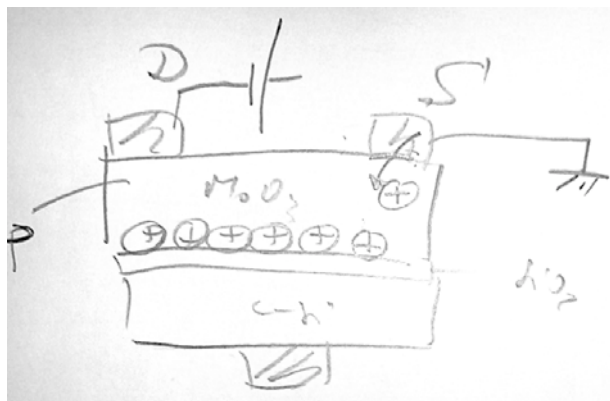


On a sideline, hole-selective contacts based on PEDOT:PSS polymer solutions were also characterized for their optoelectronic and passivation properties in n-Si heterojunctions. Of the two commercial products studied (HTL Solar and PH1000), HTL Solar exhibited a larger passivation and a lower contact resistivity, resulting in a moderate conversion efficiency of 11.6% that suffered from  $V_{OC}$  and fill factor losses (most probably attributed to an uneven coverage of the randomly-textured surface during the spin-coating process). Yet, these devices were free of an ITO layer, pointing to future concepts that avoid the utilization of this expensive and limited element (indium).

Finally, it is worth emphasizing the high degree of innovation in this thesis project, reporting for the first time the properties of these alternative contact materials in the context of c-Si photovoltaics and contributing to a more generic understanding of solar cell operation and design.

## Agradecimientos

Al parecer, fueron los antiguos griegos lo que inventaron la palabra *thesis*, que significa la *conclusión de una idea*. Esta tesis es el resultado de una idea que tuvimos Quim y yo (más Quim que yo) sobre utilizar las capas de  $\text{MoO}_3$  de las celdas orgánicas como capas tipo-p en las de silicio cristalino (a finales de Junio de 2013):



Quizás no parezca mucho, pero cuando uno entiende que las celdas de silicio se han fabricado más o menos IGUAL durante 50 años, es una idea atrevida e innovadora... y que además funcionó, y que pudimos explicar tras no sé cuántas discusiones sobre niveles de Fermi, huecos, capas de óxido, etc.

Es así que quisiera dedicar esta *conclusión* a todas aquellas personas que de alguna y otra manera han formado parte de mi vida y sin los cuales no habría recorrido este camino: a mis padres, por el invaluable ejemplo y educación que me dieron, que después de darme tantas alas decidí volar muy lejos; a mis hermanas, que me hacen ver la realidad de las cosas; a mis abuelos, por que sin ellos no estaría aquí; a mis amigos y demás familiares, porque aunque no entiendan qué es lo que hago, siempre muestran interés y sorpresa; y en especial, a Montse, mi compañera de vida de estos últimos 6 años... gracias por tu infinita paciencia.

Igualmente, agradezco a las siguientes personas:

- A Kim y Cristóbal, como directores de tesis, como amigos y como compañeros de viajes y cervezas, ya fuera en el verano de Finlandia o en el invierno de Boston... los voy a extrañar.

- A Gema, el pilar de la sala blanca: gracias por estar siempre dispuesta a ayudarme en lo que fuera; a Anna Belén, que me enseñó todo lo que sé de los equipos de la sala; a Sergi Galindo y Mehrad, que me enseñaron todo lo que sé sobre la glovebox.

- A Som, por sus experimentos con las celdas de PEDOT; a Osbel/Germá, por las medidas de capacitancia; a Thomas, por sus simulaciones y medidas de conductividad; a Raul Perea, por sus medidas de Suns-Voc; y al resto de los estudiantes que pasaron por el ‘organic group’ (Mulugeta, Maria, Robert, Denis, Thomas, Eloi y a los que olvido); a Vikas (y al profesor M. K. Jayaraj) de CUSAT, por recibirme durante aquella estancia exprés en Cochin.

- A Xavi y Miguel, por su apoyo técnico y por mantener la sala blanca siempre operativa.

- A Montse Domínguez (XPS) y Trifon Trifonov (SEM) del centro nano; a Kim Portillo (TEM) de la UB; a Judith Linacero (ToF-SIMS) del IBEC.

- A Joan Bertomeu y Miguel Asensi (Grupo de Energia Solar de la UB), por su introducción a la fotovoltaica durante el máster; y al resto de los profesores del grupo MNT: Isidro, Pablo, Moisés, Sandra; y a Ramón, por dirigir el mejor grupo de fotovoltaica de España (la verdad sea dicha).

- Y al resto de los compañeros del grupo MNT: Mónica, Arnau, Eric, Chen, Teresa, Sergi, Lucas, Chenna, David C., Didac, Dani, Mohammed, David y a los que olvido; y sobretodo al Gerard, el heredero de los TMOs (cuida’ls bé).

En materia de apoyo económico, agradecer al Consejo Nacional de Ciencia y Tecnología (CONACyT) en México, por la beca otorgada durante de 5 años para realizar el máster/doctorado; y al gobierno de España, por la financiación de los proyectos ENE2013-48629-C41R, ENE2014-56237-C41R y ENE2016-78933-C41R.

# Abbreviations

## Chapter 1

PV: photovoltaic	c-Si: crystalline silicon
CIGS: Copper-Indium-Gallium Selenide	a-Si:H: hydrogenated amorphous silicon
ARC: anti-reflection coating	BSF: Back-surface field
TCO: Transparent conductive oxide	PBDT: Poly(benzodithiophene)
P3HT: Poly(3-hexylthiophene-2,5-diyl)	MAPbI <sub>3</sub> : Methylammonium lead iodide
PCBM: Phenyl-C <sub>61</sub> -butyric acid methyl ester	SHJ: silicon heterojunction
PTAA: Polytriarylamine	IBC: Interdigitated back-contact solar cell
HIT: Heterojunction with intrinsic thin-film	$E_{gap}$ : Energy band gap (eV)
$E_C$ : Conduction band energy (eV)	$E_V$ : Valence band energy (eV)
PERL/T: Passivated-emitter rear locally/totally-diffused solar cell	PEDOT:PSS: Poly(3,4-ethylenedioxythiophene)-poly(styrenesulfonate)

## Chapter 2

$\eta$ : electrochemical potential (eV)	$\mu_{chem}$ : the chemical potential (eV)
$\varphi$ : electric potential (eV)	$e / h$ : electron/hole
$\gamma$ : photon	$\vec{E}$ : electric field (V/cm)
$q$ : carrier elementary charge (C)	$E_F$ : Fermi energy level (eV)
$E_{F0}$ : equilibrium Fermi energy level (eV)	$E_{Fn} / E_{Fp}$ : quasi-Fermi energy levels
$\Phi$ : work function (eV)	$E_c / E_v$ : conduction/valence band (eV)
$J_e / J_h$ : current density (A/cm <sup>2</sup> )	$V$ : voltage (V)
$\nabla$ : the gradient operator	$\sigma_e / \sigma_h$ : conductivity (S/cm, $\Omega^{-1}\text{cm}^{-1}$ )
$k$ : Boltzmann constant (eV/K)	$J_{rec}$ : recombination current (A/cm <sup>2</sup> )
$n$ : ideality factor	$kT/q$ : thermal voltage (V)
$\varphi_B$ : barrier height (eV)	$J_{ph}$ : photocurrent (A/cm <sup>2</sup> )
$V_{OC}$ : open-circuit voltage (V)	$J_{SC}$ : short-circuit current (A/cm <sup>2</sup> )
$V_{bi}$ : built-in voltage (V)	$N$ : volume concentration (cm <sup>-3</sup> )
$n / p$ : electron/hole concentrations (cm <sup>-3</sup> )	$n_i$ : intrinsic carrier concentration
$\mu$ : carrier mobility (cm <sup>2</sup> /Vs)	$D$ : carrier diffusivity (cm <sup>2</sup> /s)
MPP: maximum power point	$P$ : power (W/cm <sup>2</sup> )
$FF$ : fill factor (%)	$PCE$ : power conversion efficiency (%)
$R_S / R_P$ : series/parallel resistance ( $\Omega\cdot\text{cm}^2$ )	$R_C$ : contact resistance ( $\Omega$ )
$R_{sh}$ : sheet resistance ( $\Omega / \square$ )	$\lambda$ : wavelength (nm)
$\alpha$ : absorption coefficient (cm <sup>-1</sup> )	$n$ : refractive index
$W$ : absorber thickness ( $\mu\text{m}$ )	$A$ : absorptance (%)

*Z*: optical path enhancement factor  
*S*: surface recombination velocity (cm/s)  
 $\sigma_{CCS}$ : electron/hole capture cross section ( $\sim 10^{-15}$  cm<sup>2</sup>)  
 $R_0$ : cumulative recombination (cm<sup>2</sup> s<sup>-1</sup>)  
 $v_{th}$ : thermal velocity ( $\sim 10^7$  cm/s)  
 $S_\phi$ : index of interface behavior  
 $\Phi_B$ : metal-semiconductor barrier (V)  
*I*: ionization potential (eV)  
 $C_A$ : Auger recombination rate constant ( $1.66 \times 10^{30}$  cm<sup>-6</sup>)  
 $N_C / N_V$ : effective density of states in the conduction/valence bands (cm<sup>-3</sup>)  
 $J_M$ : majority carrier current densities (A/cm<sup>2</sup>)  
 $f_c$ : contacted area fraction

SRH: Shockley-Read-Hall  
 $\tau_{eff}$ : effective lifetime ( $\mu$ s)  
 $N_C / N_V$ : effective density of states in the conduction/valence bands (cm<sup>-3</sup>)  
 $D_{it}$ : density of surface states (cm<sup>-2</sup>)  
 $\phi_s$ : surface band bending (V)  
 $\chi$ : electron affinity (eV)  
 $\Delta_d$ : interface dipole (V)  
 $S_{I0}$ : logarithmic selectivity  
 $J_{TE}$ : thermionic emission current pre-factor (A/cm<sup>2</sup>)  
 $J_0$ : dark saturation/thermal generation current (A/cm<sup>2</sup>)  
 $J_m$ : minority carrier current densities (A/cm<sup>2</sup>)  
 $\rho_c$ : specific contact resistance ( $\Omega \cdot \text{cm}^2$ )

### Chapter 3

RCA: wafer cleaning standard  
*R*: Reflectance (%)  
 SEM: scanning electron microscopy  
 RF: radio frequency  
*p*: pitch  
 $\rho$ : film resistivity ( $\Omega \cdot \text{cm}$ )  
*G*: conductance ( $\Omega^{-1}$ )  
 UV: ultraviolet  
 IQE: internal quantum efficiency (%)  
 $R_{spr}$ : spreading resistance ( $\Omega$ )  
 $L_T$ : effective transfer length (cm)  
*d*: distance between contacts (cm)  
*Z*: impedance ( $\Omega$ )  
 $\epsilon$ : permittivity (F/cm)  
 XPS: x-ray photoelectron spectroscopy  
 PECVD: plasma-enhanced chemical vapor deposition  
 amu: atomic mass units

ITO: indium-tin oxide  
 TMAH: tetramethyl ammonium hydroxide  
*r*: laser crater radius  
 DMSO: dimethyl-sulfoxide  
*d*: film thickness (nm)  
 EQE: external quantum efficiency (%)  
 NIR: near-infrared  
 $A_c$ : contact area (cm<sup>2</sup>)  
 TLM: transfer length method  
*Z*: contact width (cm)  
 $\omega$ : angular frequency (radians)  
*C*: capacitance (F/cm<sup>2</sup>)  
*T*: transmittance (%)  
 TEM: transmission electron microscopy  
 FIB: focused ion beam  
 ToF-SIMS: time of flight secondary ion mass spectrometry

## Chapter 4

$h$ : Plank's constant (eV·s),

$T$ : transmittance (%)

$G$ : Gibbs free energy (kJ/mol)

$\Delta BE$ : chemical shift (eV)

$R$ : average intra-cation distance (Å)

$\nu$ : wave frequency (s<sup>-1</sup>)

BE: binding energy (eV)

$h$ : Plank's constant (eV·s)

$C$ : cation concentration (%)

## Chapter 5

$E_a$ : activation energy (eV)

$W_j$ : depletion layer width (nm)

# 1 Introduction

*On how the current global energy problem can be alleviated by solar photovoltaic technology: lowering its fabrication cost through innovative processes and novel carrier-selective materials it's the motivation of this thesis.*

## 1.1 Context

Ever since the first commercial oil field began exploitation in the late 1800s, a cheap and apparently unlimited source of energy made possible a second industrial revolution whose prime technological commodity, the internal combustion engine, led to modern electricity generation and land transportation. However, the extraction of millions of tons of hydrocarbons from the underground has had the expected consequence of perturbing the carbon cycle, releasing into other natural sinks (atmosphere, oceans) a carbon reservoir that was probably meant to stay untouched. Although accounting techniques for global carbon inventories are complex and widely spread, it has become clear that CO<sub>2</sub> in the atmosphere is increasing as a consequence of anthropogenic green house emissions, which could lead to an average increase in global temperatures of 1–2 °C by the year 2050 under current energy consumption scenarios [1]. Given that energy helps to satisfy basic needs (cooking, heating) and triggers productivity and socioeconomic growth, it is also clear that the global warming problem is being catalyzed by the exponential energy demand of an exponentially growing population (Fig. 1.1).

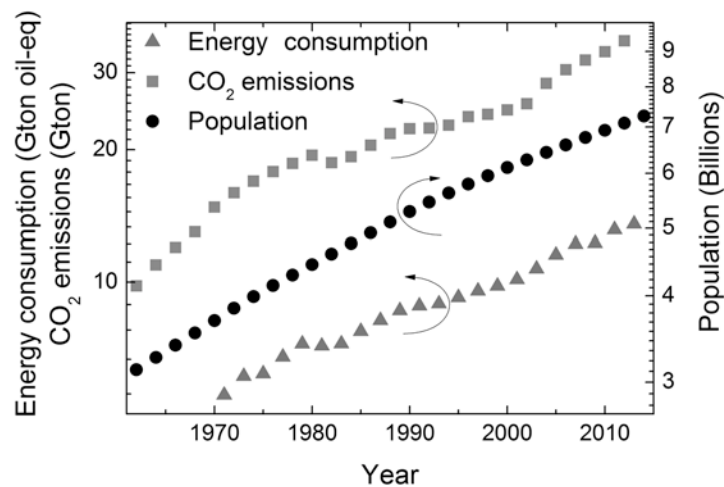


Figure 1.1 Evolution of the global energy consumption (Gton oil-equivalents), CO<sub>2</sub> emissions (Gton) and population during the last 50 years [2].

In addition to the unsustainability aspect, this situation is exacerbated by the unequal access to energy sources, leading to large disparities in human development. A snapshot of the Human Development Index (HDI) versus energy consumption per capita (Fig. 1.2) poses the following questions. How to provide electricity to 1.2 billion people that has no access to it? How to increase the welfare of 2.7 billion people that still depend on biomass for heating and cooking [3]? What will be the environmental impact of India and China when they reach the living standard of European countries? Even though the strategy to overcome this problematic situation is multifaceted, the technological answer is one and only: renewable energies, which are non-polluting, unlimited and widely accessible, will have to substitute fossil-based energy sources.

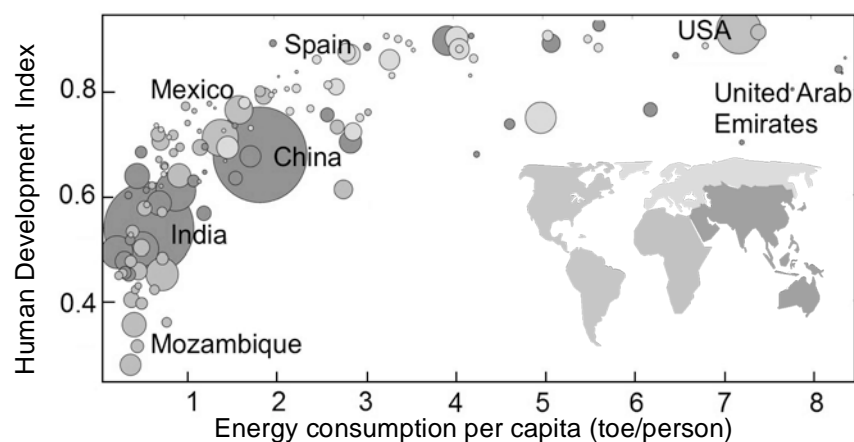


Figure 1.2 Human Development Index (HDI) vs. energy consumption per capita (in ton of oil equivalents, toe) for the year 2010. Size of bubble represents country population. Adapted from [4].

Consequently, renewable energy installations have boomed in the past 15 years, globally accounting for 19.2% of the final energy needs and 23.7% of the electricity market [5]. Furthermore, the share of renewables in electricity generation is expected to increase to 60% by 2040, with wind and solar comprising more than half of new installed capacity [6]. In particular, solar is the largest energy resource with  $120 \times 10^3$  TWh reaching the Earth surface every hour, enough to satisfy the global energy needs during a whole year.

### 1.1.1 Solar photovoltaic energy

Solar energy can be harvested in two different ways: 1) via temperature gradients, storing heat in a fluid and later releasing it by mechanical (steam turbine) or thermal (hot-water irradiators) processes; and 2) via electrochemical gradients, transforming the energy of the solar spectrum directly into electricity, a process known as photovoltaic (PV) effect. Ever since the first PV



solar cell was invented in the 1950s, research has allowed going from a mere 6% conversion efficiency to a record 46%<sup>1</sup> [7]. This has allowed solar cells to become a commercial product and cost-competitive technology, totaling an installed capacity of 227 GW<sup>2</sup> worldwide at the end of 2015. During the same year, one third of new electrical capacity was photovoltaic, most of it in China and Japan [5]. The impulse behind this massive deployment is being driven by:

- Minimum operational and maintenance costs along with a steady decrease in PV module prices from 10 to 0.6 €/W<sub>peak</sub> in the past 25 years [8].
- High resource availability, making PV financially viable even in countries with low solar irradiation (such as Germany, the leading country in PV installations).
- Installation flexibility as centralized grid-connected plants (>100 MW) or decentralized (and sometimes grid-independent) stations (<100 kW).
- Local and country level regulations with renewable energy targets, along with financial schemes that favor its installation (feed-in tariffs, net-metering, etc.).
- The capability to power zero-emission technologies, such as electric vehicles.

In essence, a solar cell consists of a semiconductor material that absorbs photons from the electromagnetic spectrum and generates charge carriers of opposite polarity, negative (n) electrons and positive (p) holes, whose flow results in a photocurrent (Fig. 1.3). Carrier separation occurs due to electrochemical gradients established by hole- and electron-selective contacts adjacent to the absorber [9]. The purpose of such contacts, accomplished by selectively doping the absorber (homojunction) or another semiconductor (heterojunction), is to preferentially conduct one type of carrier while blocking the other. Therefore, each carrier is collected in opposite metal electrodes (anode and a cathode). Failure to collect carriers results in electron-hole recombination, measured as a reduction of the effective carrier lifetime. Recombination is primarily promoted by structural defects in the absorber, either on its bulk (grain boundaries, impurities) or its surface (dangling bonds), and it is the most important detrimental factor to solar cell performance.

---

<sup>1</sup> 6% for silicon single junction device; 46% for III-V semiconductor four-junction device under light concentration.

<sup>2</sup> 1 GW (giga-watt) = 1,000,000 kW (kilo-watt), average power consumption in 200,000 households.

Taking as an example a classic p-type c-Si solar cell [10], where the boron-doped wafer is the main absorber<sup>3</sup>, the front electron contact (emitter) is formed by thermally diffusing phosphorous from a gas source at a precise concentration profile, turning the surface into n-type. Similarly, the rear hole contact (i.e. the back-surface field, BSF) is formed by p<sup>+</sup>-doping with aluminum (Al) metal during a contact-firing step. Following photon absorption, photogenerated carriers are then collected by a pair of metal electrodes, a silver (Ag) front grid and the Al rear electrode. Additional layers that improve device performance include anti-reflection coatings (ARC) to maximize light absorption, passivation layers to decrease carrier recombination at the surfaces and transparent conductive oxides (TCO) for carrier collection. Under this simplified model, the basic structure of all PV technologies becomes evident in spite of the enormous differences in materials and architecture, as seen in Table 1.

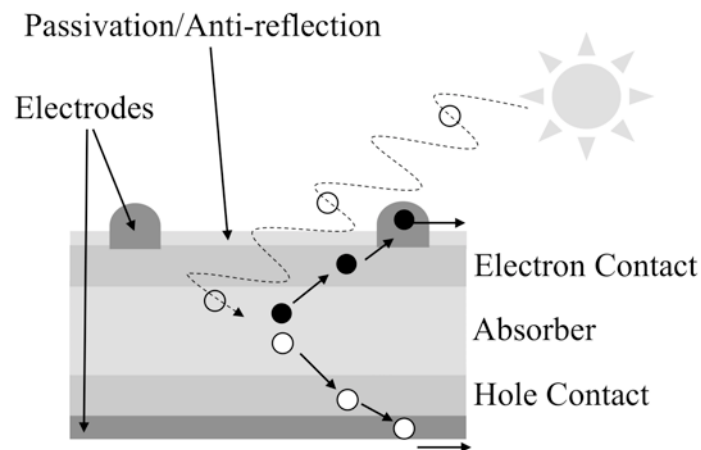


Figure 1.3 Elements of a solar cell

Crystalline silicon (c-Si) is traditionally the semiconductor of choice in photovoltaic applications and accounts for 93% of the PV market,  $\frac{3}{4}$  of which is multi-crystalline (Bridgman process) and the rest mono-crystalline (Czochralski process) [8]. The remaining 7% comprises thin-film semiconductor materials like cadmium telluride (CdTe), copper-indium-gallium diselenide (CuInGaSe<sub>2</sub>, or CIGS) and hydrogenated amorphous silicon (a-Si:H), materials whose higher absorption coefficient allows for thinner absorber layers compared to c-Si. As for PV technologies based on III-V elements, such as gallium arsenide (GaAs) and multi-junction devices, they are produced exclusively for high-end applications (light concentration, satellites), while organic PV devices are just in the initial commercialization phase [11].

<sup>3</sup> Although ~35% of incident photons are absorbed in the first 0.3  $\mu\text{m}$  (emitter region), the rest of the wafer is the main absorber.

Table 1.1 Material components of the main PV technologies under current development.

Technology	p-Contact	Absorber	n-Contact	Electrodes
c-Si Homojunction [10]	Al doped (p <sup>+</sup> )	B doped c-Si (p)	P doped (n <sup>+</sup> )	Al/Ag
c-Si Heterojunction [12]	B doped a-Si:H (p <sup>+</sup> )	P doped c-Si (n)	P doped a-Si:H (n <sup>+</sup> )	TCO/Ag
GaAs [13]	Zn doped GaAs (p <sup>+</sup> )	GaAs (p)	Si doped GaAs (n <sup>+</sup> )	Au-Be/Au-Ge
a-Si:H [14]	B doped a-Si:H (p <sup>+</sup> )	a-Si:H (i)	P doped a-Si:H (n <sup>+</sup> )	TCO/Al
CdTe [15]	C:Cu <sub>x</sub> Te (p <sup>+</sup> )	CdTe (p)	CdS (n)	TCO/Ag
CIGS [16]	MoSe <sub>2</sub> (p <sup>+</sup> )	CuInGaSe <sub>2</sub> (p)	CdS (n)	Mo/TCO
Organic [17]	PEDOT:PSS (p <sup>+</sup> )	PBDT(p):PCBM(n)	Mg (n <sup>+</sup> )	Al
Quantum Dots [18]	PbS (p <sup>+</sup> )	PbS (p)	ZnO (n)	TCO/Au
Dye-sensitized [19]	iodide/triiodide (p <sup>+</sup> )	Ru organometallic (p)	TiO <sub>2</sub> (n)	TCO/Pt
Kesterite [20]	Mo-ZnO (p <sup>+</sup> )	Cu <sub>2</sub> ZnSnS <sub>4</sub> (p)	CdS:Zn (n)	Mo/TCO
Perovskite [21]	PTAA (p <sup>+</sup> )	MAPbI <sub>3</sub> (p)	TiO <sub>2</sub> (n)	TCO

Since its conception in the 1950s, the development of thin-film PV has been oriented towards lowering fabrication ( $\text{€}/W_{\text{peak}}$ ) and produced energy costs ( $\text{€}/\text{kWh}$ ). However, they offer additional advantages from a life-cycle<sup>4</sup> perspective such as low environmental impact and short energy pay-back times, especially when energy-intensive process conditions such as vacuum and high temperatures are avoided (see appendix A for a further discussion of these assessment variables). This is as a direct result of a lower material utilization ( $<10 \mu\text{m}$  absorber) in comparison to c-Si (180  $\mu\text{m}$  wafers), although real deployment costs are very similar for both technologies because of the higher industrial maturity of c-Si [8].

The most important and common parameter used to assess the viability of novel materials and new solar cell designs is the power conversion efficiency (*PCE*), defined as an output/input energy ratio (electric power/incident solar radiation). Every PV technology strives for high efficiencies even if it is not representative of their true potential, given that *PCE* is area-dependent<sup>5</sup> and not all cells are easily scalable into practical-size modules. Fig. 1.4 summarizes all PV technologies and their certified milestone conversion efficiencies. It is worth noting that c-Si efficiencies have been approximately steady since 1995 while new-coming perovskites have increased from 14% to 22% in only five years.

<sup>4</sup> Considering all the material/energy inputs and outputs that occur during fabrication, installation, operation and decommission.

<sup>5</sup> Organic PV demonstrations rarely exceed 1  $\text{cm}^2$ , while record efficiencies for c-Si have been achieved in 180  $\text{cm}^2$ .

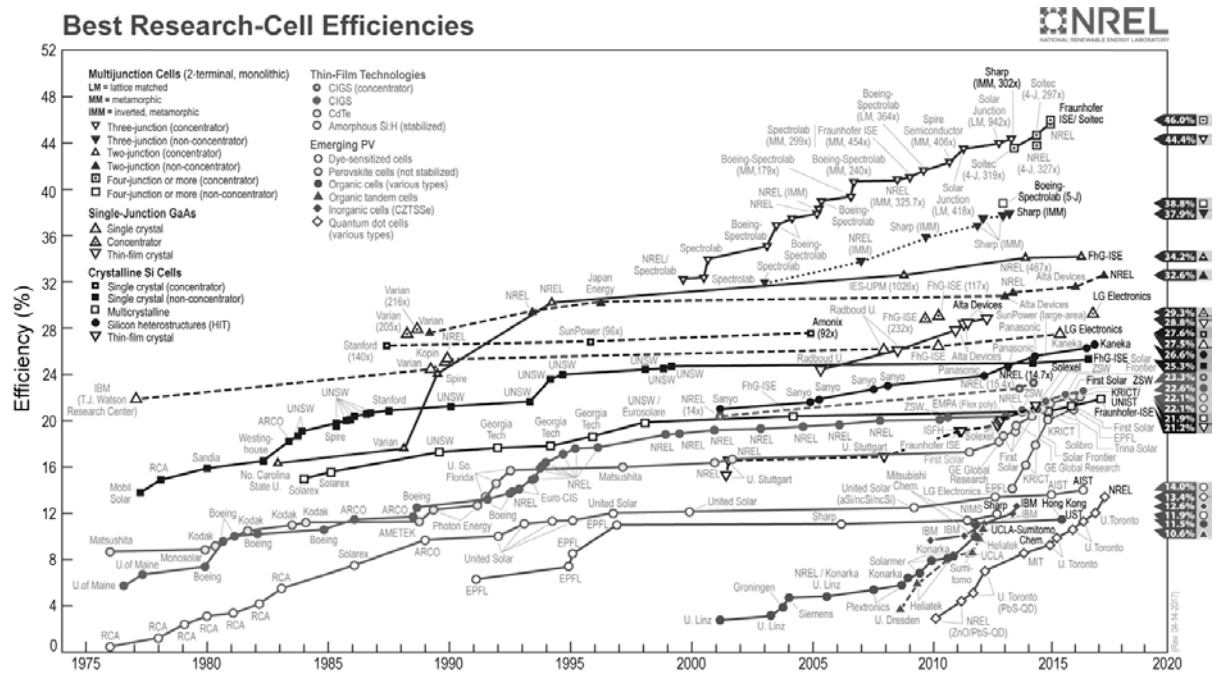


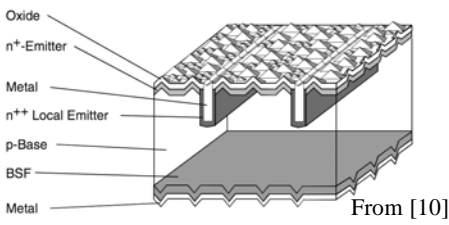
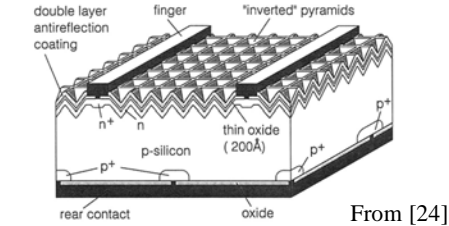
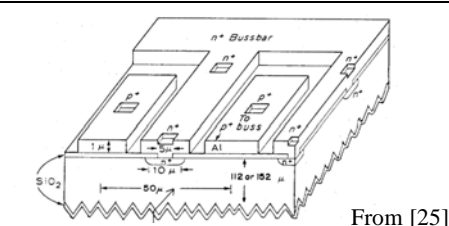
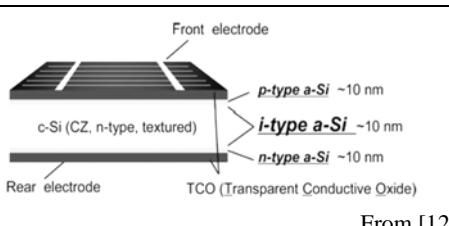
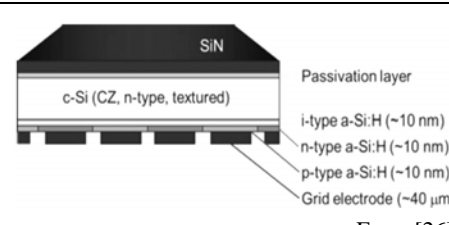
Figure 1.4 Evolution of record conversion efficiencies by PV technologies [22].

### 1.1.2 Crystalline silicon solar cells

For many years, the industrialization of c-Si PV has relied on Al BSF solar cells with p-type wafers that reach conversion efficiencies between 16% (multi c-Si) and 18% (mono c-Si) (Table 1.2a). This design, although simple and economic, is severely limited by high recombination losses at the backend, where c-Si is in direct contact with Al [23]. These and other limitations were overcome in 1995 with the passivated-emitter rear locally-diffused (PERL) concept [24], with SiO<sub>2</sub> passivating most of the wafer surface except for local openings where p<sup>+</sup> (rear) and n<sup>+</sup> (front) regions are in contact with the metal electrodes (Table 1.2b). Additionally, light absorption was maximized by an inverted pyramid patterning and a double ARC, resulting in a milestone conversion efficiency of 24% that remained, with minor differences, as the state-of-the-art technology for 20 years.

The next logical improvement in design was to maximize light absorption by eliminating the shadow losses from the front electrode grid and have both anode and cathode electrodes in the rear side of the device, known as interdigitated back-contact (IBC) solar cell (Table 1.2c). This concept, originally designed for light concentration applications in the 1970s [25], has demonstrated an efficiency of 25.2% and is currently being commercialized by SunPower [11].

Table 1.2. Different c-Si solar cells architectures available on the market.

Architecture of c-Si solar cell	Characteristic improvement	Record PCE/year
 <p>From [10]</p>	<p>a) <i>Al BSF</i></p> <p>Full-area rear p-contact. Screen-printed electrodes. Passivated front, local contacts. Contact-firing step.</p>	<p>&lt;19.5% / 2016 [23]</p>
 <p>From [24]</p>	<p>b) <i>PERL/PERT/PERC</i></p> <p>Passivated front/rear, local contacts. Double ARC/inverted pyramids. Screen-printed electrodes. Contact-firing step.</p>	<p>25.0% / 2015 [11]</p>
 <p>From [25]</p>	<p>c) <i>IBC</i></p> <p>Full area front/rear passivation. Rear local contacts. No front grid shadow losses. n-type wafer; no contact-firing.</p>	<p>25.2% / 2012 [11]</p>
 <p>From [12]</p>	<p>d) <i>HIT</i></p> <p>Full area front/rear passivated contacts + TCO (ARC, electrode). a-Si:H deposition at T&lt;250 °C. 110 μm thick n-type wafer.</p>	<p>24.7% / 2014 [12]</p>
 <p>From [26]</p>	<p>e) <i>HIT-IBC</i></p> <p>Full area front/rear passivation. Rear local contacts. No front grid shadow losses. a-Si:H deposition at T&lt;250 °C.</p>	<p>26.6% / 2017 [27]</p>

For both IBC and PERL solar cells, up scaling to industry levels is complicated and expensive due to their multilayered structure and sub-millimeter intra-contact patterning. These shortcomings are resolved by silicon heterojunction technology, which utilizes a semi-insulating material to accomplish full-area passivation of the rear and front surfaces while permitting carrier transport. To achieve this, a thin bilayer (<20 nm) of intrinsic/doped a-Si:H is deposited on both sides of the c-Si wafer by plasma-enhanced chemical vapor deposition, using silane (SiH<sub>4</sub>) as gas precursor and boron/phosphorous sources as dopants. This results in a heterojunction with intrinsic thin-film (HIT) solar cell (Table 1.2d), the state-of-the-art PV

technology currently commercialized by Panasonic with efficiencies above 24% [12]. Through the utilization of a thin-film material, the HIT design also benefits from a lower deposition temperature ( $T \sim 250 \text{ }^\circ\text{C}$  for a-Si:H) in comparison to standard thermal diffusion ( $T \sim 900 \text{ }^\circ\text{C}$ ). The most recent advance in SHJ technology combines the IBC and HIT concepts (Table 1.2d), profiting from no shadow losses and full-area passivation, recently attaining a record efficiency of 26.6% as disclosed by Kaneka Corporation [27].

Considering that state-of-the-art c-Si devices are not far from the practical efficiency limit of 29.4% [28]<sup>6</sup>, it could be said that the most serious technological challenges have been overcome. Yet, further improvements in efficiency will require a number of innovations for the near future, both in research and in industry [23,29,30]:

- Given that c-Si wafers<sup>7</sup> comprise 35–50% of the final module cost and 75% of the manufacturing energy input [31], wafer thickness will continue to decrease below  $180 \text{ } \mu\text{m}$ <sup>8</sup>. In this regard, kerf-less alternatives are being developed including direct casting [32], epitaxial growth [33] and film re-crystallization [34].
- Materials with restrictive costs, such as screen-printing Ag pastes and indium-based TCOs, could eventually be replaced by more Earth-abundant materials such as Cu plating [35] and Zn-based TCOs [36].
- Losses in photocurrent or photovoltage will be avoided as much as possible using the following approaches: *a)* maximizing photon absorption through highly transparent front layers [37] coupled with advanced optics strategies such as nanotextured front [38] and rear surfaces [39]; *b)* minimizing recombination in the bulk and carrier-selective regions; *c)* minimizing contact resistivities in metal-semiconductor interfaces [40] and increasing TCO bulk conductivities [41] (although practical limits exist as every material has a finite conductivity).

---

<sup>6</sup> This practical limit is ~4% lower than the theoretical maximum of 33% (known as Shockley-Queisser limit) due to unavoidable Auger recombination losses and other technical limitations.

<sup>7</sup> Includes the production of metallurgical grade silicon (Siemens process), ingot formation and diamond-wire wafering.

<sup>8</sup> Considering that kerf losses during diamond-wire wafering account to  $\sim 100 \text{ } \mu\text{m}$  for every cut wafer [23].

- Since manufacturing simplicity favors higher throughputs, full-area depositions will be preferred to localized or interdigitated designs [42], unless some of the patterning steps could be avoided or simplified.
- N-type substrates will increase their market share due to higher effective lifetimes and lack of light-induced degradation (caused by the formation of boron–oxygen complexes [23]). Nonetheless, no metallic element is capable of n<sup>+</sup>-doping an n-type wafer by simple contact-firing (as is the case of Al in p-type wafers), which means that most n-type cells will continue to be fabricated with HIT/IBC architectures.
- Finally, depending on the development of new deposition techniques, lower thermal budgets will be preferred, mainly to increase compatibility with ultra-thin wafers but also to reduce energy consumption and cost [29,43]. This could be facilitated by novel heterojunctions between c-Si and other thin-film materials, in the same manner as a-Si:H/c-Si heterojunctions led to the development of HIT technology.

This latter point, the implementation of carrier-selective thin-film materials into c-Si heterojunction solar cells, constitutes the major motivation behind this thesis, as will be discussed next.

## 1.2 Thesis motivation

Revisiting the simplified solar cell model in Fig 1.3, it is clear that the p- and n-type layers used in c-Si absorbers act as ‘semi-permeable filters’ whose selectivity towards a particular charge carrier enables the separation of electrons from holes. However, the utilization of the *carrier-selective contact* concept in c-Si PV is relatively new [9,44], even though it presents a more accurate interpretation of the underlying physics than the popular terminology *emitter*, *base* and *back-surface field*, adopted from the bipolar transistor field. For instance, no actual emission of carriers occurs during solar cell operation, whereas it has been shown that electric fields do not play a determining role under illumination conditions [9,44].

For the micro- and nano-technologies (MNT) group at UPC, these ideas came naturally as a result of our previous experience in organic PV and organic electronics<sup>9</sup>, two research fields where significant improvements in device performance can be attributed to the exploitation of selective contacts and their properties [45]. In this aspect, the experimental work performed in 2013 during the master thesis [46] can be considered as a prelude to the present work, posing the following questions: Why not utilize dopant-free selective materials in c-Si heterojunctions? Could a semi-insulating metal oxide with n-type conductivity substitute phosphorous doping? Furthermore, could a semi-transparent conductive polymer work as front collecting electrode? What are the energetic and cost benefits of depositing selective contacts by low-temperature/vacuum-free processes?

In order to justify the selection of a particular carrier-selective material, it is useful to address the disadvantages attributed to boron- and phosphorous-doped layers. In this sense, the material of choice must have a few basic characteristics:

*Dopant-free:* thermal diffusion at high doping concentrations increases carrier recombination and band gap narrowing [47]. Similarly, doped a-Si:H is highly recombinative and forcefully requires a buffer intrinsic layer [48]. Ideally, a dopant-free contact could avoid these undesirable effects while maintaining its selectivity.

*Passivating:* insulator materials ( $\text{SiN}_x$ ,  $\text{SiO}_2$ ,  $\text{Al}_2\text{O}_3$ ) are commonly used as surface passivants, but their insulating nature prevents carrier conduction. By using a semiconducting material with passivation properties (analog to a-Si:H), carriers can be extracted while keeping recombination and resistive losses to a minimum, yielding a *passivating/selective* contact [40,49].

*Highly transparent:* even though intrinsic/doped a-Si:H layers in HIT devices are no thicker than 20 nm, their optical transparency is far from optimal (energy band gap  $E_{gap} \sim 1.7$  eV) resulting in parasitic absorption losses at the front of the device. Wider band gap ( $E_{gap} > 3\text{eV}$ ) materials would be more transparent to the incident light and therefore more appropriate as selective contacts.

---

<sup>9</sup> Including Organic Light Emitting Diodes (OLEDs) and Organic Thin-Film Transistors (OTFTs).



*Low-temperature deposited:* as c-Si substrates become thinner, the probability of wafer warping and thermal strain between dissimilar materials increases [50]. In this sense, a multitude of carrier-selective materials can be deposited at ambient temperature and/or ambient pressure conditions, including solution-based processes [51]. This in turn reduces the cost and energy input of fabrication.

*Non-toxic/non-flammable:* the dopant-carrying compounds used in homojunctions ( $\text{POCl}_3/\text{BBr}_3$  from liquids) and heterojunctions ( $\text{PH}_3/\text{B}_2\text{H}_6$  in  $\text{SiH}_4$  gas mixtures) are usually toxic and/or flammable, making redundant safety measures mandatory<sup>10</sup>. The utilization of non-toxic/non-flammable dopant-free materials would greatly reduce process complexity and occupational safety considerations.

*Mechanically/chemically stable:* the most important feature of c-Si solar cells is their stability (25 or more years expected lifetime). Any novel material must have good adherence/stability properties with c-Si and its contact electrodes, both during the fabrication and long-term operation of the device.

Taking into account the evolution of c-Si technology up to date, and given the large variety of carrier-selective contacts complying with the above characteristics (Table 1.1), three types of materials will be considered as alternative contacts in this doctoral work:

- 1) *Transition metal oxides* (inorganic), wide band gap semiconductors with marked p- or n-type characteristics and a broad range of work functions [52].
- 2) *Conductive polymers* (organic) deposited by solution casting, of which PEDOT:PSS<sup>11</sup> is the hole-selective material ‘par excellence’ [53].
- 3) *Alkali/alkaline earth* compounds (inorganic), electric insulators which facilitate electron transport when used as thin layers in the semiconductor/metal interface [54].

---

<sup>10</sup> Historical data (1994-2004) shows that 28% of incidents/injuries in PV industry are due to HF handling, 8% (including 4 fatalities) due to precursor gases ( $\text{SiHCl}_3$ ,  $\text{SiH}_4$ ) and only 1% due to doping compounds [77].

<sup>11</sup> Abbreviation for poly(3,4-ethylenedioxythiophene):poly(styrene-sulfonate)

Fig. 1.5 shows the energy band diagram of the carrier-selective materials that will be studied in the course of this thesis, referenced to the valence ( $E_V$ ) and conduction ( $E_C$ ) band of c-Si. Also shown is the approximate work function  $\Phi$  (Fermi level) of these materials, which dictates how they interact with either p- or n-type c-Si in order to form hole-selective ( $V_2O_5$ ,  $MoO_3$ ,  $WO_3$ ,  $ReO_3$ , NiO and PEDOT:PSS) or electron-selective (LiF,  $TiO_2$ <sup>12</sup>) contacts. In this sense, it is worth noting the relative abundance of hole-selective materials in the literature whereas electron-selective materials are scarcer [52].

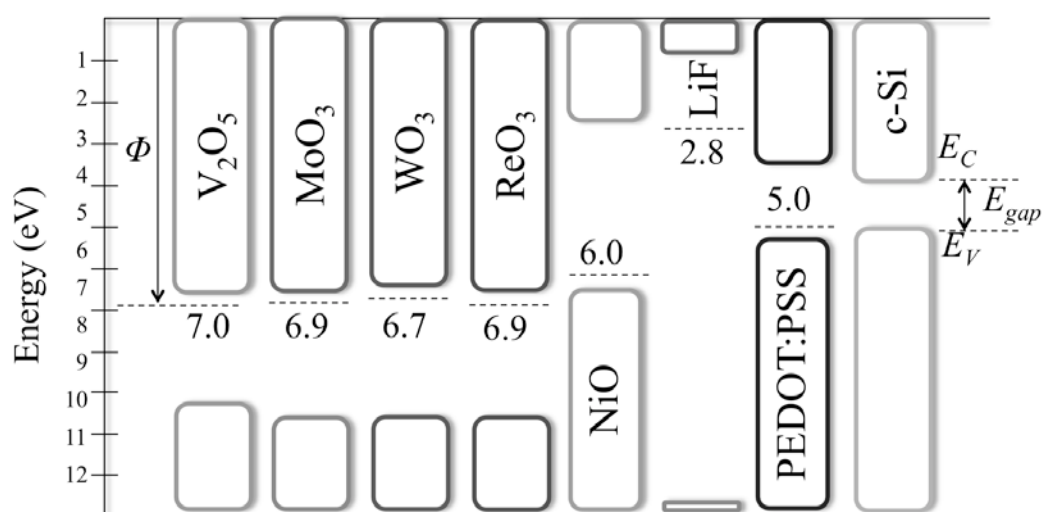


Figure. 1.5 Energy band diagram of c-Si and selected carrier-selective materials, showing their work function  $\Phi$  (eV).

### 1.2.1 State-of-the-art

Given our group's trajectory on HIT and IBC solar cell fabrication, the implementation of a dopant-free selective contact into a c-Si device was relatively straightforward. In a first proof-of-concept at the end of 2013,  $MoO_3$  thin films (a frequently used hole-selective contact in organic PV) were thermally evaporated as a front contact in a full-area configuration followed by an ITO capping layer (similar to the HIT cell architecture), leading to a conversion efficiency of 12.5% [55]. Before this demonstration, only a few reports existed regarding TMO/c-Si hybrid devices, namely  $TiO_2$  [56] as an electron contact and none for TMO-based hole-contacts (except for TCO/n-Si devices [57]). In early 2014, Battaglia et al. published another proof-of-concept solar cell with  $MoO_3$ -based hole-selective contacts, reaching a conversion efficiency of 14.3% [58].

<sup>12</sup>  $TiO_2$  contacts deposited by atomic layer deposition (ALD) were developed in parallel to this thesis by other members of the MNT group, resulting in one publication (see Appendix C).

This initiated a trend in the development of TMO/c-Si devices, with MoO<sub>3</sub> as a hallmark study case [59–61] but also including WO<sub>3</sub> [62], V<sub>2</sub>O<sub>5</sub> [63] and NiO [64], demonstrating a record efficiency of 22.5% for a MoO<sub>3</sub> device using an a-Si:H passivating interlayer in a HIT-like configuration [65]. Most recent advances include IBC-like architectures [66,67] (19% conversion efficiency) and TMO deposition by solution-based processes [68,69].

For the case of hybrid polymer/c-Si devices, several precedents existed including poly(3-hexylthiophene) (P3HT) [70] and PEDOT:PSS [71,72] as hole-selective contacts, of which an outstanding 20.6% conversion efficiency has been recently reported [73]. Heterojunctions with electron-selective contacts based on alkali/alkaline earth materials such as LiF [74] have been scarcer but with promising results approaching 20% conversion efficiency [75]. Most of the above reports have focused on n-type c-Si substrates, with all of them substituting only one type of carrier-contact (i.e. MoO<sub>3</sub> instead of p-type a-Si:H) while using standard doping for the other (n-type a-Si:H). However, showcase examples that substitute both carrier-contacts by dopant-free materials have also been reported [66–68], attaining a record conversion efficiency of 19.4% in a MoO<sub>3</sub>/n-type c-Si/LiF device with a-Si:H and TiO<sub>2</sub> passivating interlayers [76].

### 1.3 Objective and thesis structure

The main objective of this thesis is the implementation of dopant-free carrier-selective materials into c-Si solar cells as an alternative to boron/phosphorous doped layers, developing novel proof-of-concept solar cell architectures that could potentially reduce the fabrication cost by simple low-temperature/vacuum-free processes while maintaining competitive conversion efficiencies.

More specifically, this thesis project was undertaken in three parallel stages:

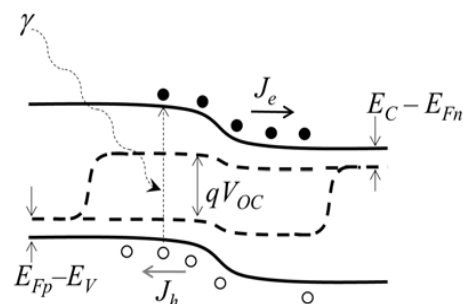
- I. Material characterization, focusing on the optoelectronic properties of TMOs and (in a minor degree) of PEDOT:PSS and LiF, with emphasis on the chemical nature of the heterojunction interface;
- II. Elucidation of the physics behind the passivation of the c-Si surface, the energy band structure and the carrier transport processes across the heterojunction;

- III. Fabrication and characterization of finished solar cell devices, with attention to all relevant design variables.

Accordingly, this thesis is divided in the following chapters:

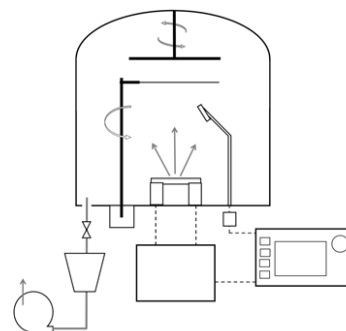
### Chapter 2: Theoretical background

A review on the solar cell operation principles is given, putting emphasis on electrochemical potentials as the driving force for current flow. The main performance parameters are defined, while the requirements for recombination, selectivity and contact resistivity justify the need for *passivating-selective* contacts.



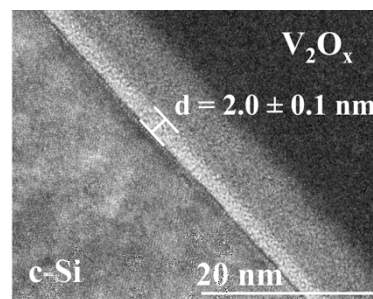
### Chapter 3: Experimental methods

This chapter describes the experimental methods for solar cell fabrication and characterization, including the techniques used for determining the optoelectronic, structural and compositional properties of the carrier-selective materials under study.



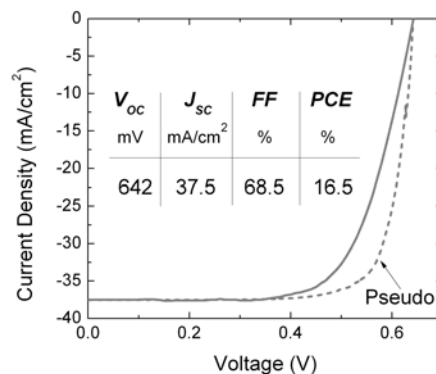
### Chapter 4: Material characterization

A thorough characterization of the structural and optoelectronic properties of transition metal oxides (TMOs) and PEDOT:PSS is presented, with emphasis on their applicability as hole-selective contacts in crystalline silicon solar cells.



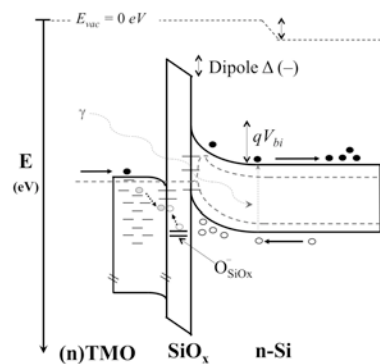
### Chapter 5: Solar cell results

The main performance parameters of solar cell devices are presented and correlated to the material optoelectronic properties, also determining the carrier transport mechanisms, thermal stability and built-in potential of the heterojunction. After the optimization of the rear contact, a 16.5% efficiency is obtained.



### Chapter 6: Conclusions

This final chapter summarizes the main findings of this thesis work, resulting in an overall understanding of the properties and working principles of TMO/n-Si heterojunctions and their application into novel solar cell devices.



## 1.4 References

- [1] IPCC - Intergovernmental Panel on Climate Change, Climate Change 2014 Synthesis Report, Geneva, Switzerland, 2014.
- [2] World bank, Open data and indicators, (2016). <http://data.worldbank.org/> (accessed November 1, 2016).
- [3] International Energy Agency, World Energy Outlook 2015. Executive Summary, Paris, France, 2015.
- [4] Gapminder World, Global Trends, *Data Source UNDP, World Bank.* (2016). <https://www.gapminder.org/tools> (accessed November 1, 2016).
- [5] Renewable Energy Policy Network for the 21st Century (REN21), Renewables 2016 global status report, Paris, France, 2016. [www.ren21.net](http://www.ren21.net).
- [6] Bloomberg New Energy Finance, New Energy Outlook 2015 - Long-term projections of the global energy sector, 2016.
- [7] A. Luque, S. Hegedus, Handbook of photovoltaic science and engineering, 2nd ed., Wiley, Chichester (UK), 2011.
- [8] Fraunhofer Institute for Solar Energy Systems, Photovoltaics report, Freiburg, Germany, 2016. [www.ise.fraunhofer.de](http://www.ise.fraunhofer.de).

- [9] P. Würfel, *Physics of solar cells*, 1st ed., Wiley-VCH, Darmstadt, 2005.
- [10] S.W. Glunz, New concepts for high-efficiency silicon solar cells, *Sol. Energy Mater. Sol. Cells*. **90** (2006) 3276–3284.
- [11] M.A. Green, K. Emery, Y. Hishikawa, W. Warta, E.D. Dunlop, Solar cell efficiency tables (version 47), *Prog. Photovolt Res. Appl.* **24** (2016) 3–11.
- [12] M. Taguchi, A. Yano, S. Tohoda, K. Matsuyama, Y. Nakamura, T. Nishiwaki, et al., 24.7% Record efficiency HIT solar cell on thin silicon wafer, *IEEE J. Photovoltaics*. **4** (2014) 96–99.
- [13] S. Moon, K. Kim, Y. Kim, J. Heo, J. Lee, Highly efficient single-junction GaAs thin-film solar cell on flexible substrate, *Sci. Rep.* **6** (2016) 30107.
- [14] T. Matsui, A. Bidiville, K. Maejima, H. Sai, T. Koida, T. Suezaki, et al., High-efficiency amorphous silicon solar cells: Impact of deposition rate on metastability, *Appl. Phys. Lett.* **106** (2015) 53901.
- [15] X. Wu, High-efficiency polycrystalline CdTe thin-film solar cells, *Sol. Energy*. **77** (2004) 803–814.
- [16] P. Jackson, D. Hariskos, R. Wuerz, O. Kiowski, A. Bauer, T.M. Friedlmeier, et al., Properties of Cu(In,Ga)Se<sub>2</sub> solar cells with new record efficiencies up to 21.7%, *Phys. Status Solidi RRL*. **9** (2015) 28–31.
- [17] S. Zhang, L. Ye, W. Zhao, B. Yang, Q. Wang, J. Hou, Realizing over 10% efficiency in polymer solar cell by device optimization, *Sci. China Chem.* **58** (2015) 248–256.
- [18] X. Lan, O. Voznyy, F.P. García De Arquer, M. Liu, J. Xu, A.H. Proppe, et al., 10.6% certified colloidal quantum dot solar cells via solvent-polarity-engineered halide passivation, *Nano Lett.* **16** (2016) 4630–4634.
- [19] B.E. Hardin, J. Snaith, M.D. McGehee, The renaissance of dye-sensitized solar cells, *Nat. Photonics*. **6** (2012) 162–169.
- [20] S. Lopez-Marino, M. Placidi, A. Perez-Tomas, J. Llobet, V. Izquierdo-Roca, X. Fontane, et al., Inhibiting the absorber/Mo-back contact decomposition reaction in Cu<sub>2</sub>ZnSnSe<sub>4</sub> solar cells: the role of a ZnO intermediate nanolayer, *J. Mater. Chem. A*. **1** (2013) 8338–8343.
- [21] W.S. Yang, J.H. Noh, N.J. Jeon, Y.C. Kim, S. Ryu, J. Seo, et al., High-performance photovoltaic perovskite layers fabricated through intramolecular exchange, *Science*. **348** (2015) 1234.
- [22] NREL - National Renewable Energy Laboratory, Efficiency chart, 2017.
- [23] C. Battaglia, A. Cuevas, S. De Wolf, High-efficiency crystalline silicon solar cells: status and perspectives, *Energy Environ. Sci.* **9** (2016) 1552–1576.
- [24] J. Zhao, A. Wang, P.P. Altermatt, S.R. Wenham, M.A. Green, 24% Efficient per silicon solar cell: Recent improvements in high efficiency silicon cell research, *Sol. Energy Mater. Sol. Cells*. **41–42** (1996) 87–99.
- [25] R.A. Sinton, Y. Kwark, J.Y. Gan, R.M. Swanson, 27.5-Percent silicon concentrator solar cells, *IEEE Electron Device Lett.* **7** (1986) 567–569.
- [26] T. Yamaguchi, Y. Ichihashi, T. Mishima, N. Matsubara, T. Yamanishi, Achievement of more than 25% conversion heterojunction solar cell, *IEEE J. Photovoltaics*. **4** (2014) 1433–1435.
- [27] K. Yoshikawa, H. Kawasaki, W. Yoshida, T. Irie, K. Konishi, K. Nakano, et al., Silicon heterojunction solar cell with interdigitated back contacts for a photoconversion efficiency over 26%, *Nat. Energy*. **2** (2017) 17032.
- [28] A. Richter, S.W. Glunz, A. Richter, M. Hermle, S.W. Glunz, Reassessment of the Limiting Efficiency for Crystalline Silicon Solar Cells, *IEEE J. Photovoltaics*. **3** (2013) 1184–1191.
- [29] A. Goodrich, P. Hacke, Q. Wang, B. Sopori, R. Margolis, T.L. James, et al., A wafer-based

- monocrystalline silicon photovoltaics road map: Utilizing known technology improvement opportunities for further reductions in manufacturing costs, *Sol. Energy Mater. Sol. Cells*. **114** (2013) 110–135.
- [30] ITRPV, International Technology Roadmap for Photovoltaic, Frankfurt am Main, Germany, 2016. [www.itrpv.net](http://www.itrpv.net).
- [31] M.J. De Wild-Scholten, Energy payback time and carbon footprint of commercial photovoltaic systems, *Sol. Energy Mater. Sol. Cells*. **119** (2013) 296–305.
- [32] R. Jonczyk, A. Lorenz, A. Ersen, J. Hofstetter, K. Hübener, K. Duncker, et al., Low-cost kerfless wafers with gradient dopant concentration exceeding 19% cell efficiency in PERC production line, *Energy Procedia*. **92** (2016) 822–827.
- [33] E. Kobayashi, Y. Watabe, R. Hao, T.S. Ravi, Heterojunction solar cells with 23% efficiency on n-type epitaxial kerfless silicon wafers, *Prog. Photovolt Res. Appl.* **24** (2016) 1295–1303.
- [34] S. Kühnappel, S. Gall, B. Rech, D. Amkreutz, Towards monocrystalline silicon thin films grown on glass by liquid phase crystallization, *Sol. Energy Mater. Sol. Cells*. **140** (2015) 86–91.
- [35] J. Geissbühler, S. De Wolf, A. Faes, N. Badel, Q. Jeangros, A. Tomasi, et al., Silicon heterojunction solar cells with copper - plated grid electrodes: status and comparison with silver thick - film techniques, *IEEE J. Photovoltaics*. **4** (2014) 1055–1062.
- [36] D. Garcia-Alonso, S.E. Potts, C.A.A. van Helvoirt, M. a. Verheijen, W.M.M. Kessels, Atomic layer deposition of B-doped ZnO using triisopropyl borate as the boron precursor and comparison with Al-doped ZnO, *J. Mater. Chem. C*. **3** (2015) 3095–3107.
- [37] Z.C. Holman, A. Descoedres, L. Barraud, F.Z. Fernandez, J.P. Seif, S. De Wolf, et al., Current losses at the front of silicon heterojunction solar cells, *IEEE J. Photovoltaics*. **2** (2012) 7–15.
- [38] H. Savin, P. Repo, G. von Gastrow, P. Ortega, E. Calle, M. Garín, et al., Black silicon solar cells with interdigitated back-contacts achieve 22.1% efficiency., *Nat. Nanotechnol.* **10** (2015) 624.
- [39] A. Ingenito, O. Isabella, M. Zeman, Experimental demonstration of 4n2 classical absorption limit in nanotextured ultrathin solar cells with dielectric omnidirectional back reflector, *ACS Photonics*. **1** (2014) 270–278.
- [40] A. Cuevas, T. Allen, J. Bullock, Skin care for healthy silicon solar cells, in: 42nd Photovolt. Spec. Conf., IEEE, New Orleans, LA, USA, 2015: pp. 1–6.
- [41] L. Barraud, Z.C. Holman, N. Badel, P. Reiss, A. Descoedres, C. Battaglia, et al., Hydrogen-doped indium oxide/indium tin oxide bilayers for high-efficiency silicon heterojunction solar cells, *Sol. Energy Mater. Sol. Cells*. **115** (2013) 151.
- [42] S.W. Glunz, A. Richter, The irresistible charm of a simple current flow pattern - 25 % with a solar cell featuring a full-area back contact, in: 31st Eur. Photovolt. Sol. Energy Conf., Hamburg, Germany, 2015.
- [43] A. Louwen, W.G.J.H.M. van Sark, R.E.I. Schropp, W.C. Turkenburg, A.P.C. Faaij, Life-cycle greenhouse gas emissions and energy payback time of current and prospective silicon heterojunction solar cell designs, *Prog. Photovolt Res. Appl.* **23** (2015) 1406–1428.
- [44] A. Cuevas, S. Member, D. Yan, S. Member, A.O. Example, Misconceptions and misnomers in solar cells, *IEEE J. Photovoltaics*. **3** (2013) 916–923.
- [45] T.-H. Lai, S.-W. Tsang, J.R. Manders, S. Chen, F. So, Properties of interlayer for organic photovoltaics, *Mater. Today*. **16** (2013) 424–432.
- [46] L.G. Gerling, Master thesis, Characterization of small molecule organic solar cells by variable light intensity measurements, Universitat Politècnica de Catalunya, 2013. <http://upcommons.upc.edu/handle/2099.1/19346>.

- [47] J. Fossum, F. Lindholm, M. Shibib, The importance of surface recombination and energy-bandgap arrowing in p-n-junction silicon solar cells, *IEEE Trans. Electron Devices*. **26** (1979) 1294–1298.
- [48] S. De Wolf, M. Kondo, Nature of doped a-Si:H/c-Si interface recombination, *J. Appl. Phys.* **105** (2009) 103707.
- [49] J. Melskens, B.W.H. van de Loo, B. Macco, M.F.J. Vos, J. Palmans, S. Smit, et al., Concepts and prospects of passivating contacts for crystalline silicon solar cells, in: 42nd Photovolt. Spec. Conf., IEEE, New Orleans, LA, USA, 2015.
- [50] K.A. Münzer, K.T. Holdermann, R.E. Schlosser, S. Sterk, Thin monocrystalline silicon solar cells, *IEEE Trans. Electron Devices*. **46** (1999) 2055–2061.
- [51] F. Wang, Z. Tan, Y. Li, Solution-processable metal oxides/chelates as electrode buffer layers for efficient and stable polymer solar cells, *Energy Environ. Sci.* **8** (2015) 1059–1091.
- [52] M.T. Greiner, Z.-H. Lu, Thin-film metal oxides in organic semiconductor devices: their electronic structures, work functions and interfaces, *NPG Asia Mater.* **5** (2013) e55.
- [53] K. Sun, S. Zhang, P. Li, Y. Xia, X. Zhang, D. Du, et al., Review on application of PEDOTs and PEDOT:PSS in energy conversion and storage devices, *J. Mater. Sci. Mater. Electron.* **26** (2015) 4438–4462.
- [54] C. Ganzorig, K. Suga, M. Fujihira, Alkali metal acetates as effective electron injection layers for organic electroluminescent devices, *Mater. Sci. Eng. B.* **85** (2001) 140–143.
- [55] G. Gerling, A. Morales, M. Colina, C. Voz, J. Puigdollers, R. Alcubilla, Novel crystalline silicon heterojunction structure based on hole selective MoO<sub>3</sub> emitter, in: 29th Eur. Photovolt. Sol. Energy Conf. Exhib., Amsterdam, Netherlands, 2014.
- [56] S. Avasthi, W.E. McClain, G. Man, A. Kahn, J. Schwartz, J.C. Sturm, Hole-blocking titanium-oxide/silicon heterojunction and its application to photovoltaics, *Appl. Phys. Lett.* **102** (2013) 203901.
- [57] O. Bethge, M. Nobile, S. Abermann, M. Glaser, E. Bertagnolli, ALD grown bilayer junction of ZnO:Al and tunnel oxide barrier for SIS solar cell, *Sol. Energy Mater. Sol. Cells*. **117** (2013) 178–182.
- [58] C. Battaglia, X. Yin, M. Zheng, I.D. Sharp, T. Chen, S. McDonnell, et al., Hole Selective MoO<sub>x</sub> contact for Si solar cells, *Nano Lett.* **14** (2014) 967–971.
- [59] J. Bullock, A. Cuevas, T. Allen, C. Battaglia, Molybdenum oxide MoO<sub>x</sub>: A versatile hole contact for silicon solar cells, *Appl. Phys. Lett.* **105** (2014) 232109.
- [60] L. Ding, M. Boccard, Z.C. Holman, M.I. Bertoni, Evaluation of transition metal oxides as carrier-selective contacts for silicon heterojunction solar cells, in: MRS Spring Meet. Exhib., San Francisco, CA, USA, 2015.
- [61] B. Macco, M.F.J. Vos, N.F.W. Thissen, a. a. Bol, W.M.M. Kessels, Low-temperature atomic layer deposition of MoO<sub>x</sub> for silicon heterojunction solar cells, *Phys. Status Solidi - Rapid Res. Lett.* **9** (2015) 393–396.
- [62] M. Bivour, J. Temmler, H. Steinkemper, M. Hermle, Molybdenum and tungsten oxide: High work function wide band gap contact materials for hole selective contacts of silicon solar cells, *Sol. Energy Mater. Sol. Cells*. **142** (2015) 34–41.
- [63] L.G. Gerling, S. Mahato, A. Morales-Vilches, G. Masmitja, P. Ortega, C. Voz, et al., Transition metal oxides as hole-selective contacts in silicon heterojunctions solar cells, *Sol. Energy Mater. Sol. Cells*. **145** (2016) 109–115.
- [64] R. Islam, P. Ramesh, J.H. Nam, K.C. Saraswat, Nickel oxide carrier selective contacts for silicon solar cells, in: 42nd Photovolt. Spec. Conf., IEEE, New Orleans, LA, USA, 2015: pp. 1–4.
- [65] J. Geissbühler, J. Werner, S. Martin de Nicolas, L. Barraud, A. Hessler-Wyser, M. Despeisse, et



- al., 22.5% efficient silicon heterojunction solar cell with molybdenum oxide hole collector, *Appl. Phys. Lett.* **107** (2015) 81601.
- [66] H.D. Um, N. Kim, K. Lee, I. Hwang, J.H. Seo, K. Seo, Dopant-free all-back-contact Si nanohole solar cells using MoOx and LiF films, *Nano Lett.* **16** (2016) 981–987.
- [67] W. Wu, W. Lin, J. Bao, Z. Liu, B. Liu, K. Qiu, et al., Dopant-free multilayer back contact silicon solar cells employing V2Ox/metal/V2Ox as an emitter, *RSC Adv.* **7** (2017) 23851–23858.
- [68] R. Devkota, Q. Liu, T. Ohki, J. Hossain, K. Ueno, H. Shirai, Solution-processed crystalline silicon double-heterojunction solar cells, *Appl. Phys. Express.* **9** (2016) 22301.
- [69] J. Tong, Y. Wan, J. Cui, S. Lim, N. Song, Alison Lennon, Solution-processed molybdenum oxide for hole-selective contacts on crystalline silicon solar cells, *Appl. Surf. Sci.* **423** (2017) 139–146.
- [70] J.C. Nolasco, R. Cabré, L.F. Marsal, M. Estrada, J. Pallarès, J.C. Nolasco, et al., Extraction of poly(3-hexylthiophene) (P3HT) properties from dark current voltage characteristics in a P3HT/n-crystalline-silicon solar cell, *J. Appl. Phys.* **107** (2010) 44505.
- [71] T.-G. Chen, B.-Y. Huang, E.-C. Chen, P. Yu, H.-F. Meng, Micro-textured conductive polymer/silicon heterojunction photovoltaic devices with high efficiency, *Appl. Phys. Lett.* **101** (2012) 033301–033305.
- [72] K.A. Nagamatsu, S. Avasthi, J. Jhaveri, J.C. Sturm, A 12% efficient silicon/PEDOT:PSS heterojunction solar cell fabricated at <100°C, *IEEE J. Photovoltaics.* **4** (2014) 260–264.
- [73] D. Zielke, C. Niehaves, W. Lövenich, A. Elschner, M. Hörteis, J. Schmidt, Organic-silicon solar cells exceeding 20 % efficiency, *Energy Procedia.* **77** (2015) 331–339.
- [74] Y. Zhang, R. Liu, S.-T. Lee, B. Sun, The role of a LiF layer on the performance of poly(3,4-ethylenedioxythiophene):poly(styrenesulfonate)/Si organic-inorganic hybrid solar cells, *Appl. Phys. Lett.* **104** (2014) 83514.
- [75] Y. Wan, C. Samundsett, J. Bullock, T. Allen, M. Hettick, D. Yan, et al., Magnesium fluoride electron-selective contacts for crystalline silicon solar cells, *ACS Appl. Mater. Interfaces.* **8** (2016) 14671.
- [76] J. Bullock, M. Hettick, J. Geissbühler, A.J. Ong, T. Allen, C.M. Sutter-Fella, et al., Efficient silicon solar cells with dopant-free asymmetric heterocontacts, *Nat. Energy.* (2016) 15031.
- [77] V.M. Fthenakis, H.C. Kim, Photovoltaics: Life-cycle analyses, *Sol. Energy.* **85** (2011) 1609–1628.

## 2 Theoretical background

*A review on the solar cell operation principles is given, putting emphasis on electrochemical potentials as the driving force for current flow. The main performance parameters are defined, while the requirements for recombination, selectivity and contact resistivity justify the need for passivating-selective contacts.*

### 2.1 Solar cell operation principles

The semiconductor physics that describe solar cell operation, as first established by W. Shockley in the 1950s, are based on the static and dynamic carrier balance across a p-n junction under excitation by an applied voltage and/or under illumination. Here, the general concepts and equations will be given with special emphasis on solar cell design, whereas further details can be found in the references [1,2].

#### 2.1.1 Electrochemical potentials as a driving force

The driving forces behind electron ( $e$ ) and hole ( $h$ ) transport can be described by a simple system comprising a semiconductor material (e.g. n-type) sandwiched between two metal contacts labeled source (S) and drain (D), as depicted in the energy band diagram in Fig. 2.1, where the y-axis is the system energy (in eV) [3]. Both contacts act as carrier reservoirs, while the n-type semiconductor is merely a supplier of conduction states determined by an effective volumetric density. By definition, the semiconductor and contacts have a finite electrochemical potential  $\eta$ :

$$\eta = \mu_{chem} + q\varphi \quad (2.1)$$

where  $\mu_{chem}$  is the chemical potential (a function of electron concentration),  $\varphi$  the electric potential (a function of the electric field  $\vec{E}$ ) and  $q$  is the carrier elementary charge (negative for  $e$ , positive for  $h$ ). In semiconductor physics, electrochemical potentials are equivalent to Fermi energies ( $E_F$ ) and to work functions ( $\Phi$ ), both referenced to the energy level of a free stationary electron under vacuum ( $E_{vac} = 0$  eV). If a positive step voltage  $qV = \eta_S - \eta_D$  is applied, the electrochemical potential at D will displace towards lower energies with respect to S, causing a

“downward” electron flow into the available states of the semiconductor conduction band  $E_C$ <sup>1</sup>. As electrons flow into D, its electrochemical potential will increase until a complete charge transfer has occurred, reaching the condition of equilibrium ( $\eta = \eta_S = \eta_D$ ).

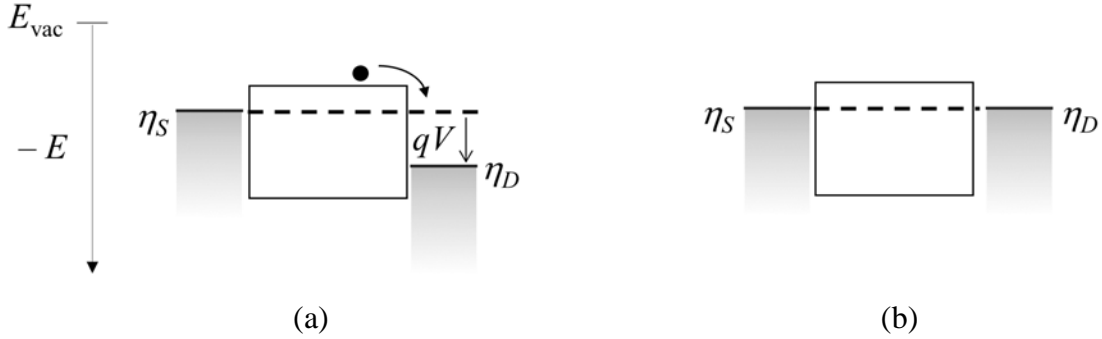


Figure 2.1 Energy (eV) band diagram of a contact/n-type semiconductor/contact structure (a) under an applied voltage and (b) in equilibrium.

In this sense, a change in the local electrochemical potential of electrons ( $\eta_n = E_{Fn}$ ) and holes ( $\eta_p = E_{Fp}$ ) is the driving force behind the current densities  $J_e$  and  $J_h$ , as defined by [2]:

$$\begin{aligned} J_e &= \frac{\sigma_e}{q} \nabla E_{Fn} \\ J_h &= \frac{\sigma_h}{q} \nabla E_{Fp} \end{aligned} \quad (2.2)$$

where  $\nabla$  is the gradient operator<sup>2</sup>. The carrier conductivity  $\sigma$  (in  $\Omega^{-1}\cdot\text{cm}^{-1}$ ), a measure of carrier selectivity, is the material property that determines how carriers react to the driving forces [4].

### 2.1.2 The diode model

In its most simple conception, the operation of a solar cell is usually described by its energy band diagram, as shown in Fig. 2.2 for a metal/p-contact/absorber/n-contact/metal structure where p and n are the hole- and electron-selective contacts. In this example, the absorber is undoped (i.e. intrinsic), in contrast with the solar cells architectures discussed in Table 1.1. However, a solar cell with an undoped absorber is viable as long as each carrier-selective contact is able to collect

<sup>1</sup> Conversely, after a positive voltage is applied to a p-type semiconductor, the electrochemical potential at D will displace towards higher energies with respect to S, causing an “upward” hole flow into the valence band states  $E_V$ .

<sup>2</sup>  $\nabla = \partial/\partial x + \partial/\partial y + \partial/\partial z$ .

electrons and holes efficiently [4]. As a first approach, the electrochemical potential of all cell elements is constant ( $\eta_{metal} = \eta_{p,n\ contact} = \eta_{Abs}$ ) when the solar cell is in the dark and under thermal equilibrium (Fig. 2.2a), i.e. there is a balance<sup>3</sup> between the radiative recombination rate and thermal generation rate of electron-hole pairs [5]. These rates can be expressed as equal but opposite current flows  $-J_0 = J_{rec}$ .

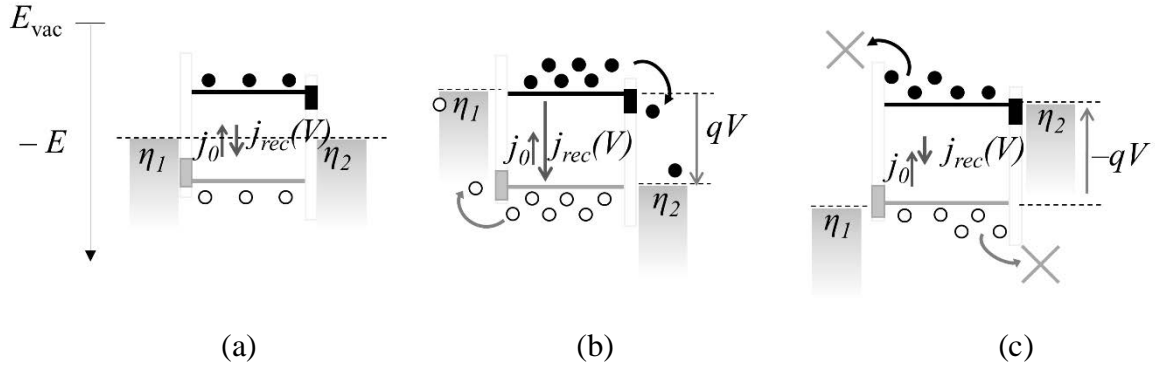


Figure 2.2 Descriptive solar cell energy band diagram in the dark (a) under thermal equilibrium, (b) when a forward bias is applied, (c) when a reverse bias is applied.

Whenever the equilibrium is disturbed by applying a positive voltage (forward bias), the electrochemical potentials of the metal contacts will displace each other by a magnitude  $qV$ , lowering the energy barrier between the metal electrodes and the conduction/valence bands so that electrons/holes can flow (Fig. 2.2b). Carriers surpassing the barrier will recombine within the absorber as a recombination current whose dependence with voltage is exponential<sup>4</sup>, namely  $J_{rec}(V) = J_0 \exp(qV/nkT)$ . Then, by adding both current contributions  $J(V) = J_{rec} - J_0 = J_0 [\exp(qV/nkT) - 1]$  the Schottky diode equation is obtained, where  $kT/q$  is the thermal voltage (25.9 mV at 25 °C) and  $n$  is a factor that accounts for deviations from ideality [2]. When a negative voltage (reverse bias) is applied (Fig. 2.2c), the metal electrodes displace each other by  $-qV$  and the energy barriers increase, making carrier transport null. Then,  $J(-V)$  saturates at a value  $J_0$  (usually referred as the dark saturation current).

Further deviations from equilibrium are caused by illuminating the absorber, resulting in the generation of excess electron-hole pairs that can be extracted as a photocurrent  $-J_{ph}$ . This photocurrent is opposite to  $J_{rec}$  and accounts for the transfer of excess electrons and holes into their respective conduction and valence bands. Moreover, a difference in the Fermi levels of free

<sup>3</sup> In other words, a balance between absorption and emission of blackbody radiation ( $\gamma \leftrightarrow e + h$ ) at a finite temperature  $T > 0$  K.

<sup>4</sup> For an energized particle, the probability of crossing a potential barrier  $\phi_B$  varies as  $\exp(-\phi_B/kT)$  [2].

electrons ( $E_{Fn}$ ) and holes ( $E_{Fp}$ ) inside the absorber is established, yielding a photovoltage of magnitude  $E_{Fn} - E_{Fp}$  [2]. The maximum photocurrent can be measured with an ammeter at short-circuit conditions when  $J(0V) = J_{SC}$ , while the maximum photovoltage can be measured with a voltmeter at open-circuit conditions when  $J(V_{OC}) = 0 \text{ A/cm}^2$ , as depicted in Fig. 2.3a,b.

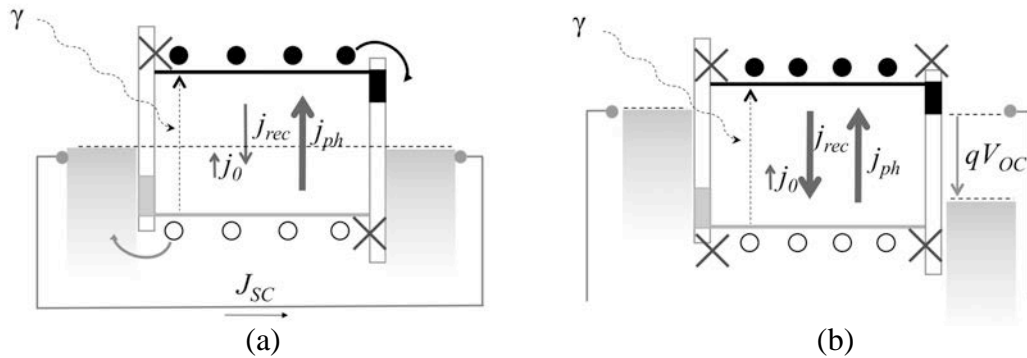


Figure 2.3 Descriptive solar cell energy band diagram under illumination (a) in short-circuit conditions ( $V=0$ ), and (b) in open-circuit conditions ( $J=0$ ).

Overall, the current-voltage behavior can be described by:

$$J = -J_{ph} + J_0 \left[ \exp\left(\frac{qV}{nkT}\right) - 1 \right] \quad (2.3)$$

Eq. 2.3 shows that  $J_0$  is a background generation-recombination pre-factor that invariably limits  $J_{ph}$ , despite being  $\sim 10^{13}$  orders of magnitude smaller (in the case of c-Si). Moreover, it is worth mentioning that the Fermi level of the electrodes should have no influence in the  $V_{OC}$  of the device<sup>5</sup> (i.e. they act only as carrier sinks) provided an efficient  $e$  and  $h$  collection takes place at each selective contact (Eq. 2.2).

### 2.1.3 The p/n junction in c-Si

Practically ideal electron- and hole-selective contacts can be achieved via p/n junctions, the most studied selective contacts and the strategy of choice for c-Si solar cells, by introducing electron donor (D) and acceptor (A) dopant impurities at a specific concentration  $N$ . In a typical n/p junction, the electron-contact is n-type doped ( $N_D \sim 10^{18} \text{ cm}^{-3}$ ) and the hole-contact is p-type doped ( $N_A \sim 10^{16} \text{ cm}^{-3}$ ). In the vicinity of the junction, a depletion region forms due to the

<sup>5</sup> Unless the metal electrode is itself a carrier-selective contact, as in a Schottky (metal/semiconductor) junction.

opposing polarity of ionized impurities, inducing a built-in voltage  $V_{bi} \approx (kT/q) \ln(N_D N_A / n_i^2)$  that works as a potential barrier for carriers [2]. Under thermal equilibrium in the dark (Fig 2.4a), the Fermi levels of electrons and holes are equal to an equilibrium value  $E_{F0} = E_{Fn} = E_{Fp}$ , while their equilibrium concentrations are defined as  $n_0$  and  $p_0$  (related by  $n_0 p_0 = n_i^2$ , where  $n_i$  is the intrinsic carrier concentration  $\sim 8.6 \times 10^9 \text{ cm}^{-3}$  at 25 °C).

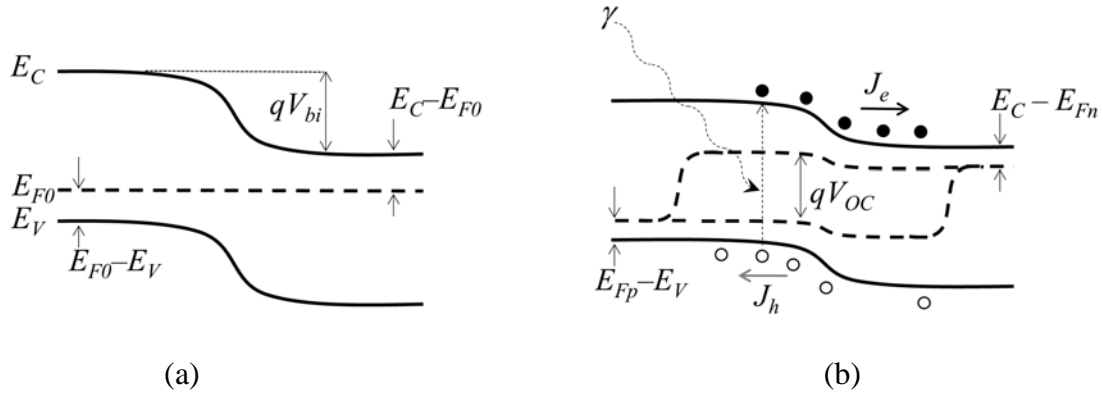


Figure 2.4 Energy band diagram of a c-Si p/n junction (a) in the dark and thermal equilibrium, and (b) under illumination at open-circuit conditions.

When photons  $\gamma$  are absorbed (Fig. 2.4b), excess electrons and holes ( $\Delta n \approx \Delta p$ ) are photogenerated and the equilibrium  $F_0$  splits into two distinct quasi-Fermi levels  $E_{Fn}$  and  $E_{Fp}$ . These quasi-energies define the total carrier population ( $n, p$ ) within the semiconductor via Fermi-Dirac statistics in non-equilibrium conditions [6]:

$$\begin{aligned} n &= n_0 + \Delta n = N_C \exp\left(\frac{E_{Fn} - E_C}{kT}\right) \\ p &= p_0 + \Delta p = N_V \exp\left(\frac{E_V - E_{Fp}}{kT}\right) \end{aligned} \quad (2.4)$$

where  $N_C$  and  $N_V$  are the effective density of states in the conduction and valence bands. On each junction side, the equilibrium concentration of majority carriers is equivalent to the doping concentration (e.g.  $p_0 = N_A \sim 10^{16} \text{ cm}^{-3}$  in the p-region), whereas the concentration of minority carriers is approximately 12 orders of magnitude smaller ( $n_0 = n_i^2/p_0 \sim 10^4 \text{ cm}^{-3}$ ). Similarly, the difference  $E_{Fn} - E_{Fp}$  fixes the maximum photovoltage achievable by the device [6]:

$$V_{max} = \frac{E_{Fn} - E_{Fp}}{q} = \frac{kT}{q} \ln\left(\frac{np}{n_i^2}\right) \quad (2.5)$$

After photogeneration takes place, the built-in potential barrier<sup>6</sup> facilitates electron/hole transport into the respective conduction/valence bands, aided by the preferential conductivities within each doped region. The total current is then comprised by the sum of the carrier currents ( $J_e + J_p$ ), which can be rewritten in terms of the physical properties of c-Si as [2]:

$$\begin{aligned} J_e &= qD_n \nabla n + q\mu_n n \bar{E} \\ J_h &= qD_p \nabla p + q\mu_p p \bar{E} \end{aligned} \quad (2.6)$$

where  $\mu$  and  $D$  are the mobility and diffusivity of carriers in the semiconductor bulk (correlated by Einstein's relation  $D = \mu kT/q$ ). The first term in Eq. 2.6 (diffusion current) is the main carrier transport mechanism in c-Si under low injection levels ( $\Delta n \ll p_0$  for the p-type absorber), while the second term (drift current) becomes relevant only at high injection conditions ( $\Delta n \geq p_0$ ), which is the operation regime for highly efficient devices even at low bias voltages.

An important characteristic of p/n junctions is that  $J_e$  and  $J_h$  are determined by the injection of minority carriers, whose concentration changes many orders of magnitude from  $(n_0, p_0) \sim 10^4 \text{ cm}^{-3}$  to  $(\Delta n, \Delta p) \sim 10^{15} \text{ cm}^{-3}$  (at 1 sun illumination). This change is reflected in the drastic change of quasi-Fermi levels  $E_{Fp}$  and  $E_{Fn}$  nearby the contacts (see Fig. 2.4b). In terms of the applied voltage, the individual electron and hole currents (under low injection) are [2]:

$$\begin{aligned} J_e &= qD_n \nabla(\Delta p_n) = \frac{qD_n n_i^2}{L_n N_A} \left[ \exp\left(\frac{qV}{kT}\right) - 1 \right] \\ J_h &= qD_p \nabla(\Delta n_p) = \frac{qD_p n_i^2}{L_p N_D} \left[ \exp\left(\frac{qV}{kT}\right) - 1 \right] \end{aligned} \quad (2.7)$$

where  $\Delta p_n$  and  $\Delta n_p$  are the excess minority carrier concentrations (holes on the n-side and electrons on the p-side) while  $L$  is the diffusion length or average distance over which carriers can diffuse before recombining. By analogy with Eq. 2.3,  $J_0$  can also be modeled in terms of the bulk properties of silicon considering the long base approximation ( $L \ll W$ ) where the surfaces have no effect on  $J_0$  [2]:

$$J_0 = J_{0,e} + J_{0,h} = qn_i^2 \left[ \frac{D_n}{L_n N_A} + \frac{D_p}{L_p N_D} \right] \quad (2.8)$$

---

<sup>6</sup> Characterized by a small gradient in  $E_{Fn}$  and  $E_{Fp}$ , almost unnoticeable in Fig. 2.4b.

### 2.1.4 Design parameters

As introduced in the previous section, the maximum current and voltage achievable by a solar cell are delimited by the open-circuit voltage  $V_{OC}$  and the short circuit current  $J_{SC}$  respectively. When connected to a resistive load  $R_L = V_{MPP}/J_{MPP}$ , solar cells operate midway between the  $V_{OC}$  and  $J_{SC}$  conditions at a maximum power point (MPP) in order to provide voltage and current simultaneously, achieving a maximum power output at  $P_{out} = J_{MPP}V_{MPP}$ . Then, the ratio:

$$FF = \frac{J_{MPP} V_{MPP}}{J_{SC} V_{OC}} \quad (2.9)$$

is the fill factor  $FF$ , a measure of how the  $J_{MPP}V_{MPP}$  product approaches  $J_{SC}V_{OC}$  (see Fig. 2.5a). In an ideal c-Si solar cell without resistive losses, the maximum theoretical  $FF$  is limited by recombination losses to  $\sim 89\%$  [7], while record HIT-IBC devices have a  $FF$  close to  $\sim 83\%$  [8]. In practice, fill factor values are hindered by the series and parallel resistances  $R_S$  and  $R_P$  (Fig. 2.5b). The series resistance comprises all ohmic losses, including the metal/semiconductor contacts ( $R_C$ ), the carrier-collector<sup>7</sup> sheet resistance ( $R_{sh}$ ) and the metallic grid electrode ( $R_{grid}$ ). Parallel resistance losses account for current leakage across non-resistive paths (shunts). A design rule of thumb establishes tolerable values for  $R_S < R_L/100$  and  $R_P > 100R_L$  in order to consent to a maximum power loss of 1% [9]. This yields limit values of  $R_S < 0.2 \Omega \cdot \text{cm}^2$  and  $R_P > 1.6 \text{ k}\Omega \cdot \text{cm}^2$  for a state-of-the-art device [8].

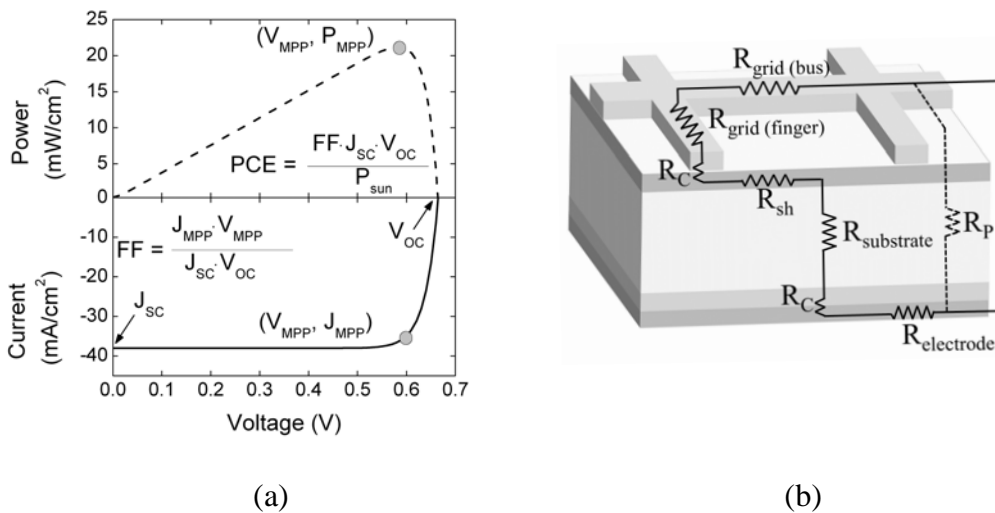


Figure 2.5. (a) Typical solar cell current-voltage and power-voltage response, along with the main performance parameters. (b) Resistance losses in a solar cell.

<sup>7</sup> Either a highly-doped layer in a homojunction or a TCO in a heterojunction.



By considering the above performance parameters, the power conversion efficiency ( $PCE$ ) is the ratio between the output power (at MPP) and the illumination power of the sun  $P_{sun}$ :

$$PCE = \frac{P_{out}}{P_{sun}} = FF \frac{J_{SC} V_{OC}}{P_{sun}} \quad (2.10)$$

For normalization purposes,  $P_{sun}$  has a magnitude of  $1,000 \text{ W/m}^2$  under the AM1.5g<sup>8</sup> standard [10]. Photocurrent generation in a photovoltaic absorber is a wavelength-dependent ( $\lambda$ ) parameter, i.e. it is a function of how closely its absorption coefficient  $\alpha$  matches the solar photon flux spectrum  $\Phi_{sun}$ , as depicted in Fig. 2.6. Then, the theoretical short-circuit current is equal to the photocurrent generated inside the absorber by the absorption of incoming photons with energy  $E(\lambda) \geq E_{gap \text{ c-Si}}$ :

$$J_{SC} = J_{abs} = \int_{-\infty}^{\lambda(E_{gap})} \Phi_{sun}(\lambda) \cdot [1 - \exp(-\alpha(\lambda) \cdot W)] \quad (2.11)$$

where  $W$  is the absorber thickness and  $\lambda(E_{gap}) \sim 1,100 \text{ nm}$ . For a 100% photon absorption (e.g. with a substrate thickness of  $1 \text{ cm}$ ),  $J_{SC}$  matches the theoretical photocurrent  $J_{ph} \sim 46.5 \text{ mA/cm}^2$  [9], although in practice this value is hard to achieve due to optical and recombination losses.

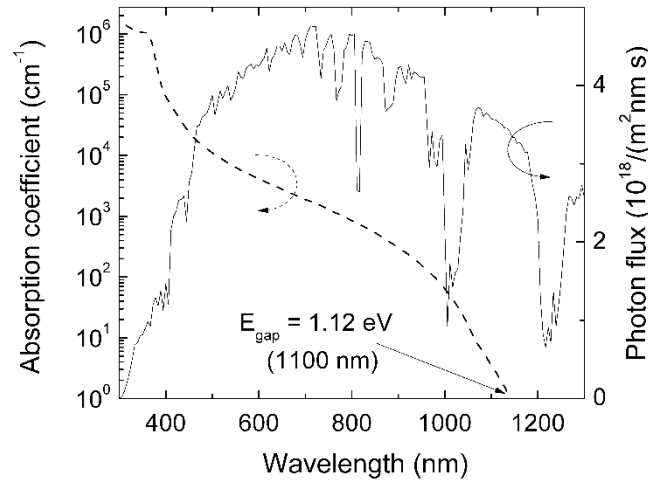


Figure 2.6 Absorption coefficient of c-Si (left axis) and AM1.5g sun spectrum (right axis) as a function of wavelength.

Optical losses are caused by reflection, transmission or parasitic absorption. Transmission losses across the silicon bulk can easily be avoided by a metal back-reflector, usually the rear electrode

<sup>8</sup> Defined by the optical path of global (direct + scattered) irradiation at  $48.2^\circ$  zenith angle, normalized to the atmosphere thickness.

(Fig. 2.7). Parasitic absorption is particularly important in heterojunction devices where the selective contacts (a-Si:H) and TCOs do not contribute to photogeneration, justifying the need for optically transparent window layers. Regarding reflection losses, they can be considerably reduced through anisotropic texturing of the front surface and by semi-transparent anti-reflection coatings with refractive index values  $n = 1.7 - 2.1$  [9]. Moreover, photon absorption can also be increased by texturing the rear surface, scattering light into multiple angles until a total internal reflection (light-trapping) is achieved. Theoretically, the effective optical path<sup>9</sup> can be increased up to a factor  $4n_{cSi}^2$  (known as Lambertian limit [11]), collecting most of  $J_{ph}$  even at wafer thicknesses below  $10 \mu\text{m}$ .

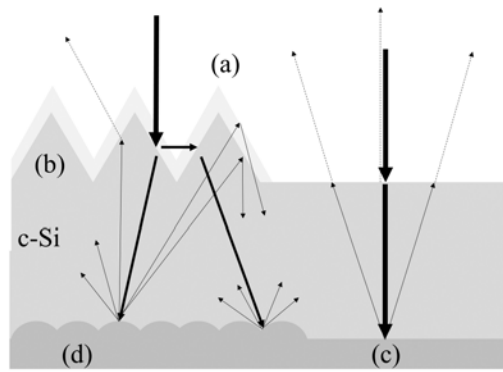


Figure 2.7 Minimization of reflection losses by (a) antireflection coatings and (b) surface texturing. Increase of the effective optical path by metallic (c) flat and (d) scattering back-reflectors.

Electron-hole recombination is also a source of photocurrent loss, especially for the ultraviolet and near-infrared photons that are absorbed at the front and rear surfaces respectively. However, recombination effects are more critical to the open-circuit voltage, as seen from Eq. 2.3 with  $J(V) = 0$ , which yields the maximum  $V_{OC}$  of an ideal solar cell:

$$V_{OC} = \frac{kT}{q} \ln \left( \frac{J_{sc}}{J_0} + 1 \right) \quad (2.12)$$

showing how the minimization of  $J_0$  is one of the most important tasks in solar cell design. Finally, the strong temperature dependence of the intrinsic carrier concentration<sup>10</sup> results in higher recombination losses that drop the  $V_{OC}$  by about  $-2.3 \text{ mV}/^\circ\text{C}$ , an unavoidable loss when solar cells operate at  $20\text{--}40 \text{ }^\circ\text{C}$  above ambient temperatures [1].

<sup>9</sup> The increase in photon absorption is given by  $A = 1 - \exp[-\alpha(\lambda) \cdot W \cdot Z]$ , where  $Z$  is the optical path enhancement factor.

<sup>10</sup> Defined by  $n_i = \sqrt{N_C N_V} \cdot e^{-E_{gap}/nkT}$ , where the effective density of conduction and valence states ( $N_C$  and  $N_V$ ) are  $\propto T^{3/2}$ .

## 2.2 Recombination

In section 2.1.2,  $J_0$  was equated to the thermal generation-recombination current  $J_{rec}$  considering only radiative recombination, a process where conduction band electrons recombine with valence band holes (band-to-band transition) emitting a photon with an energy equal to  $E_{gap}$ . Nonetheless, other non-radiative recombination processes are also present in a c-Si absorber, each contributing to the total  $J_0$  value. In Auger recombination, the energy of the band-to-band transition is transferred to a third carrier, while in Shockley-Read-Hall (SRH) recombination the transition takes place in traps located within  $E_{gap}$ . These traps arise from crystallographic defects (as in multi-crystalline c-Si) and/or atomic impurities (Fe, O) in the bulk [2]. The total recombination current is then the sum of all contributions, i.e.  $J_0 = J_{0\ Rad} + J_{0\ Auger} + J_{0\ SRH}$ . Just as shown in Eq. 2.5, where  $V_{max}$  is a function of the product of electron and hole concentrations ( $np$ ), the recombination rate for each of these mechanisms is also proportional (with variations) to  $np$ , asserting the competing nature between photovoltage generation and recombination [12].

Of the three recombination mechanisms (all of which occur in the volume bulk), Auger and radiative are intrinsic to the material and cannot be avoided, while SRH can be minimized in high quality c-Si wafers with mono-crystalline structure. However, state-of-the-art technologies are limited by SRH recombination occurring at the surfaces, where the silicon atomic lattice is interrupted. The very high density of surface dangling bonds act as trap states where electron and holes recombine at a surface recombination velocity  $S = J_0/(q\Delta n)$  [13]. Parting from the equivalence  $J_0 = qR_0 \approx q\Delta nW/\tau_{eff}$ , where  $R_0$  ( $\text{cm}^{-2}\text{s}^{-1}$ ) is the cumulative recombination rate of minority carriers  $\Delta n$  within a p-type absorber of thickness  $W$ , each recombination mechanism can be expressed as a function of the minority carrier lifetime  $\tau_j$ , which quantifies the average time a carrier can diffuse before recombining. Then, it is possible to group all different recombination processes in a single term known as effective lifetime  $\tau_{eff}$  [13]:

$$\frac{1}{\tau_{eff}} = \sum \frac{1}{\tau_j} = \left( \frac{1}{\tau_{Rad}} + \frac{1}{\tau_{Auger}} + \frac{1}{\tau_{SRH}} \right)_{bulk} + \frac{S_{front}}{W} + \frac{S_{rear}}{W} \quad (2.13)$$

where  $S_{front}$  and  $S_{rear}$  are the front and rear surface recombination velocities and the terms in parenthesis can be grouped as an effective bulk lifetime  $1/\tau_{bulk}$ . The contribution of each recombination process is depicted in Fig. 2.8 for a high efficiency solar cell where  $\tau_{bulk} > 15$  ms (at low injection), so that  $1/\tau_{eff} \approx 1/\tau_{SRH\ Surface}$ . It is interesting to note that  $\tau_{SRH}$  increases with

injection level while  $\tau_{Auger}$  and  $\tau_{Rad}$  decrease, ultimately limiting the effective lifetime and the maximum achievable efficiency of a c-Si solar cell. To put these numbers in perspective, world record HIT-IBC devices with a-Si:H passivated surfaces exhibit  $\tau_{eff}$ ,  $J_0$  and  $S_{eff}$  values of 8.8 ms, 3.0 fA/cm<sup>2</sup> and <2 cm/s respectively [14].

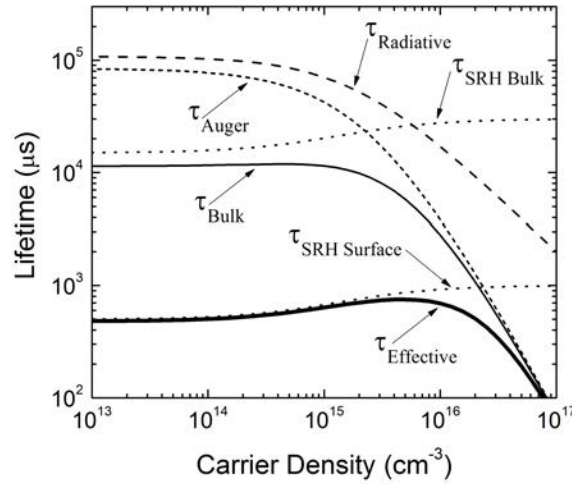


Fig. 2.8 Effective lifetime and its individual contributions. Plotted with models [15–17] using PV-Lighthouse recombination calculator [18] (n-type c-Si, 2.5 Ω.cm resistivity, surface SRH model with  $E_{trap} = E_i$  and  $\tau_{min} = 500 \mu s$ ).

At this point, it is useful to define a minimum lifetime condition  $\tau_{min}$  [9]:

$$\tau_{min} \geq 9 \alpha^2 / D \quad (2.14)$$

which correlates the optical and electronic properties of the c-Si absorber by defining *a*) the minimum absorber thickness required to absorb at least 95% of incident light ( $d_{abs} \geq 3\alpha^{-1}$ ); and *b*) the minimum diffusion length required to collect the photogenerated carriers at their respective selective contacts ( $L_{min} = d_{abs} \geq \sqrt{D \tau_{min}}$ ). For c-Si the minimum lifetime condition is  $\tau_{min} \approx 100 \mu s$ , which can then be equated to the surface SRH mechanism as:

$$\tau_{SRH surf,hi}^{min} = \frac{W}{2 \sigma_{css} v_{th} D_{it}} \quad (2.15a)$$

where  $\sigma_{css}$  is the carrier capture cross section (cm<sup>2</sup>),  $v_{th}$  the thermal velocity and  $D_{it}$  the density of interface traps (cm<sup>-2</sup>). For a wafer thickness of 200 μm,  $\tau_{min}$  sets the maximum allowed density of interface traps at  $\sim 10^{10} \text{ cm}^{-2}$ , a considerably low value considering the density of dangling bonds in an unpassivated c-Si surface is  $D_{it} \sim 10^{14} \text{ cm}^{-2}$ . In practice,  $D_{it}$  values below  $10^{10} \text{ cm}^{-2}$  can

be achieved by high quality chemical (a-Si:H, SiO<sub>2</sub>) or charge-assisted<sup>11</sup> (Al<sub>2</sub>O<sub>3</sub>, SiN<sub>x</sub>) passivation layers, lowering significantly the SRH contribution to the effective lifetime, as depicted in Fig. 2.9.

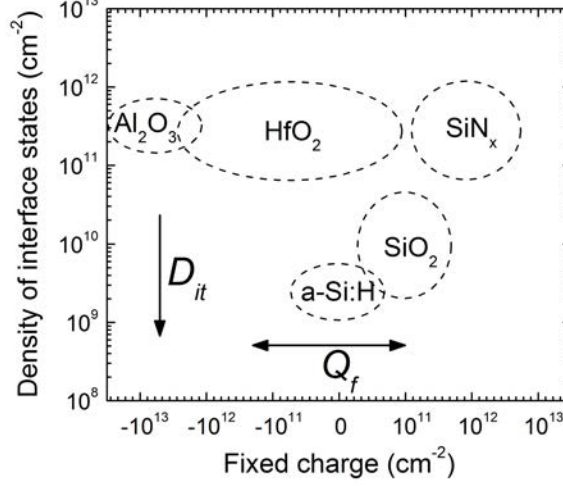


Fig. 2.9 Dielectric/semiconductor materials used for c-Si passivation, either by low density of interface traps  $D_{it}$  (chemical) or by fixed charges  $Q_f$  (charge-assisted). Adapted from [19].

Similarly, carrier-selective contacts based on highly-doped layers are limited by Auger recombination even at low injection conditions [7], defining  $\tau_{min}$  as:

$$\tau_{Auger,li}^{min} = \frac{1}{C_A N^2} \quad (2.15b)$$

where  $C_A$  is the Auger recombination rate constant. Then, the maximum allowable doping is  $N \sim 5 \times 10^{16} \text{ cm}^{-3}$ , far lower than the routine doping concentrations  $> 10^{18} \text{ cm}^{-3}$  used for p<sup>+</sup> or n<sup>+</sup> regions. Furthermore, highly doped regions induce a band gap narrowing effect ( $\Delta E_{gap}$ ) that not only reduces photon absorption but also increases the effective intrinsic carrier concentration by  $n_{i,eff} = n_i \exp(\Delta E_g/2kT)$ , with  $\Delta E_{gap}$  values of  $\sim 30$  and  $\sim 60$  meV for  $10^{18}$  and  $10^{19} \text{ cm}^{-3}$  dopant concentrations respectively [20]. These two efficiency limitations, imposed by surface defects and high doping concentrations, open a window of opportunity for alternative dopant-free surface-passivating selective contacts, as stated in the objective of this thesis.

<sup>11</sup> Usually known as ‘field-effect’ passivation, it makes use of fixed charges  $Q_f$  in an insulator to induce attracting (accumulation) or repelling (inversion) forces on the c-Si surface.

## 2.3 Contacts

By revisiting the simplified solar cell structure in Fig. 1.3, two kinds of contacts are needed to extract the photo-carriers generated in the c-Si absorber: *a)* selective contacts, which transport carriers towards their respective electrodes, and *b)* ohmic contacts, which extract carriers into metal electrodes with minimum resistance losses.

### 2.3.1 Selective contact strategies

As discussed in section 2.1.3, the p- and n-sides of a p/n homojunction act as carrier-selective contacts. However, high-efficiency c-Si solar cells have required more advanced strategies to increase contact selectivity, such as the  $n^+$ /p-Si/ $p^+$  homojunction solar cell. Then, a selective contact can be defined as all the layers lying between the absorber bulk (p-Si) and the metal electrode [21] (i.e. the  $p^+$  and  $n^+$  doped layers).

Selective contacts can be understood as filters or membranes that conduct one type of charge carrier while blocking the other. Ideally, they must fulfill the following requirements [5]:

- 1) Carrier separation: the direction of carrier flow must be towards lower electrochemical potentials (see Eq. 2.2) with electrons following a “downward” gradient ( $\nabla E_{Fn}$ ) and holes an “upward” gradient ( $\nabla E_{Fp}$ ).
- 2) Carrier selectivity: dissimilar conductivities between electrons and holes, i.e.  $\sigma_e \neq \sigma_h$ , facilitate the transport and collection of majority carriers while restricting the flow of minority carriers ( $\sigma_{maj} \gg \sigma_{min}$ ).
- 3) Reduced recombination: selectivity also ensures that the concentration of minority carriers  $n_{min}$  (i.e. electrons in a p-contact) is reduced, resulting in a lower recombination current at the metal interface  $J_0 = q n_{min} S$ . In turn, the concentration of majority carriers  $p_{maj}$  is high enough for an efficient hole extraction towards the metal electrode<sup>12</sup>.

---

<sup>12</sup> This occurs via recombination with the multiple defect states located at the metal/c-Si interface, at a maximum recombination velocity of  $S \sim 10^7$  cm/s.

Different strategies can be applied to form carrier-selective contacts, all of which involve the modification of the semiconductor surface before contacting with the metal [22], as depicted in Fig. 2.10 for a hole-contact in p-Si. Heavy doping of the silicon substrate is the industrial approach to form a  $p^+$  doped layer (Fig. 2.10a). Alternatively, hole accumulation<sup>13</sup> can be induced by external materials (Fig. 2.10b), either by dielectrics with a fixed charge  $-Q_f$  or by metals with a large work function ( $\Phi_m < E_{FpSi}$ ). A third possibility is the formation of energy barriers through heterojunctions with wide band gap materials (Fig. 2.10c), where the magnitude of the conduction band offset  $\Delta E_C$  must be greater than  $qkT$  (the thermal energy of free carriers).

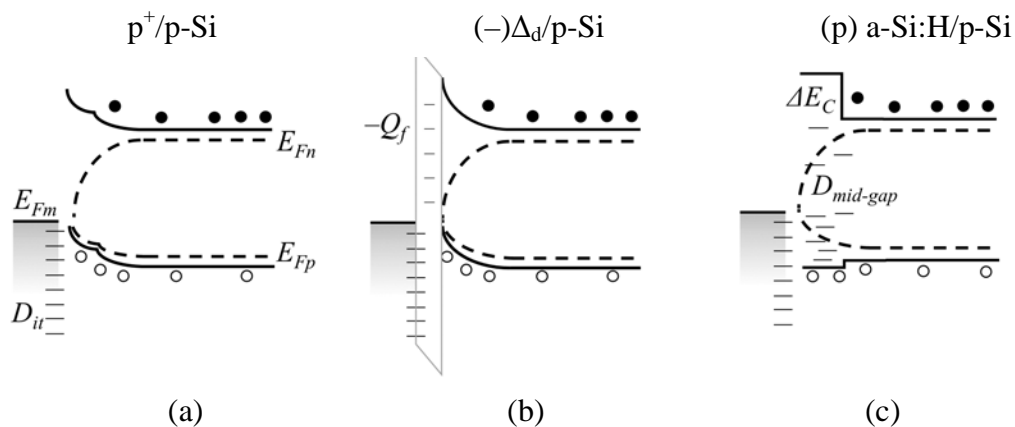


Fig. 2.10 Band diagram of a p-type absorber with different hole-selective contact strategies at open-circuit conditions, including (a)  $p^+$  doping, (b) induced band bending (accumulation) and (c) band offset ( $\Delta E_C$ ). For these cases, the metal electrode does not form part of the selective contact.

From the above discussion, several remarks can be done. First, selective contacts are confined within the region where quasi- $E_F$  levels make a transition from full splitting in the absorber to null splitting in the metal electrode [21]. Second, all strategies have in common the formation of a barrier that reduces the concentration of minority carriers at the interface (electrons, in this example), therefore decreasing  $J_0$  [22]. Third, an efficient hole extraction takes place despite the large  $E_{Fn}$  gradient observed by electrons (much larger than the  $E_{Fp}$  gradient observed by holes). However, the preferential hole conductivity  $\sigma_h \gg \sigma_e$  in the contact region contributes more to hole selectivity [4]. Finally, the same selectivity strategies can be applied to the formation of electron-selective contacts in either p- or n-type silicon (i.e.  $n^+/p$ -Si or  $n^+/n$ -Si contacts). For example, a  $p^+_{IL}$  inversion layer could be induced on the n-Si surface by a large work function metal ( $\Phi_m > E_{FnSi}$ ), forming a so-called *induced junction* [23].

<sup>13</sup> See §2.3.2 for the formation principles of accumulation or inversion conditions in metal/semiconductor contacts.

Since decreasing minority carrier recombination is usually insufficient, mixed passivation strategies are needed to offset the high density of surfaces defects. One example is wide band gap insulating dielectrics such as  $\text{SiO}_2$ ,  $\text{Al}_2\text{O}_3$  and  $\text{SiN}_x$  (see Fig. 2.9), which provide both chemical and charge-assisted passivation by blocking both electrons and holes indistinctively, a result of the large band offsets  $\Delta E_C$  and  $\Delta E_V$  and a layer thickness that is larger than the tunneling length ( $> 2$  nm) (Fig. 2.11a) [24]. With other wide band gap semiconductors like a-Si:H, dangling bonds are effectively passivated while a high density of mid-gap states ( $D_{mid-gap}$ ) permits carrier transport through defect-assisted tunneling (hopping) (Fig. 2.11b) [9]. In order to achieve passivation and selectivity, these two kinds of wide band gap materials can be combined with any of the carrier-selective arrangements from Fig. 2.10, either in full area configurations (a-Si:H in HIT concept) or as localized contacts ( $\text{SiO}_2$  in PERL concept).

One example of a mixed passivation/selective strategy is the utilization of intrinsic/doped a-Si:H stacks (Fig. 2.11c) where the alignment between the valence bands of a-Si:H and p-Si (i.e.  $E_{V_{a-si}} \sim E_{Fp}$ ) reduce the barrier for majority carriers, while minority carriers are repelled away from the contact [22]. Another example is the *top-con* (tunnel-oxide passivated contacts) approach that uses tunneling  $\text{SiO}_2$  layers  $< 2$  nm and doped poly-silicon stacks, delivering a remarkable passivation ( $S_{eff} < 1$  cm/s) while permitting carrier transport through tunneling [25]. These two examples, showing the combination of both passivation and selective carrier transport, endorse the definition of *passivating/selective* contacts, which are the topic of this thesis.

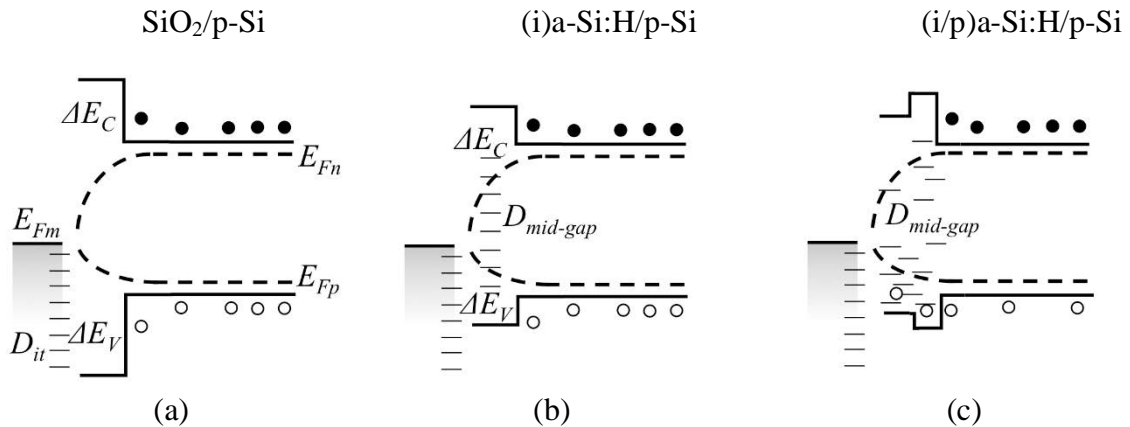


Fig. 2.11 Band diagram of a p-type absorber with wide bandgap (a) dielectrics and (b) defect-rich semiconductors at open-circuit conditions. (c) shows a p-doped/intrinsic a-Si:H *passivating/hole-selective* contact.



### 2.3.2 Ohmic contacts

Ohmic contacts are the connecting interface between the solar cell and the external load, extracting majority carriers with negligible voltage drops. They are typically realized by metal electrodes, which are not carrier-selective and therefore cannot support Fermi level splitting. In an ideal ohmic contact, the Fermi energy (or work function) of the metal electrode  $E_{Fm}$  is perfectly aligned with the quasi- $E_F$  levels of c-Si ( $E_{Fn}$  or  $E_{Fp}$ ), resulting in the extraction of majority carriers by recombination ( $S \sim 10^7$  cm/s) in a non-resistive manner. Since this condition of ideal  $E_F$  alignment is seldom met, a potential barrier  $\Phi_B$  is usually present at the interface, with its magnitude being determined by the difference between the metal work function and the electron affinity of the semiconductor ( $\Phi_{Bn} = \Phi_m - \chi_{cSi}$  for electrons), or alternatively, its ionization potential ( $\Phi_{Bp} = I_{cSi} - \Phi_m$  for holes, where  $I = \chi + E_{gap}$ ). Depending on the silicon doping type and the value of  $\Phi_m$ , majority carrier extraction can be affected by accumulation/inversion conditions at the metal/c-Si interface (Fig. 2.12), causing an upward/downward band bending  $\varphi_s$  of the energy bands [2]:

$$q\varphi_s = \Phi_{Bn} - (E_C - E_{F0}) \quad (2.16)$$

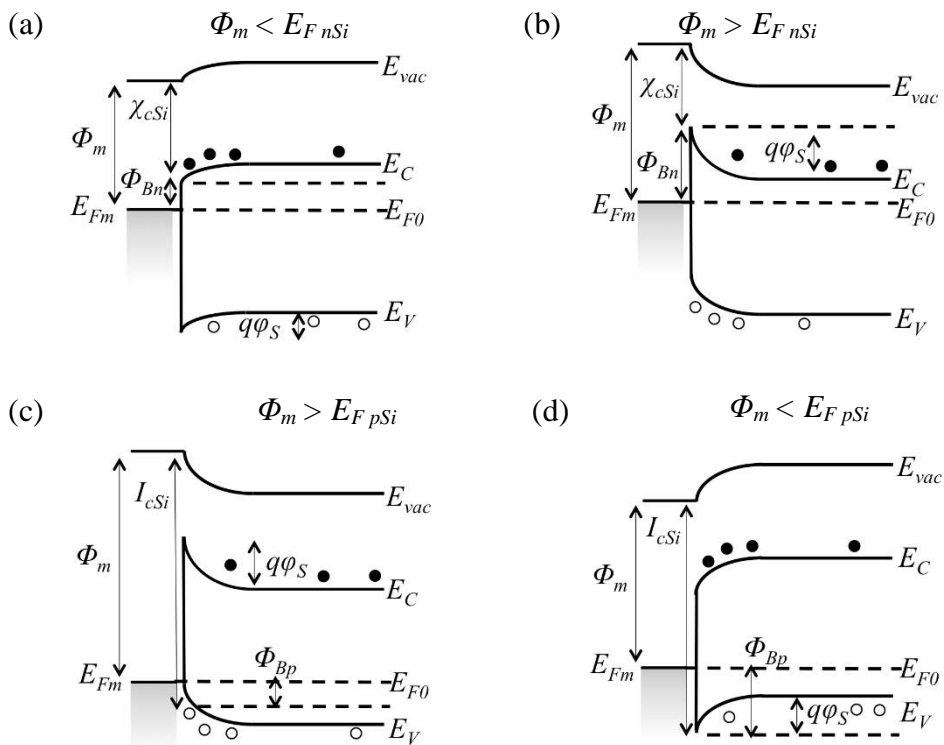


Fig. 2.12 Band diagram of possible accumulation (a,c) and inversion (b, d) conditions for metal/n-Si and metal/p-Si.

From the ohmic contact perspective, inversion conditions are detrimental since majority carriers need to surpass a larger  $\varphi_s$  barrier in order to reach the metal electrode, forming a Schottky contact (Fig. 2.12b,d). Alternatively, accumulation conditions favor ohmic transport via negative  $\varphi_s$  barriers, a condition met when  $\Phi_m \sim \chi_{n-Si}$  or when  $\Phi_m \sim I_{pSi}$  (Fig. 2.12a,c)

In practice, the metal/c-Si interface is far from perfect due to residual contamination or atom interdiffusion across the interface, giving rise to interlayers several Å thick that modify  $\Phi_B$  through interface defect states[9]. These states can have a certain donor/acceptor quality that, depending on their level of occupancy, can produce negative or positive electric dipoles  $\Delta_d$  that shift the electrostatic balance as [26]:

$$\Phi_{Bn} = \Phi_m - \chi_{cSi} + \Delta_d \quad (2.17)$$

In occasions,  $D_{it}$  is high enough ( $\sim 10^{13} \text{ cm}^{-2}$ ) to immobilize the Fermi level of the semiconductor at a fixed energy with respect to  $E_C$  or  $E_V$ , so that  $\varphi_s$  becomes independent of the applied voltage or the metal work function. This situation is known as Fermi level pinning and can be quantified by the index of interface behavior  $S_\phi = \partial\Phi_B/\partial\Phi_m$ , with values ranging from  $S = 1$  for no pinning (Mott-Schottky rule) to  $S = 0$  for complete pinning. When  $E_F$  is partially pinned to the surface, a change in  $\Phi_m$  will be accommodated by the surface dipole according to [26]:

$$S_\phi = \frac{1}{1 + q^2 \delta \cdot D_{it}(E_F)/\varepsilon_i \varepsilon_0} \quad (2.18)$$

where  $\delta$  is the thickness of the dipole (in the order on Å),  $\varepsilon_i \varepsilon_0$  the dipole permittivity and  $D_{it}(E_F)$  is the interfacial density of states that varies with the position of the Fermi level. Note that the presence of dipoles must be represented with a corresponding shift in the vacuum level.

For moderate doping levels, the transport of majority carriers across the barrier  $\Phi_B$  occurs by thermionic emission (TE), yielding a barrier height-dependent current density  $J(V) = J_{TE} [\exp(qV/nkT) - 1]$  with  $J_{TE} \propto \exp(q\Phi_B/kT)$ . By defining the specific contact resistance  $\rho_c$  as the instantaneous reciprocal derivate of current with respect to voltage  $(dJ/dV|_V)^{-1}$ ,  $\rho_c$  is also a function of  $\exp(q\Phi_B/kT)$ . The inherent presence of barriers makes really difficult to achieve true ohmic contacts in c-Si [2,27]. Therefore, heavily doped layers ( $N^+ > 10^{19} \text{ cm}^{-3}$ ) and small barriers ( $\Phi_B < 0.3 \text{ eV}$ ) are needed to decrease the thickness of the depletion

width below 2 nm, enabling majority carrier transport through tunneling<sup>14</sup> [9]. Then, the specific contact resistance can be decreased exponentially with doping, enabling close to ideal ohmic connections (at the cost of increased Auger recombination):

$$\rho_c \propto \exp\left(\frac{q\Phi_B}{\sqrt{N^+}}\right) \quad (2.19)$$

The specific contact resistance is an important figure of merit for metal/c-Si contacts since it determines the rate at which majority carriers can be extracted. Tolerable  $\rho_c$  values are in the order of  $\sim 10^{-3} \Omega \cdot \text{cm}^2$  for standard Al-BSF devices, even though the overall series resistance  $R_S$  is primarily dominated by the front metal grid [28]. However, as the contacted area fraction is reduced to reduce the passivation losses,  $\rho_c$  must be further reduced to values  $< 10^{-4} \Omega \cdot \text{cm}^2$  in order to meet the requirements of high efficiency devices.

### 2.3.3 Definition of selectivity

In essence, the main reason for improving an ohmic contact by means of doping or carrier accumulation is the enhancement of majority carrier selectivity. Therefore, it is also possible to exploit surface inversion conditions for minority carrier selectivity, forming induced junctions like  $p^+/n$ -Si (Fig. 2.12b) or  $n^+/p$ -Si (Fig. 2.12d). In both cases, the band bending  $\phi_s$  repels the majority carriers towards the opposite contact, favoring the accumulation of minority carriers at the metal/silicon interface for their extraction. Whenever this interface is passivated by ultra-thin ( $< 3$  nm) oxides, a metal-insulator-semiconductor (MIS) structure is formed. This is the operation principle in so-called MIS solar cells, where photogenerated minority carriers are able to tunnel through the oxide while majority carriers are depleted by a strong inversion layer at the semiconductor surface [2,29].

In this thesis, the behavior of selective contacts in c-Si heterojunctions will be described by the induced junction model, where work function differences ( $\Phi_{sel.cont.} - \Phi_{cSi}$ ) will induce either accumulation or inversion layers on the c-Si surface. Therefore, the metal/contact/c-Si heterojunction will be characterized by a specific contact resistance for majority carrier extraction, while recombination losses will be determined by the residual concentration of

---

<sup>14</sup> In reality, heavy doping densities push  $E_F$  beyond the  $E_C$  or  $E_V$  bands, bringing the semiconductor into degeneracy.

minority carriers in the vicinity of the contact. This kind of tradeoff between recombination losses ( $J_0$ ) and contact resistance ( $\rho_c$ ) will always be present and should be optimized while designing a selective contact.

By generalizing the previous discussion on metal/c-Si contacts to any other kind of semiconductor/c-Si junction, carrier selectivity could also be achieved by any of the strategies proposed in Fig. 2.10a-c (doping, induced accumulation/inversion or barrier formation). To begin with, Eq. 2.16 can be reformulated in terms of the selective contact  $\Phi_{sel.cont.}$  and c-Si absorber  $\Phi_{c-Si}$  work functions, obtaining an expression for the induced band bending [23,26]:

$$\Phi_{sel.cont.} - \Phi_{c-Si} = \varphi_s \approx V_{bi} \quad (\text{for } S_\phi = 1) \quad (2.20)$$

where  $\varphi_s$  is equivalent to the built-in potential  $V_{bi}$  of the junction. Taking the n-Si bulk as an example ( $\Phi_{n-Si} \sim 4.2$  eV), a heavily doped p<sup>+</sup> contact ( $\Phi_{p^+} \sim 5.1$  eV) will produce the same built-in potential as a p<sup>+</sup> induced junction caused by a large work function TMO ( $\Phi_{TMO} \geq 5.1$  eV), i.e.  $\Delta\Phi = V_{bi} \approx 0.9$  V. In both cases,  $V_{bi}$  serves as a potential barrier for electrons (minority) while the high concentration of holes (majority) increases  $\sigma_h$ . In this sense, only by controlling the work function difference  $\Delta\Phi$  and irrespectively of the nature of the junction, it is possible to achieve selectivity by providing a preferential conductivity for majority carriers while imposing an energy barrier for minority carriers.

Based on these assumptions, Figure 2.13 illustrates a simulation study by Bivour *et al.* [23] on how contact selectivity affects the external  $V_{OC}$  of an ideal c-Si solar cell with perfect chemical passivation<sup>15</sup> ( $S = 1$  cm/s) and no Fermi level pinning effects ( $S_\phi = 1$ ). Each simulated selective region, e.g. the hole contact in n-Si, assumes the opposite contact is ideal. Then, a lossless voltage extraction ( $i-V_{OC} = V_{OC}$ ) would occur for hole contact work functions lying close to the valence band ( $\Phi_h \approx E_V$ ). As  $\Phi_h$  decreases,  $V_{OC}$  losses augment until no useful voltage can be extracted from the device in the vicinity of the conduction band ( $\Phi_h \approx E_C$ ). The same trend is followed by the electron contact in n-Si with an ideal hole extraction, reaching a maximum  $V_{OC}$  when  $\Phi_e \approx E_C$ . When chemical passivation is not ideal, a lower  $i-V_{OC}$  limit is established and the same trend is followed. In parallel, the fill factor follows a similar dependence on  $\Delta\Phi$ , reaching maximum values when  $\Phi_h \approx E_V$  (hole contact) and  $\Phi_e \approx E_C$  (electron contact).

---

<sup>15</sup> And maximum quasi-Fermi level separation  $(E_{Fn} - E_{Fp})/q \approx 760$  mV

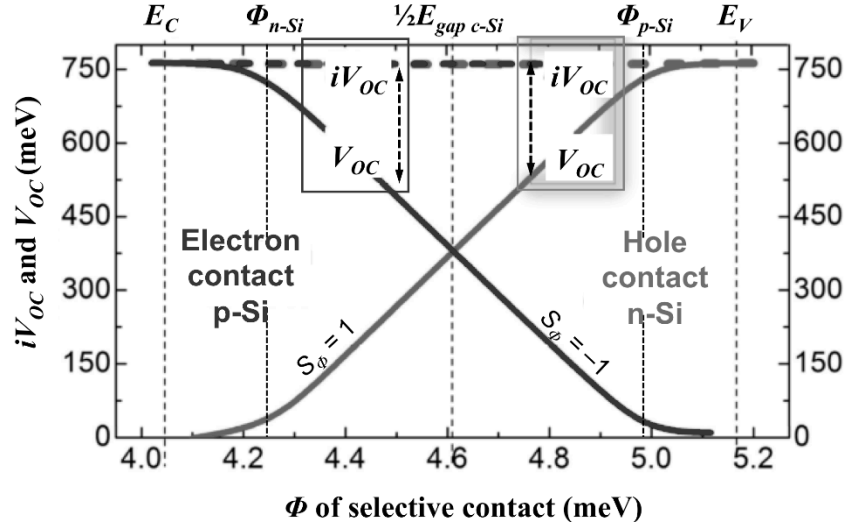


Fig. 2.13 Influence of the selective-contact work functions on the external  $V_{OC}$  for a perfectly passivated surface ( $S = 1$  cm/s) and without Fermi level pinning effects ( $S_\phi = 1$ ). The c-Si work functions are specified for a doping density of  $1 \Omega\cdot\text{cm}$  resistivity. For the hole-contact case (right panel), the electron contact is ideal; for the electron-contact case (left panel), the hole contact is ideal. Adapted from [23].

In this idealized example, the slope of the  $V_{OC}$  trend is  $1 \text{ eV/eV}$  due to the  $\Delta\Phi = \phi_s$  premise, a direct consequence of a pinning-free interfaces ( $S_\phi = 1$ ). However, interfaces with bare c-Si are usually abundant in interfacial states ( $D_{it} \sim 10^{13} \text{ cm}^{-2}$ ) that can accommodate a large amount of charge without any variation of the Fermi level, as indicated by experimental  $S_\phi$  values of  $\sim 0.05$  for metal/c-Si interfaces [2]. Whenever the surface is passivated by a-Si:H ( $D_{it} \sim 10^9 \text{ cm}^{-2}$ ),  $S_\phi$  can improve to  $\sim 0.25$  for metal/a-Si:H/c-Si interfaces [23], whereas TMO/c-Si interfaces can have higher pinning factors of  $0.25\text{--}0.6$  [30], still behind the ideal  $S_\phi = 1$  case. In theory, ideal selectivity could be reached only by operating the contact under low injection conditions at all times, a difficult premise considering the high concentration of excess minority carriers ( $>10^{16} \text{ cm}^{-3}$ ). In practice, this can be met if very large built-in potentials are established, so that  $V_{bi} \approx \Phi_{sel.cont} - \Phi_{c-Si} \geq iV_{OC}$  [23]. Moreover, parasitic junctions between the selective contacts and the overlying electrode also influence the induced band bending in c-Si [31], affecting even more the  $V_{OC}$  dependence on  $\Phi_{sel.cont} - \Phi_{c-Si}$ .

In summary, non-ideal selectivity decreases the external open-circuit voltage according to:

$$qV_{OC} \approx q iV_{OC} - (\Phi_h - \Phi_{pSi}) \quad (\text{with an ideal electron contact}) \quad (2.20a)$$

$$qV_{OC} \approx q iV_{OC} - (\Phi_e - \Phi_{nSi}) \quad (\text{with an ideal hole contact}) \quad (2.20b)$$

Notice how contact work functions exceeding these requirements ( $\Phi_h \geq 5.17$  and  $\Phi_e \leq 4.05$  eV) should maintain  $V_{OC}$  unchanged, i.e. the  $E_F$  alignment between TMO and c-Si stays constant with further increases/decreases of  $\Phi_{TMO}$ . A similar ‘pinning’ behavior has been amply documented in organic electronics for weakly interacting TMO/organic interfaces, where potential barriers are linearly dependent on the electrode’s work function [32]. In this sense, the  $V_{OC}$  of an organic solar cell will be maximized only when the selective contacts surpass the organic’s highest occupied molecular orbital ( $\Phi_h > \text{HOMO}$ ) and lowest unoccupied molecular orbital ( $\Phi_e < \text{LUMO}$ ) levels.

After this qualitative definition of carrier selectivity, we now define it in a quantitative manner as proposed by Brendel *et al.* [33]. Parting from the definition of the minority ( $J_m$ ) and majority ( $J_M$ ) carrier current densities in terms of the recombination current and the specific contact resistance (assuming a linear current-voltage response for  $J_M$ ):

$$J_m = J_0 \left[ \exp\left(\frac{qV}{kT}\right) - 1 \right] \quad (2.19a)$$

$$J_M = \frac{V}{\rho_c} \quad (2.19b)$$

Also, we define the contact selectivity  $S$  as the ratio of minority carrier to majority carrier resistances  $\rho_m/\rho_M$ , using the general resistance definition  $\rho = (dJ/dV|_{V=0})^{-1}$  evaluated at an arbitrary voltage  $V = 0$ . In order to avoid handling large numbers, a logarithmic selectivity  $S_{10} = \log(S)$  can be used [33]:

$$S_{10} = \log\left(\frac{\rho_m}{\rho_M}\right) = \log\left(\frac{kT}{J_0 \rho_c}\right) \quad (2.20)$$

obtaining a parameter that is exclusively a function of  $J_0$  and  $\rho_c$ , independently of contact geometry. Note that recombination and contact resistance are a function of the contacted area fraction  $f_c$  (where  $1 - f_c$  is the passivated area with negligible  $J_0$  values), thus reducing recombination by a factor  $f_c \cdot J_0$  at the expense of a higher contact resistance  $\rho_c / f_c$ . Fig 2.14 depicts an example simulation of the optimal contact fraction for multiple  $\rho_c$ - $J_0$  combinations as well as the resulting power conversion efficiency, with all other solar cell parameters being close to their idealized values (see Ref. [34] for simulation details). The iso-selectivity lines ( $S_{10}$ ) calculated as per Eq. 2.20 are also plotted, which show that similar efficiencies can be achieved

by either low  $\rho_c$ -high  $J_0$  or high  $\rho_c$ -low  $J_0$  parameter pairings. Under this approach, we see how selectivity is a sole function of the majority carrier contact resistance and the minority carrier recombination current, emphasizing its importance when designing a solar cell.

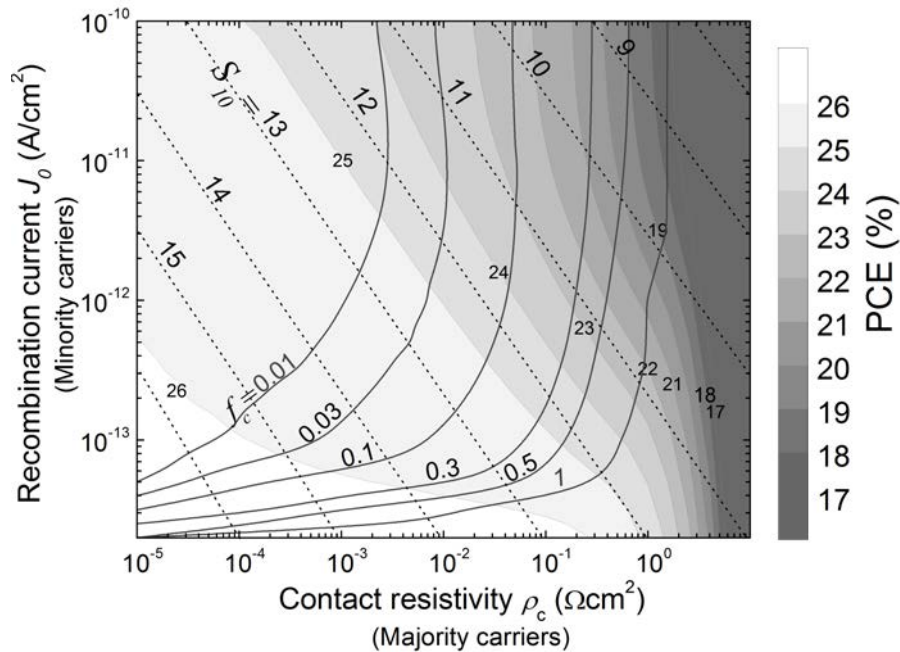


Fig. 2.14 Representative simulation of the conversion efficiency as a function of recombination current ( $J_0$ ) and specific contact resistance ( $\rho_c$ ) for  $p^+$  contacts, also showing the optimum contact fraction ( $f_c$ ) for different ( $J_0$ ,  $\rho_c$ ) combinations. Data obtained from the original source [34], with iso-selectivity lines ( $S_{10}$ ) calculated as per Eq. 2.20.

## 2.4 References

- [1] A. Luque, S. Hegedus, Handbook of photovoltaic science and engineering, 2nd ed., Wiley, Chichester (UK), 2011.
- [2] S.M. Sze, K.K. Ng, Physics of semiconductor devices, 3rd ed., Wiley, Hoboken, NJ, 2007.
- [3] S. Datta, Lessons from nanoelectronics: a new perspective on transport, World Scientific, Singapore, 2012.
- [4] U. Wurfel, A. Cuevas, P. Wurfel, Charge carrier separation in solar cells, *IEEE J. Photovoltaics*. **5** (2015) 461–469.
- [5] P. Wurfel, Physics of solar cells, 1st ed., Wiley-VCH, Darmstadt, 2005.
- [6] C. Battaglia, A. Cuevas, S. De Wolf, High-efficiency crystalline silicon solar cells: status and perspectives, *Energy Environ. Sci.* **9** (2016) 1552–1576.
- [7] A. Richter, S.W. Glunz, A. Richter, M. Hermle, S.W. Glunz, Reassessment of the limiting efficiency for crystalline silicon solar cells, *IEEE J. Photovoltaics*. **3** (2013) 1184–1191.

- [8] T. Yamaguchi, Y. Ichihashi, T. Mishima, N. Matsubara, T. Yamanishi, Achievement of more than 25% conversion heterojunction solar cell, *IEEE J. Photovoltaics*. **4** (2014) 1433–1435.
- [9] T. Dittrich, Materials concepts for solar cells, 1st ed., Imperial College press, London, UK, 2015.
- [10] IEC (International Electrotechnical Commission), Photovoltaic devices - Part 3: Measurement principles for terrestrial photovoltaic (PV) solar devices with reference spectral irradiance data (2nd ed.), 2008.
- [11] E. Yablonovitch, G.D. Cody, Intensity enhancement in textured optical sheets for solar-cells, *IEEE Trans. Electron Devices*. **29** (1982) 300–305.
- [12] A. Cuevas, The recombination parameter  $J_0$ , *Energy Procedia*. **55** (2014) 53–62.
- [13] A. Cuevas, R.A. Sinton, M. Stuckings, Determination of recombination parameters in semiconductors from photoconductance measurements, in: Conf. Optoelectron. Microelectron. Mater. Devices Proc., IEEE, 1996: pp. 16–19.
- [14] K. Yoshikawa, H. Kawasaki, W. Yoshida, T. Irie, K. Konishi, K. Nakano, et al., Silicon heterojunction solar cell with interdigitated back contacts for a photoconversion efficiency over 26%, *Nat. Energy*. **2** (2017) 17032.
- [15] W. Shockley, W.T. Read, Statistics of the recombinations of holes and electrons, *Phys. Rev.* **87** (1952) 835–842.
- [16] T. Trupke, M.A. Green, P. Würfel, P.P. Altermatt, A. Wang, J. Zhao, et al., Temperature dependence of the radiative recombination coefficient of intrinsic crystalline silicon, *J. Appl. Phys.* **94** (2003) 4930.
- [17] A. Richter, S.W. Glunz, F. Werner, J. Schmidt, A. Cuevas, Improved quantitative description of Auger recombination in crystalline silicon, *Phys. Rev. B - Condens. Matter Mater. Phys.* **86** (2012) 165202.
- [18] PV lighthouse, Recombination calculator (Version 1.2.6), (2017). [www2.pvlighthouse.com.au](http://www2.pvlighthouse.com.au) (accessed January 6, 2017).
- [19] A. Cuevas, T. Allen, J. Bullock, Skin care for healthy silicon solar cells, in: 42nd Photovolt. Spec. Conf., IEEE, New Orleans, LA, USA, 2015: pp. 1–6.
- [20] D. Yan, A. Cuevas, Empirical determination of the energy band gap narrowing in highly doped n+ silicon, *J. Appl. Phys.* **114** (2013) 44508.
- [21] P. Koswatta, M. Boccard, Z. Holman, Carrier-selective contacts in silicon solar cells, in: MRS Spring Meet. Exhib., San Francisco, CA, USA, 2015.
- [22] J. Melskens, B.W.H. van de Loo, B. Macco, M.F.J. Vos, J. Palmans, S. Smit, et al., Concepts and prospects of passivating contacts for crystalline silicon solar cells, in: 42nd Photovolt. Spec. Conf., IEEE, New Orleans, LA, USA, 2015.
- [23] M. Bivour, Silicon heterojunction solar cells analysis and basic understanding. PhD Thesis., Albert Ludwig University of Freiburg, 2016.
- [24] J. Schewchun, R. Singh, M. Green, Theory of metal-insulator-semiconductor solar cells, *J. Appl. Phys.* **48** (1977) 765–770.
- [25] F. Feldmann, M. Bivour, C. Reichel, H. Steinkemper, M. Hermle, S.W. Glunz, Tunnel oxide passivated contacts as an alternative to partial rear contacts, *Sol. Energy Mater. Sol. Cells*. **131** (2014) 46–50.
- [26] J. Bisquert, Nanostructured energy devices: equilibrium concepts and kinetics, 1st ed., CRC Press, Boca Raton, Florida, USA, 2014.
- [27] D.K. Schroder, D.L. Meier, Solar Cell Contact Resistance-A Review, *IEEE Trans. Electron Devices*. **31** (1984) 637–647.



- [28] D.L. Meier, D.K. Schroder, Contact resistance: its measurement and relative importance to power loss in a solar cell, *IEEE Trans. Electron Devices*. **31** (1984) 647–653.
- [29] M.A. Green, R.B. Godfrey, MIS solar cell - general theory and new experimental results for silicon, *Appl. Phys. Lett.* **29** (1976) 610–612.
- [30] R. Islam, K.N. Nazif, K.C. Saraswat, L. Fellow, Si heterojunction solar cells : a simulation study of the design issues, *IEEE Trans. Electron Devices*. **63** (2016) 4788–4795.
- [31] R. Varache, J.P. Kleider, M.E. Gueunier-Farret, L. Korte, Silicon heterojunction solar cells: Optimization of emitter and contact properties from analytical calculation and numerical simulation, *Mater. Sci. Eng. B Solid-State Mater. Adv. Technol.* **178** (2013) 593–598.
- [32] M.T. Greiner, Z.-H. Lu, Thin-film metal oxides in organic semiconductor devices: their electronic structures, work functions and interfaces, *NPG Asia Mater.* **5** (2013) e55.
- [33] R. Brendel, R. Peibst, Contact selectivity and efficiency in crystalline silicon photovoltaics, *IEEE J. Photovoltaics*. **6** (2016) 1413–1420.
- [34] J. Bullock, A. Cuevas, D. Yan, B. Demarex, A. Hessler-Wyser, S. De Wolf, Amorphous silicon enhanced metal-insulator-semiconductor contacts for silicon solar cells, *J. Appl. Phys.* **116** (2014) 163706.

### 3 Experimental methods

*This chapter describes the experimental methods for solar cell fabrication and characterization, including the techniques used for determining the optoelectronic, structural and compositional properties of the carrier-selective materials under study.*

All the experimental work on this thesis was performed in two different facilities: (1) a 100 m<sup>2</sup> clean room (class 100–1000) used for most of the solar cell fabrication sequence and characterization, located in the electronic engineering department at UPC; (2) the Center for Research in Nano-Engineering (CRNE), a research center associated to UPC where deposition of TMOs and PEDOT:PSS films was carried out as well as some material characterization techniques (XPS, SEM, FIB, UV-visible-NIR spectrophotometry). Other material characterization services were provided by the Scientific and Technological Centers of the University of Barcelona (HR-TEM) and the IBEC Nanotechnology Platform (ToF-SIMS).

#### 3.1 Solar cell fabrication

As mentioned before, the main focus of this thesis is the development of dopant-free carrier-selective contacts for n-type c-Si (n-Si) heterojunction solar cells. Accordingly, transition metal oxides (TMOs) and PEDOT:PSS were explored as hole-selective contacts in a front-side full-area configuration, similar to a HIT solar cell architecture, as shown in the solar cell structures in Fig. 3.1. For the TMO/n-Si devices, an indium-tin oxide (ITO) layer was employed both as front transparent conductive electrode (TCO) and anti-reflection coating (ARC), while the PEDOT:PSS/n-Si devices spared the use of an ITO layer thanks to the good conducting/transparency properties of the polymer. Regarding the rear electron-selective contact, two a-Si:H contacting approaches were explored: (1) localized laser-doping (Fig. 3.1a,c) and (2) full-area heterojunction with ITO (Fig 3.1b). The characterization of these structures comprises the majority of the results described in Chapters 4 and 5, while other materials (NiO, LiF, etc.) are briefly discussed in Appendix B.

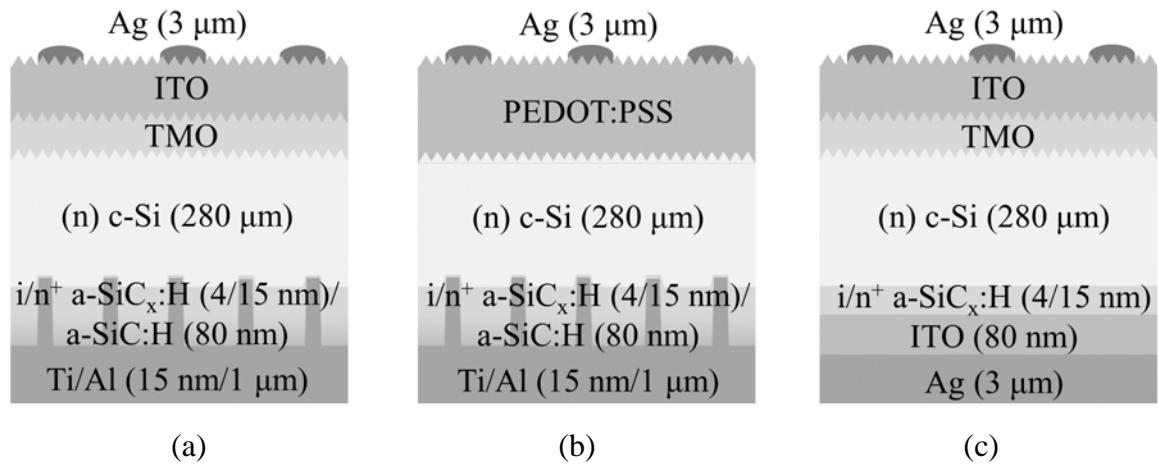


Figure 3.1 Schematic of the fabricated HIT-type heterojunction solar cells. (a) TMO/n-Si with rear laser-doping, (b) PEDOT:PSS/n-Si with rear laser-doping and (c) TMO/n-Si with rear ITO.

### 3.1.1 Cleaning and texturing

The first step in solar cell fabrication is the removal of surface contaminants like micron-sized particles (dust) and residual chemical elements (ions and metals), which can lead to thin film imperfections, shunts or highly active recombination centers. For this reason, bare wafers are cleaned following the standard RCA procedure [1] that consists in two oxidizing steps with a  $\text{H}_2\text{O}_2$  solution at  $70^\circ\text{C}$ , the first one with  $\text{NH}_3$  (alkaline) for removing organics and metals (Au, Ag, Ni, Cu), and a second one with HCl (acidic) for removing alkali ions and other metals. In-between both steps a dilute solution of HF (1%) is used to etch the ultra-thin  $\text{SiO}_2$  layer ( $<1\text{ nm}$ ) that grows during the oxidative processes, leaving behind an H-terminated surface where hydrogen atoms passivate the silicon dangling bonds [2], a configuration that is stable only for a few hours after air exposure. During this and subsequent processes, deionized water ( $18\text{ M}\Omega\cdot\text{cm}$  resistivity) must be used at all times in order to avoid unnecessary contamination.

Following substrate cleaning, a flat wafer with (100) crystal orientation is textured to effectively reduce reflection losses ( $R$ ) from 30% to below 10%, increasing photon absorption. Random pyramidal texturing is usually achieved by chemical anisotropic etching along the (111) crystal planes using a tetramethyl ammonium hydroxide (TMAH) and isopropyl alcohol solution at  $80^\circ\text{C}$  [3]. Figure 3.2 shows a scanning electron microscope (SEM) image of the resulting textured surface, which is restricted only to the front side of the wafer by protecting the rear side with a thermally-grown  $\text{SiO}_2$  layer ( $\sim 100\text{ nm}$ ) that is removed afterwards. One disadvantage of textured

surfaces is a lower effective passivation in comparison to planar ones, a result of a larger surface area (which increases by a factor of  $\sim 1.7$ ) with higher dangling bond densities.

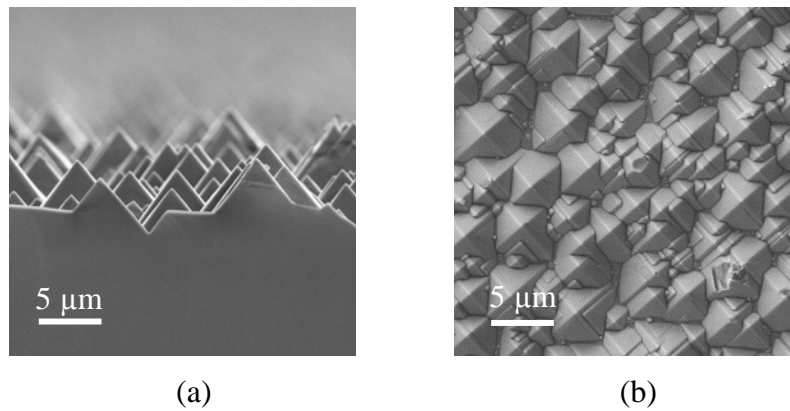


Figure 3.2 SEM image displaying (a) lateral and (b) top views of random pyramidal texturing.

### 3.1.2 a-SiC<sub>x</sub>:H electron-selective contact

Plasma-enhanced chemical vapor deposition (PECVD) is the preferred method for depositing a-Si:H thin films, parting from the decomposition of silane gas (SiH<sub>4</sub>) into a plasma of free ions and radicals, as generated by radio-frequency (RF) voltage discharges between two parallel plates [4]. Fig. 3.3 depicts a schematic of the RF-PECVD system (Elettrorava S. p. A, Italy) used in this work, whose main components are (1) a loading pre-chamber, (2) a deposition chamber with the plate electrodes and substrate heater, (3) a mechanic/turbo-molecular pumping system, (4) a gas delivery system with mass flow controllers, (5) an RF (13.56 MHz) power supply and (6) a gas exhaust system. Both chambers are separated by transfer gate valve, keeping the reaction chamber at a base pressure of  $\sim 10^{-6}$  mbar permanently.

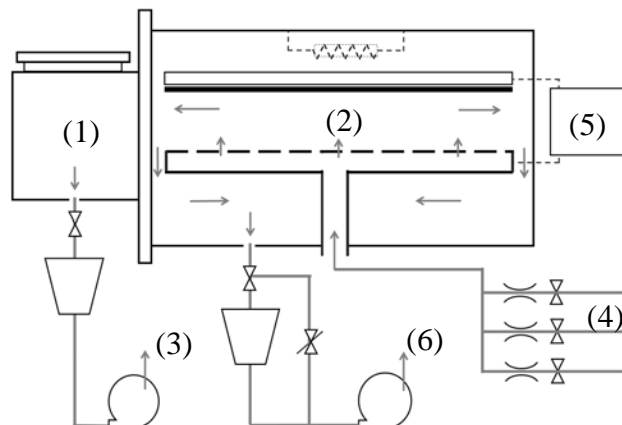


Figure 3.3 Schematic of the PECVD deposition system used for deposition of a-SiC<sub>x</sub>:H thin films.

The growth of a-Si:H films is a complex process determined by the plasma properties and the gas/solid reaction kinetics [5]. For this thesis, the deposition process was previously optimized in the MNT group for hydrogenated amorphous silicon carbide (a-SiC<sub>x</sub>:H, x~0.2), an alternative passivating wide band gap semiconductor with demonstrated surface recombination velocities  $S_{eff} < 50$  cm/s [6]. For the deposition process, mixtures of SiH<sub>4</sub>, CH<sub>4</sub> and PH<sub>3</sub> precursor gases are used to deposit an intrinsic/n<sup>+</sup> layer stack, yielding a thin film of approximately 20 nm (Table 3.1). An advantage of a-SiC<sub>x</sub>:H is that its conductivity and refractive index can be tuned by varying the carbon content, allowing the deposition of a dielectric back-reflector (a-SiC<sub>x</sub>:H, x~1) during the same vacuum stage, improving photon collection at the rear side.

Table 3.1 Deposition parameters for the (i/n<sup>+</sup>) a-SiC<sub>x</sub>:H electron-selective contact deposited by the PECVD process.

Film		Precursors	Flow (sccm)	T (°C)	P (mbar)	Power (W)	Time (min)	Thickness (nm)
intrinsic	a-SiC <sub>x</sub> :H	SiH <sub>4</sub> /CH <sub>4</sub>	36/12	300	0.5	6	0.5	~4
n <sup>+</sup>	(x~0.2)	SiH <sub>4</sub> /PH <sub>3</sub>	36/4				2	~15
intrinsic	a-SiC <sub>x</sub> :H	SiH <sub>4</sub> /CH <sub>4</sub>	1.2/60	300	1	18	18	~80

\*Used as rear reflector (insulating), given its refractive index  $n_{SiC} \sim 2$ .

This back-reflector layer, 80 nm thick and fully insulating, is then punctured<sup>1</sup> by laser-firing with an infrared nanosecond laser (Starmark SMP100 II, Rofin-Baasel GmBh, Germany) forming point contacts equally separated by a separation  $p$  (pitch), a procedure also optimized in the MNT group [7] (Fig. 3.4a). The dissipation of energy locally diffuses the n<sup>+</sup> material inside the substrate and forms a crater whose effective radius  $r$  accounts for the contacted area fraction  $f_c = \pi (r/p)^2$  (Fig. 3.4b). By adjusting parameters such as laser power, pulse duration and pitch, a compromise value between contact resistance and surface passivation can be obtained for a  $f_c \sim 2.4\%$  ( $p = 400 \mu\text{m}$ ) with contact resistance values as low as  $\rho_c < 5 \text{ m}\Omega \cdot \text{cm}^2$ . After laser-firing, the electron-selective contact is contacted to a Ti/Al electrode stack (Fig. 1.3a,c).

As an alternative to laser-doped contacts, a full area hetero-contact is also explored (Fig. 1.3c), directly contacting the (i/n<sup>+</sup>) a-SiC<sub>x</sub>:H layer with the ITO electrode, avoiding the passivation damage of the laser process. Since ITO's refractive index is  $\sim 2$ , it also works as a conductive back-reflector in direct contact with a Ag electrode.

<sup>1</sup> In a preliminary test, the heat of the laser strike was able to trespass the whole width of the wafer and damage the front TMO layer; consequently, it was decided that the laser-doping step had to be done before the TMO deposition.

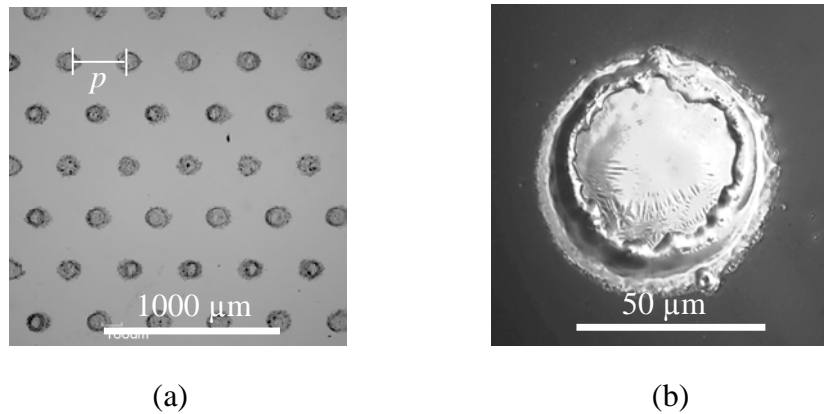


Figure 3.4 Microscope images of laser-doped contacts showing (a) dot pattern with a pitch  $p$  of  $300\ \mu\text{m}$ , and (b) contact crater with a radius ( $r$ ) of  $\sim 40\ \mu\text{m}$ .

### 3.1.3 Carrier-selective contacts

In contrast to the chemical nature of the PECVD process, TMOs are deposited by vacuum thermal evaporation using a resistive element as a heat source (Joule effect). This process is carried out inside an evaporation chamber whose main components are (1) a material evaporation source, (2) a quartz crystal sensor, (3) a rotatory substrate holder, (4) an adjustable high DC current supply, (5) a deposition controller (SQC-310, Inficon, Switzerland) and (6) mechanic/turbo-molecular pumps (Fig. 3.5a). The chamber is located inside a  $\text{N}_2$  atmosphere glovebox (MB200B, MBraun, Germany), avoiding sample degradation by air and humidity.

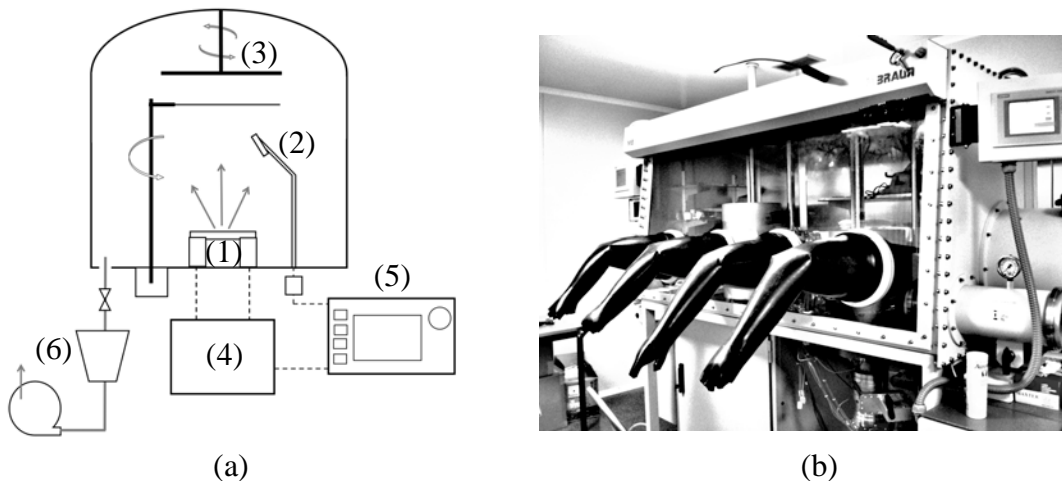


Figure 3.5 (a) Schematic of the vacuum thermal evaporation chamber. (b) Inert atmosphere glovebox.

For the TMO thermal evaporation, powdered material (99.99%, Sigma Aldrich) is placed in a refractory tantalum boat. After a vacuum of  $\leq 10^{-6}$  mbar is reached, power is supplied until the

vapor pressure of the solid (sublimation) or liquid (evaporation) is overcome and molecules are ejected ballistically towards the substrate surface. Table 3.2 lists some material properties that are relevant during thermal evaporation. The deposition rate (kept at 0.1 nm/s or less) is monitored by a quartz crystal microbalance whose resonance frequency is proportional to the added mass. These microbalance thickness readings need to be calibrated against other techniques like contact profilometry or TEM imaging. An appropriate vacuum is critical to ensure the mean-free path of the molecules is larger than the source–substrate distance. Moreover, the substrate stays close to ambient temperature provided that the material evaporation temperature is below 1,000 °C.

Table 3.2 Material properties relevant for vacuum thermal evaporation.

<b>Material</b>	<b>Melting point °C</b>	<b>Density g/cm<sup>3</sup></b>	<b>Sublimes (S)/ Decomposes (D)</b>
MoO <sub>3</sub>	795	4.69	S
WO <sub>3</sub>	1,473	7.16	S
V <sub>2</sub> O <sub>5</sub>	690	3.36	D
ReO <sub>3</sub>	400	6.92	D
NiO	1,984	6.67	-
LiF	845	1.74	-

### 3.1.4 PEDOT:PSS hole-selective contact/transparent conductive electrode

PEDOT:PSS is a water-soluble polymer electrolyte consisting of positively charged PEDOT and negatively charged PSS monomers [8]. It can be deposited by a variety of solution-processing techniques, of which spin-coating is the laboratory standard (Fig 3.6a). For this work, two different polymer solutions are investigated (HTL Solar and PH1000, Heraeus, USA[9]), pre-conditioned with 5%<sup>v/v</sup> DMSO (Sigma Aldrich) to increase the conductivity and 0.1%<sup>v/v</sup> fluorosurfactant (Capstone FS-31, Dupont, USA) to improve the wettability of the surface [10]. The latter is particularly important and was carefully optimized by measuring the contact angle between the PEDOT:PSS solution and the highly-hydrophobic c-Si surface, showing a decrease of the contact angle (improved wettability) for the surfactant-treated solutions (Fig. 3.6b). The solution is spin-coated at 1,000 rpm during 60 s, followed by a thermal anneal (30 min) at 130 °C in a N<sub>2</sub> atmosphere, eliminating all remnant moisture and yielding a uniform film.

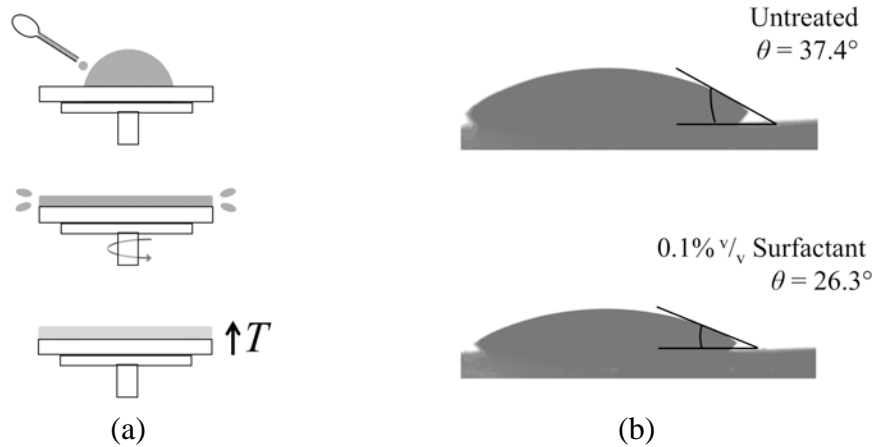


Figure 3.6 (a) Schematic of the spin-coating process. (b) Contact angle of untreated and surfactant-treated HTL Solar PEDOT:PSS solution on hydrophobic c-Si.

### 3.1.5 ITO transparent conductive electrode

Given that the lateral conductivity of TMOs is relatively low, a transparent conductive oxide must be deposited on top with the purpose of collecting carriers for their extraction through the metal grid. Then, the ITO sheet resistance  $R_{sh}$  (in  $\Omega/$  ), defined by the film resistivity  $\rho$  to thickness  $d$  ratio, becomes an important contributor to the series resistance of the device. In optical terms, the refractive index of ITO is already very close to the optimal<sup>2</sup> value  $n_{opt} \sim 2$ , with an optimal coating thickness  $t = \lambda/4n = 70\text{--}100$  nm [11]. Considering that TMOs also have an  $n \sim 2$ , the thicknesses of the TMO and ITO layers need to be optimized according to their refractive index values, ultimately lowering reflection losses below 1% for the wavelengths where the photon flux is maximum (600–700 nm).

The deposition of ITO is carried out in a RF-assisted sputtering system (Fig. 3.7), where highly-energized argon ions collide with an ITO target (1) and eject the material towards a rotating substrate (2). Magnetron-induced electric fields are used to confine the charged plasma near the vicinity of the target, avoiding re-sputtering of the already deposited material. An adequate baseline vacuum ( $10^{-6}$  mbar), a mild argon pressure ( $\sim 1.3 \times 10^{-3}$  mbar) and moderate power densities ( $2.5 \text{ W/cm}^2$ ) are needed to obtain both transparent and conductive ( $R_{sh} \sim 100 \Omega/$  ) films at reasonable deposition rates (2 nm/min) [12].

<sup>2</sup> Defined by the geometric mean of the air and c-Si refractive indexes  $n_{opt} = \sqrt{n_{air} n_{cSi}}$ .



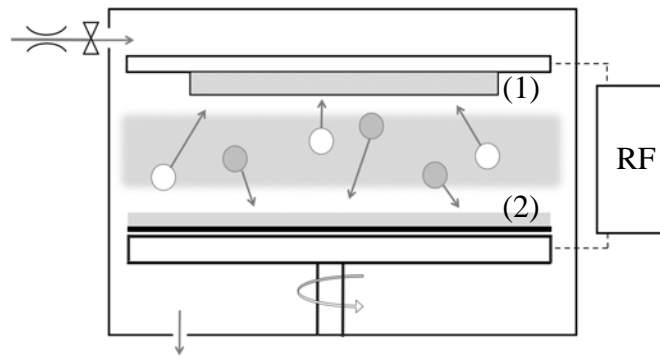


Figure 3.7 Schematic of the sputtering process.

### 3.1.6 Active area definition

Delimiting the active area of a solar cell is very important, not only for an accurate efficiency calculation ( $J$  is measured in  $A/cm^2$ ) but also to avoid edge effects like current leakage or shunts. For this purpose, photolithography is used to imprint squared patterns on a positive-photoresist (SUSS MicroTec, Germany), previously spin-coated on the front face of the substrate. After removing the UV-exposed resin with a developer solution, both the ITO and TMO layers are wet-etched in a HF (1%), delimiting the active area of the cells to  $1 \times 1 \text{ cm}^2$  and  $2 \times 2 \text{ cm}^2$  sizes.

### 3.1.7 Front/rear electrodes

Metallic front and rear electrodes are needed to extract current with a minimal  $R_S$ . For the case of the front electrode, a carefully designed grid is mandatory in order to balance maximum current collection with minimum shadow losses. Figure 3.8 shows the grid design used for the solar cells, including a variable-width central bus bar connected to  $30 \mu\text{m}$  fingers. The Ag grid is deposited by thermal evaporation through a shadow mask, obtaining a  $3 \mu\text{m}$  thick grid with a total shadow loss of 4.2%. For the full area rear electrodes, a Ti/Al ( $15 \text{ nm}/1 \mu\text{m}$ ) stack is deposited by vacuum electron-beam<sup>3</sup> (e-beam) evaporation on the laser-doped devices, while a Ag ( $3 \mu\text{m}$ ) layer is deposited by thermal evaporation on the rear-ITO cells.

<sup>3</sup> Similar to thermal evaporation, where the heat source is an electron beam accelerated towards the high melting point material. One drawback of this technique is the emission of x-rays that could lead to passivation damage.

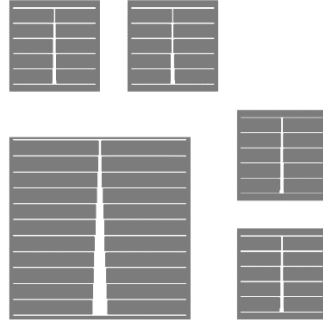


Figure 3.8 Sketch of front finger grid, with an estimated 4.2% shadow loss.

## 3.2 Solar cell characterization

### 3.2.1 Carrier lifetime

Measurement of the effective carrier lifetime  $\tau_{eff}$  by contactless photoconductance allows evaluating the passivation properties of device precursors at different fabrication stages (Fig. 3.9a). Originally developed by R.A. Sinton and A. Cuevas [13], this technique correlates current photogeneration  $J_{ph}$  (measured with a calibrated sensor) with photoconductance transients  $\Delta G$  inside the sample (measured by inductive coupling). Since all photogenerated carriers recombine inside the c-Si substrate, it can be assumed that  $J_{ph} = J_{rec} = q \Delta n_{avg} W / \tau_{eff}$ , where  $\Delta n_{avg}$  is the average excess carrier concentration inside the wafer bulk (extracted from the photoconductance transients by  $\Delta G = \Delta(W\sigma) = W \cdot q(\mu_e + \mu_h)\Delta n_{avg}$ ). As a result, the following explicit expression for  $\tau_{eff}$  is obtained:

$$\tau_{eff} = \frac{\Delta(W\sigma)}{J_{ph}(\mu_e + \mu_h)} \quad (3.1)$$

which yields the standard  $\tau_{eff}(\Delta n)$  curves described in §2.2. In the measurement equipment used in this work (WCT-120, Sinton Consulting, USA), two illumination regimes are possible [14]: (1) quasi-steady state (QSS-PC), with a monotonic intensity decay of  $\sim 2.3$  ms, instantly evaluating  $\tau_{eff}$  at different injection levels; (2) transitory state (PCD), with a short illumination flash of  $\sim 15$   $\mu$ s, evaluating  $\tau_{eff}$  independently of  $J_{ph}$ . The PCD regime is used to assess the effective absorption inside the wafer, which could be smaller than the reference sensor due to optical effects (texturization, ARC layer, etc.).

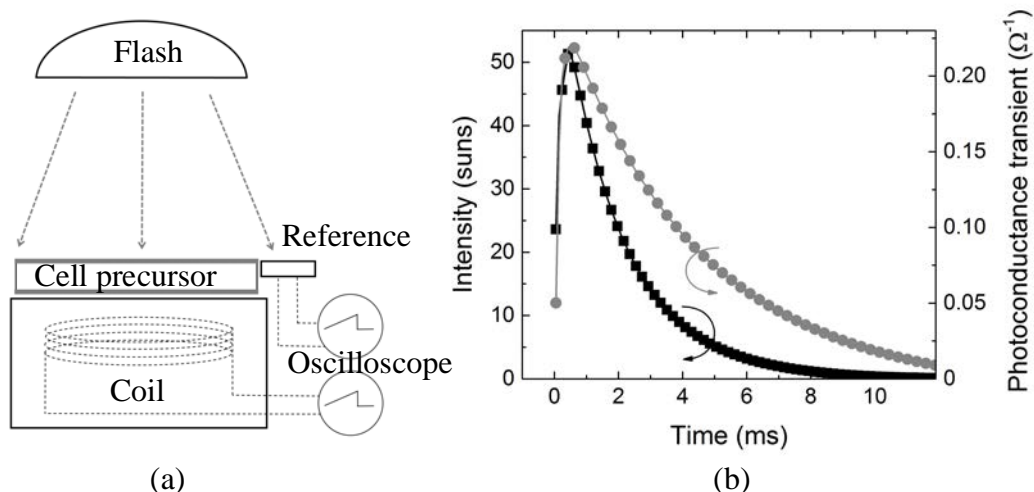


Figure 3.9 (a) Schematic of the contactless photoconductance technique and (b) representative time dependence of the light intensity (suns) and photoconductance transients ( $\Omega^{-1}$ ).

A common experimental approach in lifetime measurements is the deposition of the material of interest on both sides of the wafer (e.g. a TMO/c-Si/TMO). If the intrinsic bulk lifetime ( $\tau_{bulk}$ ) is large enough, the effective lifetime of this symmetric sample is only limited by the front and rear surfaces, simplifying Eq. 2.13 to:

$$\frac{1}{\tau_{eff}} - \frac{1}{\tau_{bulk}} \approx \frac{2S_{eff}}{W} \approx \frac{2J_0 \Delta n}{qn_i^2 W} \quad (3.2)$$

Eq. 3.2 also implies that a plot of  $(1/\tau_{eff} - 1/\tau_{bulk})$  vs.  $\Delta n$  will yield a linear response with a slope proportional to  $J_0$ . Consequently, lifetime measurements contain implicit information about the  $V_{OC}$  of the device, the so-called *implied- $V_{OC}$*  [13]:

$$i-V_{OC} = \frac{kT}{q} \ln \left( \frac{\Delta n(N + \Delta p)}{n_i^2} + 1 \right) \quad (3.3)$$

Finally, since the front and rear surfaces usually limit the lifetime of the device,  $J_0$  can also be approximated as the sum  $J_{0,front} + J_{0,rear}$ , each term determined independently from lifetime measurements.

### 3.2.2 Current-Voltage

The current density-voltage  $J(V)$  response of a solar cell is essential to evaluate its performance. It is measured at a controlled ambient temperature (25 °C) in the dark and under standard

AM1.5g illumination, as provided by a solar simulator equipped with a xenon lamp (450 W, ABB-class, Oriel 94041A, Newport, USA). Measurements are performed with a source/meter (2601B, Keithley, USA) in a four-point configuration (two on each electrode) so as to minimize the resistance contribution from the measurement cables, which can be as high as 2  $\Omega$ . The data is then collected by an in-house Matlab routine.

Typically, the  $J(V)$  response of a c-Si solar cell is far from the ideal model described by Eq. 2.3, where the effect of the series and parallel resistances  $R_S$  and  $R_P$  are not included. Moreover, although 80–90% of the photocurrent is generated in the bulk of the absorber and is limited by diffusion of minority carriers, the rest is generated in the space-charge region and is limited by SRH recombination [15]. These two transport regimes determine the value of the ideality factor, varying between  $n = 1$  for the diffusion current (forward bias 0.3 – 0.6 V) and  $n = 2$  for the recombination current (small forward bias 0.1 – 0.3 V). The inclusion of these parameters leads to a modified diode-model [4]:

$$J(V) = -J_{ph} + J_{01} \left[ \exp\left(\frac{qV - R_S J}{kT}\right) - 1 \right] + J_{02} \left[ \exp\left(\frac{qV - R_S J}{2kT}\right) - 1 \right] + \frac{V - R_S J}{R_P} \quad (3.4)$$

where  $J_{01}$  and  $J_{02}$  are the saturation current densities for the diffusion- and recombination-limited diodes respectively, each with its characteristic ideality factor. Note that a large series resistance will cause a voltage drop (ohmic loss) whereas a small parallel resistance will cause current losses through low resistive paths.

Fig. 3.10a shows the typical dark  $J(V)$  response of a c-Si solar cell fitted to Eq. 3.4, clearly distinguishing the two diodes  $J_{01}$  and  $J_{02}$ ,  $R_S$  at high injection levels and of  $R_P$  near the origin. Depending on the quality of the device, the contribution of  $R_P$  could be difficult to observe, while highly recombinative devices could show a single  $J_0$  with an  $n$  value between 1 and 2. Fig. 3.10b depicts the resulting equivalent circuit with its two diodes, two resistive elements and a current source  $J_{ph}$ . Due to different current flow dynamics, the value of  $R_S$  determined from the dark  $J(V)$  response is usually underestimated in comparison to the real  $R_S$  under illumination [16]. Therefore, a more accurate procedure consists in measuring  $J(V)$  at different illumination intensities and calculating  $R_S$  by the ratio  $\Delta V/\Delta J_{SC}$  (Fig 3.11). Alternatively, the Suns- $V_{OC}$  methodology (see §3.2.4) can estimate  $R_S$  unambiguously from resistance-free  $J(V)$  measurements, while  $R_P$  can be calculated from the  $\delta V/\delta J$  derivative near  $V = 0$ .

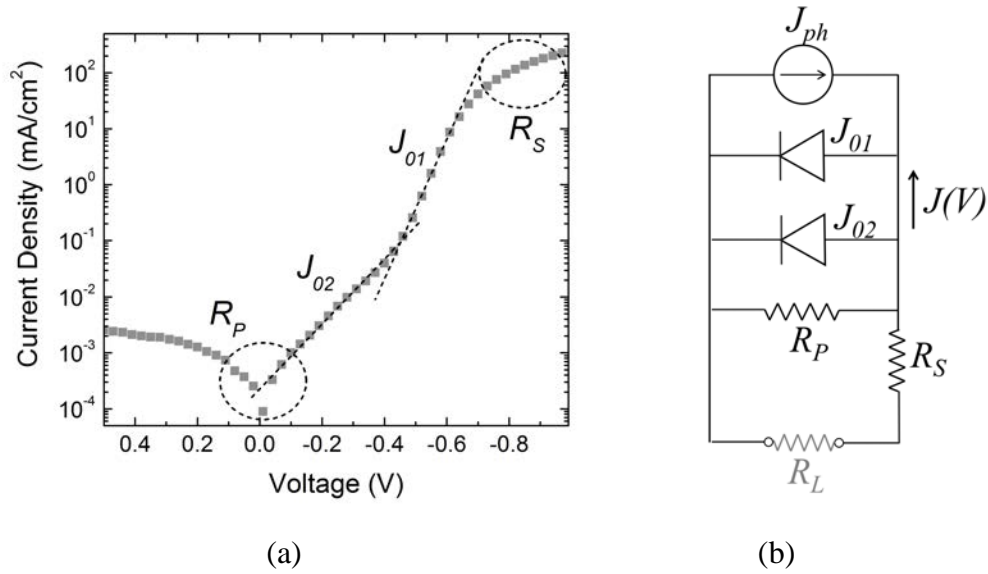


Figure 3.10 (a) Representative  $J(V)$  response of a c-Si solar cell, showing its two diode components ( $J_{01}$  and  $J_{02}$ ) and the effect of  $R_S$  and  $R_P$ . (b) Equivalent circuit of a solar cell.

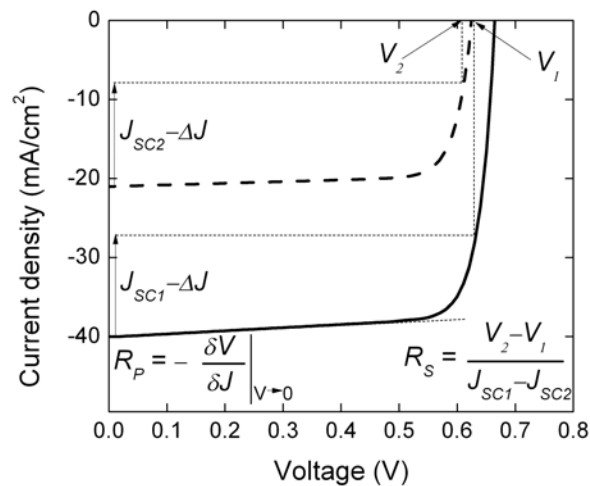


Figure 3.11 Estimation of  $R_S$  and  $R_P$  from the  $J(V)$  solar cell characteristic.

### 3.2.3 Quantum efficiency

The external quantum efficiency EQE, defined as the fraction of collected electron-hole pairs per incident photon, is measured as a function of wavelength at short-circuit conditions with a commercial equipment (QEX10, PVmeasurements, USA). Its operation is based on a white light source dispersed into monochromatic light of adjustable bandwidth. The generated current is

measured with a lock-in amplifier and compared to the incident power, calculating  $J_{SC}$  from the integral of the EQE times the solar photon flux  $\Phi_{sun}$ :

$$J_{SC} = q \int_{-\lambda}^{\lambda} \Phi_{sun}(\lambda) \text{EQE}(\lambda) d\lambda \quad (3.5)$$

where the upper bound for  $\lambda \sim 1100$  nm is determined by the  $E_{gap}$  of c-Si.

Fig. 3.12 shows a representative EQE curve for a c-Si solar cell whose inspection can readily reveal possible current loss mechanisms. For example, a reduced EQE for the ultraviolet ( $\lambda_{UV} < 450$  nm) and near-infrared ( $\lambda_{NIR} > 1000$  nm) wavelengths can be ascribed to absorption ( $A$ ) and/or recombination ( $S$ ) losses at the front and rear surfaces respectively. Short diffusion lengths ( $L_{diff}$ ) will also reduce the EQE in the near-infrared (NIR), while front reflection losses ( $R$ ) will mostly manifest in the mid-range  $\lambda$ . If no optical or recombination losses were present, EQE would be 1. Finally, if the front reflection of the solar cell is available from spectrophotometry measurements (see §3.3.3), it is useful to calculate the internal quantum efficiency (IQE):

$$\text{IQE}(\lambda) = \frac{\text{EQE}(\lambda)}{1 - R(\lambda)} \quad (3.6)$$

which represents the fraction of collected electron-hole pairs per absorbed photon.

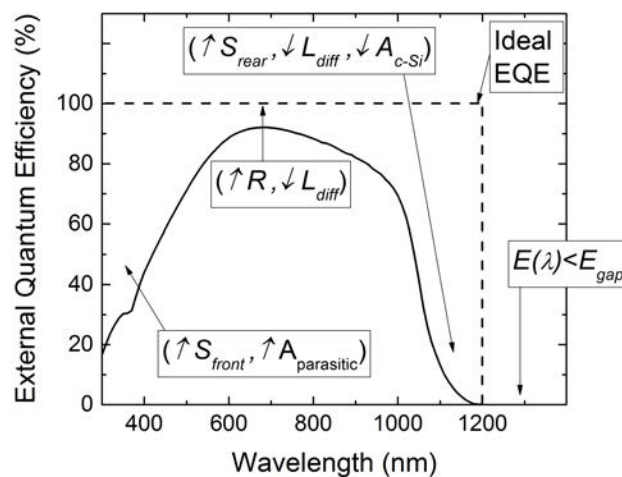


Figure 3.12 EQE losses and their possible causes. The dashed line represents an EQE of 100%.

### 3.2.4 Suns- $V_{OC}$

The Suns- $V_{OC}$  technique, conceived to characterize both precursor and finished devices, measures the  $V_{OC}$  in quasi-steady equilibrium in response to a slowly-varying illumination in sun-equivalents ( $I_{sun}$ ) [17]. Since the device is measured in open-circuit conditions and no current flows through the device, the obtained data (similar to Fig. 3.9a) has no  $R_S$  contributions from the substrate, selective contacts, TCO or metal electrodes, allowing to calculate a pseudo- $J(V)$  curve that represents the intrinsic quality of the materials (absorber and selective contacts). The simple in-house experimental setup consists of a stroboscopic flash lamp, a calibrated reference cell to measure the light intensity and an oscilloscope that measures  $V_{OC}$  and  $I_{sun}$ .

Suns- $V_{OC}$  measurements are also useful to measure the effective lifetime  $\tau_{eff}$  of a finished (front/rear metallized) device, an unviable task in the QSS-PC method which easily saturates for metal layers thicker than 50 nm. Following the methodology described in [18], the Suns- $V_{OC}$  data must be processed in order to obtain the basic expression  $\tau_{eff} = \Delta p/G$  (with  $G$  being the generation rate in  $\text{cm}^{-3} \text{s}^{-1}$ ). First,  $\Delta p$  can be determined from the relation between the minority carrier product  $np$  and the measured  $V_{OC}$ :

$$np \approx (N_d + \Delta p)\Delta p = n_i^2 e^{(qV_{OC}/kT)} \quad (3.7)$$

and solving for the excess minority carrier concentration  $\Delta p$ :

$$\Delta p = \frac{\sqrt{N_d^2 + 4n_i^2 \exp(qV_{OC}/kT)} - N_d}{2} \quad (3.8)$$

As for the generation rate, it can be approximated by the illumination intensity  $I_{sun}$  corrected for the cell short-circuit current at 1 sun illumination (1.5AMg standard):

$$G \approx I_{suns} \frac{J_{SC}|_{1 \text{ sun}}}{qW} \quad (3.9)$$

By comparing the  $\tau_{eff}$  values of cell precursors (before contacts) and finished devices, it is possible to quantify the lifetime degradation occurring after contact formation.

### 3.3 Other characterization techniques

#### 3.3.1 Contact resistance

In this work, the specific contact resistance  $\rho_c$  is an area-independent quantity that includes the metal/selective-contact and the selective-contact/c-Si interfaces, as well as the regions in close proximity [19]. For a specific contact area  $A_c$ , the contact resistance  $R_c = \rho_c/A_c$  can be obtained from the linear  $R = V/I$  response<sup>4</sup> measured between two electrodes. Depending on the polarity of the selective contact (electron or hole extraction) and the c-Si substrate (p-Si or n-Si), two types of structures can be fabricated using the same deposition methods previously described along with shadow masks with different electrode patterns (~50 nm thick Au films), as shown in Fig. 3.13.

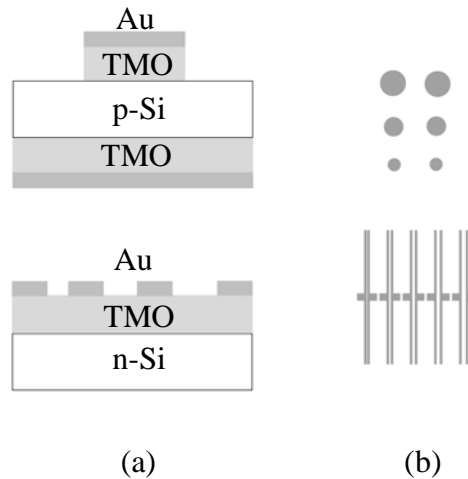


Figure 3.13 (a) Fabricated structures and (b) evaporation masks used for  $\rho_c$  measurements.

For majority carrier contacts (e.g. hole-selective TMO/p-Si), a two-contact vertical structure is used, where the total measured resistance  $R$  is defined as [20]:

$$R = \frac{\rho_c}{\pi r^2} + R_{spr} + R_0 \quad (3.10)$$

where  $r$  is the radius of the top circular contact,  $R_{spr}$  the spreading resistance<sup>5</sup> and  $R_0$  other minor resistive elements such as the metal electrode resistance (negligible), the probe resistance

<sup>4</sup> The response need not be necessarily linear, as long as the ohmic voltage drop is negligible [19].

<sup>5</sup>  $R_{spr}$  accounts for the spread-out current pattern from a small to a large contact area.



(minimized by 4-point probing) and the full-area back contact resistance. For accurate measurements, a small contact  $r$  should be used so that  $R_{spr} \ll R_c$  [19].

For minority carrier extraction (e.g. hole-selective TMO/n-Si), a multiple-contact horizontal structure is used, where the total measured resistance  $R$  is defined as [19]:

$$R = \frac{\rho_c}{L_T Z} + \frac{R_{sh} d}{Z} + R_0 \quad (3.11)$$

where  $Z$  is the contact width,  $d$  is distance between contacts,  $L_T$  the effective transfer length (smaller than the true contact length) and  $R_{sh}$  is the sheet resistance of the c-Si substrate or the accumulation/inversion layer (if present). This technique is known as the transfer length method (TLM), needing small  $d$  values so that  $R_{sh} \ll R_c$ .

### 3.3.2 Impedance spectroscopy

The impedance spectroscopy (IS) technique measures the current  $\hat{i}$  passing through a solar cell when an small-signal AC voltage  $\hat{u}$  is applied (usually 10 mV), obtaining a frequency-dependent impedance  $Z(\omega) = \hat{u}(\omega)/\hat{i}(\omega)$ . Depending on the equivalent circuit model and on the  $\omega$  magnitude,  $Z(\omega)$  can be directly correlated to different electronic processes in a solar cell such as internal capacitances, recombination and series resistances [21]. For instance, the most simple IS model (dotted lines in Fig. 3.14a) measures the capacitance  $C(\omega) = 1/(i\omega Z(\omega))$  (in F/cm<sup>2</sup>) at a fixed frequency for different dc bias  $V$ . By plotting  $1/C^2$  (V) the so-called Mott-Schottky plot is obtained (Fig. 13.14b), showing two distinctive elements, the junction capacitance  $C_j$  at negative bias and the diffusion (chemical) capacitance  $C_d$  at positive bias. Moreover, by assuming the one-sided abrupt junction approximation, a linear fitting using the relation:

$$\frac{1}{C_j^2} = \frac{2}{q \varepsilon_{cSi} N} \left( V_{bi} - V - \frac{2kT}{q} \right) \quad (3.12)$$

allows to determine the built-in voltage  $V_{bi}$  from the x-axis intercept and the substrate doping density  $N$  from the slope (with  $\varepsilon_{cSi}$  as the permittivity of c-Si). Further information can be obtained by plotting the real vs. imaginary  $Z(\omega)$  components in a Nyquist plot, which allows to differentiate between the series resistance (due to ohmic losses) and the recombination resistance

$R_{rec}$  (related to  $S_{eff}$ ). Since each capacitive element has a characteristic response time  $\tau = R_{rec}C_d$ , it is possible to calculate the effective lifetime from  $\tau = \tau_e + \tau_h$  [22].

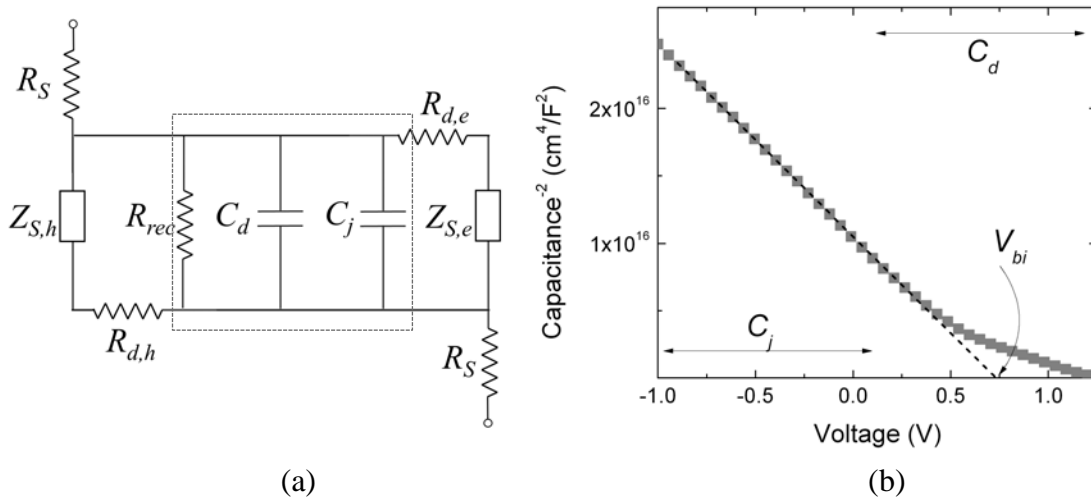


Fig 3.14 (a) Equivalent circuit model for a solar cell, showing capacitive elements (junction  $C_j$  and diffusion  $C_d$ ) as well as resistive elements (series  $R_s$ , bulk recombination  $R_{rec}$ , electron/hole diffusion  $R_d$  and surface recombination at the selective-contacts  $Z_s$ ). Adapted from [21]. (b)  $1/C^2(V)$  plot showing  $C_j$  and  $C_d$ .

### 3.3.3 Spectrophotometry

A commercial UV-visible-NIR spectrophotometer (Shimadzu 3600, Japan) is used to quantify the parasitic absorption and reflection losses occurring in a solar cell as a function of wavelength. Fig. 13.15 depicts the main components of a spectrophotometer where a white light source is dispersed into its constituting wavelengths by a monochromator, which are then isolated into narrow bandwidth (1–10 nm) beams by a mechanical slit. The monochromatic beam is then directed towards the sample, after which a photodetector measures the fraction of transmitted (or reflected) radiant energy. For the materials used as selective contacts or TCO electrodes, the total transmittance  $T$  is measured across thin layers deposited on borosilicate glass slides.

By subtracting the reflection/absorption contribution from the glass substrate, the internal transmittance due to film absorption can be calculated. For the front reflection losses of a solar cell, the total reflectance  $R$  is measured in a finished device without the Ag grid. For this measurement, the sample is placed in an integrating sphere that concentrates the reflected light and compares it to a white background.

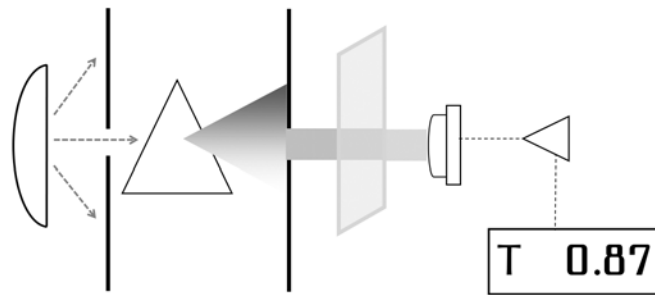


Fig. 13.15 Main components of a UV-visible-NIR spectrophotometer.

### 3.3.4 X-ray photoelectron spectroscopy (XPS)

XPS is a surface sensitive technique that probes the sample's outer surface ( $\leq 10$  nm) by X-ray photons and measures the characteristic kinetic energy ( $E_{KE}$ ) of the emitted photoelectrons. Photoemission is directly related to the distinctive binding energies ( $E_{BE}$ ) of core level electrons in a chemical element with a particular oxidation state. Therefore, XPS can determine the material composition as well as chemical shifts due to redox reactions [23]. An energy balance of the photoemission process allows determining  $E_{BE}$  by:

$$E_{BE} = E_{X-ray} - E_{KE} - \Phi \quad (3.13)$$

where  $\Phi$  is the material work function and  $E_{X-ray} \sim 1,486$  eV is the energy of the non-monochromatic Al- $K_{\alpha}$  source from the equipment used (SPECS, Germany). A typical XPS survey spectrum is shown in Fig. 13.16, with each peak representing a particular orbital of a particular element in the sample. Since the area under each peak is proportional to the atomic concentration of each chemical species, a quantitative analysis of the film composition (in atomic %) can be done by data processing software (CasaXPS). Special care must be taken to reduce surface contamination by carbon-based compounds that instantly adsorb at the sample surface. In addition to core level electrons, XPS is capable of detecting the valence band states located at binding energies  $< 10$  eV (with the Fermi level located at 0 eV), although a UV radiation source (UPS) is needed for an accurate probing of the valence band states [24]<sup>6</sup>.

<sup>6</sup> Similarly, inverse photoelectron spectroscopy (IPES) is needed to probe the density of empty states at the conduction band.

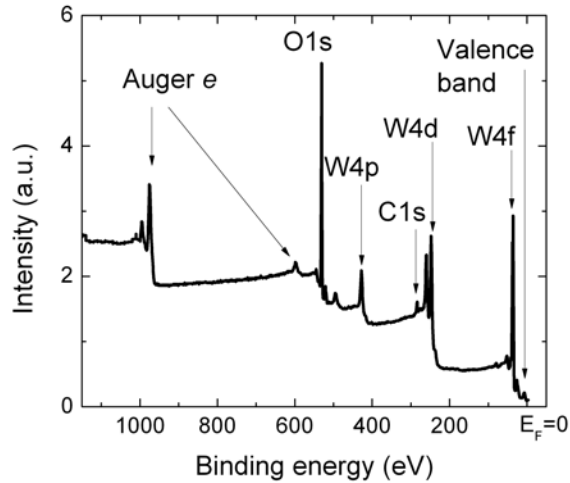


Figure 13.16 XPS survey spectrum of a  $\text{WO}_3$  thin film. A binding energy of 0 eV is equivalent to the  $E_F$  level.

### 3.3.5 Electron microscopy

Detailed imaging of surface topography and layer interfaces can be obtained by scanning (SEM) and transmission (TEM) electron microscopy, where an electron beam is accelerated by a voltage source (10 – 200 kV) and then focused by electromagnetic lenses, illuminating the sample with a resolution proportional to the electron wavelength ( $\lambda \sim 10^{-3}$  nm) [23]. SEM imaging (NEON40, Carl Zeiss, Germany) is based on the detection of emitted secondary electrons from a bulk surface, revealing details in the  $\mu\text{m}$  range as shown in Fig. 3.2 for a texturized c-Si wafer.

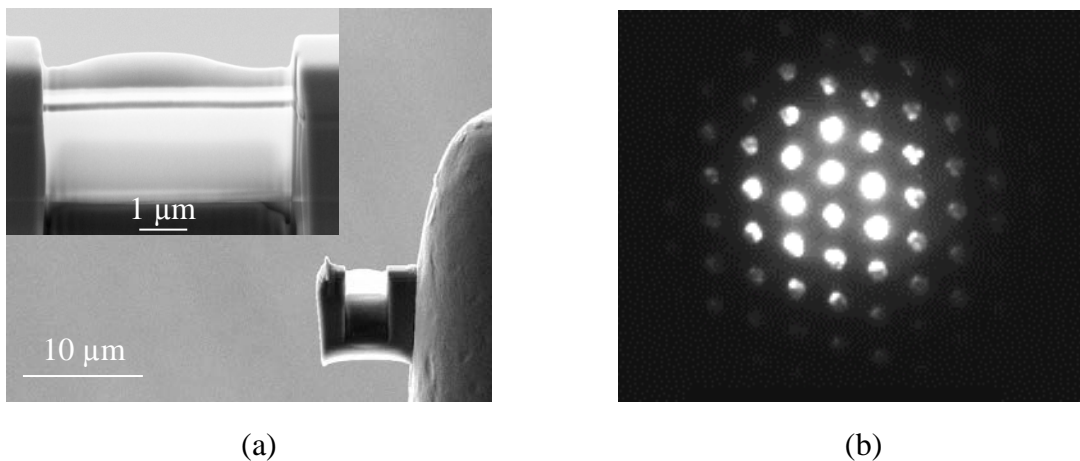


Figure 3.17 (a) Milled lamella welded to a TEM holder (b) electron diffraction pattern.

Alternatively, TEM (2010F, JEOL, Japan) is based on the detection of transmitted electrons through an ultra-thin sample cross-section known as lamella, revealing sub-nm details such as atomic lattices. Lamella preparation is carried out by focused ion beam (FIB) milling with  $\text{Ga}^+$  ions, removing bulk material until an electron-transparent ( $<50$  nm) cross-section is obtained (Fig. 3.17a). Then, the lamella is extracted by a micro-manipulator needle and welded to a TEM holder. TEM is also capable of obtaining electron diffraction patterns used to determine the crystalline structure of solids, as shown in Fig. 3.17b for the c-Si substrate.

### 3.3.6 Time-of-flight secondary ion mass spectrometry (ToF-SIMS)

The ToF-SIMS technique determines the chemical composition of thin-films as a function of depth, sputtering the surface with a primary ion beam and analyzing the ejected secondary ions with depth resolution of 1 nm and large sensitivities (parts per trillion) [23]. A depth-profile of the fabricated solar cells is performed by sputtering with  $\text{Cs}^+$  ions under high vacuum ( $10^{-8}$  mbar) followed by the identification of the ion masses from their different velocities (i.e. different travel times from the sample to the detector) at a fixed kinetic energy of 25 keV (ION-TOF IV, Ion-tof, Germany). Mass is detected in atomic mass units (amu) with a resolution of  $10^{-3}$  amu, recording the complete mass spectrum for every sputtering pulse of 200 ps duration.

## 3.4 References

- [1] W. Kern, The evolution of silicon wafer cleaning technology, *J. Electrochem. Soc.* **137** (1990) 1887–1892.
- [2] H. Neergaard, J.T. Yates, Surface chemistry of silicon, *Chem. Rev.* **95** (1995) 1589–1673.
- [3] P. Papet, O. Nichiporuk, A. Kaminski, Y. Rozier, J. Kraiem, J.F. Lelievre, et al., Pyramidal texturing of silicon solar cell with TMAH chemical anisotropic etching, *Sol. Energy Mater. Sol. Cells.* **90** (2006) 2319–2328.
- [4] A. Luque, S. Hegedus, Handbook of photovoltaic science and engineering, 2nd ed., Wiley, Chichester (UK), 2011.
- [5] M.J. Kushner, A model for the discharge kinetics and plasma chemistry during plasma enhanced chemical vapor deposition of amorphous silicon, *J. Appl. Phys.* **63** (1988) 2532–2551.
- [6] I. Martín, M. Vetter, M. Garín, A. Orpella, C. Voz, J. Puigdollers, et al., Crystalline silicon surface passivation with amorphous  $\text{SiC}_x\text{H}$  films deposited by plasma-enhanced chemical-vapor deposition, *J. Appl. Phys.* **98** (2005) 114912.
- [7] P. Ortega, A. Orpella, I. Martin, M. Colina, G.Lopez, C. Voz, et al., Laser-fired contact

- optimization in c-Si solar cells, *Prog. Photovolt Res. Appl.* **20** (2012) 173–180.
- [8] K. Sun, S. Zhang, P. Li, Y. Xia, X. Zhang, D. Du, et al., Review on application of PEDOTs and PEDOT:PSS in energy conversion and storage devices, *J. Mater. Sci. Mater. Electron.* **26** (2015) 4438–4462.
- [9] Heraeus GmbH (Germany), Clevios: Advanced materials for new organic solar cell technologies, (2015). [www.heraeus-clevios.com](http://www.heraeus-clevios.com) (accessed June 1, 2017).
- [10] D. Chi, B. Qi, J. Wang, S. Qu, Z. Wang, High-performance hybrid organic-inorganic solar cell based on planar n-type silicon, *Appl. Phys. Lett.* **104** (2014) 193903.
- [11] T. Dittrich, *Materials concepts for solar cells*, 1st ed., Imperial College press, London, UK, 2015.
- [12] A.B. Morales Vilches, *Desarrollo de tecnologías de baja temperatura para la fabricación de células solares de heterounión de silicio*. PhD Thesis., Universitat Politècnica de Catalunya, 2015.
- [13] R. Sinton, A. Cuevas, Contactless determination of current–voltage characteristics and minority-carrier lifetimes in semiconductors from quasi-steady-state photoconductance data, *Appl. Phys. Lett.* **69** (1996) 2510.
- [14] Sinton Instruments, WCT-120 photoconductance lifetime tester user manual, (2013) Available at: [www.sintoninstruments.com](http://www.sintoninstruments.com).
- [15] S.M. Sze, K.K. Ng, *Physics of semiconductor devices*, 3rd ed., Wiley, Hoboken, NJ, 2007.
- [16] D. Pysch, A. Mette, S.W. Glunz, A review and comparison of different methods to determine the series resistance of solar cells, *Sol. Energy Mater. Sol. Cells.* **91** (2007) 1698–1706.
- [17] R. Sinton, A. Cuevas, A quasi-steady-state open-circuit voltage method for solar cell characterization, in: 16th Eur. Photovolt. Sol. Energy Conf., Glasgow, 2000: pp. 1–4.
- [18] M.J. Kerr, A. Cuevas, R.A. Sinton, Generalized analysis of quasi-steady-state and transient decay open circuit voltage measurements, *J. Appl. Phys.* **91** (2002) 399–404.
- [19] D.K. Schroder, *Semiconductor material and device characterization*, 3rd ed., Wiley, Hoboken, USA, 2006.
- [20] R.H. Cox, H. Strack, Ohmic contacts for GaAs devices, *Solid. State. Electron.* **10** (1967) 1213–1218.
- [21] I. Mora-Sero, G. Garcia-Belmonte, P.P. Boix, A. V Miguel, J. Bisquert, Impedance spectroscopy characterisation of highly efficient silicon solar cells under different light illumination intensities, *Energy Environ. Sci.* **2** (2009) 678–686.
- [22] I. Mora-sero, Y. Luo, G. Garcia-Belmonte, J. Bisquert, D. Munoz, C. Voz, et al., Recombination rates in heterojunction silicon solar cells analyzed by impedance spectroscopy at forward bias and under illumination, *Sol. Energy Mater. Sol. Cells.* **92** (2008) 505–509.
- [23] D. Abou-Ras, T. Kirchartz, U. Rau, *Advanced characterization techniques for thin film solar cells*, Wiley-VCH, Weinheim, Germany, 2011.
- [24] J. Meyer, S. Hamwi, M. Kröger, W. Kowalsky, T. Riedl, A. Kahn, Transition metal oxides for organic electronics: energetics, device physics and applications., *Adv. Mater.* **24** (2012) 5408–5427.

## 4 Materials characterization

*A thorough characterization of the structural and optoelectronic properties of transition metal oxides and PEDOT:PSS is presented, with emphasis on their applicability as hole-selective contacts in c-Si solar cells.*

Understanding the multiple correlations between a material's chemistry (internal structure, composition, reactivity) and its optoelectronic properties is critical for a successful implementation into c-Si solar cells. Table 4.1 lists several selective contact properties that are relevant for solar cell operation. For instance, a wide energy band gap ( $E_{gap} > 3\text{eV}$ ) is a trademark characteristic of transition metal oxides (TMOs), making them suitable as front window layers in HIT-type solar cell architectures. Another important property is conductivity, with TMOs exhibiting negligible values ( $\sigma \sim 10^{-7} \Omega^{-1}\text{cm}^{-1}$ ) that prevent their use as front collector electrodes, also limiting film thicknesses to a few tenths of nanometers so that resistive losses are not excessive. Accordingly, the solar cell structures presented in Fig. 3.1a and 3.1c display very thin TMO layers (20 nm) capped by a TCO layer. In contrast, PEDOT:PSS has a moderate  $E_{gap}$  ( $\sim 1.6$  eV) and a higher  $\sigma$  ( $\sim 10^1 \Omega^{-1}\text{cm}^{-1}$ ), facilitating both carrier collection and hole-selectivity as in the ITO-free solar cell structure shown in Fig. 3.1b.

Table 4.1 Material properties reported in literature. The film deposition methods are thermal evaporation (e), in-situ oxidation (ox), sputtering (sp) and solution spin-coating (s).

Material	$E_{gap}$ eV	$\sigma$ $\Omega^{-1}\text{cm}^{-1}$	$\Phi^{(1)}$ eV	Type	Selectivity with c-Si	Ref.
(e) MoO <sub>3</sub>	3.0 – 3.2	$10^{-7} - 10^{-5}$	5.1 – 6.9	n	hole	[1–3]
(e) WO <sub>3</sub>	3.1 – 3.3		6.0 – 6.7	n	hole	[1,4,5]
(e) V <sub>2</sub> O <sub>5</sub>	2.1 – 2.8		5.3 – 7.0	n	hole	[1,6,7]
(e) ReO <sub>3</sub>	2.5 – 3.4		6.0 – 6.9	n	hole	[8–10]
(ox/sp) NiO	3.1 – 4.0	$10^{-2} - 10^2$	5.2 – 6.8	p	hole	[11–13]
(e) LiF <sup>(2)</sup>	$\sim 13.6$	Insulator	2.8 – 3.0	n	electron	[14–16]
(s) PEDOT:PSS	$\sim 1.6$	$10^1 - 10^2$	4.7 – 5.2	p	hole	[17–19]

<sup>(1)</sup> The lowest values correspond to oxygen-deficient structures, usually after air exposure.

<sup>(2)</sup> The n-type character and  $\Phi$  value are not inherent to LiF, but associated to a  $\Phi$  reduction of a metal like Al [15].

Table 4.1 also lists the carrier selectivity of these materials with c-Si (electron or hole contacts), a property that does not depend necessarily on their inherent semiconductivity (i.e. p- or n-type) but on how their work functions ( $\Phi$ ) align with the Fermi levels of c-Si (see §2.3.2 and §2.3.3). For example, n-type  $\text{MoO}_3$  ( $\Phi > 5.1$  eV) cannot perform as an efficient electron contact due to misalignment with the electron quasi-Fermi level ( $E_{Fn} \sim 4.2$  eV). Yet, it aligns favorably with the hole quasi-Fermi level ( $E_{Fp} \sim 5.0$  eV), facilitating the extraction of holes<sup>1</sup>.

Depending on the doping character of the c-Si substrate (n- or p-type), large work function TMOs will form a hole-selective contact via two pathways [20,21]: (1) inducing an accumulation layer on the p-Si surface, equivalent to a  $p^+/p$  contact; (2) inducing an inversion layer on the n-Si surface, equivalent to a  $p^+/n$  junction. Considering that TMOs will provide a certain degree of surface passivation, these type of heterojunctions can be described as genuine *passivating induced junctions*. Figure 4.1 illustrates the energy band diagram after Fermi level alignment, with the built-in potential  $V_{bi}$  being equal to the work function difference  $\Phi_{TMO} - \Phi_{c-Si}$ .

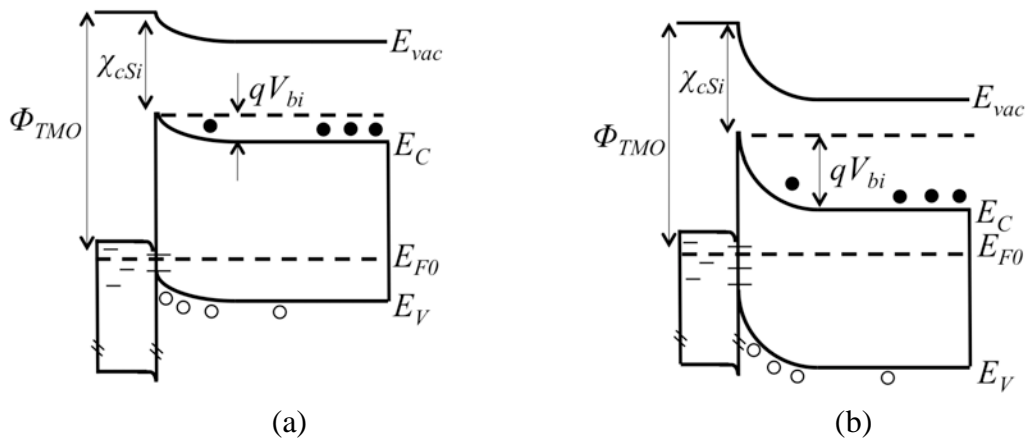


Figure 4.1 Expected energy band alignment (under equilibrium in the dark) between high work function TMOs ( $\Phi_{TMO} > 5.1$  eV) and (a) p-Si or (b) n-Si.

Two more TMOs, NiO and  $\text{ReO}_3$ , were also tested for hole selectivity. However, the quick degradation of  $\text{ReO}_3$  films (even under  $\text{N}_2$ ) and the high evaporation temperatures of NiO ( $\sim 1950$  °C) prevented their implementation into finished devices. Likewise, LiF was also tested for electron selectivity, but the negligible passivation properties of LiF/n-Si heterojunctions resulted in very poor solar cell performance. Consequently, the characterization details for these three materials will be treated separately in Appendix B.

<sup>1</sup> As for the mechanisms involved in hole conduction and extraction across the TMO/n-Si interface, see §4.3.2.



## 4.1 Transition metal oxides

Transition metal oxides are characterized by an electronic configuration<sup>2</sup> with one or more  $d$ -orbital electrons in their outer electron shell whose degree of occupancy largely determines the electronic behavior [5,22]. Fig. 4.2 depicts representative energy band diagrams for different TMOs, with a valence band mostly composed by O  $2p$  states and a conduction band by metal  $d$ -states whose occupancy is determined by the oxide stoichiometry. Accordingly, two TMO categories can be distinguished [5]:

- (1) As the lowest  $d$ -band becomes filled ( $d_1$ ), TMOs transition from stoichiometric insulators to metallic-like conductors, e.g.  $\text{MoO}_3$  and  $\text{MoO}_2$  respectively. In between this transition, n-type semiconductivity is observed for oxygen-deficient materials ( $\text{MoO}_{3-x}$ ) due to occupied defect states within  $E_{gap 1}$ , very close to the conduction band.
- (2) Once the  $d_1$ -band is full, the above  $d_2$ -band becomes filled and TMOs transition from insulators<sup>3</sup> to semiconductors, e.g.  $\text{NiO}$  and  $\text{Ni}_{1-x}\text{O}$  respectively. For the latter, p-type semiconductivity is observed due to cation-deficiency and unoccupied defect states lying within the next-highest  $E_{gap 2}$ , very close to the  $d_2$  valence band.

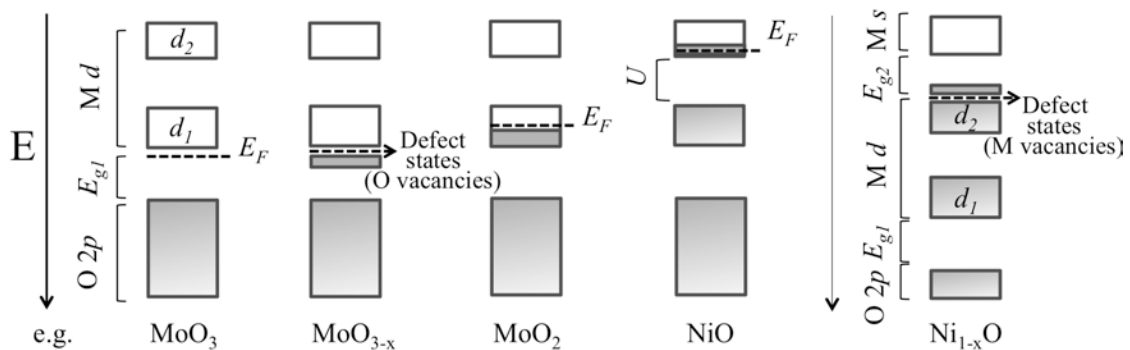


Figure 4.2 Electronic band structure for some TMO semiconductors, reflecting  $d$ -band occupancy. Adapted from [5].

In summary, deviations from stoichiometry in TMOs lead to oxygen vacancies (excess electrons) or cation vacancies (excess holes) that position the Fermi level in the vicinity of the conduction or valence bands respectively.

<sup>2</sup> Of the form  $[\text{inert gas}](n-1)s^{1-2}d^m$ , where  $n$  is the electron shell and  $m$  the occupancy (1–10).

<sup>3</sup> Known as Mott-Hubbard or charge-transfer insulators, with an energy gap  $U$  between  $d_1$  and  $d_2$ .

This thesis is focused on oxygen-deficient n-type semiconductors  $\text{MoO}_{3-x}$ ,  $\text{WO}_{3-x}$  and  $\text{V}_2\text{O}_{5-x}$ , obtained from stoichiometric materials that tend to lose oxygen during the deposition process by vacuum thermal evaporation. Since oxide stoichiometry largely determines the electrochemical potential [5], it is no surprise the large  $\Phi$  variation reported in the literature, where many diverse deposition methods (in-situ oxidation, thermal evaporation, solution processes) and environments (vacuum,  $\text{N}_2$ , air) are used. Additional factors like impurities, surface dipoles and TMO/substrate chemical reactions also impede the fine-tuning strategy and reproducibility of TMO's selectivity.

Fig. 4.3a summarizes the general trend in  $\Phi$  and  $\sigma$  variation with TMO stoichiometry, where a high oxygen deficiency results in lower work functions but increased conductivity values [5]. As an example,  $\text{MoO}_3$  has a  $\Phi \sim 6.8$  eV and a coplanar  $\sigma \sim 10^{-7} \Omega^{-1}\text{cm}^{-1}$  when fully oxidized (insulating), transitioning to  $\sim 5.9$  eV and  $\sim 10^{-5} \Omega^{-1}\text{cm}^{-1}$  as it reduces to  $\text{MoO}_2$  [5,23]. Similarly, oxygen loss results in a stronger optical absorption, with an  $E_{\text{gap}}$  transition from  $\sim 3$  to  $\sim 0$  eV for  $\text{MoO}_3$  and  $\text{MoO}_2$  respectively [23]. This compromise between  $\Phi$ ,  $\sigma$  and  $E_{\text{gap}}$  must then be taken into account during selective-contact selection<sup>4</sup>. Furthermore, TMO properties vary also with thickness due to composition changes near adjacent materials, i.e. the first TMO monolayers are oxygen-poor and evolve towards stoichiometry as the film thickens (Fig 4.3b). This TMO/substrate interaction, which can be justified by thermodynamic and/or charge-transfer considerations [2], will be used to describe the TMO/c-Si interface in §4.2.3.

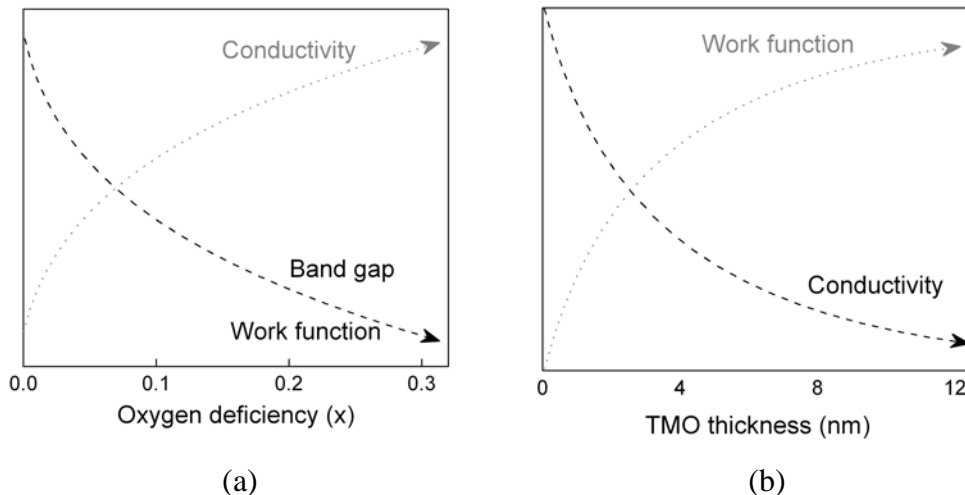


Figure 4.3 Illustrative dependence of TMO properties with (a) stoichiometry and (b) film thickness. Adapted from [5].

<sup>4</sup> However, it is possible that oxygen-deficiency control may not be too critical for solar cell performance, as manifested by relatively constant contact resistivities (§4.2.1) and unvarying implied- $V_{OC}$  values (§4.2.2).

TMO properties are also sensitive to redox environments and deposition conditions. Reducing  $N_2$  atmospheres under moderate temperatures can increase oxygen vacancies in  $MoO_3$  considerably (up to the point of  $MoO_2$  formation), whereas oxidative  $O_2$  treatments can reverse these composition changes [24]. Similarly, amorphous to crystalline transitions occur at substrates temperatures  $T > 300$  °C, increasing the conductivity up to  $10^3 \Omega^{-1}cm^{-1}$  at the expense of  $E_{gap}$  reduction (color centers) [25]. Moreover, humidity and airborne contaminants can easily adsorb to the TMO surface lowering its work function by several eV, as is the case with air-exposed  $MoO_3$  ( $\Phi \sim 5.3$  eV) [2]. Finally, TMO properties can also vary with the deposition rate and oxygen partial pressure [26,27], even though this was not thoroughly explored in this thesis.

#### 4.1.1 Electronic structure

The presence of atomic vacancies, indicative of metal cation redox transitions ( $M^{+n} \leftrightarrow M^{-n}$ ), were investigated from the x-ray photoelectron spectroscopy (XPS) spectra of TMO thin films ( $\sim 15$  nm), after fitting by Gaussian-Lorentzian curves and performing a multi-peak deconvolution by use of the binding energies referenced in the literature [28]. The integration of the peak areas allowed quantifying the relative content of each oxidation state and the oxygen to metal (O/M) ratios. Given that samples were briefly exposed to air ( $\sim 1$  min), adventitious (adsorbed) contamination in the form of C–OH compounds was subtracted from the overall oxygen content. Fig. 4.4 shows the core level spectra for the oxides under study while Table 4.2 summarizes their peak binding energies and relative composition.

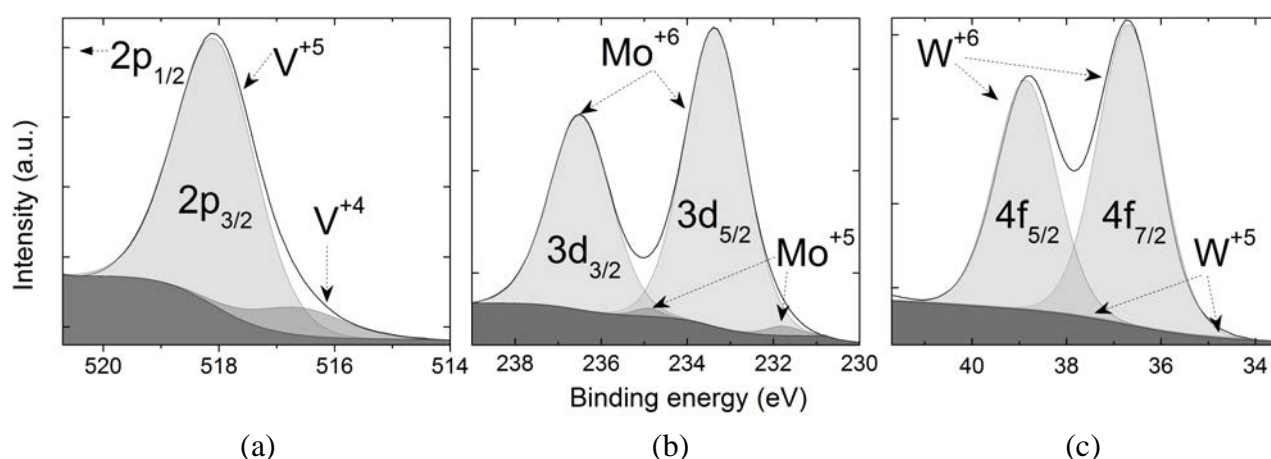


Figure 4.4. XPS spectra of the core levels in (a)  $V_2O_5$ , (b)  $MoO_3$  and (c)  $WO_3$ , showing the multi-peak deconvolution for different oxidation states  $M^n$ .

Cation species with reduced valence states were identified for the V  $2p$  (Fig. 4.4a) and Mo  $3d$  (Fig. 4.4b) doublet peaks, indicative of the  $V^{+5} \rightarrow V^{+4}$  and  $Mo^{+6} \rightarrow Mo^{+5}$  reduction transitions [7,29]. As a result, the oxygen content for  $V_2O_x$  and  $MoO_x$  was estimated at  $x \sim 4.6$  and  $x \sim 2.5$  respectively, confirming the semiconductive nature of the deposited films. Conversely, no reduced valence states were identified for the W  $4f$  peaks (Fig. 4.4c), indicating the absence of  $W^{+6} \rightarrow W^{+5}$  transitions [4]. This is further supported by the oxygen content of the  $WO_x$  films with  $x \sim 3.2$ , confirming that oxygen vacancies are absent and that the deposited film is not of semiconductive nature. An over-oxidized  $WO_{3.2}$  film could be the result of high oxygen partial pressures, requiring an ultra-high vacuum environment ( $\ll 10^{-6}$  mbar) to generate vacancies [30].

Table 4.2 Binding energy (eV) of V, Mo and W core levels (reflecting  $M^{+n} \leftrightarrow M^{-n}$  transitions), as fitted from the XPS spectra. The relative content of M and O 1s components yield the film stoichiometry (O/M ratio).

TMO	Core level peaks (eV)			Content (%)			Stoichiometry	
	Transition <sup>(1)</sup> :	$M^{+n} \leftrightarrow$	$M^{-n}$	$M^{+n} \leftrightarrow$	$M^{-n}$	O 1s	O/M ratio	O content
$V_2O_x$	V $2p_{3/2}$	518.1	516.6	27.3	3.1	69.6	2.3	$x \sim 4.6$
	V $2p_{1/2}$	525.7	524.2					
$MoO_x$	Mo $3d_{5/2}$	233.4	231.8	28.1	0.5	71.4	2.5	$x \sim 2.5$
	Mo $3d_{3/2}$	236.5	234.9					
$WO_x$	W $4f_{7/2}$	36.8	34.8	23.6	<0.1	76.4	3.2	$x \sim 3.2$
	W $4f_{5/2}$	38.9	37.0					

<sup>(1)</sup>  $V^{+5} \rightarrow V^{+4}$ ;  $Mo^{+6} \rightarrow Mo^{+5}$ ;  $W^{+6} \rightarrow W^{+5}$

Moreover, measuring the emission of photoelectrons with the lowest binding energies ( $< 10$  eV) allows probing the valence band and near Fermi level ( $E_F = 0$  eV) states. Fig. 4.5 shows the presence of defect states at  $\sim 1$  eV lying between the valence band maximum (VBM) and  $E_F$  (i.e. within the  $E_{gap}$ ), as expected for oxygen-deficient TMOs. These mid-gap states originate from the reduced cation species ( $V^{+4}$ ,  $Mo^{+5}$ ,  $W^{+5}$ ) whose excess electrons displace  $E_F$  towards the conduction band, providing an n-type character [1,5]. However, the defect state density is relatively small and there is no consensus in the literature whether it plays a significant role in carrier conduction or not [1]. The intensities of the measured defect peaks were stronger for  $V_2O_x$  and  $MoO_x$ , in accordance with their larger oxygen deficiencies, while the defect peak in over-stoichiometric  $WO_x$  was almost unnoticeable. In the following sections, the obtained TMO stoichiometries will be useful to explain the passivation properties of TMO/c-Si heterojunctions and the performance of solar cell devices.

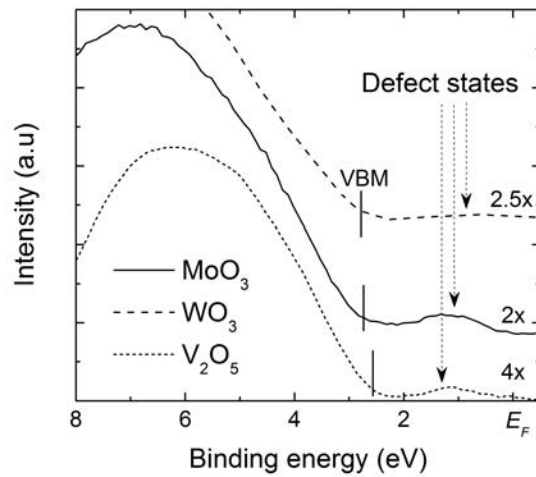


Figure 4.5. XPS spectra of the valence band region, showing mid-gap defect states between the valence band maximum (VBM) and the Fermi level ( $E_F = 0$  eV).

#### 4.1.2 Optical properties

As mentioned above, one of TMOs advantages over a-Si:H-based selective contacts is a wider energy band gap, resulting in fewer parasitic absorption losses when used as front window layers in HIT architectures [16,31,32]. In order to compare the optical attributes among different TMOs, the optical transmittance ( $T$ ) of 25 nm thick films is shown in Fig. 4.6a, as measured by spectrophotometry and after subtraction of the glass substrate contribution. Of the three oxides, MoO<sub>3</sub> exhibits the highest transmittance in the whole wavelength range and has the largest cutoff beyond 400 nm, while V<sub>2</sub>O<sub>5</sub> drops at around 420 nm. The above observations are in agreement with experimental  $E_{gap}$  values obtained from the inverse square proportionality between the absorption coefficient  $\alpha$  and the photon energy  $h\nu$  (Tauc's law), characteristic of indirect band gap transitions [33]:

$$\alpha(h\nu)^{1/2} \propto (h\nu) - E_{gap} \quad (4.2)$$

where  $h$  is Plank's constant (eV·s),  $\nu$  the frequency (s<sup>-1</sup>) and  $\alpha$  is calculated from the relationship  $\alpha = -\ln(T)/d$  with  $d$  as the film thickness. Fig. 4.6b shows Tauc's plot, where the extrapolation to the  $h\nu$  (energy) axis yields  $E_{gap}$  values of 3.0, 2.9 and 2.5 eV for MoO<sub>3</sub>, WO<sub>3</sub> and V<sub>2</sub>O<sub>5</sub> respectively. These  $E_{gap}$  values are in accordance with those reported in Table 4.1, although finer measurements of the absorption coefficient by more sensitive techniques (e.g. photothermal deflection spectroscopy - PDS) could help quantify sub-bandgap absorption [25].

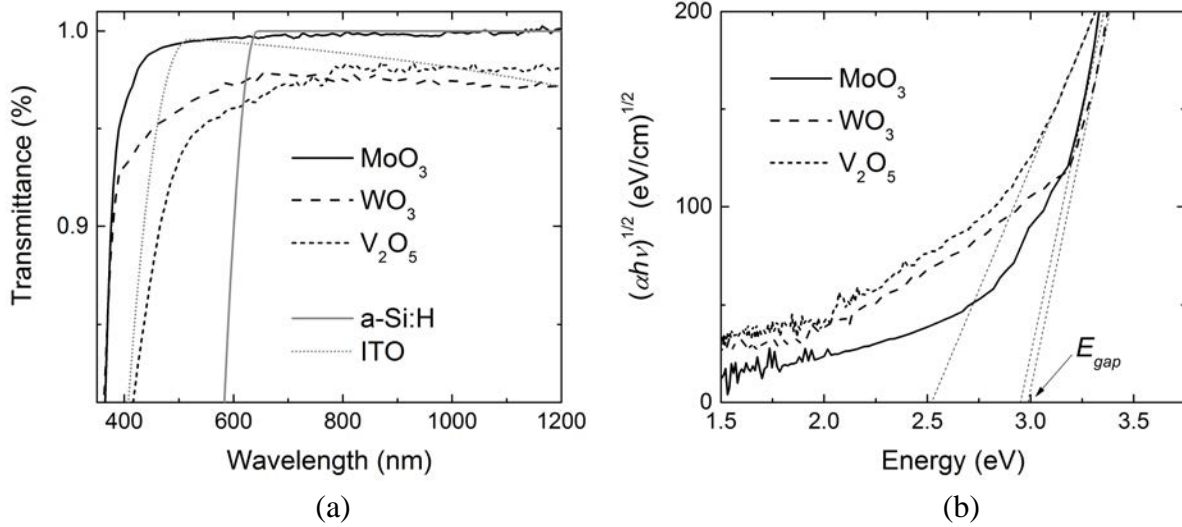


Figure 4.6 (a) Transmittance measurements for different TMOs, including a p-type a-Si:H and ITO references (calculated). (b) Tauc's plot indicating the  $E_{gap}$  values at the intersection with the energy axis.

Fig. 4.6a also shows the optical transmittance of a reference p-type a-Si:H (20 nm) and ITO layers (80 nm) calculated from absorption coefficient data [34]. By comparison, all three TMOs exhibit higher transmittance in the near UV–visible range due to a larger cutoff than a-Si:H (~590 nm), confirming the potential of TMOs for reduced absorption losses in solar cell devices.

In the proposed HIT-type structures (Fig. 3.1a,c), the front window layer consists of a ITO/TMO stack that works as a double anti-reflection coating (ARC), needed to minimize reflection losses and maximize absorption in c-Si. For this purpose, the refractive indexes  $n$  of the studied TMOs<sup>5</sup> and of ITO ( $n_{ITO} \sim 2.1$ ) are conveniently very close to the optimal index  $n_{opt} \sim 2$ . Before the fabrication of the devices, an optimization procedure was carried out by ray-tracing modeling with the online tool *Wafer Ray Tracer* [35]. This tool calculates the total reflectance, transmittance and absorptance across a multi-layer structure, each with a particular refractive index and absorption coefficient, yielding the theoretical photocurrent density ( $J_{ph}$ ) under a 1.5AMg illumination spectrum. Fig. 4.7 shows the simulated  $J_{ph}$  for a planar (un-texturized) solar cell as a function of MoO<sub>3</sub> and ITO thickness. Since the ITO sheet resistance obtained by the sputtering equipment is limited to  $R_{sh} \sim 110 \Omega/\square$ , a minimum ITO thickness of 70–80 nm was established in order to minimize resistive losses<sup>6</sup>. Then, a maximum photocurrent of  $\sim 35.7 \text{ mA/cm}^2$  can be expected for a TMO thickness of 15–20 nm.

<sup>5</sup>  $n_{MoO_3} \sim 2.2$ ,  $n_{WO_3} \sim 2.1$  and  $n_{V_2O_5} \sim 2.1$  (at 600 nm).

<sup>6</sup> Fixing in 1% the maximum power loss attributed to  $R_{sh}$ , under the current front grid design.

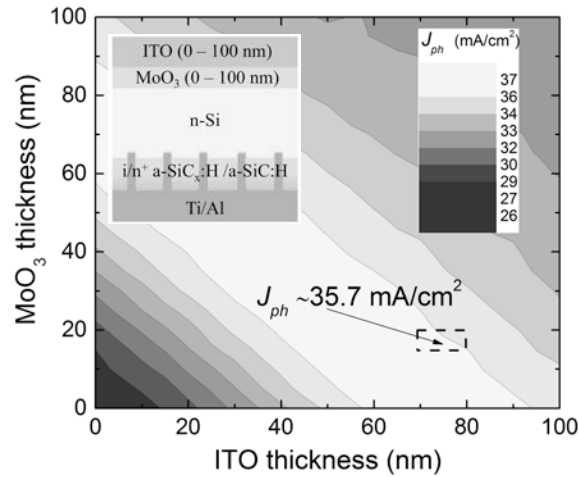


Figure 4.7 Ray-tracing simulation of the theoretical photocurrent density ( $J_{ph}$ ) in a  $\text{MoO}_3/\text{n-Si}$  planar solar cell, showing an approximate photogeneration of  $\sim 35.7 \text{ mA/cm}^2$  for the 70–80 nm ITO/15–20 nm  $\text{MoO}_3$  ranges.

Finally, photocurrent differences between a-Si:H ( $E_{gap} \sim 1.7 \text{ eV}$ ) and TMO ( $E_{gap} > 2.5 \text{ eV}$ ) hole contacts were also calculated by ray-tracing modeling for a front-textured substrate (Fig. 4.8a), showing a large reduction in the front absorption losses equivalent to  $\sim 1.6 \text{ mA/cm}^2$ , in accordance with other reports in the literature [31,32]. Similarly, Fig. 4.8b shows the c-Si absorptance profile as a function of wavelength (equivalent to a recombination-free EQE curve), demonstrating the  $J_{ph}$  gain is indeed delimited to the 400–600 nm range where TMOs exhibit lower parasitic absorption. Regarding the front reflection and rear absorption losses, similar values were obtained for both hole contact materials, proving the feasibility of double ARC strategies based on ITO/TMO stacks.

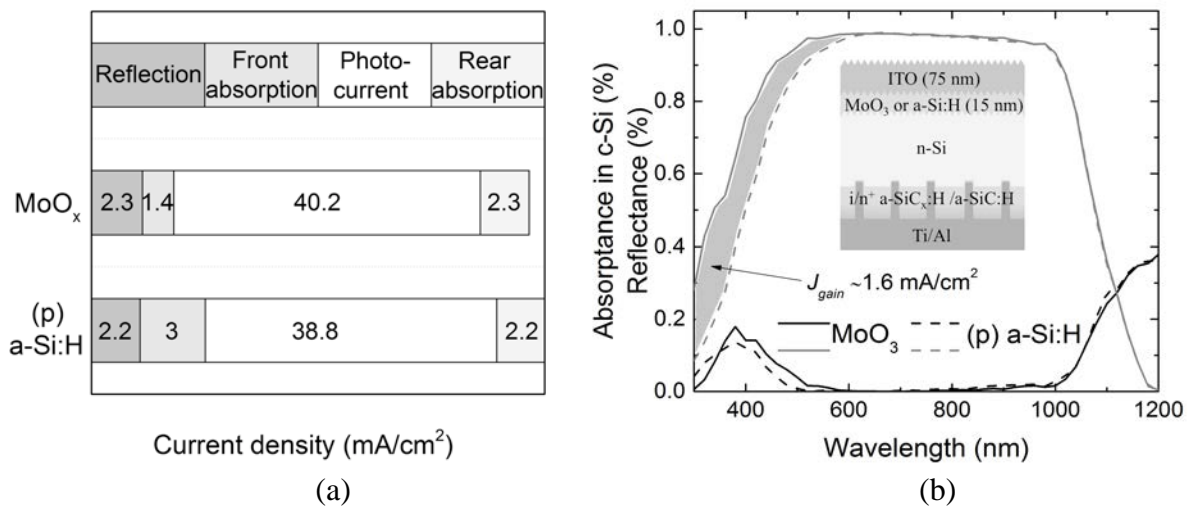


Figure 4.8 (a) Optical losses and photocurrent comparison between 15 nm thick  $\text{MoO}_3$  and a-Si:H hole contacts (75 nm ITO) for a front-textured solar cell. (b) c-Si absorptance and total reflectance profiles.

## 4.2 TMO/n-Si characterization

### 4.2.1 Electric properties

Even if stoichiometry variations allow for enhancements in conductivity, transition metal oxides are in general poor conductors when compared to doped silicon or TCOs. In order to pin down the conductivity of our thermally evaporated TMOs, 50 nm thick films were deposited on glass and measured<sup>7</sup> by the transfer length methodology (TLM) with Au electrodes, obtaining an ohmic response for each contact spacing  $d$ , as shown in Fig. 4.9a for the  $\text{MoO}_x$  sample but equally obtained for  $\text{V}_2\text{O}_x$  and  $\text{WO}_x$ . A linear fit of the total resistance  $R$  as a function of  $d$  (as per Eq. 3.11 and plotted in Fig. 4.9b) yielded sheet resistance values  $R_{sh}$  of  $10^9$ – $10^{11} \Omega/$  that translate into coplanar conductivities of  $8.6 \times 10^{-5}$  and  $6.1 \times 10^{-5} \Omega^{-1}\text{cm}^{-1}$  for  $\text{V}_2\text{O}_x$  and  $\text{MoO}_x$  respectively. For the case of  $\text{WO}_x$ ,  $\sigma$  was two orders of magnitude smaller, most probably related to the absence of oxygen vacancies determined by XPS. Note that measurements were performed under mild vacuum (1 mbar) in order to get a low-noise repeatable response, an indication of TMO's high sensibility to air. Despite the low measured conductivities, they are similar to p-type a-Si:H ( $10^{-5} \Omega^{-1}\text{cm}^{-1}$ )[36] and should not cause excessive resistive losses if very thin layers (<100 nm) are used.

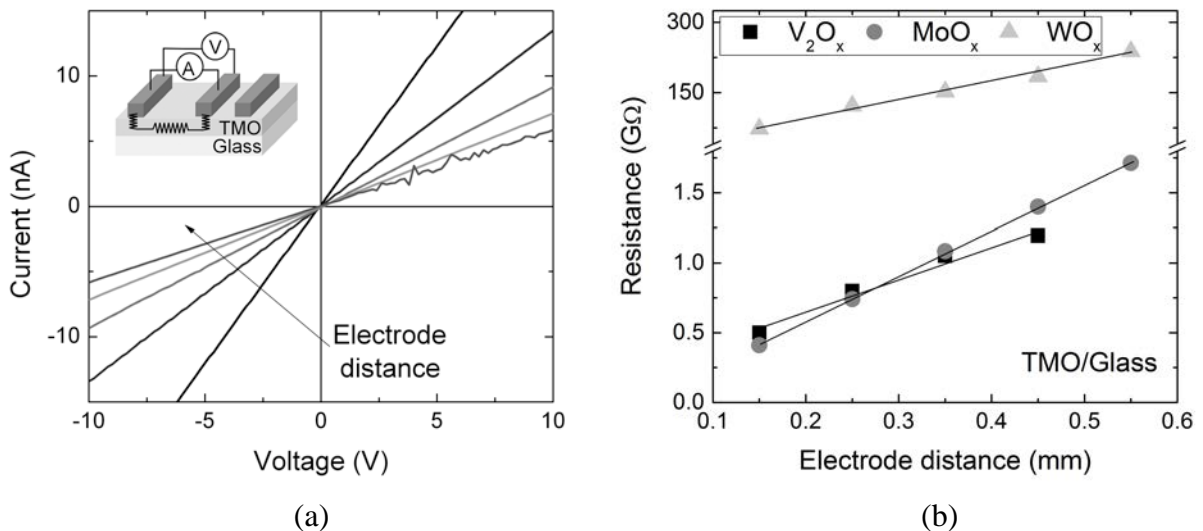


Figure 4.9 TLM measurements for 50 nm thick TMOs deposited on glass. (a) Example ohmic current-voltage response (dark) and (b) linear fit for different electrode intervals.

<sup>7</sup> Measurements were also performed with four-point probing, giving an infinite (unmeasurable)  $R_{sh}$  value.



Next, TLM measurements were repeated for 20 nm thick TMO films deposited on n-Si wafers ( $1.2 \Omega\cdot\text{cm}$  wafer resistivity) under dark and vacuum conditions. As in the glass substrate samples, an ohmic response was obtained for each contact spacing and for each oxide sample except this time much lower sheet resistances were obtained, namely  $\sim 10.7$ ,  $\sim 18.8$  and  $\sim 1,600 \text{ k}\Omega/$  for  $\text{V}_2\text{O}_x$ ,  $\text{MoO}_x$  and  $\text{WO}_x$  respectively (Fig. 4.10). When compared to the  $R_{sh}$  of bare n-Si ( $\sim 40 \Omega/$ ), it is clear that carrier conduction is restricted to a conduction channel between the TMO and the n-Si wafer. This is the first indication of the presence of an inversion layer (IL) induced upon the n-Si surface, as predicted by the energy band diagram in Fig 4.1b after Fermi level alignment has taken place. As it will be later discussed in §4.2.4, this hole-rich surface layer is most probably responsible for hole selectivity in n-Si. The obtained inversion layer  $R_{sh,IL}$  values are in accordance with the literature [20,37] and show a slight decrease upon illumination due to coupling between IL and the n-type base [37]. Considering an average inversion layer thickness of 1.5 nm [38] with a hole mobility  $\mu_{IL} \sim 200 \text{ cm}^2/\text{V}\cdot\text{s}$  [39], it is possible to estimate an equivalent inversion layer conductivity  $\sigma_{IL} \sim 10^2 \Omega^{-1}\text{cm}^{-1}$  as well as a hole surface concentration  $p_{IL} \sim 10^{19} \text{ cm}^{-3}$ , similar to the conductivity and dopant concentrations achieved by standard phosphorous doping [40].

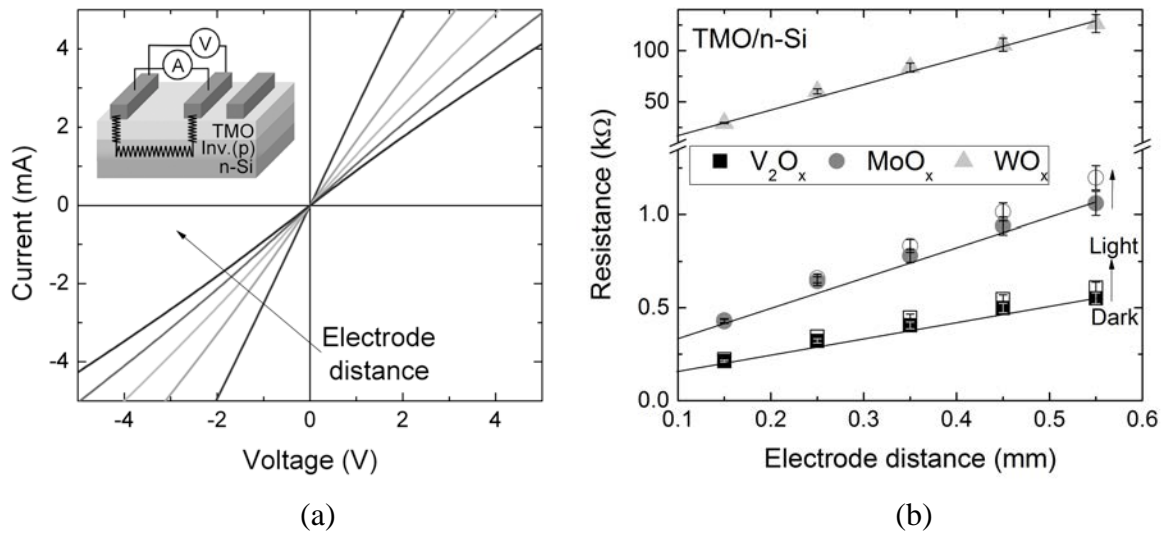


Figure 4.10 TLM measurements for 20 nm thick TMOs deposited on n-Si. (a) Example ohmic current-voltage response and (b) linear fit for different electrode intervals (under dark and light). Error bars (5%) account for current leakage outside the channel. Regression coefficients were  $R^2 > 0.99$ .

The specific contact resistance  $\rho_c$  can also be extracted from TLM measurements (see Eq. 3.11), accounting for the transversal current flow across the Au/TMO and TMO/IL interfaces as well as

the TMO bulk. The obtained  $\rho_c$  values were  $\sim 110$ ,  $\sim 370$  and  $\sim 670$   $\text{m}\Omega\cdot\text{cm}^2$  for  $\text{V}_2\text{O}_x$ ,  $\text{MoO}_x$  and  $\text{WO}_x$  respectively, in the same order of magnitude as other passivated/carrier-selective contacts [16,20,41] but much higher than industrial aluminum-fired or poly-Si/ $\text{SiO}_2$  hole contacts ( $\rho_c \sim 10$   $\text{m}\Omega\cdot\text{cm}^2$ ) [42,43]. Given the high bulk resistivity of TMOs, an increase in  $\rho_c$  could be expected for thicker films; yet, resistive losses are relatively constant [20] or tend to decrease [44] with film thickness (10–60 nm range). Nonetheless, TMO/n-Si heterojunctions are greatly influenced by the overlying contact metal, affecting not only  $\rho_c$  but also the inversion/accumulation characteristics. This could be related to work function misalignments or to chemical reaction in the metal/TMO interface [2,45]. In this sense, the electric properties measured here for Au/TMO contacts might vary when implemented into a solar cell (ITO/TMO).

Even though most of the work in this thesis is focused on hole-selective TMOs for n-Si devices, contact resistance measurements were also performed for Au/TMO (20 nm)/p-Si samples following the methodology in §3.3.1. Fig. 4.11 shows the representative ohmic response and the total resistance  $R$  as a function of contact radius  $r$ , extracting very similar  $\rho_c$  values for all three oxides (37–45  $\text{m}\Omega\cdot\text{cm}^2$ ) but slightly larger than those reported for Pd/ $\text{MoO}_x$ /p-Si contacts ( $\rho_c \sim 1$   $\text{m}\Omega\cdot\text{cm}^2$ ) [20]. Similar to the n-Si case, hole selectivity in p-Si is promoted by an induced accumulation layer formed during Fermi level alignment (Fig 4.1a). Given that  $\rho_c$  values are smaller than those measured for n-Si, it could be said that hole extraction through carrier accumulation is more favorable than hole extraction through surface inversion [20,46].

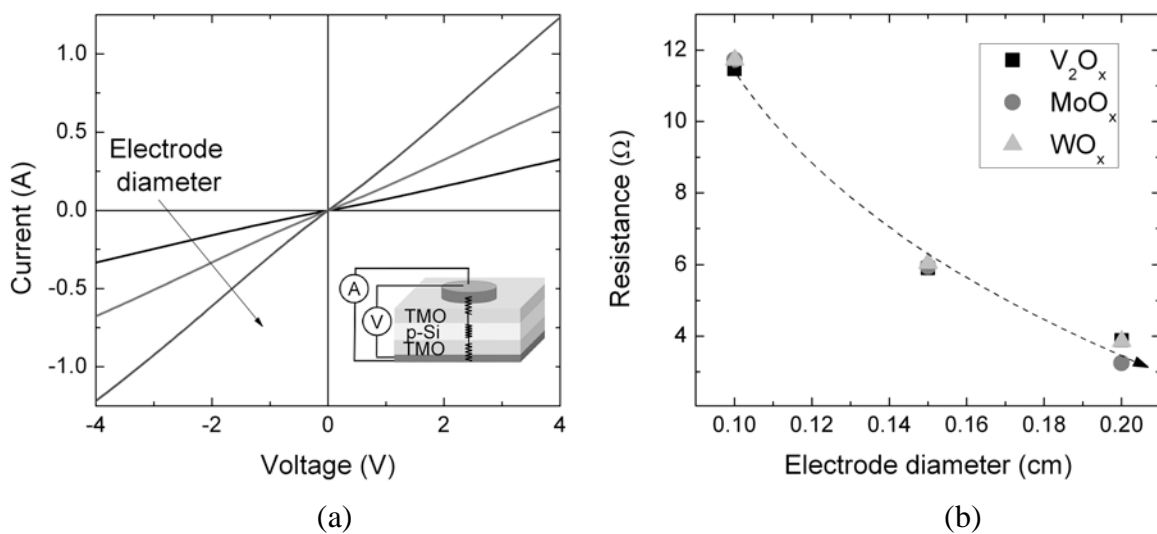


Figure 4.11 Contact resistance measurements for 20 nm thick TMOs deposited on p-Si. (a) Example ohmic current-voltage response and (b) resistance values for three electrode diameters.

Table 4.3 summarizes the sheet resistance, conductivity and specific contact resistance values measured for the TMOs under study. Overall,  $V_2O_x$  outperformed  $MoO_x$  by exhibiting a less resistive bulk, inversion layer and contact with n-Si, whereas  $WO_x$  contacts were consistently the most resistive. This trend might be explained by the previously obtained film stoichiometry, where oxygen vacancies were highest for  $V_2O_x$ . Regarding the  $\rho_c$  contribution to the total series resistance  $R_S$  of a device, it will depend on the contacted area fraction ( $\rho_c \cdot f_c$ ). Taking a HIT-type  $V_2O_x/n$ -Si solar cell with a  $\rho_c$  value of  $\sim 100 \text{ m}\Omega \cdot \text{cm}^2$  and a full<sup>8</sup> contacted area fraction  $f_c = 1$ , the contribution to  $R_S$  can be as low as  $\sim 0.1 \text{ }\Omega \cdot \text{cm}^2$ . This is about half the maximum permitted  $R_S \leq 0.2 \text{ }\Omega \cdot \text{cm}^2$  defined in §2.1.4, confirming the viability of TMO/n-Si heterostructures as alternative hole-selective contacts.

Table 4.3 Summary of the electric properties for the TMOs under study. All measurements were performed in the dark unless noted otherwise.

Substrate TMO	Glass		n-Si				p-Si
	$R_{sh}$ G $\Omega$ /	$\sigma$ $\Omega^{-1} \text{cm}^{-1}$	$R_{sh IL}^{(1)(2)}$ k $\Omega$ /	$\sigma_{IL}^{(3)}$ $\Omega^{-1} \text{cm}^{-1}$	$\rho_c$ $\text{m}\Omega \cdot \text{cm}^2$	$R_{sh IL light}^{(1)}$ k $\Omega$ /	$\rho_c$ $\text{m}\Omega \cdot \text{cm}^2$
$V_2O_x$	2.3	$8.6 \times 10^{-5}$	10.7	$3.5 \times 10^2$	110	9.4	39
$MoO_x$	3.3	$6.1 \times 10^{-5}$	18.8	$6.2 \times 10^2$	370	15.6	37
$WO_x$	390	$5.1 \times 10^{-7}$	1,600	4.2	670	NA	45

<sup>(1)</sup> Values for the induced inversion layer IL.

<sup>(2)</sup> Compare to the  $R_{sh} \sim 40 \text{ }\Omega$  of bare silicon ( $1.2 \text{ }\Omega \cdot \text{cm}$  resistivity).

<sup>(3)</sup> Assuming an inversion layer width of 1.5 nm.

Regarding the temperature stability of TMO's electric properties, temperature annealings in a  $N_2$  atmosphere were performed for the  $MoO_x/n$ -Si TLM structures in order to evaluate their compatibility with industrial post-processing, e.g. silver paste drying. Fig 4.12 shows a 70–150% increase in both  $R_{sh}$  and  $\rho_c$  for a 160 °C anneal, while a 250 °C anneal completely degraded the ohmic character of the contacts ( $R_{sh} > 10^6 \text{ }\Omega$ ). A similar deterioration in the conductivity of  $V_2O_x/n$ -Si contacts was also observed for  $T > 160 \text{ }^\circ\text{C}$  [44], which is close to the transition temperature from amorphous to crystalline. These temperature instabilities have already been correlated to fill factor losses in finished devices (see ref. [47] and solar cell results in Chapter 5), occurring at temperatures as low as 130 °C and imposing a severe limit on the post-processing of the device.

<sup>8</sup> As an example,  $V_2O_x/n$ -Si solar cells with  $f_c < 1$  (IBC structure) are presented in a co-authored paper [44].

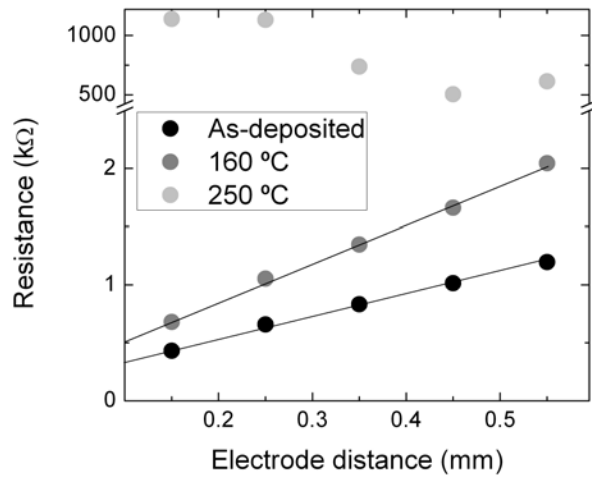


Figure 4.12 TLM measurements of MoO<sub>x</sub>/n-Si structures after temperature annealings of 160 and 250 °C.

#### 4.2.2 Passivation properties

The surface passivation quality TMO/n-Si heterojunctions was studied by depositing 20 nm thick films on both sides of planar n-Si wafers (1.2 Ω·cm resistivity) and measuring the photoconductance in the quasi-steady state regime (QSSPC). Fig. 4.13a shows the effective lifetime  $\tau_{eff}$  of photogenerated carriers as a function of carrier density  $\Delta n$ , while Fig. 4.13b shows the implied open-circuit voltage<sup>9</sup>  $i-V_{OC}$  as a function of the illumination level in sun-equivalents. The  $i-V_{OC}$  can be interpreted as a measure of the maximum theoretical  $V_{OC}$  for the TMO/n-Si heterojunction (the quasi-Fermi level separation  $qE_{Fn} - qE_{Fp}$ ) for an illumination of 1 sun. The highest passivation is achieved by V<sub>2</sub>O<sub>x</sub> with a  $\tau_{eff}$  ( $i-V_{OC}$ ) of 240 μs (671 mV) followed by MoO<sub>x</sub> with 142 μs (655 mV). This level of passivation is far below state-of-the-art a-Si:H technology ( $i-V_{OC} > 740$  mV), yet, it is remarkably high considering that it arises from a simple oxide/n-Si junction with no additional passivation interlayers. Also shown in Fig. 4.13 are the passivation characteristics for the two ( $i/n^+$ ) a-SiC<sub>x</sub>:H electron contact strategies, with measured  $\tau_{eff}$  ( $i-V_{OC}$ ) of 70 μs (631 mV) for the laser-doped and 1,150 μs (730 mV) for ITO-contacted.

Up to now, most research efforts on TMO/c-Si heterojunctions have boosted surface passivation to  $\tau_{eff} > 2$  ms by including a thin (5–10 nm) intrinsic a-Si:H interlayer, reaching  $i-V_{OC} > 700$  mV [16,32,47]. Naturally, this strategy was tested in this work by intercalating a 4 nm intrinsic a-SiC<sub>x</sub>:H layer deposited by PECVD. However, the reported increase in passivation could not be replicated, obtaining similar  $V_{OC}$  values for TMO/a-SiC<sub>x</sub>:H/n-Si and TMO/n-Si finished devices

<sup>9</sup> Corrected by a factor  $kT \ln(2) \approx 17.8$  mV, due to the sample's symmetric structure.

(see Appendix B), suggesting that our a-SiC<sub>x</sub>:H films were either too thin or chemically incompatible with thermally evaporated TMOs.

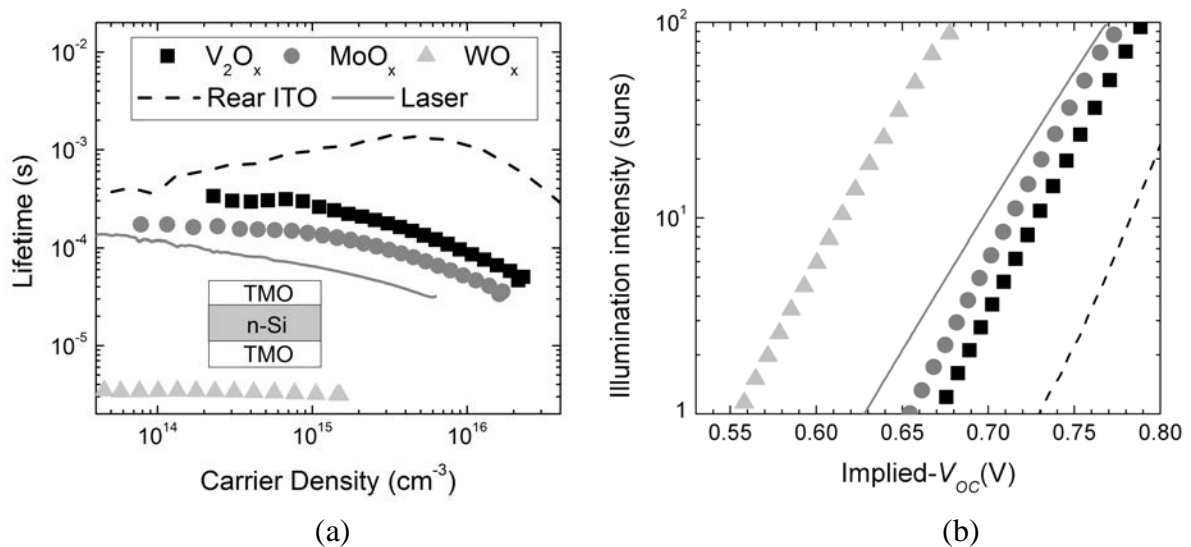


Figure 4.13 (a) Effective carrier lifetime for TMO/n-Si/TMO structures. (b) Implied- $V_{OC}$  as a function of illumination (sun equivalents). The ( $i/n^+$ ) a-SiC<sub>x</sub>:H electron contact strategies (laser-doped and ITO-contacted) are also shown.

Concerning WO<sub>x</sub>, no substantial passivation was obtained ( $\tau_{eff} < 10 \mu s$ ) resulting in negligible  $i$ - $V_{OC}$  values that contrast with the results reported by Bivour et al. where WO<sub>x</sub>/n-Si heterojunctions exhibited some degree of passivation ( $V_{OC} > 620$  mV for finished devices) [31]. As mentioned in the previous sections, failure to passivate could be related to over-stoichiometry in the evaporated films (WO<sub>3.2</sub>), suggesting that oxygen deficiency plays a role in the effective passivation of the c-Si surface. Another cause could be the difficult processing of evaporated WO<sub>3</sub> powders (higher melting point).

Figure 4.14a shows a plot of  $(1/\tau_{eff} - 1/\tau_{bulk})$  as a function of carrier density, whose linear fit (Eq. 3.2) yields the recombination currents  $J_0_{V_2O_x} \sim 130$  and  $J_0_{MoO_x} \sim 230$  fA/cm<sup>2</sup>, the latter in accordance with the values reported by Bullock et al. [20]. Moreover, this kind of symmetric structures allow a straightforward extraction of the effective surface recombination velocity  $S_{eff}$ :

$$S_{eff} \lesssim \frac{W}{2\tau_{eff}} \quad (4.1)$$

with  $S_{eff_{V_2O_x}} \sim 60$  and  $S_{eff_{MoO_x}} \sim 100$  cm/s. Putting these numbers in perspective, reported  $J_0$  values for industrial aluminum-fired hole-contacts are  $\sim 550$  fA/cm<sup>2</sup> [42], making TMO hole contacts a feasible option for industrial application. Table 4.4 summarizes the obtained passivation

parameters for TMO/n-Si heterojunctions, along with the  $(i/n^+)$  a-SiC<sub>x</sub>:H electron contact strategies. An rough estimation of the attainable  $V_{OC}$  in the final device can be made by summing the  $J_0$  contributions for both selective contacts,  $J_{0\text{TMO}} + J_{0(i/n^+)a\text{-SiC}_x\text{:H}}$ , and evaluating Eq. 2.12. As an example, a  $\text{V}_2\text{O}_x/\text{n-Si}/(i/n^+)a\text{-SiC}_x\text{:H}$  heterojunction could reach a maximum  $V_{OC}$  of approximately 640 and 680 mV for the laser-doped and rear-ITO structures respectively, without considering the effects of the front ITO layer and front/rear metallization.

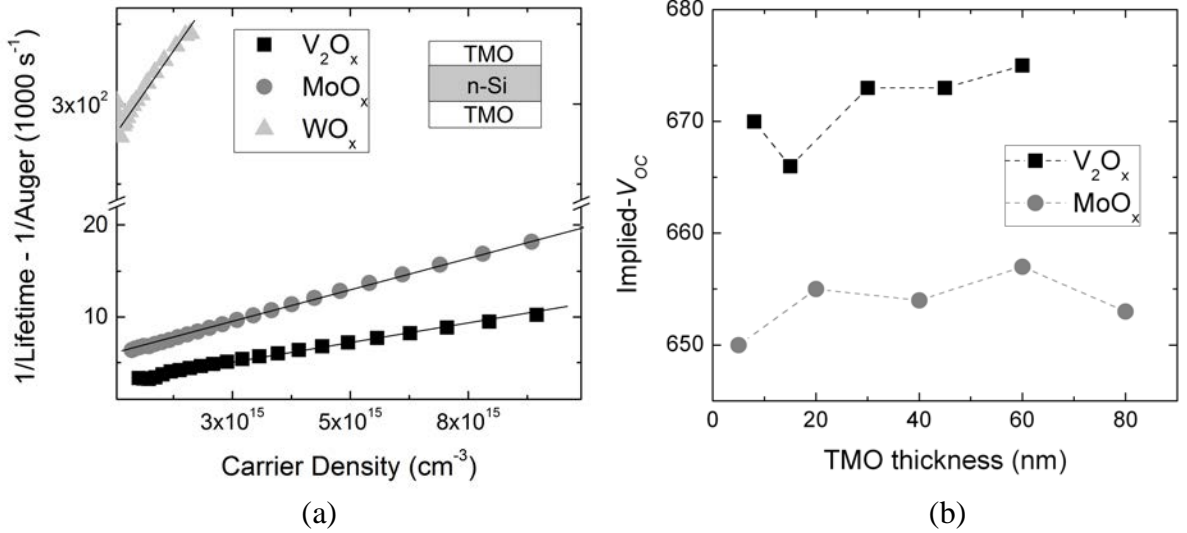


Figure 4.14 (a) Auger-corrected inverse effective lifetime for symmetric TMO/n-Si/TMO structures, whose linear fit yields the recombination current ( $2J_0$ ). (b) Implied- $V_{OC}$  dependence on TMO thickness.

Table 4.4 Summary of the TMO passivation properties extracted from QSSPC measurements in symmetric TMO/n-Si/TMO structures. The  $(i/n^+)$  a-SiC<sub>x</sub>:H electron contact strategies are also shown.

TMO	$\tau_{eff}$ μs	$i-V_{OC}^{(1)}$ mV	$J_0$ fA/cm <sup>2</sup>	$S_{eff}$ cm/s
V <sub>2</sub> O <sub>x</sub>	240	671	~130	~60
MoO <sub>x</sub>	142	655	~230	~100
WO <sub>x</sub>	<10	553	~3,630	~410
<b><math>(i/n^+)</math> a-SiC<sub>x</sub>:H</b>				
Laser-doped	70	631	~510	~200
ITO-contacted	1,150	730	~12	~10

<sup>(1)</sup> At 1 sun illumination intensity.

The dependence of passivation on increasing TMO thickness was also investigated (Fig. 4.14b), showing a minor improvement (V<sub>2</sub>O<sub>x</sub>) and no variation (MoO<sub>x</sub>) in the 25–80 nm thickness range, as reported in [20]. However, very thin films <10 nm should be avoided due to: (1) possible non-uniform coverage, especially in textured surfaces with increased roughness; (2) a more

pronounced passivation damage induced by ITO sputtering (see next section); and (3) a greater chemical influence from the c-Si substrate (see §4.3.1) Also, as suggested above, film stoichiometry and crystallinity could be important variables to consider, but so far no comprehensive study has been performed relating these variables to the passivation quality<sup>10</sup>.

#### 4.2.2.1 Passivation stability

Due to TMO's sensitivity to redox environments and airborne adsorbents, the passivation stability after air exposure was studied (Fig. 4.15a). While  $\text{MoO}_x$  showed a relatively stable passivation, a strong degradation was seen for  $\text{V}_2\text{O}_x$  with an  $i\text{-}V_{OC}$  decrease from 671 to 617 in just 24 hours. This is in accordance with the general instabilities shown by amorphous  $\text{V}_2\text{O}_5$  films deposited at ambient temperature, which readily react with humid air and are easily scratched [48]. Film degradation can be avoided by ~5 nm capping layers (deposited without interrupting the vacuum), as confirmed by stable  $i\text{-}V_{OC}$  values up to 40 days after fabrication [44]. However, since the devices presented here are intended as front window layers, metal capping is only useful in rear-contacted structures [44], where a high work function metal (e.g. niquel,  $\Phi_{Ni} \sim 5.6$  eV) could also favor a better ohmic contact than ITO ( $\Phi_{ITO} \sim 4.8$  eV).

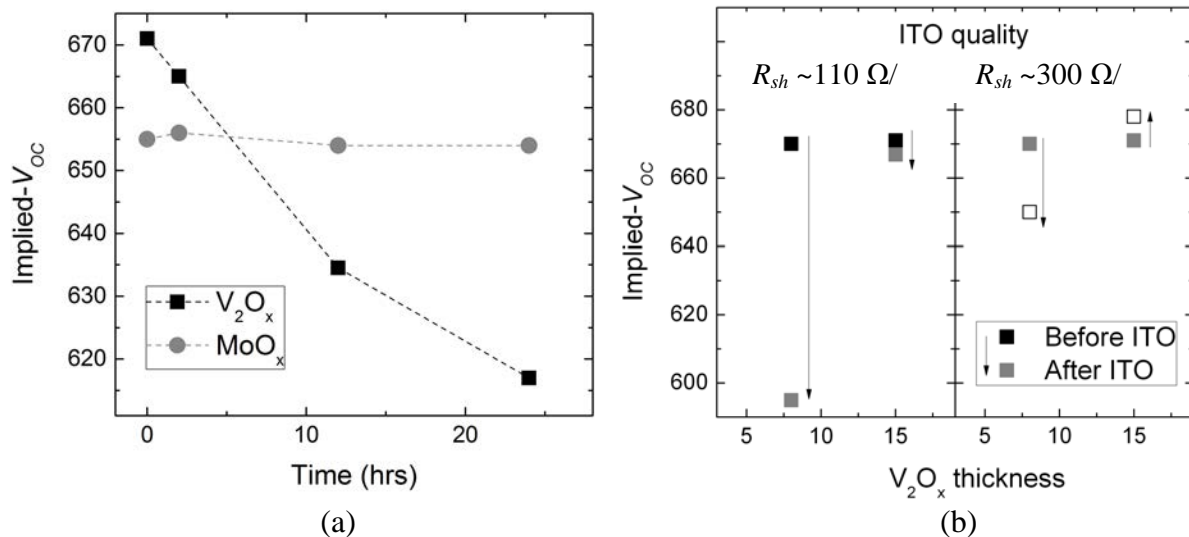


Figure 4.15 (a) TMO passivation stability after air exposure. (b) Passivation damage induced during ITO sputtering for different ITO resistivities and TMO thicknesses

<sup>10</sup> See reference [27], where lower surface potentials (band bending) were correlated to increased  $\text{WO}_x$  oxygen vacancies.

The passivation stability with temperature has been recently reported for  $V_2O_5/n\text{-Si}$  by subjecting the samples to cumulative annealings in the 160–400 °C range under a  $H_2/N_2$  atmosphere [44]. Contrary to the rapid degradation of the electric properties,  $i\text{-}V_{OC}$  values remained relatively stable up to 300 °C, after which a rapid decrease was noticed. Finally, passivation damage was also noticed as a consequence of the ITO sputtering process, a well-documented disadvantage in a-Si:H/c-Si heterojunctions and attributed to UV-luminescence and (in a lesser degree) to ion bombardment [49]. In the  $V_2O_x/n\text{-Si}$  case, a stronger damage was seen for either very thin TMO films <10 nm or for highly-conductive ITO films with  $R_{sh} \sim 110 \Omega/$  (Fig. 4.15b). This means that the sputtering damage can be partially subdued by keeping TMO thicknesses >15 nm or by using thinner films (<10 nm) with less conductive ITO ( $R_{sh} \sim 300 \Omega/$ ). Still, further studies are needed to establish the damage mechanism and how it could be avoided/recovered.

### 4.3 Origin of passivation in TMO/n-Si heterojunctions

After determining the passivation potential in TMO/c-Si heterojunctions, a detailed characterization of the interface was carried out. A few questions that came to mind were: was the induced band bending the only passivation component (i.e. “field-effect”)? Or was there a chemical contribution through dangling bond passivation?

#### 4.3.1 The $SiO_x$ interlayer

As a first characterization approach, a lattice resolution cross-section image of ITO/TMO/n-Si structures was obtained by HR-TEM, revealing the presence of an unexpected interfacial layer between the TMO and the n-Si surface. As shown in Fig. 4.16, this interlayer was clearly discerned at the lowest magnifications because of its high contrast to the adjacent materials, exhibiting an abrupt interface with the HF-cleaned (and therefore  $SiO_2$  free) c-Si surface but a slightly diffused boundary with the oxide. Its thickness varied at 2.0, 2.3 and  $2.5 \pm 0.1$  nm for the  $V_2O_x$ ,  $MoO_x$  and  $WO_x$  samples respectively, but it was quite uniform and without any apparent pinholes. In comparison with the clearly defined crystal planes of c-Si, this interlayer was amorphous in nature and showed no signs of epitaxial growth. Likewise, TMOs were also amorphous as previously reported for thermally evaporated films [24].



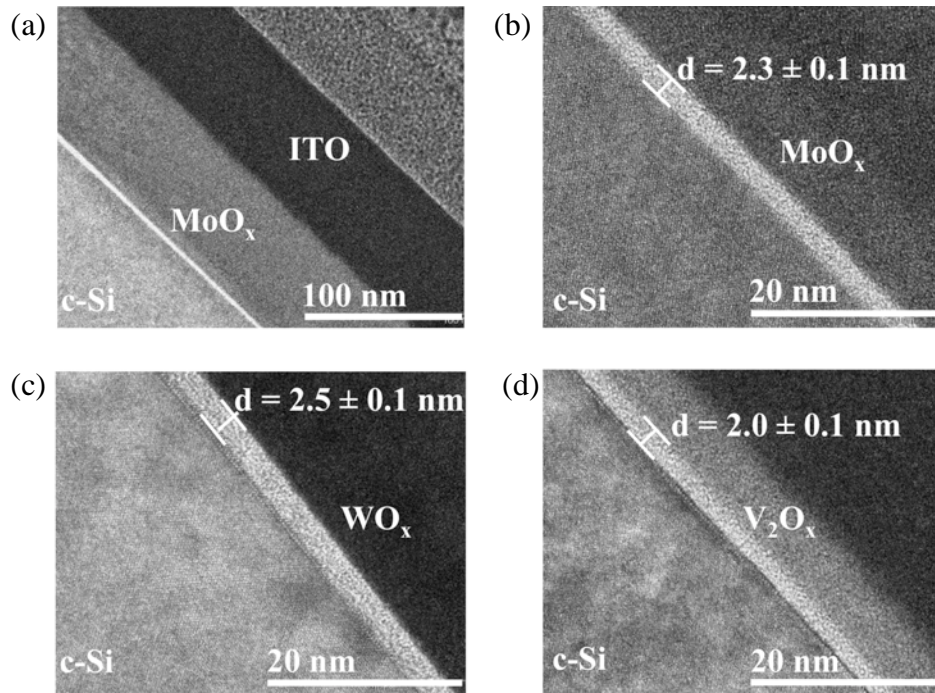


Figure 4.16 HR-TEM cross-section image of ITO/TMO/n-Si heterojunctions, showing an interlayer between n-Si and (a,b) MoO<sub>x</sub>, (c) WO<sub>x</sub> and (d) V<sub>2</sub>O<sub>x</sub>.

#### 4.3.1.1 ToF-SIMS

Next, the composition of the identified interlayer was qualitatively determined by ToF-SIMS in dynamic operation mode. Figure 4.17a-c shows the depth profile of the ITO/TMO/n-Si samples as a function of sputtering time, where the three distinct layers were clearly differentiated by their respective InO<sub>2</sub><sup>-</sup>/SnO<sub>2</sub><sup>-</sup>, TMO<sup>-</sup> and Si<sup>-</sup> ions. For all three TMO samples, a peak signal with 59.97 atomic mass units (amu) corresponding to SiO<sub>2</sub><sup>-</sup> ions was detected in the TMO/n-Si interface at an intensity of  $\sim 3 \times 10^4$  counts, suggesting that the previously observed interlayer is composed of silicon oxide (SiO<sub>2</sub>) or silicon sub-oxide (SiO<sub>x</sub>) species. Since the HF-etched silicon surface was practically free of any native oxide (as it will be confirmed by XPS), it can be inferred that such SiO<sub>x</sub> interlayer is formed during the TMO evaporation process, chemically passivating the c-Si dangling bonds. Likewise, the presence of reduced TMO species (MoO<sup>-</sup>, WO<sub>2</sub><sup>-</sup>, VO<sub>2</sub><sup>-</sup>) can be related to oxidation by-products, e.g.  $\text{Si} + \text{MoO}_3 \rightarrow \text{SiO}_2 + \text{MoO}$ . Composite SiO<sub>2</sub>-TMO signals were also detected at  $< 10^2$  counts, two orders of magnitude lower than SiO<sub>2</sub><sup>-</sup> and following the same trend, meaning that M<sub>x</sub>Si<sub>y</sub>O<sub>z</sub> silicates could also be present at very low concentrations [50]. Finally, SiOH<sup>-</sup> ion signals were also detected, following the same trend as SiO<sub>2</sub><sup>-</sup> but 10 times weaker.

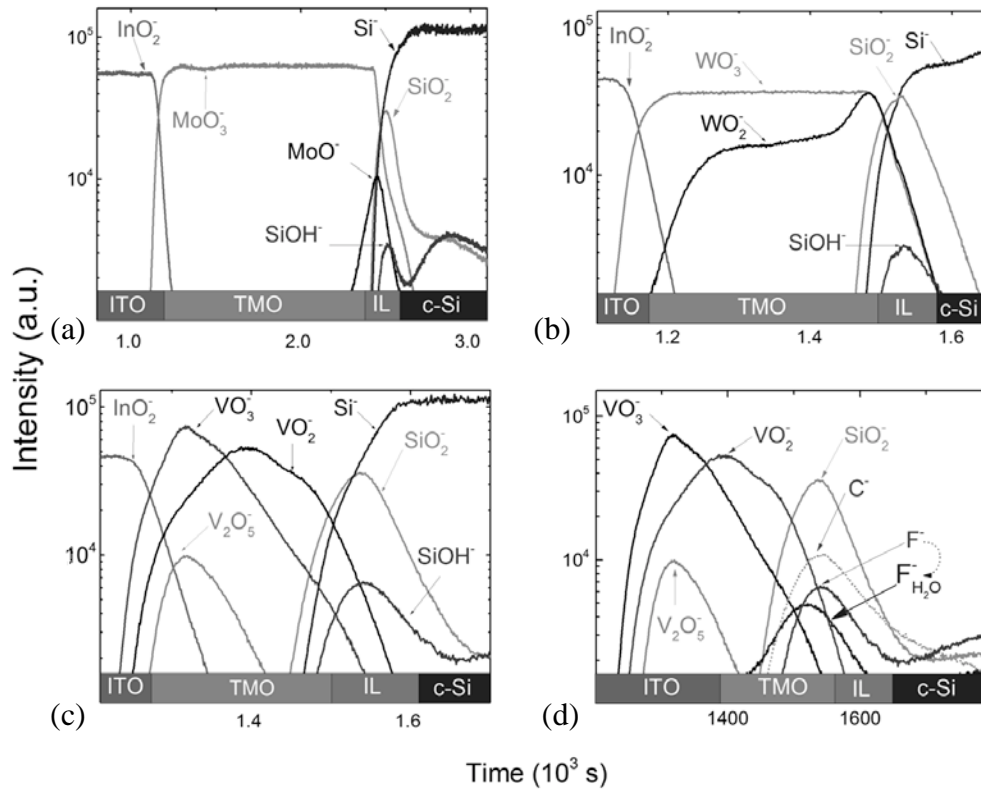


Figure 4.17 ToF-SIMS depth profile (dynamic mode) of ITO/TMO/n-Si structures for (a) MoO<sub>x</sub>, (c) WO<sub>x</sub> and (c) V<sub>2</sub>O<sub>x</sub>, showing a SiO<sub>2</sub><sup>-</sup> signal at the TMO/n-Si interface. (d) shows extraneous C<sup>-</sup> and F<sup>-</sup> signals at the V<sub>2</sub>O<sub>x</sub>/n-Si interface.

Given that the SiO<sub>2</sub><sup>-</sup> peak intensities were about the same order of magnitude as their respective TMO signals ( $3\text{--}6 \times 10^4$  counts), it can be concluded that the surface was completely and uniformly oxidized, in agreement with the TEM images. For the V<sub>2</sub>O<sub>5</sub> case, where a much thinner layer was deposited on purpose, the reduction reaction extended across several nanometers so that VO<sub>2</sub><sup>-</sup> and VO<sub>3</sub><sup>-</sup> species surpass V<sub>2</sub>O<sub>5</sub><sup>-</sup> in intensity (as later confirmed by XPS). The detection of HF remnants from the F<sup>-</sup> signal (Fig. 4.17d) within the same time window confirms that SiO<sub>2</sub><sup>-</sup> is restricted to the TMO/n-Si interface. However, the relatively high F<sup>-</sup> concentration ( $1 \times 10^4$  counts) suggests that residual fluorine could also be chemically bonded to Si [51]. In order to confirm this, a separate V<sub>2</sub>O<sub>5</sub> sample was washed with abundant deionized water after the HF dip. While ToF-SIMS showed a decrease in F<sup>-</sup> intensity by a factor of 2, both the SiO<sub>2</sub><sup>-</sup> signal and the effective lifetime (not shown) remained unchanged, discarding that F<sup>-</sup> provides additional dangling bond passivation. Then, it is probable that F<sup>-</sup> species are only physisorbed, since Si–F terminations are not kinetically viable during HF etching [52]. Finally, Fig. 4.17d also shows the presence of carbon contamination during air exposure.

A detailed composition of the SiO<sub>x</sub> interlayer was obtained by performing the ToF-SIMS analysis in static operation mode. For this purpose, a sufficiently low ion current ( $1\text{--}10 \text{ nA/cm}^2$ )

was used so that secondary ions can reveal details of the very first monolayers, such as chemical structure and adsorbed species. Figure 4.18 shows the SIMS spectra of the  $V_2O_x/SiO_x/n$ -Si structure, analyzed at sputtering time intervals of  $t = 4$  s. Beginning with the topmost spectra ( $t = 0$  s), the surface is rich in reduced  $V^{+4}$  and  $V^{+2}$  species whereas stoichiometric  $V^{+5}$  species are already quite low. At  $t = 4$  s,  $SiO_2$  and other related bonding structures like Si–OH and Si–(O<sub>3</sub>H) are detected, reaching a maximum concentration at  $t = 8$  s. Around the same time frame, the elemental Si peak is detected and rapidly becomes saturated, corroborating that the interlayer thickness is in the order of few nm. It is worth noting the high spectral sensitivity offered by this technique, being able to separately identify the Si (27.97 amu) and Si–H (28.98 amu) signals as well as elemental H. In this respect, the presence of hydrogen-bound species like –H and –OH is a clear indication that the c-Si surface has been chemically passivated.

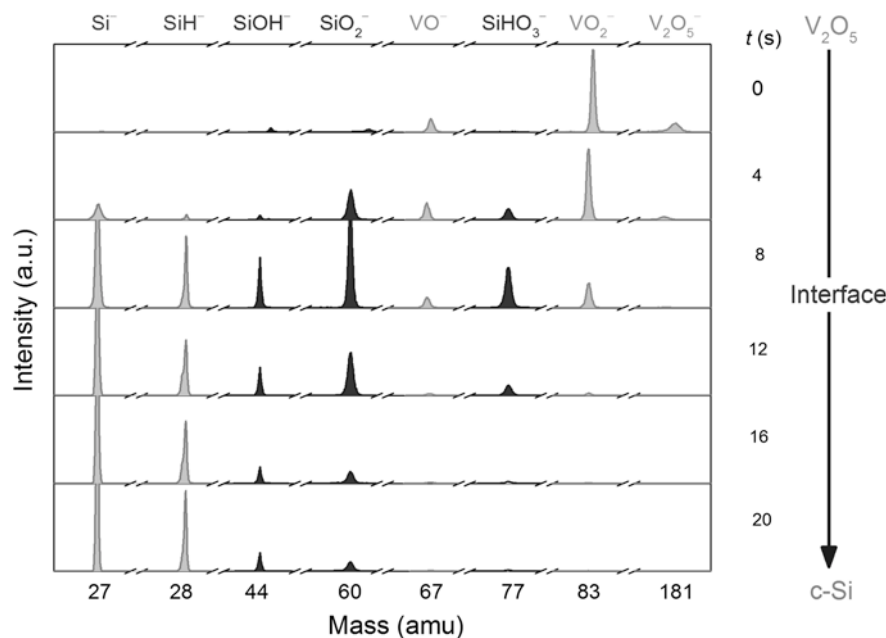
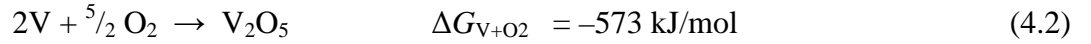
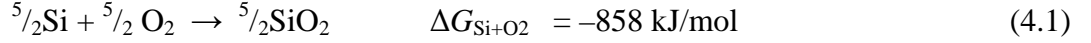
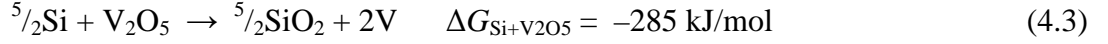


Figure 4.18 ToF-SIMS depth profile (static mode) of the  $V_2O_x/n$ -Si interface, showing the  $SiO_2^-$  signal as well as hydrogen-bound Si–H and Si–OH species.

The oxidation of highly reactive H-terminated c-Si surfaces [52] by dielectric ( $Al_2O_3$ ,  $HfO_2$ ,  $Ta_2O_5$ ,  $SrTiO_3$ ) [50] and conductive (ITO) [53] oxides is amply documented, forming interlayers with varying stoichiometries ( $SiO_x$ ,  $Hf_{1-x}Si_xO_2$ ) and film thicknesses (0.7–9 nm). For the case of TMOs, a chemical reaction with c-Si can be expected purely from thermodynamic considerations [2]. Parting from the oxidation of Si and V by molecular  $O_2$ , the reaction feasibility is given by the Gibbs formation energy ( $\Delta G$ ) of the reaction:



where negative  $\Delta G$  values indicate the reaction is spontaneous. By subtracting Eq. 4.2 from Eq. 4.1, the Si oxidation reaction by  $\text{V}_2\text{O}_5$  is also spontaneous:



The same condition is met for the rest of the TMOs under study, with  $\Delta G_{\text{Si}-\text{WO}_3} = -348 \text{ kJ/mol}$  and  $\Delta G_{\text{Si}-\text{MoO}_3} = -406 \text{ kJ/mol}$ . Hence, the oxidation of c-Si by the thermally evaporated TMOs under study is thermodynamically feasible<sup>11</sup>. An exception to this rule is observed for  $\text{HfO}_2$  and  $\text{Al}_2\text{O}_3$  (positive  $\Delta G$ ), indicating that reaction spontaneity is not the only factor to consider but also metastable equilibrium conditions, kinetic rates and surface reactivity. In this sense,  $\text{SiO}_x$  formation could be occurring via two different mechanisms [2]: (1) TMO reduction driven by the reactivity of c-Si substrate, and (2) electron transfer from Si to the TMO<sup>12</sup>, i.e.  $\text{Si}^0 - 2e \rightarrow \text{Si}^{+2}$ . Regarding the relative  $\Delta G$  magnitudes ( $\text{V}_2\text{O}_5 > \text{WO}_3 > \text{MoO}_3$ ), no evident correlation was found with interlayer thickness (Fig. 4.16) nor with the TMO work function (Table 4.1). However, given the large dispersion in reported  $\Phi_{\text{TMO}}$  values, a correlation cannot be completely dismissed.

These thermodynamic considerations are also applicable to O vacancy formation. For example, the chemical equation for oxygen vacancy formation in  $\text{V}_2\text{O}_5$  is [2]:



where  $\text{O}_\text{O}^x$  and  $\text{M}^{+6}$  represent an oxygen and metal cation on its neutral lattice position, whereas  $\text{v}_\text{O}^{+2}$  and  $\text{Mo}^{+5}$  represent an oxygen vacancy (with a +2 charge relative to the neutral lattice) and a reduced metal cation in the non-stoichiometric lattice. Eq. 4.4 shows that each oxygen vacancy produces two reduced  $\text{V}^{+5}$  cations. As for the Gibbs energy change, it can be approximated by the inverse  $\Delta G$  value of  $\text{VO}_2$  oxidation ( $4\text{VO}_2 + \text{O}_2 \rightarrow 2\text{V}_2\text{O}_5$ ), in which case it yields a non-spontaneous (positive) reaction that becomes viable for the overall  $\text{Si} + \text{V}_2\text{O}_5$  system.

---

<sup>11</sup> Using standard Gibbs formation energies at 300 K [82].

<sup>12</sup> Note that this charge transfer mechanism is equivalent to electron transfer from the Si Fermi level to the TMO conduction band during Fermi level alignment, as explained in §4.3.2.

### 4.3.1.2 XPS

As implied from the presence of reduced oxide species in the ToF-SIMS spectra, the completion degree of TMO + Si reactions (Eq. 4.3) is probably less than unity, so that a mixture of sub-stoichiometric  $\text{SiO}_x$  and  $\text{TMO}_x$  species can coexist in the interlayer. Therefore, the detailed chemical composition of the TMO/n-Si interface was also acquired from the XPS analysis of  $\text{V}_2\text{O}_5$  films deposited at incremental thicknesses (1–10 nm), monitoring film growth and the chemical/electronic changes taking place at the interface. Fig. 4.19a shows the Si  $2p^{3/2}$  core level spectra as a function of binding energy (BE). For the reference case (0 nm  $\text{V}_2\text{O}_x$ ), only the characteristic peak of the  $\text{Si}^0$  substrate was observed at a BE of 99.4 eV [54]. Subsequent  $\text{V}_2\text{O}_5$  films of 1 nm and above exhibited an additional peak with a chemical shift  $\Delta\text{BE}$  of  $\sim 2.5$  eV referenced to  $\text{Si}^0$  (see Fig. 4.19a inset for clarity), characteristic of a  $\text{Si}^{+3}$  oxidation state [54]<sup>13</sup>. These sub-stoichiometric  $\text{SiO}_{x-1.5}$  species can then be identified as one of the components of the interlayer previously identified by HR-TEM and ToF-SIMS. The sub-stoichiometry of this interlayer was evident when compared to a reference  $\text{SiO}_2$  oxide grown by  $\text{HNO}_3$  oxidation ( $\Delta\text{BE} \sim 3.9$  eV for  $\text{Si}^{+4}$  [54]). Furthermore, the atomic concentration of  $\text{Si}^{3+}$  species (as obtained from the peak areas) was 0.9–2.0% and relatively constant for every sample, suggesting that  $\text{SiO}_x$  growth takes place during the first deposition stages until it saturates at a fixed thickness.

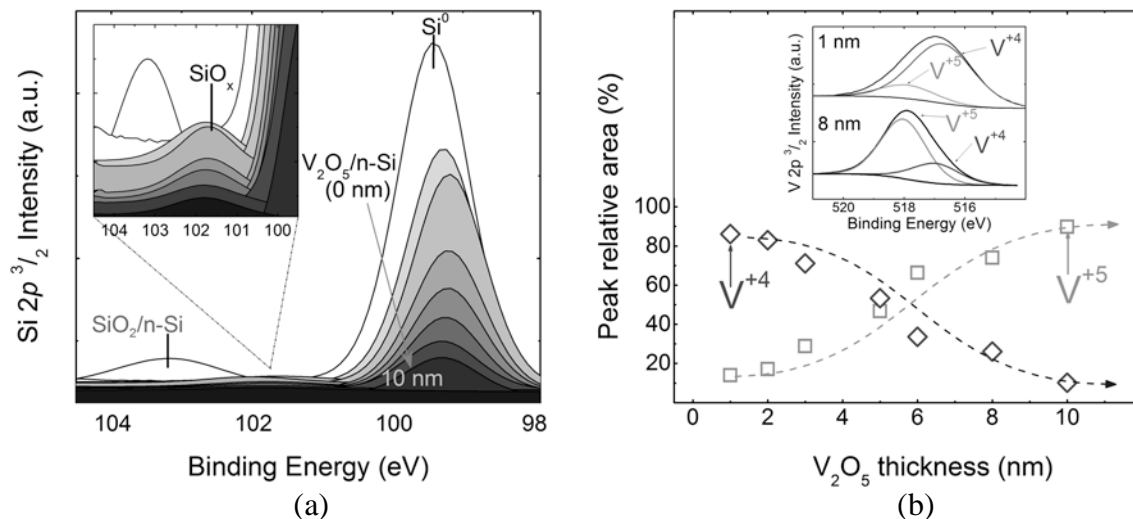


Figure 4.19 XPS analysis of the  $\text{V}_2\text{O}_x/\text{n-Si}$  interface for various  $\text{V}_2\text{O}_x$  thicknesses (1–10 nm). (a) Si  $2p^{3/2}$  core level showing a sub-stoichiometric  $\text{SiO}_{x-1.5}$  peak. (b) Evolution of the  $\text{V}^{+4}$  and  $\text{V}^{+5}$  species. Inset shows the V  $2p^{3/2}$  core for two different layer thicknesses.

<sup>13</sup> But also related to silicates (Si–M bonds) in the 101.6–103.8 eV range, making it impossible to separate its contribution. However, the low Si–M signal in the ToF-SIMS analysis indicates that  $\text{SiO}_x$  species are much more abundant.

Oxygen deficient  $V_2O_x$  was also detected as a by-product of the partial Si oxidation reaction. Fig. 4.19b shows the relative abundance of  $V^{+5}$  and  $V^{+4}$  cation species as a function of film thickness, as obtained from the deconvoluted V  $2p^{3/2}$  spectra (Fig. 4.19b inset). The observed trend was the following:  $V^{+4}$  species were primarily found in the vicinity of the  $SiO_x$  interlayer and declined as the  $V_2O_x$  film thickened. Inversely, the concentration of  $V^{+5}$  species was low near the interface and increased until reaching a steady concentration in the bulk, away from the interface and its influence. The results are in accordance with the ToF-SIMS depth profiles where  $VO_2^-$  ions were detected adjacent to the  $SiO_x$  interlayer, following similar trends as those reported for  $MoO_3$ /metal [2] systems. Therefore, although no detailed XPS analyses were performed for the  $MoO_x$ /c-Si and  $WO_x$ /c-Si interfaces, the similarity between the ToF-SIMS/HR-TEM results indicate that analogue interlayers with  $SiO_{x<2}$  composition and reduced cation transitions ( $Mo^{+6} \rightarrow Mo^{+5}$ ,  $W^{+6} \rightarrow W^{+5}$ ) can be expected as well [55,56].

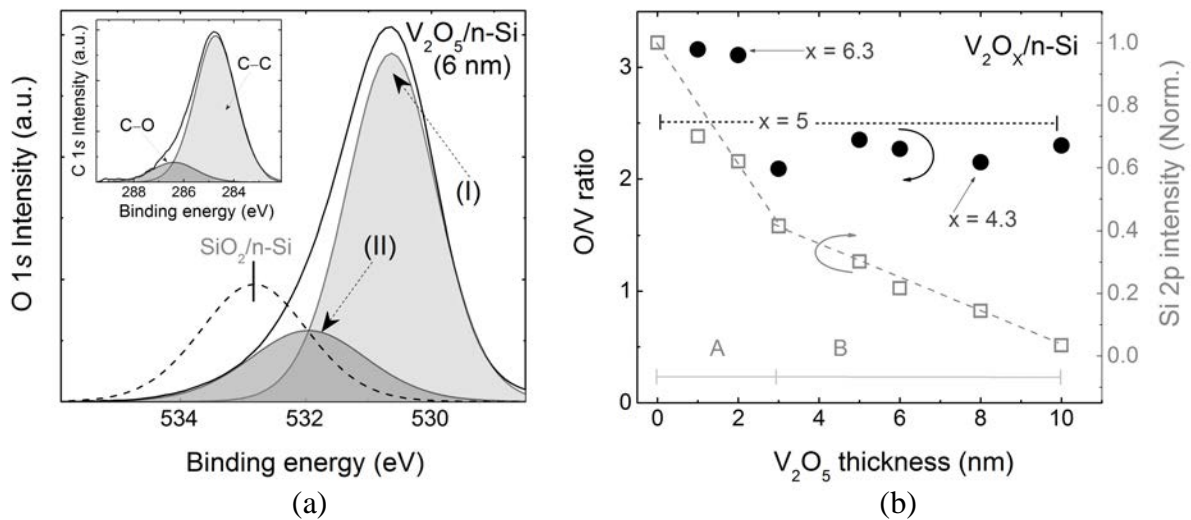


Fig. 4.20 (a) O 1s spectra of the  $V_2O_x(6 \text{ nm})/n\text{-Si}$  region, showing two peak contributions. Inset shows the C 1s spectra. (b) Evolution of O/V ratios (left axis) and normalized area of the Si  $2p^{3/2}$  peak (right axis) with film thickness.

Two growth regimes (A and B) are observed.

Regarding the specific distribution of oxygen species in the  $SiO_x$  and  $V_2O_x$  layers, the O 1s spectra of the  $V_2O_5/SiO_x/n\text{-Si}$  region was deconvoluted into two different components (Fig. 4.20a): a primary peak centered at 530.9 eV and attributed to O in vanadium oxide [57], and a secondary peak centered at 532.3 eV, comprising ~25% of the total O 1s area. This secondary-O has itself two contributions: (1) surface hydroxides ( $-\text{OH}$ ) and carbon ( $\text{C}-\text{O}$ ) physisorbed during

exposure to humid air [2]<sup>14</sup>; and (2) Si–O bonds from the SiO<sub>x</sub> interlayer, which lie very close to the SiO<sub>2</sub> reference (532.8 eV). After subtraction of these secondary-O contributions, oxygen to metal (O/V) ratios as a function of V<sub>2</sub>O<sub>x</sub> thickness were calculated, as shown in Fig. 4.20b left axis. Even though under-stoichiometric V<sub>2</sub>O<sub>x</sub> films were expected across the whole thickness range (see Fig. 4.19b), this does not occur for the thinnest films which appear to be over-stoichiometric (V<sub>2</sub>O<sub>x-6.3</sub>). This apparent contradiction could be explained by the presence of uncoordinated (dangling) oxygen atoms, an inherent characteristic of TMOs with large stoichiometries and multi-layered bulk structures [58,59]. It is worth noting the continuous presence of adsorbed carbon species any time the samples are exposed to air (e.g. after the HF dip). Fig. 4.20a inset shows the C 1s core level deconvoluted into its C–C (284.7 eV) and C–O (286.3 eV) bond contributions. Since all samples had a relatively high C concentration of 9 ±3.1%, it is possible that C–O bonds could be contributing to the SiO<sub>x</sub> interlayer formation [60].

Finally, a qualitative description of TMO growth dynamics was obtained from the reduction of the Si 2p<sup>3/2</sup> peak area as the substrate is buried under the V<sub>2</sub>O<sub>x</sub> films (Fig. 4.20b right axis), noticing two growth regimes [26]. In the first regime (labeled A), a rapid linear decrease is observed for the first nanometers where film growth is limited by the reaction rate between Si and the metal oxide, forming a uniform SiO<sub>x</sub> interlayer as a result. Then, V<sub>2</sub>O<sub>x</sub> begins to grow by island (Volmer–Weber) nucleation until saturation at ~3 nm. In the second growth regime (labeled B), a less steep and monotonic decrease in intensity is caused by uniform V<sub>2</sub>O<sub>x</sub> growth on a layer-by-layer basis until the film achieves a bulk-like quality (>10 nm), where oxygen vacancies may still be present in the TMO bulk independently of the substrate influence.

### 4.3.2 The inversion layer

In the last section, chemical passivation of surface dangling bonds by SiO<sub>x</sub> was identified as one component of the observed passivation in TMO/c-Si heterojunctions. Nevertheless, the SiO<sub>x</sub> interlayer effectiveness could be insufficient given its non-stoichiometry, leaving some dangling sites unpassivated. Another concern comes from oxygen deficiency in the atomic matrix and the possibility of highly recombinative metal–Si bonds, as inferred from the low concentration of silicates detected by ToF-SIMS.

---

<sup>14</sup> Described in the literature as a *defective oxide*, inherent to many other TMOs [57].



An additional passivation component, the so-called “field-effect” passivation, can be expected on the basis of Fermi level alignment and charge transfer across the TMO/n-Si interface [21]. As mentioned in the introduction to this chapter, the large work function difference between n-Si ( $E_{F_{nSi}} \sim 4.2$  eV) and TMOs ( $E_{F_{TMO}} > 5.1$  eV) is expected to induce an up-bending of silicon’s energy bands during  $E_F$  equilibration. As  $E_{F_{nSi}}$  approaches the silicon valence band  $E_V$ , a transition from n-type in the bulk to p-type character near the surface takes place, forming a  $p^+/n$ -Si junction with a characteristic built-in potential. Sheet resistance measurements in §4.2.1 confirmed the presence of the  $p^+$  inversion layer through which hole conduction takes place, thus establishing hole selectivity by driving photogenerated electrons away from the anode interface.

Clear indications of band bending in the vicinity of the TMO/c-Si interface were deduced from chemical shifts in the XPS spectra for incremental  $V_2O_x$  thickness. For n-Si, the  $Si^0$  peak shifted to lower binding energies meaning an increase in the energy difference  $Si^0 - Si^0_{V_2O_x}$  [61] (Fig. 4.21a). This shift is proportional to an up-bending of the Si bands, reaching a maximum value of 0.3 eV for the 2 nm film. As for  $V_2O_x$  (after subtraction of the Si substrate spectra), the valence band maximum  $VBM_{V_2O_x}$  shifted to lower binding energies meaning a decrease in the energy difference  $VBM_{V_2O_x} - VBM_{nSi}$  [62] (Fig. 4.21b). This shift is proportional to a down-bending of the  $V_2O_5$  bands, reaching a maximum value of  $-0.4$  eV for the 8 nm film. Note that the largest  $VBM_{V_2O_x}$  values may also include the larger  $VBM$  corresponding to the  $SiO_x$  interlayer.

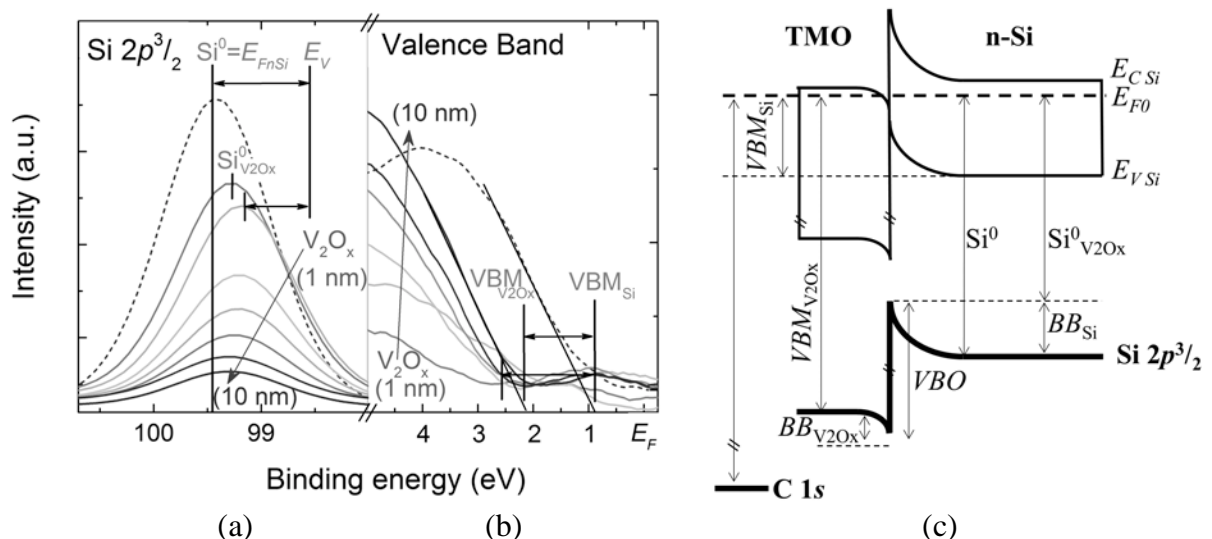


Figure 4.21 XPS chemical shifts in a  $V_2O_x/n$ -Si heterojunction for incremental film thicknesses. (a)  $Si\ 2p^{3/2}$  core level shift to lower binding energies, approaching the valence band  $E_V$  (equivalent to Si up-bending,  $BB_{Si}$ ). (b)  $V_2O_x$  valence band maximum ( $VBM$ ) shift to lower binding energies, approaching silicon’s  $VMB$  (equivalent to  $V_2O_x$  down-bending,  $BB_{V_2O_x}$ ). (c) Relative position of the XPS shifts in the energy band diagram. All energies were referenced to the C 1s signal (285 eV).



The valence band offset ( $VBO$ ) between the  $E_{V_{V_2O_x}}$  and  $E_{V_{nSi}}$  was also calculated from the difference  $VBO = VBM_{V_2O_x} - VBM_{Si}$  [62], which decreased from 1.9 to 1.3 eV as the film thickened, indicating that flat-band conditions are eventually reached (see Fig. 4.21c). Note that the  $VBO$  encloses the overall band bendings that occur on the TMO and c-Si sides. These chemical shifts are close to those reported in the literature [46,63], yet, they are only approximate considering that the photoelectron sampling depth ( $<10$  nm) is much smaller than the Si space-charge region ( $>100$  nm)<sup>15</sup>.

Based on the above observations, an energy band diagram between n-Si and  $V_2O_x$  (or similar high work function TMOs) can be proposed. Before both materials are contacted (Fig. 4.22a), a large electrochemical potential difference exists between them, as defined by the work function difference  $\Delta\Phi = \Phi_{V_2O_x} - \Phi_{nSi} \approx 5.3 - 4.2$  eV (taking the air-exposed  $\Phi_{V_2O_x}$  value [7]). This energy mismatch is the driving force behind  $E_F$  equilibration, which begins by an electron transfer from silicon's valence band ( $E_{V_{nSi}} \sim 5.2$  eV) into the mid-gap (defect) states of the TMO [21]. As electrons leave the Si surface,  $E_{V_{nSi}}$  approaches  $E_F$  and a  $p^+$  inversion layer with a characteristic band up-bending is induced. Correspondingly, holes leave the TMO surface while its conduction band  $E_{C_{TMO}}$  approaches  $E_F$ , inducing an  $n^+$  region with a characteristic band down-bending of lower magnitude. Simultaneously, an energetically favorable chemical reaction takes place and forms a  $SiO_x$  interlayer that chemically passivates the Si surface (Fig. 4.22b).

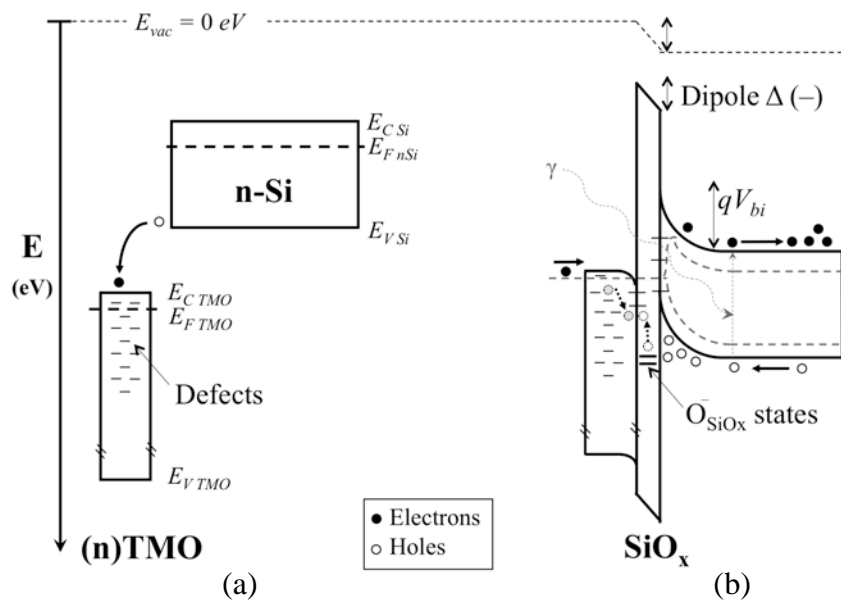


Figure 4.22 Proposed energy band diagram for TMO/n-Si heterojunctions, (a) before and (b) after contact, under forward bias and illumination.

<sup>15</sup> The calculated uncertainty was  $\pm 0.05$  eV, not including x-ray photogeneration [61] or charge accumulation [62] effects.

Given that the TMO thickness is much smaller than the depletion width in c-Si, and that oxygen vacancies in TMOs behave as fixed negative charges, it can be assumed that most of the potential difference across the heterojunction is distributed on the n-Si side (one-sided junction approximation). Furthermore, the surface potential  $\varphi_s$  at the inversion layer edge is limited by the strong inversion condition  $\varphi_s \approx 2(E_{FnSi} - E_{Fi})$ , which limits the maximum built-in voltage (and the band bending thereof) to  $V_{bi} \sim 0.7$  V [39]<sup>16</sup>. Consequently, the large work function difference  $\Delta\Phi \gtrsim 1.1$  eV can only be partially allocated by the  $V_{bi}$ , suggesting the presence of a large interfacial negative dipole  $\Delta_d$  (-), so that equilibrium conditions can be met:

$$\Delta\Phi = qV_{bi} - \Delta_d \quad (4.5)$$

delivering a dipole magnitude of  $-0.4$  eV or above, depending on the  $\Phi_{TMO}$  value.

The presence of interfacial dipoles in MoO<sub>3</sub>/n-Si heterojunctions has been recently verified by photoemission spectroscopy studies and explained on the basis of charge transfer processes [46], along the same line as other reports on TMO/organic semiconductor systems [1,3,29,64]. Regarding the specific location of the dipole in the TMO/SiO<sub>x</sub>/n-Si interface, different possibilities exist. First, as mentioned already, the six fold (MO<sub>6</sub>) octahedral coordination in TMOs is rich in dangling oxygen atoms that induce internal dipoles at exposed surfaces, as established by theory and experiment [58,59]. Second, the dipole could be originated from negative charge (excess O<sup>-</sup>) migration across the SiO<sub>x</sub>/n-Si interface (see Fig. 4.20b), driven by differences in oxygen density [65].

Returning to the SiO<sub>x</sub> interlayer identified by HR-TEM, ToF-SIMS and XPS, it is important to hypothesize about its electrical properties and carrier conduction mechanisms. With an average thickness of  $2.2 \pm 0.1$  nm, this interlayer is thicker than the reported tunneling limit of 2 nm determined from MIS device theory [66] for SiO<sub>2</sub>-based insulators, while even thicker SiO<sub>x</sub> films ( $\sim 3.5$  nm) have been recently reported for V<sub>2</sub>O<sub>x</sub>/n-Si solar cells without considerable series resistance losses [44]. Therefore, it seems that the sub-stoichiometry of the SiO<sub>x</sub> interlayer plays an important role in carrier conduction, where trap-assisted tunneling like hopping conduction or Frenkel-Poole emission might be taking place [50,53,67]. In fact, mid-gap states generated by oxygen vacancies in SiO<sub>2</sub> lie  $\sim 1$  eV below the valence band of c-Si, facilitating hole conduction

<sup>16</sup> A  $V_{bi} \sim 0.71$  V was confirmed experimentally by capacitance-voltage measurements of finished solar cells (see §5.1.3).

between the TMO and the n-Si substrate [68]. Similarly, MIS solar cells with surface state densities of  $D_{it} \sim 10^{13} \text{ cm}^{-2}$  or lower should not degrade the electronic properties across the junction, provided that a sufficiently large  $\Delta\Phi$  exists [67].

As for TMO materials, conduction through oxygen-deficient structures is generally explained in terms of small polaron hopping between defects states, specifically between low-valence  $M^{n-}$  and high-valence  $M^{n+}$  cations (Mott's theory). In this sense, TMO conductivity is directly proportional to the concentration  $C$  of  $Mo^{+5}$ ,  $V^{+4}$  and  $W^{+5}$  species and follows an Arrhenius-like thermal activation behavior, i.e.  $\sigma \propto C(1-C) \cdot e^{-E/kT}$  [22]. By considering the reduced valence ( $M^{n-}$ ) cation concentrations reported in Table 4.2, a doping level of  $N_d \sim 10^{18} - 10^{20} \text{ cm}^{-3}$  can be assumed, in agreement to reported values [48,69]<sup>17</sup>. Note that such high doping puts the TMO into the highly doped ( $n^+$ ) threshold, suggesting the one-sided junction approximation is correct (despite the negative band bending of the TMO bands observed by XPS).

Lastly, the fact that an n-type material can be used to extract holes may be found paradoxical, yet, it is useful to think of it as an extension of the overlying n-type ITO layer, which acts as a hole collecting electrode just like ITO/(p) a-Si:H contacts in HIT solar cells. In the TMO/n-Si structures under study, hole extraction can be understood by considering the ( $n^+$ )TMO/ $p^+$  junction as a sort of recombination contact (tunnel diode), frequently used in multi-junction solar cells to interconnect subcells of opposite polarity. In this sense, the very narrow space-charge region of the inversion layer provides a low resistance connection for photogenerated holes, which are extracted via recombination with the electrons 'returning' from the outer circuit.

#### 4.4 Alternative $SiO_x$ interlayers

Based on the passivation characteristics obtained for TMO/n-Si heterojunctions, it appears that the  $i-V_{OC}$  is being limited by the highly defective interface and not by insufficient built-in potentials, given that the  $\Phi_{TMO}$  values reported in the literature are sufficiently larger than  $E_V$  (see Fig. 2.13). Hence, additional passivation interlayers must be implemented to fully profit from work function differences in induced  $p^+$ /n-Si junctions.

---

<sup>17</sup> Considering  $N_d = C \cdot R^3$ , where  $R$  is the average intra-cation distance of a few Å.

As mentioned before, intrinsic a-Si:H interlayers have been successfully applied to TMO/a-Si:H/c-Si heterojunctions by several groups, obtaining excellent  $V_{OC}$  values  $>710$  mV [16,32,47]. However, these demonstrations utilize two different technologies, PECVD for a-Si:H and thermal evaporation<sup>18</sup> for TMO. Though perfectly compatible with industry, this two-step sequence increases the fabrication complexity and costs, going against the premise of achieving passivation and selectivity in a single processing step. Therefore, this thesis also studied the viability of alternative passivating SiO<sub>x</sub> interlayers grown by very simple low-temperature and ambient-pressure processes: (1) dry oxidation with ultra-violet ozone (UVO) treatments (1 min); (2) wet oxidation with a H<sub>2</sub>O<sub>2</sub>:HCl:H<sub>2</sub>O 1:1:6 solution at 70 °C (10 min), corresponding to the second step of the standard RCA cleaning procedure; (3) wet oxidation with a 67% HNO<sub>3</sub> solution at 110 °C (30 min). A fourth HF-treated substrate was used as a reference sample.

Fig. 4.23 shows the passivation quality of V<sub>2</sub>O<sub>5</sub> (15 nm)/SiO<sub>x</sub>/n-Si stacks as determined from lifetime measurements in non-symmetric samples (rear i/n<sup>+</sup> a-SiC<sub>x</sub>:H stack,  $S_{rear} \sim 10$  cm/s). The HNO<sub>3</sub> and UVO samples showed very poor passivation ( $\tau_{eff} < 30$  μs) whereas RCA2 showed a moderate lifetime ( $\sim 180$  μs) equivalent to an  $i$ - $V_{OC}$  of 630 mV (at 1 sun illumination). Contrary to expectations, the reference V<sub>2</sub>O<sub>5</sub>/SiO<sub>x</sub> stack (with the ‘naturally-grown’ SiO<sub>x</sub> interlayer) had the highest lifetime ( $\sim 540$  μs) with the characteristically high  $i$ - $V_{OC} \sim 675$  mV, outperforming the chemically-grown oxides.

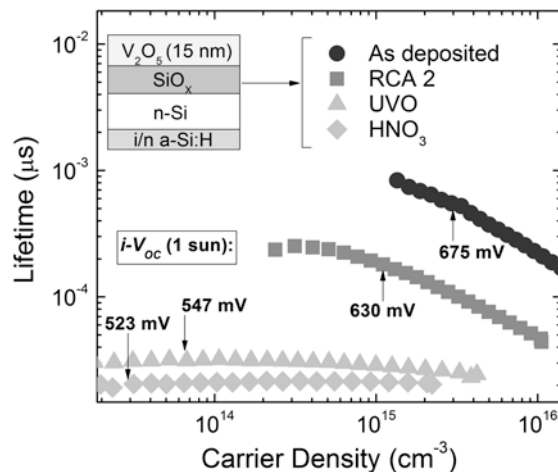


Figure 4.23 Lifetime measurements of V<sub>2</sub>O<sub>5</sub>/SiO<sub>x</sub>/n-Si structures with SiO<sub>x</sub> interlayers grown by different methods.

<sup>18</sup> Ultimately to be replaced by a large-scale industrially feasible technique, such as ALD or sputtering. However, preliminary studies show that sputtered/ALD TMOs do not perform as well as thermally evaporated films [83,84].

Next, the  $\text{SiO}_x$  films were analyzed by XPS before and after the deposition of a  $\sim 5$  nm  $\text{V}_2\text{O}_5$  film, in search of possible explanations for the differences in passivation. The XPS spectra of the  $\text{Si } 2p^{3/2}$  core level (Fig 4.24a) exhibited the characteristic  $\text{Si}^0$  substrate peak along with secondary peaks in the 102–103 eV binding energy range. By use of the  $\text{Si}^0$ – $\text{SiO}_x$  peaks chemical shift, the oxygen content ‘x’ was estimated using reported  $\Delta\text{BE}$  values of  $\text{Si}^{+1} = 0.95$ ,  $\text{Si}^{+2} = 1.75$ ,  $\text{Si}^{+3} = 2.5$  and  $\text{Si}^{+4} = 3.9$  eV [54]. An approximate stoichiometry  $x \sim 1.5$ , 1.7 and 2 was estimated for the RCA2, UVO and  $\text{HNO}_3$  oxides respectively, indicating that  $\text{HNO}_3$  is the most stoichiometric while RCA2 the least. This indicates that oxygen-deficient sub-oxides could offer better surface passivation than fully stoichiometric ones, in contrast to recent reports [70]. This observation should not apply to thermally grown vitreous  $\text{SiO}_2$ , whose far superior passivation is attributed to a radically different bond configuration, also evident from a larger  $\Delta\text{BE} = 4.4$  eV [60]).

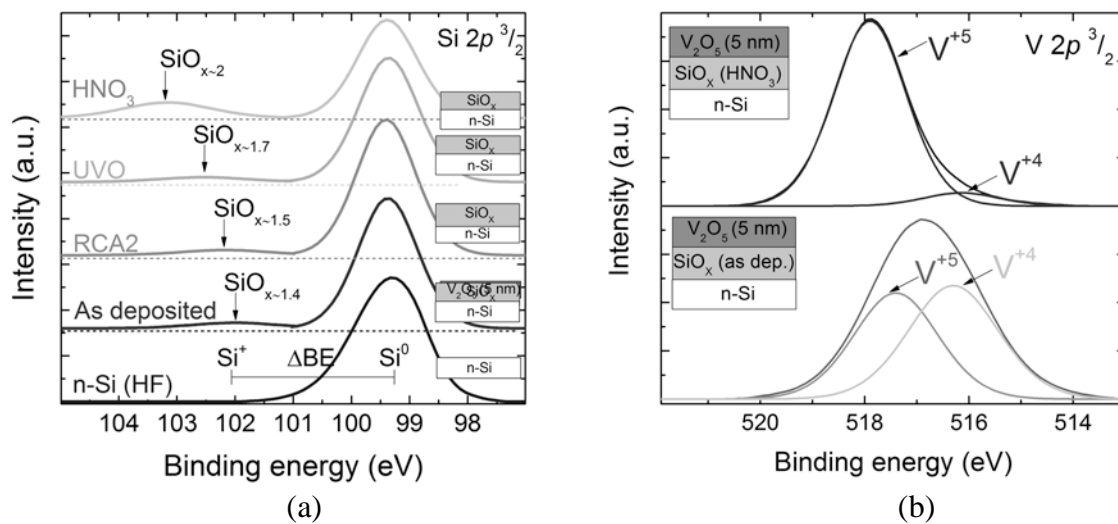


Figure 4.24 (a) XPS spectra of  $\text{Si } 2p^{3/2}$  core level showing the  $\text{SiO}_x$  peak (102–103 eV) for each oxidation method. (b) Deconvolution of the  $\text{V } 2p^{3/2}$  core level for the  $\text{HNO}_3$  and naturally-grown  $\text{SiO}_x$  layers.

Another probable cause for deficient passivation could be an inadequate coverage of the c-Si surface by too thin oxides. The approximate oxide thickness  $t_{ox}$  was estimated from the attenuation length of  $\text{Si } 2p^{3/2}$  photoelectrons in the  $\text{SiO}_x$  overlayers and the calculated peak area ratio  $\text{SiO}_x/\text{Si}^0$  [71]. The obtained oxide thicknesses were  $t_{ox} \sim 0.33$  nm for RCA2<sup>19</sup> (moderate  $\tau_{eff}$ ) and  $t_{ox} \sim 0.92$  nm for  $\text{HNO}_3$  (low  $\tau_{eff}$ ), obtaining no correlation between insufficient oxide thickness and passivation. Moreover,  $\text{V}^{+4}/\text{V}^{+5}$  ratios were also calculated from the deconvoluted

<sup>19</sup> Thinner than reported values of  $\sim 0.8$  nm [60], indicating accuracy limitations for this methodology.

V  $2p^{3/2}$  core level, showing that the V<sub>2</sub>O<sub>x</sub> layer in the reference sample is richer in V<sup>+4</sup> species (higher oxygen deficiency) than the other chemical oxides. This might offer a good explanation for the low  $i$ - $V_{OC}$  values, where the presence of a pre-grown oxide hinders charge transfer between TMOs and c-Si and minor/null inversion conditions are achieved. This observation reinforces the role of the inversion layer and the ‘field-effect’ component on the overall passivation of these structures. Table 4.5 compiles the obtained results for the different V<sub>2</sub>O<sub>5</sub>/SiO<sub>x</sub> stacks, concluding that the SiO<sub>x</sub> interlayer grown by direct oxidation of the Si substrate by the thermally evaporated TMO is the most effective one in terms of passivation.

Table 4.5. Passivation and compositional properties of the V<sub>2</sub>O<sub>5</sub>/SiO<sub>x</sub> stacks.

Sample	$i$ - $V_{OC}$ <sup>(a)</sup> mV	$\Delta BE$ eV	$x$ in SiO <sub>x</sub>	$t_{ox}$ <sup>(b)</sup> $\pm 0.1$ nm	V <sup>+4</sup> /V <sup>+5</sup> ratio <sup>(d)</sup>
As-deposited	675	2.6	~1.4	2.1 <sup>(c)</sup>	1.15
RCA2	630	2.8	~1.5	~0.33	0.11
UVO	547	3.2	~1.7	~0.25	0.11
HNO <sub>3</sub>	523	3.8	~2	~0.92	0.07

(a) With rear ( $i/n^+$ ) a-SiC<sub>x</sub>:H rear; (b) Calculated from SiO<sub>x</sub>/Si<sup>0</sup> ratios; (c) From HR-TEM; (d) Calculated from XPS

Similar SiO<sub>x</sub> interlayers grown by UVO and HNO<sub>3</sub> oxidation have been reported in the context of tunnel-oxide passivated contacts (*top-con*) with doped poly-silicon overlayers, obtaining  $i$ - $V_{OC}$  values of ~610 mV for as deposited poly-Si/SiO<sub>x</sub> stacks [72], comparable to the RCA2 and UVO samples. Additionally, a boost in  $i$ - $V_{OC}$  to ~660–720 mV was also reported after a thermal activation step at 600–850 °C followed by forming gas (H<sub>2</sub>) anneal at 400 °C [43]. This indicates that dangling bonds in freshly-grown SiO<sub>x</sub> interlayers are higher than expected and must be passivated by a high temperature hydrogen source before effectively passivating the c-Si surface. Unfortunately, thermal steps are incompatible with temperature-sensitive TMOs, although they could be applied to the SiO<sub>x</sub> layers before TMO deposition. In this matter, interface defect states  $D_{it}$  as low as  $\sim 10^{11}$  cm<sup>-2</sup> have been reported for chemical oxides grown by HCl (no H<sub>2</sub> anneal) and HNO<sub>3</sub> (after H<sub>2</sub> anneal) [70], a promising strategy for improving passivation in TMO/SiO<sub>x</sub>/c-Si heterojunctions.

## 4.5 PEDOT:PSS

Finally, a brief summary of the structural, optoelectronic and passivation properties of PEDOT:PSS solutions with n-type c-Si is given next. Figure 4.25a shows the chemical structure of conjugated polymer PEDOT:PSS with its two elemental monomers, positively charged PEDOT (poly-3,4-ethylenedioxythiophene) and negatively charged PSS (poly-styrenesulfonate), the latter acting as a surfactant that helps to disperse PEDOT in aqueous solutions. Figure 4.25b depicts the energy diagram with the corresponding HOMO/LUMO levels<sup>20</sup> originated from the hybridization of *s* and *p* orbitals, where  $\pi$ - $\pi^*$  bond transitions define an  $E_{gap} \sim 1.6$  eV. The Fermi level is located near the HOMO edge at  $\Phi \sim 5.0$  eV, giving PEDOT:PSS its characteristic p-type (hole) semiconductivity. For this thesis, two commercial PEDOT:PSS solutions amply used in organic PV were characterized [73]: (1) HTL-Solar, a hole-transport material, and (2) PH1000, specifically designed as an ITO replacement.

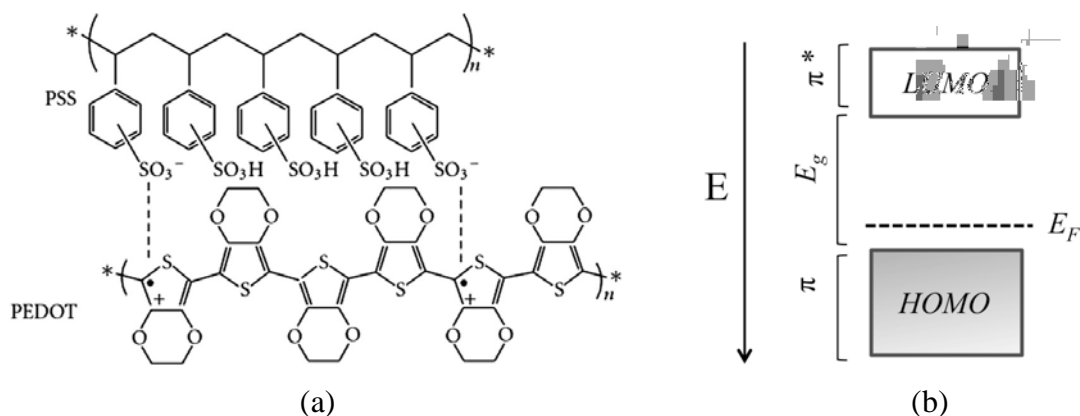


Figure 4.25 (a) Chemical structure (adopted from [18]) and (b) representative energy diagram for PEDOT:PSS.

### 4.5.1 Solution pre-conditioning

Commercial PEDOT:PSS solutions (1–1.3% concentration) are intrinsically not very conductive ( $<1 \Omega^{-1}\text{cm}^{-1}$ ) given the insulating nature of PSS [18], needing pre-conditioning treatments before the spin-coating process. In particular, dimethyl sulfoxide (DMSO) is frequently used as a co-solvent to increase  $\sigma >10^1 \Omega^{-1}\text{cm}^{-1}$  by reducing the PSS content and realigning the PEDOT domains into long stretched networks [74]. Figure 4.26a shows the XPS spectra of the (sulfur) S

<sup>20</sup> Highest occupied molecular orbital/lowest unoccupied molecular orbital.

$2p$  core level for both solutions under study after 5% $_{\text{v}}$  DMSO addition, deconvoluted into the characteristic doublet peaks for PEDOT (164.2 eV) and PSS (168.5 eV) [19]. From the integrated peak areas, the calculated PSS/PEDOT ratios for the HTL Solar and PH1000 solutions were 2.4 and 1.9 respectively, indicating that a lower PSS content should result in higher conductivities for the PH1000 films (as later confirmed by conductivity measurements).

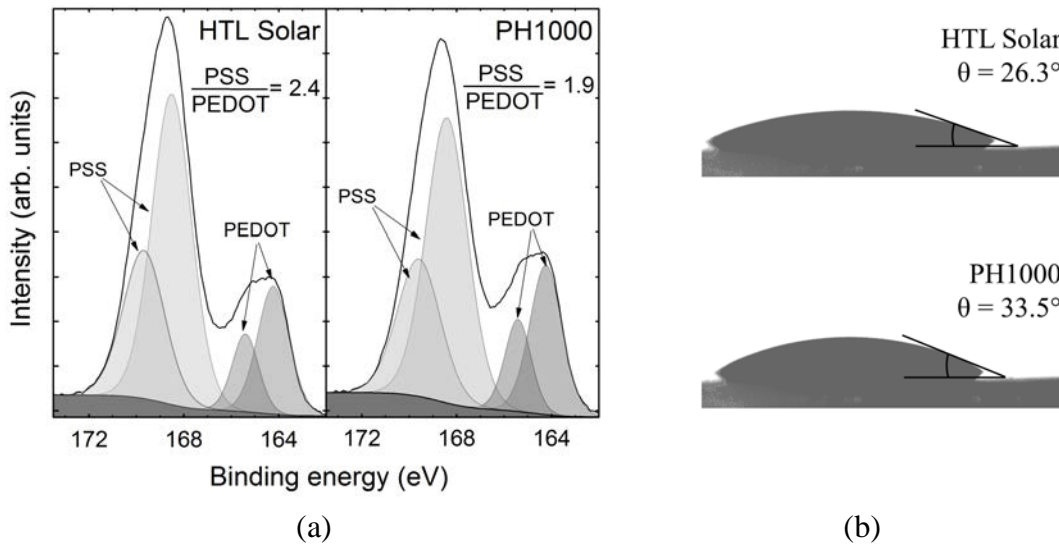


Figure 4.26 (a) XPS spectra of the S  $2p$  levels for the PEDOT:PSS solutions. (b) Contact angle for the PEDOT:PSS solutions with planar c-Si (after surfactant addition).

Another problem with water-based solutions is the high hydrophobicity of HF-treated c-Si, which can be reduced by adding small surfactant concentrations before the spin-coating process (see Fig. 3.6). An optimum surfactant concentration of 0.1% $_{\text{v}}$  was determined after achieving highly uniform layers over planar c-Si (as observed by optical microscopy), whereas the spinning rate was fixed at 1,000 rpm for a film thickness of  $\sim 70$  nm. A comparison between contact angle ( $\theta$ ) measurements after surfactant addition showed that HTL Solar ( $\theta \sim 26.3^\circ$ ) had a better surface wettability than PH1000 ( $\theta \sim 33.5^\circ$ ). This improvement allows for more uniform layers with less surface defects such as micro-holes and pinholes, which tend to form during the spin coating process [75]. Consequently, an improved contact quality and better surface passivation can be expected for HTL Solar.

In spite of the excellent layer uniformity obtained for planar c-Si substrates, several issues arose when spin-coating the PEDOT:PSS solutions unto texturized surfaces, as shown in the SEM images in Fig. 4.27. First, the film appeared highly uniform across the pyramid faces but showed an excessive accumulation at the base of the pyramids, an issue related to low spinning rates



[17]. The presence of voids in these accumulation areas was also apparent from a side view of the pyramids, a serious defect that could lead to current crowding. A higher magnification view also revealed a thickness variation of 20–70 nm from the top to the bottom of the pyramids. Given these observations, the solution spinning rate was increased to 4,000 rpm in order to increase film uniformity and avoid current losses [17]. As for the comparison between HTL Solar and PH1000 solutions, no major differences were observed.

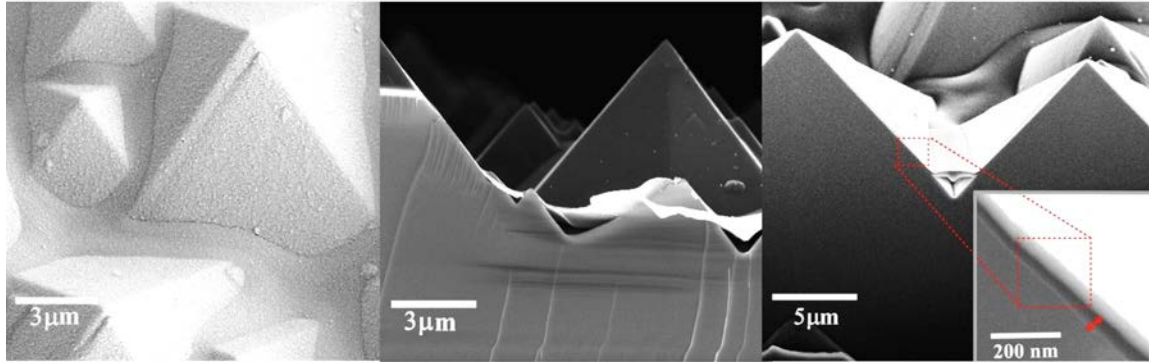


Figure 4.27 SEM images of PEDOT:PSS films spin-coated on textured c-Si substrates.

#### 4.5.2 Optoelectronic properties

The suitability of HTL Solar and PH1000 PEDOT:PSS solutions as hole-conducting/transparent electrodes was determined by a thorough study of their optoelectronic properties. Fig. 4.28a shows the optical transmittance of ~70 nm thick PEDOT:PSS films deposited on glass. Overall, both solutions exhibit a maximum  $T \sim 90\%$  at 550 nm that gradually decreases to ~65% at 1,100 nm wavelength. In this regard, a PEDOT:PSS front electrode would entail higher parasitic absorption losses in a c-Si solar cell, specially when compared to ITO films ( $T > 95\%$ ). Notice the transmission spectrum of HTL Solar is slightly above PH1000, attributed to differences in the solid content [73]. Another important factor to consider is the anti-reflection qualities provided by PEDOT:PSS, whose refractive index  $n \sim 1.5$  [76] yields an optimal film thickness ( $t_{PEDOT} = \lambda/4n$ ) of ~90 nm for minimal reflectance losses at 550 nm wavelength. When applied unto texturized substrates, reflection losses were further decreased below 7% in the 400–1,000 nm range, as shown in Fig. 4.28b. Consequently, PEDOT:PSS solutions deposited on textured c-Si will provide reasonable anti-reflection at the expense of reduced photocurrent generation.

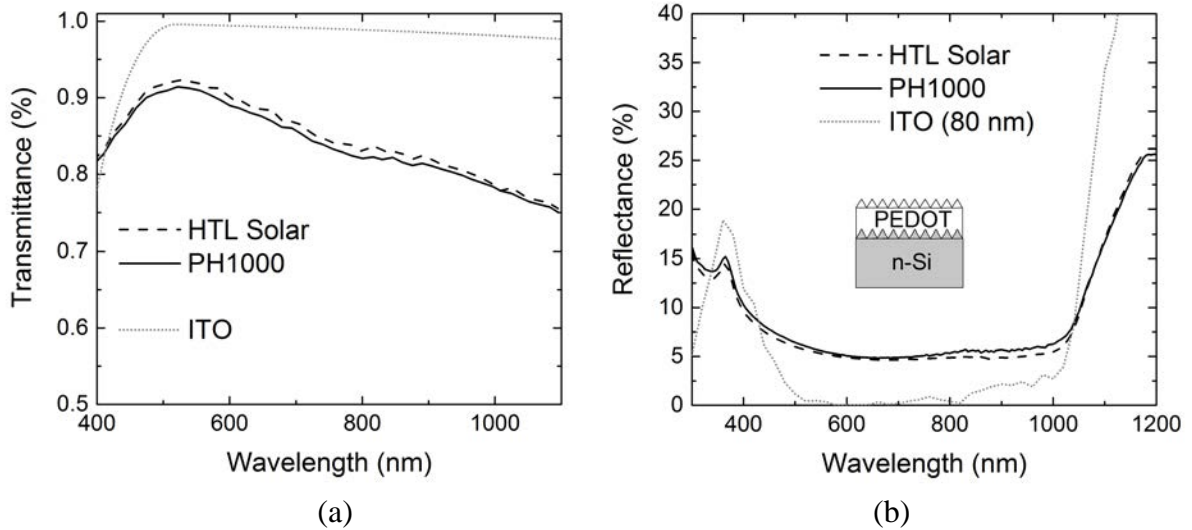


Figure 4.28 (a) Transmittance (on glass) and (b) reflectance (on textured c-Si) of PEDOT:PSS solutions, including ITO as a reference (simulated).

Next, the sheet resistance and specific contact resistivity were determined from TLM measurements of PEDOT:PSS films spin-coated on glass (50 nm Ag contacts). Fig. 4.29a shows the current-voltage response for both solutions (all ohmic) while Fig. 4.29b shows the characteristic linear fit between the total resistance and the contact spacing. The extracted  $R_{sh}$  were  $\sim 190$  and  $\sim 120 \Omega/\square$  for HTL Solar and PH1000 respectively, which translate into coplanar conductivities of  $\sim 750$  and  $\sim 1,170 \Omega^{-1}\text{cm}^{-1}$ . These results are in accordance with the PSS/PEDOT ratios determined by XPS, where a lower content of insulating PSS was measured for PH1000, making it a more appropriate replacement for ITO electrodes. By taking an average PEDOT:PSS mobility  $\mu \sim 1 \text{ cm}^2/\text{V}\cdot\text{s}$  [18], a hole concentration  $p$  in the order of  $10^{21} \text{ cm}^{-3}$  was obtained.

Even though no TLM measurements were performed on Ag/PEDOT:PSS/n-Si structures, the magnitude of the  $R_{sh}$  values indicates that current flow would be confined to the PEDOT:PSS films and not to the hypothetical inversion layer induced by the work function difference  $\Phi_{PEDOT} - \Phi_{nSi}$  [77]. In a worst case scenario, the inversion layer would increase the contact resistance between PEDOT:PSS and n-Si (estimated at  $\sim 200 \text{ m}\Omega\cdot\text{cm}^2$  [76]), a major component of the device's total  $R_S$  considering it is a full area contact. Regarding the  $\rho_c$  values estimated from the glass TLM measurements, they were very dissimilar with  $\sim 30$  and  $\sim 790 \text{ m}\Omega\cdot\text{cm}^2$  for HTL Solar and PH1000 respectively. However, since they only account for the Ag/PEDOT:PSS interface resistance, they can be considered minor contributors to  $R_S$  ( $< 5\%$  area fraction contacted by the finger grid). Table 4.6 summarizes the electrical properties of both PEDOT:PSS films.

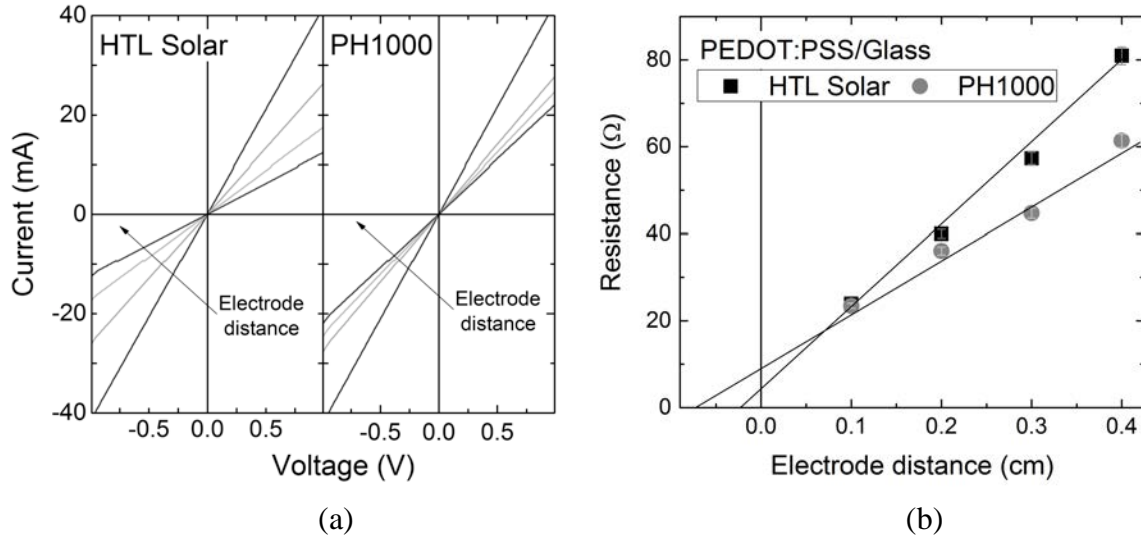


Figure 4.29 TLM measurements for 70 nm thick PEDOT:PSS films on glass. (a) Example ohmic current-voltage response (dark) and (b) linear fit for different electrode intervals.

Table 4.6 Summary of the electric properties for PEDOT:PSS solutions contacted by Ag electrodes. All measurements were performed in the dark.

Substrate	Glass			
	$R_{sh}$ $\Omega/$	$\sigma$ $\Omega^{-1}\text{cm}^{-1}$	$\rho_c$ $\text{m}\Omega\cdot\text{cm}^2$	$p^{(1)}$ $\text{cm}^{-3}$
HTL Solar	190	750	$\sim 30$	$\sim 4.3 \times 10^{21}$
PH1000	120	1,170	$\sim 790$	$\sim 2.7 \times 10^{21}$

<sup>(1)</sup> For an average mobility  $\mu \sim 1 \text{ cm}^2/\text{V}\cdot\text{s}$

### 4.5.3 Passivation

In addition to adequate optical and electrical properties, PEDOT:PSS films must also passivate the silicon surface and minimize surface recombination. The measured effective lifetime  $\tau_{eff}$  of symmetric PEDOT:PSS/n-Si/PEDOT:PSS structures was 205  $\mu\text{s}$  for HTL Solar and 82  $\mu\text{s}$  for PH1000 (at 1 sun illumination), corresponding to  $i$ - $V_{OC}$  values<sup>21</sup> of  $\sim 660$  mV and  $\sim 630$  mV respectively. These implied voltages are considerably lower than state-of-the-art values ( $\sim 690$  mV [76]), yet, they are remarkable given the following factors: (1) the apparent difference in the inorganic vs. organic nature of Si and PEDOT:PSS, which is not an impediment for the chemical passivation of silicon surfaces via Si–C and Si–O bonds [78]; (2) The simplicity of the passivation process, i.e. a liquid in direct contact with a solid, contrasting with more elaborate

<sup>21</sup> Corrected by a factor  $kT \ln(2) \approx 17.8$  mV, due to the sample's symmetric structure.

passivation schemes involving surface modification reactions and slow kinetics [79]. In this sense, the improved surface passivation obtained by HTL Solar could be attributed to a higher degree of chemical bonding with the Si dangling bonds, also related to a better deposition quality (lower contact angle) during the spin-coating process.

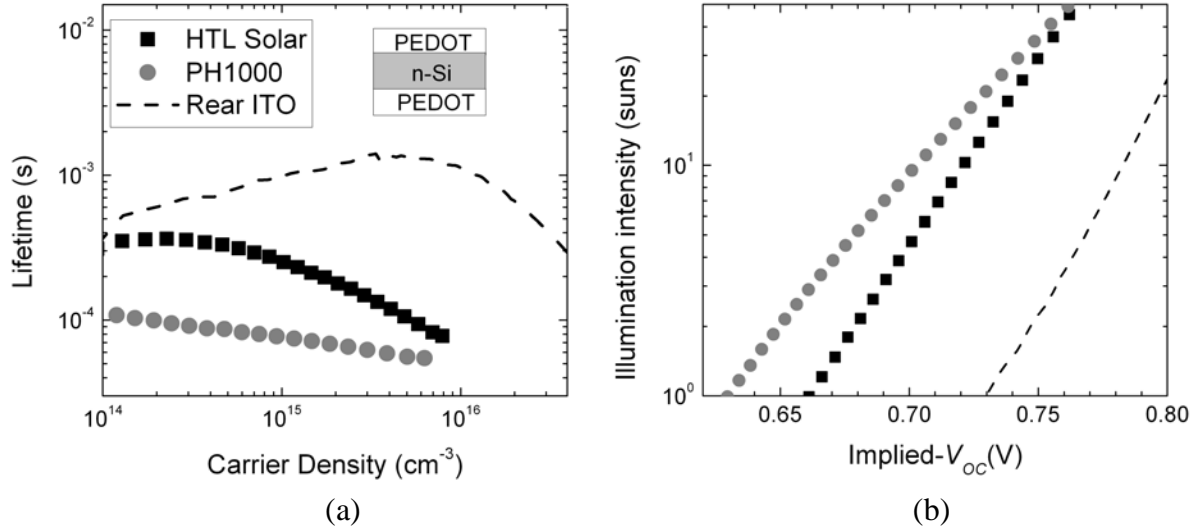
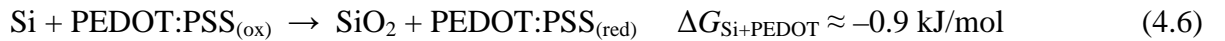


Figure 4.30 (a) Effective carrier lifetime for symmetric PEDOT/n-Si/PEDOT (b) Implied- $V_{oc}$  as a function of illumination (sun equivalents). The (n) a-SiC<sub>x</sub>H electron contact strategy (ITO-contacted) is also shown.

Finally, some general comments can be made in analogy to TMO/n-Si heterojunctions. First, a very similar energy band diagram as the one presented in Fig. 4.22 can be expected but with three modifications: (1) the absence of an interfacial dipole, given the shorter  $\Phi_{PEDOT} - \Phi_{nSi}$  difference; (2) a more pronounced band bending on the PEDOT:PSS side, given the higher density of mobile carriers in PEDOT:PSS [77]; and (3) hole transport taking place in the bulk of the hole-selective PEDOT:PSS material, given its marked p-type conductivity. As for the presence of an interfacial layer, no thorough studies have been made except for HR-TEM imaging that shows either no layer [80] or a  $\sim 0.7$  nm thick SiO<sub>x</sub> interlayer [77]. Based on thermodynamic arguments, the oxidation of silicon by PEDOT:PSS can be described by [81]<sup>22</sup>:



obtaining a barely negative Gibbs free energy of reaction. Consequently, it is important to study in more detail the bonding structure between PEDOT:PSS and c-Si, as well as possible additional passivation interlayers.

<sup>22</sup> Considering electrode potentials (referenced to the standard electrode  $E_{H_2}^0 = 0$  V) of  $E_{PEDOT}^0 = -0.15$  V and  $E_{Si}^0 = -0.14$  V.

## 4.6 References

- [1] J. Meyer, S. Hamwi, M. Kröger, W. Kowalsky, T. Riedl, A. Kahn, Transition metal oxides for organic electronics: energetics, device physics and applications., *Adv. Mater.* **24** (2012) 5408–5427.
- [2] M.T. Greiner, L. Chai, M.G. Helander, W.-M. Tang, Z.-H. Lu, Metal/metal-oxide interfaces: how metal contacts affect the Work function and band structure of MoO<sub>3</sub>, *Adv. Funct. Mater.* **23** (2013) 215–226.
- [3] Irfan, M. Zhang, H. Ding, C.W. Tang, Y. Gao, Strong interface p-doping and band bending in C60 on MoO<sub>x</sub>, *Org. Electron. Physics, Mater. Appl.* **12** (2011) 1588–1593.
- [4] M. Vasilopoulou, A. Soultati, D.G. Georgiadou, T. Stergiopoulos, L.C. Palilis, S. Kennou, et al., Hydrogenated under-stoichiometric tungsten oxide anode interlayers for efficient and stable organic photovoltaics, *J. Mater. Chem. A* **2** (2014) 1738–1749.
- [5] M.T. Greiner, Z.-H. Lu, Thin-film metal oxides in organic semiconductor devices: their electronic structures, work functions and interfaces, *NPG Asia Mater.* **5** (2013) e55.
- [6] J. Werner, J. Geissbühler, A. Dabirian, S. Nicolay, M. Morales Masis, S. De Wolf, et al., Parasitic absorption reduction in metal oxide-based transparent electrodes: application in perovskite solar cells, *ACS Appl. Mater. Interfaces* **8** (2016) 17260–17267.
- [7] K. Zilberberg, S. Trost, J. Meyer, A. Kahn, A. Behrendt, D. Lützenkirchen-Hecht, et al., Inverted organic solar cells with sol-gel processed high work-function vanadium oxide hole-extraction layers, *Adv. Funct. Mater.* **21** (2011) 4776–4783.
- [8] F. Corà, M.G. Stachiotti, C.R.A. Catlow, C.O. Rodriguez, Transition metal oxide chemistry: electronic structure study of WO<sub>3</sub>, ReO<sub>3</sub>, and NaWO<sub>3</sub>, *J. Phys. Chem. B* **101** (1997) 3945–3952.
- [9] T. Pearsall, C. Lee, Electronic transport in ReO<sub>3</sub>: dc conductivity and Hall effect, *Phys. Rev. B* **10** (1974) 2190–2194.
- [10] S.-J. Yoo, J.-H. Chang, J.-H. Lee, C.-K. Moon, C.-I. Wu, J.-J. Kim, Formation of perfect ohmic contact at indium tin oxide/N,N'-di(naphthalene-1-yl)-N,N'-diphenyl-benzidine interface using ReO<sub>3</sub>., *Sci. Rep.* **4** (2014) 3902.
- [11] K.X. Steirer, P.F. Ndione, N.E. Widjonarko, M.T. Lloyd, J. Meyer, E.L. Ratcliff, et al., Enhanced efficiency in plastic solar cells via energy matched solution processed NiO<sub>x</sub> interlayers, *Adv. Energy Mater.* **1** (2011) 813–820.
- [12] R. Islam, G. Shine, K.C. Saraswat, Schottky barrier height reduction for holes by Fermi level depinning using metal/nickel oxide/silicon contacts, *Appl. Phys. Lett.* **105** (2014) 182103.
- [13] S.-Y. Park, H.-R. Kim, Y.-J. Kang, D.-H. Kim, J.-W. Kang, Organic solar cells employing magnetron sputtered p-type nickel oxide thin film as the anode buffer layer, *Sol. Energy Mater. Sol. Cells* **94** (2010) 2332–2336.
- [14] S. Samarin, O.M. Artamonov, A.A. Suvorova, A.D. Sergeant, J.F. Williams, Measurements of insulator band parameters using combination of single-electron and two-electron spectroscopy, *Solid State Commun.* **129** (2004) 389–393.
- [15] C. Ganzorig, K. Suga, M. Fujihira, Alkali metal acetates as effective electron injection layers for organic electroluminescent devices, *Mater. Sci. Eng. B* **85** (2001) 140–143.
- [16] J. Bullock, M. Hettick, J. Geissbühler, A.J. Ong, T. Allen, C.M. Sutter-Fella, et al., Efficient silicon solar cells with dopant-free asymmetric heterocontacts, *Nat. Energy*. (2016) 15031.
- [17] T.-G. Chen, B.-Y. Huang, E.-C. Chen, P. Yu, H.-F. Meng, Micro-textured conductive polymer/silicon heterojunction photovoltaic devices with high efficiency, *Appl. Phys. Lett.* **101**

- (2012) 033301–033305.
- [18] K. Sun, S. Zhang, P. Li, Y. Xia, X. Zhang, D. Du, et al., Review on application of PEDOTs and PEDOT:PSS in energy conversion and storage devices, *J. Mater. Sci. Mater. Electron.* **26** (2015) 4438–4462.
- [19] J. Hwang, F. Amy, A. Kahn, Spectroscopic study on sputtered PEDOT:PSS - Role of surface PSS layer, *Org. Electron.* **7** (2006) 387–396.
- [20] J. Bullock, A. Cuevas, T. Allen, C. Battaglia, Molybdenum oxide MoOx: A versatile hole contact for silicon solar cells, *Appl. Phys. Lett.* **105** (2014) 232109.
- [21] J. Bisquert, Nanostructured energy devices: equilibrium concepts and kinetics, 1st ed., CRC Press, Boca Raton, Florida, USA, 2014.
- [22] P.A. Cox, Transition metal oxides: an Introduction to their electronic structure and properties, 1st ed., Oxford University Press, New York, USA, 1992.
- [23] M.T. Greiner, M.G. Helander, Z.B. Wang, W.M. Tang, J. Qiu, Z.H. Lu, A metallic molybdenum suboxide buffer layer for organic electronic devices, *Appl. Phys. Lett.* **96** (2010) 213302.
- [24] C. Battaglia, X. Yin, M. Zheng, I.D. Sharp, T. Chen, S. McDonnell, et al., Hole Selective MoOx contact for Si solar cells, *Nano Lett.* **14** (2014) 967–971.
- [25] K. Miyake, H. Kaneko, M. Sano, N. Suedomi, Physical and electrochromic properties of the amorphous and crystalline tungsten oxide thick films prepared under reducing atmosphere, *J. Appl. Phys.* **55** (1984) 2747–2753.
- [26] M. Ohring, Materials science of thin films, 2nd ed., Elsevier, San Diego, CA, 2002.
- [27] M. Mews, L. Korte, B. Rech, Oxygen vacancies in tungsten oxide and their influence on tungsten oxide/silicon heterojunction solar cells, *Sol. Energy Mater. Sol. Cells.* **158** (2016) 77–83.
- [28] National Institute of Standards and Technology, NIST x-ray photoelectron spectroscopy database (Version 4.1), (2012). <http://srdata.nist.gov/xps> (accessed June 1, 2017).
- [29] K. Kanai, K. Koizumi, S. Ouchi, Y. Tsukamoto, K. Sakanoue, Y. Ouchi, et al., Electronic structure of anode interface with molybdenum oxide buffer layer, *Org. Electron.* **11** (2010) 188–194.
- [30] C.H. Cheung, W.J. Song, S.K. So, Role of air exposure in the improvement of injection efficiency of transition metal oxide/organic contact, *Org. Electron.* **11** (2010) 89–94.
- [31] M. Bivour, J. Temmler, H. Steinkemper, M. Hermle, Molybdenum and tungsten oxide: High work function wide band gap contact materials for hole selective contacts of silicon solar cells, *Sol. Energy Mater. Sol. Cells.* **142** (2015) 34–41.
- [32] C. Battaglia, S.M. de Nicolás, S. De Wolf, X. Yin, M. Zheng, C. Ballif, et al., Silicon heterojunction solar cell with passivated hole selective MoOx contact, *Appl. Phys. Lett.* **104** (2014) 113902.
- [33] M. Anwar, C.A. Hogarth, Optical properties of amorphous thin films of MoO<sub>3</sub> deposited by vacuum evaporation, *Phys. Status Solidi.* **109** (1988) 469–478.
- [34] Z.C. Holman, A. Descoedres, L. Barraud, F.Z. Fernandez, J.P. Seif, S. De Wolf, et al., Current losses at the front of silicon heterojunction solar cells, *IEEE J. Photovoltaics.* **2** (2012) 7–15.
- [35] PV lighthouse, Wafer ray tracer calculator (Version 1.6.7), (2017). [www2.pvlighthouse.com.au](http://www2.pvlighthouse.com.au) (accessed June 1, 2017).
- [36] P.R. Cabarrocas, Deposition of intrinsic, phosphorus-doped, and boron-doped hydrogenated amorphous silicon films at 50°C, *Appl. Phys. Lett.* **65** (1994) 1674–1676.
- [37] F. Werner, Y. Larionova, D. Zielke, T. Ohrdes, J. Schmidt, Aluminum-oxide-based inversion layer solar cells on n-type crystalline silicon: Fundamental properties and efficiency potential, *J.*

- Appl. Phys.* **115** (2014) 73702.
- [38] K. Yang, Y.-C. King, C. Hu, Quantum effect in oxide thickness determination from capacitance measurement, in: Symp. VLSI Technol., IEEE, Kyoto, Japan, 1999: pp. 77–78.
- [39] S.M. Sze, K.K. Ng, Physics of semiconductor devices, 3rd ed., Wiley, Hoboken, NJ, 2007.
- [40] D. Yan, A. Cuevas, Empirical determination of the energy band gap narrowing in highly doped n-silicon, *J. Appl. Phys.* **114** (2013) 44508.
- [41] J. Bullock, A. Cuevas, D. Yan, B. Demareux, A. Hessler-Wyser, S. De Wolf, Amorphous silicon enhanced metal-insulator-semiconductor contacts for silicon solar cells, *J. Appl. Phys.* **116** (2014) 163706.
- [42] R. Brendel, R. Peibst, Contact selectivity and efficiency in crystalline silicon photovoltaics, *IEEE J. Photovoltaics.* **6** (2016) 1413–1420.
- [43] F. Feldmann, M. Bivour, C. Reichel, M. Hermle, S.W. Glunz, Passivated rear contacts for high-efficiency n-type Si solar cells providing high interface passivation quality and excellent transport characteristics, *Sol. Energy Mater. Sol. Cells.* **120** (2014) 270–274.
- [44] G. Masmitjà, L.G. Gerling, P. Ortega, J. Puigdollers, I. Martín, C. Voz, et al., V<sub>2</sub>O<sub>x</sub>-based hole-selective contacts for c-Si interdigitated back-contacted solar cells, *J. Mater. Chem. A.* **5** (2017) 9182–9189.
- [45] U. Diebold, The Surface Science of Titanium Dioxide, *Appl. Surf. Sci.* **48** (2003) 53–229.
- [46] T. Sun, R. Wang, R. Liu, C. Wu, Y. Zhong, Y. Liu, et al., Investigation of MoO<sub>x</sub>/n-Si strong inversion layer interfaces via dopant-free heterocontact, *Phys. Status Solidi.* (2017) 1700107.
- [47] J. Geissbühler, J. Werner, S. Martin de Nicolas, L. Barraud, A. Hessler-Wyser, M. Despeisse, et al., 22.5% efficient silicon heterojunction solar cell with molybdenum oxide hole collector, *Appl. Phys. Lett.* **107** (2015) 81601.
- [48] C. Sanchez, J. Livage, J.P. Audiere, A. Madi, Influence of the quenching rate on the properties of amorphous V<sub>2</sub>O<sub>5</sub> thin films, *J. Non. Cryst. Solids.* **65** (1984) 285–300.
- [49] B. Demareux, S. De Wolf, A. Descoeurdes, Z. Charles Holman, C. Ballif, Damage at hydrogenated amorphous/crystalline silicon interfaces by indium tin oxide overlayer sputtering, *Appl. Phys. Lett.* **101** (2012) 171604.
- [50] G.D. Wilk, R.M. Wallace, J.M. Anthony, High-k gate dielectrics: Current status and materials properties considerations, *J. Appl. Phys.* **89** (2001) 5243–5275.
- [51] B.R. Weinberger, G.G. Peterson, T.C. Eschrich, H.A. Krasinski, Surface chemistry of HF passivated silicon - X ray photoelectron and ion scattering spectroscopy results, *J. Appl. Phys.* **60** (1986) 3232.
- [52] W.J.I. DeBenedetti, Y.J. Chabal, Functionalization of oxide-free silicon surfaces, *J. Vac. Sci. Technol. A.* **31** (2013) 50826.
- [53] H.W. Du, J. Yang, Y.H. Li, F. Xu, J. Xu, Z.Q. Ma, Preparation of ITO/SiO<sub>x</sub>/n-Si solar cells with non-decline potential field and hole tunneling by magnetron sputtering, *Appl. Phys. Lett.* **106** (2015).
- [54] F.J. Himpsel, F.R. McFeely, A. Taleb-Ibrahimi, J.A. Yarmoff, Microscopic structure of the SiO<sub>2</sub>/Si interface, *Phys. Rev. B.* **38** (1988) 6084–6096.
- [55] Z. Liang, M. Su, Y. Zhou, L. Gong, C. Zhao, K. Chen, et al., Interaction at the silicon/transition metal oxide heterojunction interface and its effect on the photovoltaic performance, *Phys. Chem. Chem. Phys.* **17** (2015) 27409–27413.
- [56] L. Ding, M. Boccard, Z.C. Holman, M.I. Bertoni, Evaluation of transition metal oxides as carrier-selective contacts for silicon heterojunction solar cells, in: MRS Spring Meet. Exhib., San

- Francisco, CA, USA, 2015.
- [57] M.C. Biesinger, L.W.M. Lau, A.R. Gerson, R.S.C. Smart, Resolving surface chemical states in XPS analysis of first row transition metals, oxides and hydroxides: Sc, Ti, V, Cu and Zn, *Appl. Surf. Sci.* **257** (2010) 887–898.
- [58] Y. Guo, J. Robertson, Origin of the high work function and high conductivity of MoO<sub>3</sub>, *Appl. Phys. Lett.* **105** (2014) 222110.
- [59] K. Hermann, M. Witko, R. Druzinic, A. Chakrabarti, B. Tepper, M. Elsner, et al., Properties and identification of oxygen sites at the V<sub>2</sub>O<sub>5</sub>(010) surface: theoretical cluster studies and photoemission experiments, *J. Electron Spectros. Relat. Phenomena.* **98–99** (1999) 245–256.
- [60] M. Grundner, H. Jacob, Investigations on hydrophilic and hydrophobic silicon (100) wafer surfaces by X-ray photoelectron and high-resolution electron energy loss-spectroscopy, *Appl. Phys. A Solids Surfaces.* **39** (1986) 73–82.
- [61] D.C. Gleason-Rohrer, B.S. Brunshwig, N.S. Lewis, Measurement of the band bending and surface dipole at chemically functionalized Si(111)/vacuum interfaces, *J. Phys. Chem. C.* **117** (2013) 18031–18042.
- [62] E. Bersch, M. Di, S. Consiglio, R.D. Clark, G.J. Leusink, A.C. Diebold, Complete band offset characterization of the HfO<sub>2</sub>/SiO<sub>2</sub>/Si stack using charge corrected x-ray photoelectron spectroscopy, *J. Appl. Phys.* **107** (2010) 43702.
- [63] L. Ding, C. Zhang, T.U. Naerland, N. Faleev, C.B. Honsberg, M.I. Bertoni, Operando XPS characterization of selective contacts: the case of molybdenum oxide for crystalline silicon heterojunction solar cells, in: 43rd Photovolt. Spec. Conf., IEEE, Portland, OR, USA, 2016: pp. 3543–3546.
- [64] U. Würfel, M. Seßler, M. Unmüssig, N. Hofmann, M. List, E. Mankel, et al., How molecules with dipole moments enhance the selectivity of electrodes in organic solar cells – A combined experimental and theoretical approach, *Adv. Energy Mater.* **6** (2016) 1600594.
- [65] K. Kita, A. Toriumi, Intrinsic origin of electric dipoles formed at high-k/SiO<sub>2</sub> interface, *Appl. Phys. Lett.* **94** (2009) 132902.
- [66] J. Schewchun, R. Singh, M. Green, Theory of metal-insulator-semiconductor solar cells, *J. Appl. Phys.* **48** (1977) 765–770.
- [67] M.A. Green, Effects of pinholes, oxide traps, and surface states on MIS solar cells, *Appl. Phys. Lett.* **33** (1978) 178–180.
- [68] Y. Liu, P. Stradins, H. Deng, J. Luo, S.H. Wei, Suppress carrier recombination by introducing defects: The case of Si solar cell, *Appl. Phys. Lett.* **108** (2016).
- [69] G.S. Nadkarni, J.G. Simmons, Electrical properties of evaporated molybdenum oxide films, *J. Appl. Phys.* **41** (1970) 545–551.
- [70] B. Stegemann, K.M. Gad, P. Balamou, D. Sixtensson, D. Vössing, M. Kasemann, et al., Ultra-thin silicon oxide layers on crystalline silicon wafers: Comparison of advanced oxidation techniques with respect to chemically abrupt SiO<sub>2</sub>/Si interfaces with low defect densities, *Appl. Surf. Sci.* **395** (2017) 78–85.
- [71] M.P. Seah, S.J. Spencer, Ultrathin SiO<sub>2</sub> on Si II. Issues in quantification of the oxide thickness, *Surf. Interface Anal.* **33** (2002) 640–652.
- [72] A. Moldovan, F. Feldmann, K. Kaufmann, S. Richter, M. Werner, C. Hagendorf, et al., Tunnel oxide passivated carrier-selective contacts based on ultra-thin SiO<sub>2</sub> layers grown by photo-oxidation or wet-chemical oxidation in ozonized water, *Sol. Energy Mater. Sol. Cells.* **142** (2015) 123–127.
- [73] W. Lövenich, PEDOT-properties and applications, *Polym. Sci. Ser. C.* **56** (2014) 135–143.



- [74] Y.H. Kim, C. Sachse, M.L. MacHala, C. May, L. Müller-Meskamp, K. Leo, Highly conductive PEDOT:PSS electrode with optimized solvent and thermal post-treatment for ITO-free organic solar cells, *Adv. Funct. Mater.* **21** (2011) 1076–1081.
- [75] J.P. Thomas, K.T. Leung, Defect-minimized PEDOT:PSS/planar-si solar cell with very high efficiency, *Adv. Funct. Mater.* **24** (2014) 4978–4985.
- [76] D. Zielke, A. Pazidis, F. Werner, J. Schmidt, Organic-silicon heterojunction solar cells on n-type silicon wafers: The BackPEDOT concept, *Sol. Energy Mater. Sol. Cells.* **131** (2014) 110–116.
- [77] X. Mu, X. Yu, D. Xu, X. Shen, Z. Xia, H. He, et al., High efficiency organic/silicon hybrid solar cells with doping-free selective emitter structure induced by a WO<sub>3</sub> thin interlayer, *Nano Energy.* **16** (2015) 54–61.
- [78] D.D.M. Wayner, R.A. Wolkow, Organic modification of hydrogen terminated silicon surfaces, *J. Chem. Soc. Perkin Trans. 2.* **2** (2002) 23–34.
- [79] F. Zhang, D. Liu, Y. Zhang, H. Wei, T. Song, B. Sun, Methyl/allyl monolayer on silicon: efficient surface passivation for silicon-conjugated polymer hybrid solar cell, *Appl. Mater. Interfaces.* **5** (2013) 4678–4684.
- [80] S.-C. Shiu, J.-J. Chao, S.-C. Hung, C.-L. Yeh, C.-F. Lin, Morphology dependence of silicon nanowire/poly(3,4-ethylenedioxythiophene):poly(styrenesulfonate) heterojunction solar cells, *Chem. Mater.* **22** (2010) 3108–3113.
- [81] C.F. Glover, J. McGettrick, G. Williams, T.M. Watson, D. Bryant, A scanning kelvin probe investigation of the interaction of PEDOT:PSS films with metal surfaces and potential corrosion protection properties, *J. Electrochem. Soc.* **162** (2015) H799–H805.
- [82] T.B. Reed, Free energy of formation of binary compounds: an atlas of charts for high-temperature chemical calculations, MIT Press, Cambridge, MA, 1971.
- [83] M. Boccard, L. Ding, P. Koswatta, M.I. Bertoni, Z. Holman, Evaluation of metal oxides prepared by reactive sputtering as carrier-selective contacts for crystalline silicon solar cells, in: 42nd Photovoltaics Spec. Conf., IEEE, New Orleans, LA, USA, 2015: pp. 1–3.
- [84] M. Bivour, B. Macco, J. Temmler, W.M.M. Kessels, M. Hermle, Atomic layer deposited molybdenum oxide for the hole-selective contact of silicon solar cells, *Energy Procedia.* **92** (2016) 443–449.

## 5 Solar cell results

*The main performance parameters of solar cell devices are presented and correlated to the material optoelectronic properties, also determining the carrier transport mechanisms, temperature stability and built-in potential of the heterojunction. After the optimization of the rear contact, a maximum 16.5% efficiency is obtained.*

### 5.1 TMO/n-Si solar cells

#### 5.1.1 Current-voltage characteristics

Given the increased surface area of randomly-textured silicon, solar cell devices were fabricated both on planar (polished) and textured wafers in order to investigate probable differences in surface passivation. Fig. 5.1 shows the current density-voltage  $J(V)$  response of both planar and textured devices, with the optically optimized ITO(80 nm)/TMO(15 nm) front stack<sup>1</sup> and the (i/n<sup>+</sup>) a-SiC<sub>x</sub>:H laser-fired rear stack. All measurements were performed in dark and standard illumination conditions (AM1.5g solar spectrum, 1,000 W/m<sup>2</sup>, 25 °C).

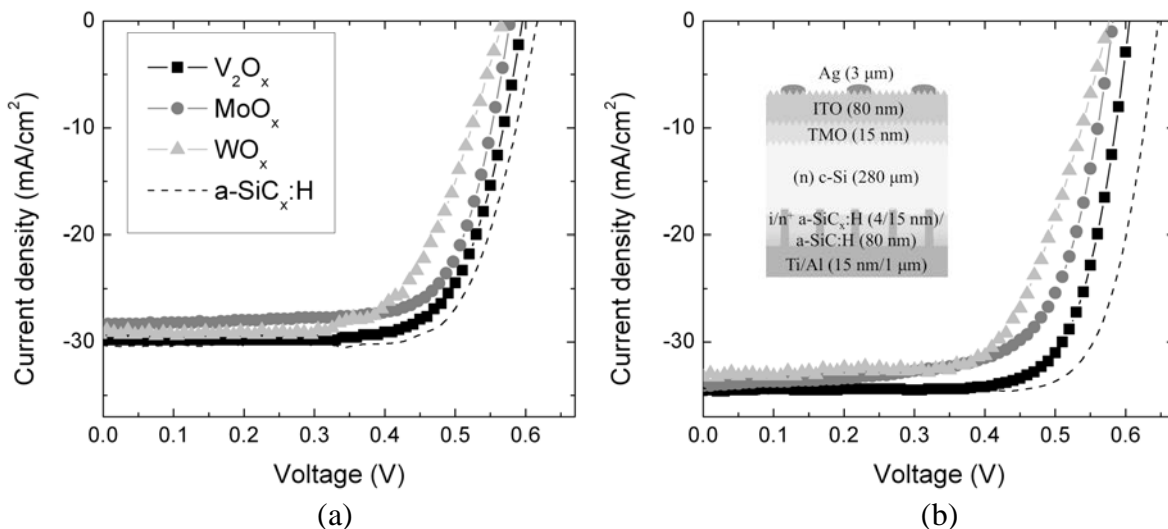


Figure 5.1 Current density-voltage response of (a) planar and (b) textured TMO/n-Si solar cells under standard illumination (highest efficiency devices).

<sup>1</sup> Considering a ~1.7 times lower deposition rate for the textured wafers, due to the enhanced surface area.

Table 5.1 Performance parameters for TMO/n-Si solar cells on planar and textured substrates (4 device average).

		$V_{OC}$	$J_{SC}$	$FF$	$PCE$	$V_{OC}$	$J_{SC}$	$FF$	$PCE$
		mV	mA/cm <sup>2</sup>	%	%	mV	mA/cm <sup>2</sup>	%	%
$V_2O_x$	<b>Planar</b>	591 ±3	29.8 ±0.7	70.7 ±1.6	12.5 ±0.6	602 ±4	33.9 ±0.8	73.6 ±2.5	15.0 ±0.8
$MoO_x$		577 ±4	28.3 ±1.5	73.6 ±1.1	12.0 ±0.6	567 ±12	33.3 ±0.5	68.7 ±2.2	13.0 ±0.6
$WO_x$		566 ±17	29.3 ±0.4	73.6 ±1.0	12.2 ±0.5	554 ±22	33.9 ±0.8	65.0 ±2.7	12.2 ±0.3
a-Si:H <sup>(1)</sup>		616	30.3	75.5	14.1	645	34.7	72.8	16.3
	<b>Textured</b>								
$V_2O_x$		602 ±4	33.9 ±0.8	73.6 ±1.6	12.5 ±0.6	602 ±4	33.9 ±0.8	73.6 ±2.5	15.0 ±0.8
$MoO_x$		567 ±12	33.3 ±0.5	68.7 ±1.1	13.0 ±0.6	567 ±12	33.3 ±0.5	68.7 ±2.2	13.0 ±0.6
$WO_x$		554 ±22	33.9 ±0.8	65.0 ±1.0	12.2 ±0.5	554 ±22	33.9 ±0.8	65.0 ±2.7	12.2 ±0.3

<sup>(1)</sup> Reference (i/n<sup>+</sup>) a-SiC<sub>x</sub>:H/p-Si device, same wafer resistivity.

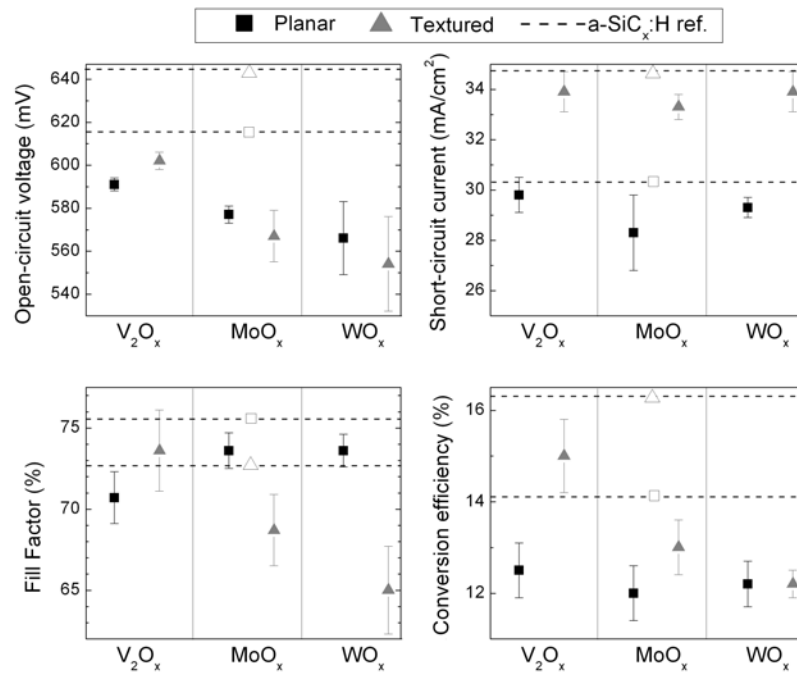


Figure 5.2 Performance parameters for TMO/n-Si solar cells on planar and textured substrates (4 device average).

Beginning with the open-circuit voltage, the observed trend was  $V_2O_x > MoO_x > WO_x$ , in agreement with the implied- $V_{OC}$  measurements (§4.2.2) and with the literature [1,2]. The maximum and minimum  $V_{OC}$  values were 606 mV ( $V_2O_x$ ) and 544 mV ( $WO_x$ ), with planar substrates having a slightly higher  $V_{OC}$  than textured ones, except for the  $V_2O_x$  case. Also,  $WO_x$  devices had a much larger variance, with one value as low as 410 mV (excluded from the statistics). It is worth noting these  $V_{OC}$  s are remarkable for such simplified structures, considering the thinness of the oxide film and the absence of additional passivation interlayers. For comparison, a reference (i/n<sup>+</sup>) a-SiC<sub>x</sub>:H/p-Si/(i)a-SiC<sub>x</sub>:H/Al<sub>laser-fired</sub> heterojunction [3] (same wafer resistivity but better front [3]) reached a  $V_{OC}$  of 616 and 645 mV for the planar and textured devices respectively.

Focusing on the short-circuit current densities, differences between TMO's were less evident than with the  $V_{OC}$ s, obtaining an average  $J_{SC}$  of  $\sim 29$  and  $\sim 33$  mA/cm<sup>2</sup> for the planar and textured devices respectively. Such increment in photogeneration can be ascribed completely to the reduced reflection losses. A maximum  $J_{SC}$  of 34.4 mA/cm<sup>2</sup> was obtained for V<sub>2</sub>O<sub>x</sub>, despite its lower energy band gap. In general, the  $J_{SC}$  values of the textured devices may seem low when compared to the literature average ( $\sim 39$  mA/cm<sup>2</sup>); yet, the difference can be attributed to poor rear absorption and low diffusion lengths, as it will be later shown in the analysis of the external quantum efficiencies (§5.1.4). Despite this shortcoming,  $J_{SC}$ s were sufficiently high and not far from the reference a-Si:H device, a proof of consistency during the fabrication process.

Next, the inspection of fill factor values reveals no clear trend among TMOs; flat substrates showed on average higher  $FF$ s (70–73%) than textured ones (65–73%), except for textured V<sub>2</sub>O<sub>x</sub> with a maximum  $FF$  of 75.3%. Although these values are below the 80–82% trademark, they are modest considering the contact resistivities previously estimated in planar substrates (§4.2.1). In this sense, final  $\rho_c$  values could be higher for textured surfaces, explaining the low  $FF$ s of MoO<sub>x</sub> and WO<sub>x</sub>. It is also worth noting the absence of S-shaped curves, a clear evidence of hole injection barriers at the TMO/n-Si interface (as has been reported for sputtered and ALD TMO layers [4,5]). Also, it means that the induced p<sup>+</sup><sub>IL</sub>/n-Si junctions are capable of sustaining carrier extraction, not only at maximum power point but also across the whole voltage range.

Altogether, the highest conversion efficiency was achieved for textured V<sub>2</sub>O<sub>x</sub> with 15.7%, followed by MoO<sub>x</sub> (13.5%) and WO<sub>x</sub> (12.5%), whose reduced efficiencies are a result of lower  $V_{OC}$  and  $FF$  values. When compared to the a-SiC<sub>x</sub>:H reference device (16.3%), the obtained efficiencies can be considered moderately good, although still bellow the standard. As it will be explained in later sections, an improvement of the overall  $V_{OC}$  by using the ITO-rear contact will boost PCE values even higher. Regarding the underperformance of WO<sub>x</sub>, it is tempting to explain it by the absence of oxygen vacancies in the characterized films (WO<sub>3.2</sub>). Yet, highly stoichiometric TMOs have a large work function that maximizes carrier selectivity, whereas oxygen-deficient TMOs tend to induce smaller band bendings as a consequence of low work function [6]. That leaves the SiO<sub>x</sub> interlayer (or its properties) as the only explanation, although more analyses are needed to confirm this. Finally, the results for the TMO/n-Si heterojunction devices passivated with a thin intrinsic a-SiC<sub>x</sub>:H interlayer (as well as a brief discussion of the probable reasons for their lower performance) are presented in Appendix B.

### 5.1.2 Diode analysis

In order to elucidate the carrier transport mechanisms in TMO/n-Si heterojunctions, the  $J(V)_{\text{dark}}$  response was measured and fitted to the double diode model (Eq. 3.4), extracting the diffusion and recombination diodes ( $J_{01}$  and  $J_{02}$ ) with their respective ideality factors  $n_1 = 1$  and  $n_2 = 2$  (Fig. 5.3a). Table 5.2 summarizes the fitting results with  $J_{01}$  values of 856, 5,200 and 17,000  $\text{fA/cm}^2$  for the  $\text{V}_2\text{O}_x$ ,  $\text{MoO}_x$  and  $\text{WO}_x$  textured devices respectively, following the same expected trend as the  $V_{OC}$  values. In some cases, fitting the diode to an exact  $n$  value was not possible, meaning that several  $(J_0, n)$  combinations are possible and that this model is only approximated.

The same fitting procedure was applied to the  $J(V)_{\text{dark}}$  measurements in the 300–370 K temperature range (Fig. 5.2a inset), plotting each  $J_0$  as a function of  $1/kT$  in Fig. 5.3b. The observed Arrhenius-like behavior can be modeled by:

$$J_0 \approx J_{00} \exp\left(\frac{-E_a}{nkT}\right) \quad (5.1)$$

where  $J_{00}$  is the saturation current pre-factor and  $E_a$  the activation energies of the diffusion ( $E_{a1} \approx E_{gap}$ ) and recombination ( $E_{a2} \approx \frac{1}{2}E_{gap}$ ) processes, as expected from semiconductor theory<sup>2</sup> [7]. This is an important finding since it suggests that TMO/n-Si heterojunctions (or rather induced  $p^+_{\text{IL}}/n\text{-Si}$  junctions) do behave like classic p/n junctions, where diffusion of minority carriers is the dominant transport mechanism for large forward bias  $>0.4$  V while carrier recombination in the space charge region (or near the TMO/n-Si interface) is dominant for small forward bias  $<0.4$  V. Note that as temperature increases,  $J_{02}$  is masked by  $J_{01}$  and the fitting becomes less accurate.

Despite the above observation, the energy band diagram in Fig. 4.22 suggests that other transport mechanisms could be present, such as [8]: (1) emission/tunneling of carriers above/across the induced barrier  $\Phi_B$  towards the TMO conduction band; and (2) multi-tunneling within the  $\text{SiO}_x$  or TMO gap states followed by capture/emission of carriers (known as the MTCE model). Both mechanisms are indistinguishable from the recombination ( $J_{02}$ ) diode at the temperature range under study, yet, recent measurements at  $T = 220$  K reveal an additional  $J_0$  component with  $n = 3\text{--}4$  and an activation energy  $E_a \sim 0.3$  eV [9], which has been previously ascribed to tunneling transport in a-Si:H/c-Si heterojunctions. However, this tunneling component is restricted to

<sup>2</sup> Actually, the global temperature dependence is  $\propto T^{3/2} \cdot e^{-E_{gap}/nkT}$ , although the exponential term dominates.

forward bias voltages  $<0.4$  V (lower than the usual operation point for solar cells) and can be considered as a minor contribution to the diffusion-dominated  $J_0$ .

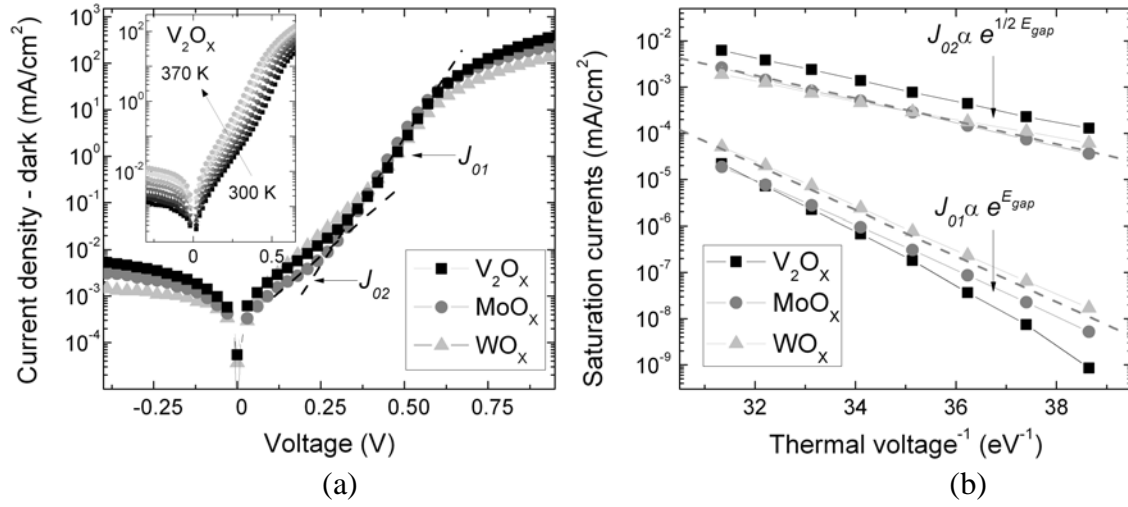


Figure 5.3 (a) Dark current-voltage response showing an example fit for the diffusion ( $J_{01}$ ) and recombination ( $J_{02}$ ) saturation currents. Inset shows  $J(V)_{\text{dark}}$  at different temperatures. (b) Arrhenius plot for both  $J_0$  components, where the exponential fit is proportional to  $E_{\text{gap}}$ .

Table 5.2 Diode fitting parameters extracted from  $J(V)_{\text{dark}}$  response of textured devices.

	$J_{01}$	$n_1$	$J_{02}$	$n_2$	$R_S$	$R_P$	$E_{a1}$	$E_{a2}$
	fA/cm <sup>2</sup>		nA/cm <sup>2</sup>		$\Omega \cdot \text{cm}^2$	k $\Omega \cdot \text{cm}^2$	eV	eV
V <sub>2</sub> O <sub>x</sub>	856		129		0.69	45		
MoO <sub>x</sub>	5,200	~1	36.5	~2	0.73	80	~1.14	~0.57
WO <sub>x</sub>	17,000		61.4		1.38	110		

As for the series and parallel resistances extracted from the diode fittings, values of  $R_P > 45$  k $\Omega \cdot \text{cm}^2$  and  $R_S \sim 0.69, 0.73$  and  $1.38$   $\Omega \cdot \text{cm}^2$  were obtained for V<sub>2</sub>O<sub>x</sub>, MoO<sub>x</sub> and WO<sub>x</sub> respectively. As expected, these  $R_S$  values are the main contributing factor to the  $FF$  of the solar cell, with the  $R_P$  influence being insignificant (all devices are greater than the minimum design  $R_P > 1.6$  k $\Omega \cdot \text{cm}^2$ ). Given that the front grid and rear contact resistances are equal for the three cell structures, the observed variation in  $R_S$  (and in  $FF$ ) can be specifically attributed to the different contact resistance values previously determined in §4.2.1 ( $\rho_c$ : V<sub>2</sub>O<sub>x</sub> < MoO<sub>x</sub> < WO<sub>x</sub>). However, a theoretical calculation of the total  $R_S$  and the resulting  $FF$  suggests the ITO/TMO/n-Si contact (and perhaps the laser-fired contact as well) could have a 10 times larger contact resistance, in order to account for the low  $FF$  values observed ( $<70\%$ )<sup>3</sup>.

<sup>3</sup> Also, the  $R_S$  values extracted from the dark diode curve are underestimated, being larger upon illumination.

Finished devices were also characterized by the Suns- $V_{OC}$  technique, which allows determining a pseudo- $J(V)$  without the effect of the series resistance. Fig. 5.4a shows the measured  $V_{OC}$  as a function of illumination intensity in sun equivalents (right axis), which can be translated into a pseudo- $J(V)_{\text{dark}}$  curve (left axis). When compared to the standard electrical measurement, the absence of  $R_S$  in the pseudo-curve allows extracting the diode parameters over a wider voltage range ( $> 0.6$  V), resulting in  $J_{01} \sim 7,600$  fA/cm<sup>2</sup> and  $n_1 \sim 1.07$  for the  $V_2O_x$  textured device, several times larger than the  $J(V)_{\text{dark}}$  fittings in Table 5.2. Likewise, the fitting of the secondary (recombination) diode yields  $J_{02} \sim 3.5$  nA/cm<sup>2</sup> and  $n_2 \sim 1.87$ .

A pseudo- $J(V)_{\text{light}}$  curve was also obtained parting from the assumption that  $J(V) = J(V)_{\text{dark}} - J_{SC}$  (superposition principle), as plotted in Fig. 5.4b. From this curve, at pseudo-fill factor of  $\sim 81.1\%$  was obtained, confirming the excellent diode quality achieved by TMO/n-Si heterojunctions once the effect of the series resistance is removed. A second estimation of  $R_S$  following [10]:

$$R_S = (\text{pseudo-}FF - FF) \frac{V_{OC} J_{SC}}{J_{mpp}^2} \quad (5.2)$$

yields an  $R_S \sim 1.1$   $\Omega \cdot \text{cm}^2$  for the  $V_2O_x$  textured device, almost twice as high as the series resistance value extracted from the  $J(V)_{\text{dark}}$  fitting (Table 5.2). This was already expected, given that carrier concentration increases several orders of magnitude upon illumination. In this sense, it can be concluded that the Suns- $V_{OC}$  methodology provides more suitable diode parameters.

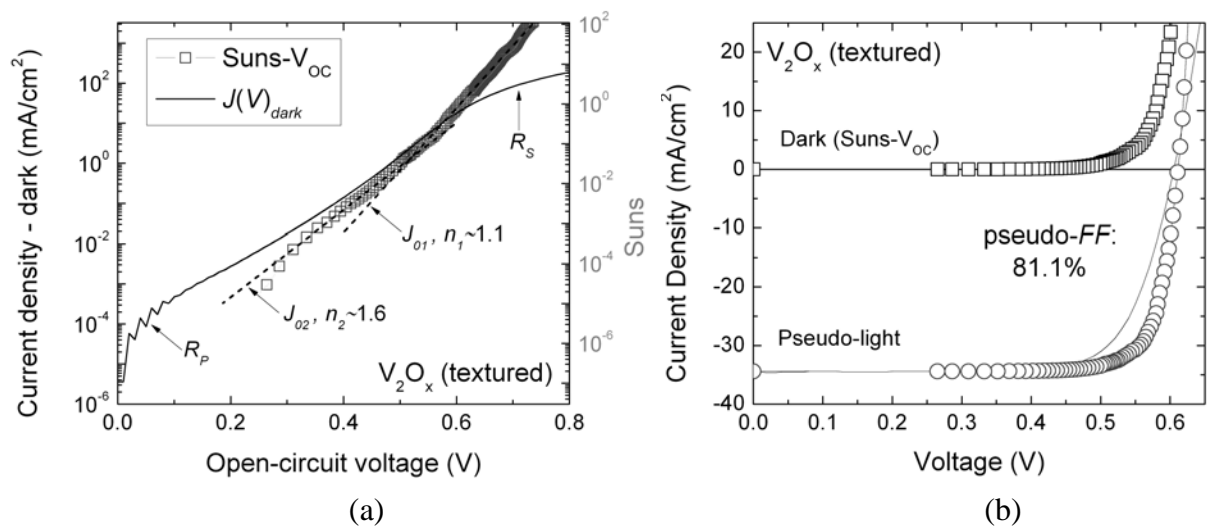


Figure 5.4 (a) Dark current density (left axis) and illumination intensity (right axis) for the  $V_2O_x$  textured device as a function of open-circuit voltage, as measured by Suns- $V_{OC}$ . (b) Pseudo current-voltage response under illumination.

In addition to the diode characteristics, Suns- $V_{OC}$  measurements were also used to determine the effective lifetime  $\tau_{eff}$  of finished devices following the procedure in §3.2.4. Fig. 5.5 shows  $\tau_{eff}$  for the  $V_2O_x$  textured device, where lifetime is slightly reduced in comparison to the device precursor measured by QSS-PC (ITO/ $V_2O_x$ /n-Si/a-SiC<sub>x</sub>:H<sub>laser</sub>). Therefore, it can be concluded that metallization barely influences the lifetime of the finished devices, although higher lifetime samples (i.e. with the rear-ITO contact) did show a larger degradation (see §5.1.7).

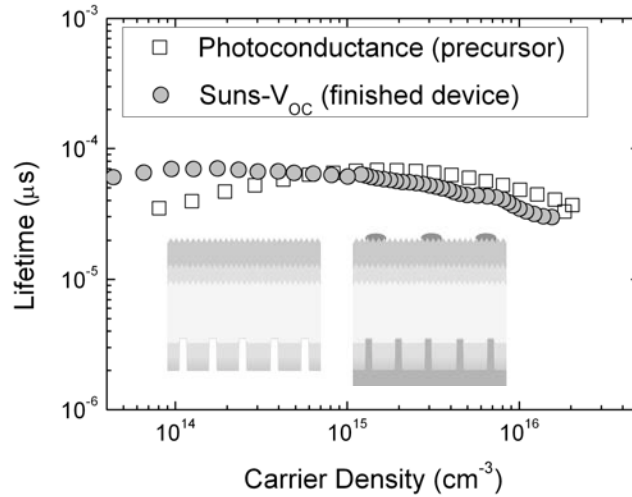


Figure 5.5 (a) Effective lifetime extracted from Suns- $V_{OC}$  measurements for the  $V_2O_x$  textured device. The overestimated  $\tau_{eff}$  at low injection is explained by differences in the assumed net generation rate [11].

Lastly, another interesting property of TMO-induced  $p^+_{IL}/n$ -Si junctions is their breakdown characteristic under very large reverse bias, determined by a sudden current runoff at a specific breakdown voltage  $V_{BD}$ . Fig. 5.6a shows the current-voltage response with  $V_{BD}$  values of ~95, 84 and 75 V for  $V_2O_x$ ,  $MoO_x$  and  $WO_x$  respectively, lower than the  $V_{BD}$  of ~150 V of a one-sided abrupt  $p^+/n$  junction (same base doping [7]) but still quite high, considering the thicknesses of the TMO (20 nm) and inversion (<3 nm) layers. Given these large  $V_{BD}$  values, the most probable mechanism by which breakdown is initiated is avalanche multiplication, which is known to damage the diode response permanently as shown in Fig. 5.6b, where a lower  $V_{BD}$  onset and a gradual current increase take place after the first breakdown.

### 5.1.3 Impedance spectroscopy (IS)

Impedance spectroscopy measurements were carried out in collaboration with Almora et al. [12] in order to determine the built-in potential ( $V_{bi}$ ) of the heterojunction from capacitance - voltage



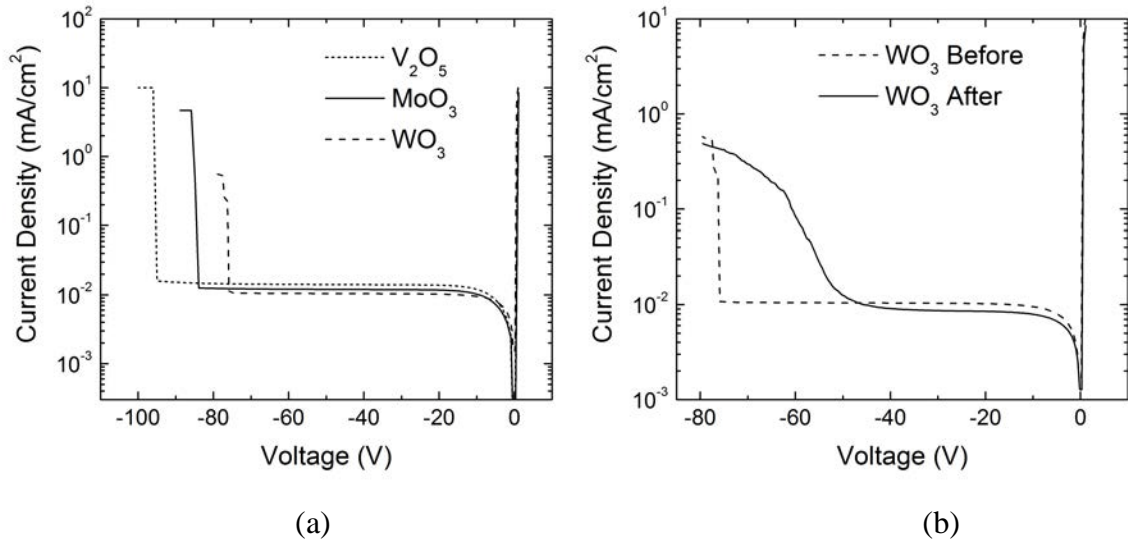


Figure 5.6 Current-voltage response under very large reverse bias until junction breakdown, shown for (a) each TMO, and (b) before and after a first breakdown ( $\text{WO}_x$  case).

measurements (10 mV AC perturbation, 1 kHz) under ambient temperature in the dark. Fig. 5.7 shows the characteristic  $1/C^2(V)$  plot with a clear linear behavior at reverse bias. By fitting to Eq. 3.12, the extrapolation into the x-axis yielded  $V_{bi}$  values of 617, 600 and 510 mV for the  $\text{V}_2\text{O}_x$ ,  $\text{MoO}_x$  and  $\text{WO}_x$  textured devices. Similarly, the slope of the linear fit is equal to the Si substrate doping  $N_d$ , with values varying from  $2\text{--}7 \times 10^{15} \text{ cm}^{-3}$ . The departure from the real doping ( $2.3 \times 10^{15} \text{ cm}^{-3}$  for a 2.5 wafer resistivity) is an indication of effective area variations and/or frequency-dependent responses (the latter a sign of trap states within  $E_{gap}$  [7]). Despite these variations, a constant slope value means that the donor density profile is also constant, translating into a quadratic potential distribution<sup>4</sup> and a quadratic band bending. Moreover, the depletion layer width of the junction  $W_j$  was also calculated from the  $1/C^2(V)$  by use of:

$$W_j = \sqrt{\frac{2\epsilon_{Si}}{qN_d} \left( V_{bi} - V - \frac{2kT}{q} \right)} \quad (5.3)$$

yielding  $W_j$  values in the order of 300–600 nm (at 0 V bias). Since these values are much larger than the TMO thickness (20 nm), the previously assumed one-sided junction approximation seems correct. Thus, by assigning most of  $V_{bi}$  to the n-Si side, it becomes evident that the n-Si surface is weakly inverted even under thermal equilibrium, i.e.  $V_{bi} > (\frac{1}{2} E_{gap} - E_{Fn})$ .

<sup>4</sup> From Poisson's equation,  $-d^2V/dx^2 \approx qN_d/\epsilon_{Si}$  [7].

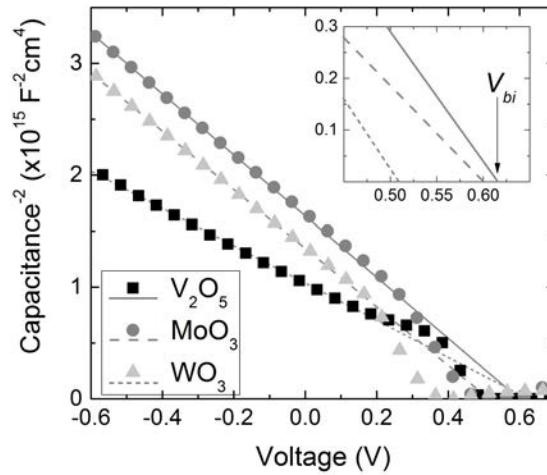


Figure 5.7 Inverse squared capacitance as a function of DC voltage. Inset shows the built-in voltage, extracted from the x-axis extrapolation of the reverse-bias data.

A more thorough IS study was also carried out by varying the device temperature and operating point ( $V_{OC}$ ), leading to the following conclusions [12]: (1) the temperature dependence (210–300 K) of the recombination resistance  $R_{rec}$  yielded effective barrier values  $\Phi_B \lesssim 50$  meV, another indication of carrier tunneling across the TMO/n-Si interface; (2) the individual electron and hole lifetimes  $\tau_e$  and  $\tau_h$  were calculated from their capacitive response times ( $\tau = R_{rec}C_d$ ), resulting in an effective lifetime  $\tau_{eff} \sim 70$   $\mu$ s ( $V_2O_x$ ) and  $\sim 50$   $\mu$ s ( $MoO_x$ ) for the textured devices (in accordance with the Suns- $V_{OC}$  measurements); and (3) effective electron and hole diffusion lengths  $L_e \sim 10^1$   $\mu$ m and  $L_h \sim 10^2$   $\mu$ m were calculated from the  $C_d(V_{OC})$  dependence, as expected from diffusion-dominated hole transport in a n-type base.

#### 5.1.4 External quantum efficiency

Quantum efficiency measurements were carried out in order to identify carrier collection losses into specific sections of the device (i.e. front/rear contacts, absorber), affecting not only the  $J_{SC}$  but also the  $V_{OC}$ . Fig. 5.8a shows the EQE response in the 300–1,200 nm wavelength range for the three TMO/n-Si textured devices, measured under a bias light of 0.1 suns and matched to the  $J_{SC}$  value obtained from the solar simulator (4.3% grid shadow included). At a first glance,  $MoO_x$  and  $WO_x$  have a similar response, while  $V_2O_x$  shows slight differences at 400 nm (lower EQE) and at 600–1,000 nm (higher EQE). This could be explained by  $V_2O_x$ 's lower  $E_{gap}$  but higher passivation quality, resulting in very similar  $J_{SC}$  values for the three TMOs as reported in Table 5.1. Irrespective of these minor differences, all three oxides exhibit a substantial EQE

improvement in the 300–550 nm range when compared to the reference a-SiC<sub>x</sub>:H stack (20 nm). Through the integration of the spectral photocurrent ( $\text{EQE} \cdot \Phi_{sun}$ ), a photocurrent gain of  $\sim 1.2 \text{ mA/cm}^2$  was calculated, directly attributed to the optical band gap difference between these TMOs and a-SiC<sub>x</sub>:H. In this sense, similar gains can be expected for passivated heterocontacts with the structure TMO (5–15 nm)/a-Si:H (5–10 nm) when compared to reference (p<sup>+</sup>/i) a-Si:H stacks, as has been recently reported [13–15]. Despite these gains, the a-SiC<sub>x</sub>:H reference stacks showed a higher response above 600 nm due to sub-band gap absorption of the TMO layers (see Fig. 4.6a), resulting in similar  $J_{SC}$  values for the TMOs and a-SiC<sub>x</sub>:H reference. The origin of TMO sub-band gap absorption lies on film coloration by reduced cation states ( $\text{Mo}^{+5}$ ,  $\text{W}^{+5}$ ,  $\text{V}^{+4}$ ), generated by the sputtering damage and partially recoverable by CO<sub>2</sub>-plasma oxidation [13,16].

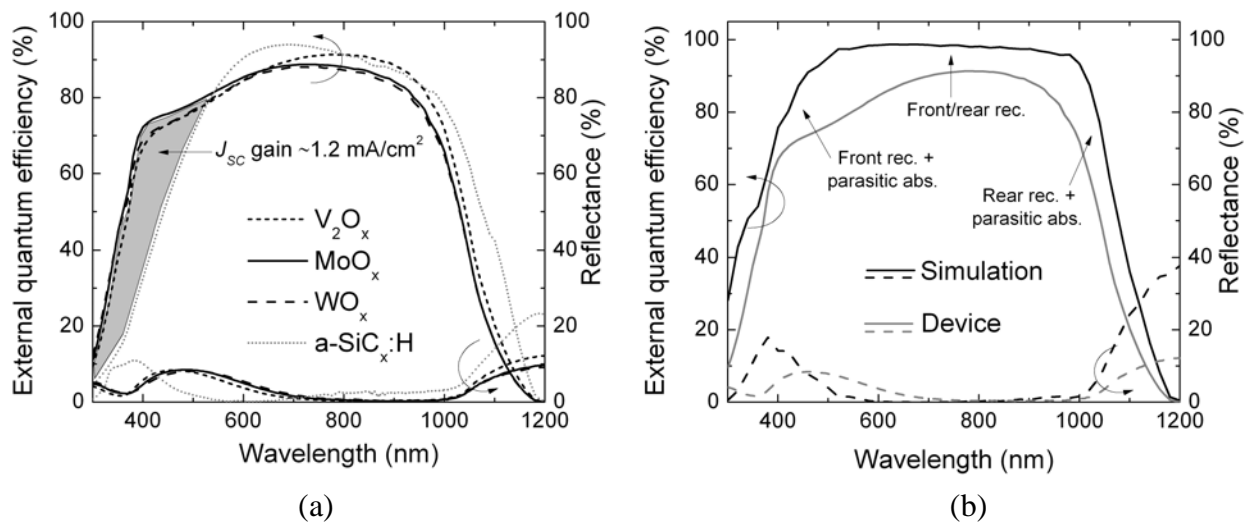


Figure 5.8 (a) External quantum efficiency and total reflectance for the TMO/n-Si devices, showing a  $J_{SC}$  gain of  $\sim 1.2 \text{ mA/cm}^2$  in comparison to a-SiC<sub>x</sub>:H. (b) Comparison between the theoretical (simulated) and actual EQE response (textured MoO<sub>x</sub>/n-Si).

In terms of total reflectance (Fig. 5.8a), TMO devices displayed slightly higher losses ( $R \sim 10\%$  at 500 nm) due to the ITO layer being thicker than the optimal value of  $\sim 65 \text{ nm}$ . This is made clear by comparing the theoretical (simulated) and measured EQE curves for the MoO<sub>x</sub>/n-Si textured device (Fig. 5.8b), where a  $J_{SC}$  mismatch of  $\sim 7 \text{ mA/cm}^2$  can be attributed to several factors: (1) front absorption losses ( $\lambda < 600 \text{ nm}$ ) due to the non-optimal ITO (80 nm)/MoO<sub>x</sub> (20 nm) stack, which was necessary to ensure a uniform TMO layer over the textured surface as well as a decent ITO sheet resistance; (2) rear absorption losses ( $\lambda > 900 \text{ nm}$ ), due to parasitic absorption at the a-SiC<sub>x</sub>:H/Ti/Al rear contact; and (3) carrier recombination both at the front and rear surfaces, which result in short diffusion lengths and low effective lifetimes.

### 5.1.5 Temperature annealing effects

Even if low temperature processing is one of the cost reduction targets, modern c-Si technology largely depends on several moderate temperatures steps (200–500°C) such as N<sub>2</sub>/H<sub>2</sub> annealings to enhance passivation (or restore it from sputtering damage [17]) and contact-firing/drying of Ag pastes for electrode formation. To this purpose, a set of planar devices was characterized before and after a mild annealing step at 160 °C during 15 min in a N<sub>2</sub>/H<sub>2</sub> atmosphere.

A summary of the measured parameters is shown in Fig. 5.9, highlighting the following observations: (1) a  $V_{OC}/J_{SC}$  improvement of 15–20 mV/0.9–1.1 mA/cm<sup>2</sup> for V<sub>2</sub>O<sub>x</sub> and WO<sub>x</sub>, in contrast to a ~20 mV/2 mA/cm<sup>2</sup> loss for MoO<sub>x</sub>; (2) a minor  $FF$  improvement for WO<sub>x</sub> (1.1% abs.) and a minor loss for MoO<sub>x</sub> (–1.7% abs.), whereas the  $FF$  of V<sub>2</sub>O<sub>x</sub> was completely downgraded to ~50% values, as also reported by [2] and probably related to amorphous-to-crystalline phase transitions [18].  $FF$  losses were distinguished by the appearance of an S-shape curve, in agreement with recent reports where a hole-blocking interlayer is formed at the ITO/MoO<sub>x</sub> interface at annealing temperatures of 130 °C and above [13]. Consequently, conversion efficiencies did not benefit from the mild thermal annealing (except for WO<sub>x</sub>, with a 0.8% absolute increase), imposing a harsh temperature limitation to TMO/n-Si processing.

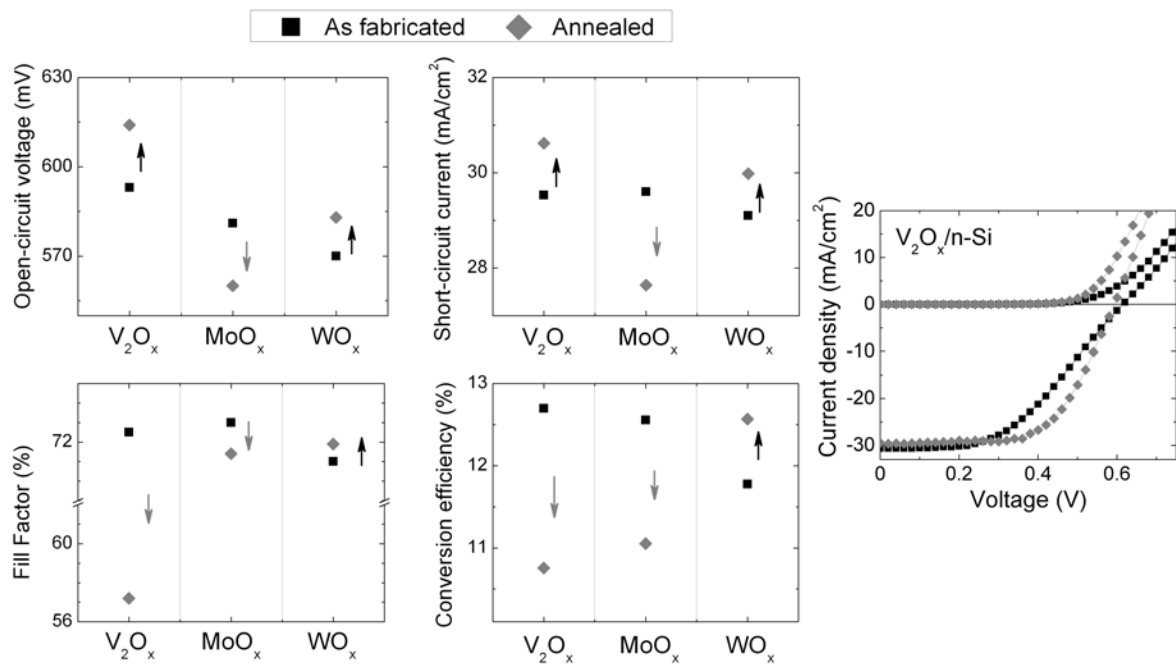


Figure 5.9 Effect of temperature annealing (160°C, N<sub>2</sub>/H<sub>2</sub>, 15 min) on the performance parameters of planar TMO/n-Si devices. An example current-voltage response is also shown.

Regarding the unsuccessful TMO/a-SiC<sub>x</sub>:H/n-Si devices, an equivalent annealing step was attempted in order to increase their low efficiencies; however, no significant improvements to  $V_{OC}$  nor  $J_{SC}$  were obtained, while S-shaped curves with  $FF < 50\%$  indicated the presence of hole-blocking barriers at the TMO/a-SiC<sub>x</sub>:H interface (see Appendix B).

### 5.1.6 Laser damage

Even though a systematic optimization of the rear contact laser-doping process was carried out<sup>5</sup>, a relatively narrow optimization window ( $1 < f_c < 10\%$ ) prevented the device from achieving the high passivation levels previously determined from lifetime measurements (e.g.  $\sim 670$  mV for V<sub>2</sub>O<sub>x</sub>). This is shown in the Fig. 5.10a where the open-circuit voltage and rear series resistance ( $R_{Srear}$ ) are simulated<sup>6</sup> as a function of  $f_c$ , obtaining an optimum  $V_{OC} \sim 620$  mV and  $R_{Srear} \sim 0.5 \Omega \cdot \text{cm}^2$  for a 2.4% contacted fraction. In order to increase  $V_{OC}$ , a  $f_c < 2.4\%$  could be used at the expense of higher resistance and conversion efficiency losses. Therefore, it can be concluded that this solar cell design is intrinsically limited by the laser-fired contact structure (as already inferred from the lifetime measurements of laser-doped structures in section 4.2.2), which leads to the  $J_{0rear}$  contribution being greater than  $J_{0front}$  (Fig. 5.10b).

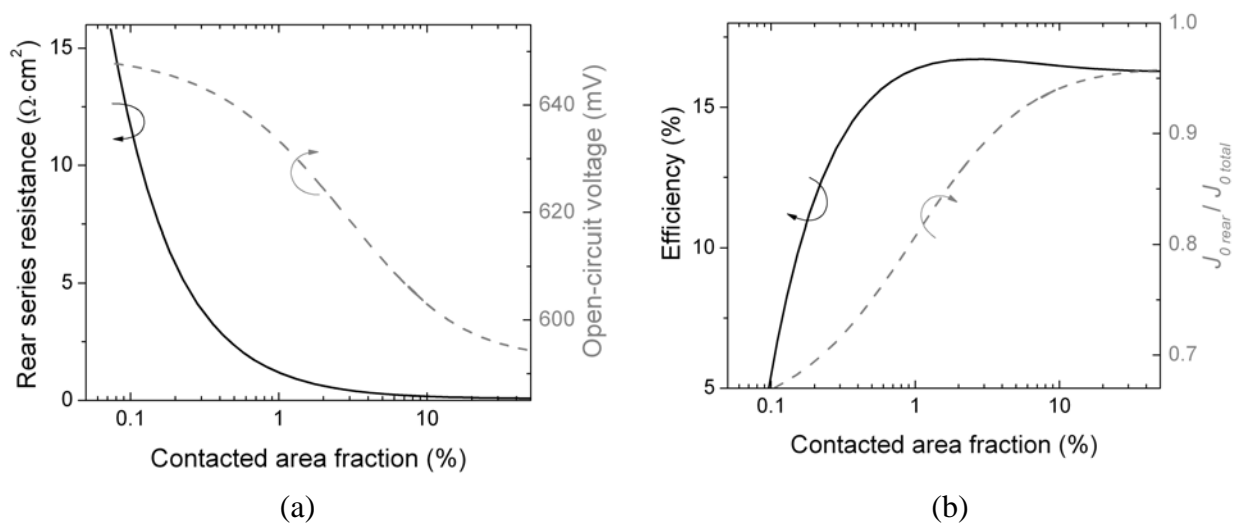


Figure 5.10 Laser simulation, showing the limitation by the rear contact.

<sup>5</sup> This included determining the optimum laser fluencies for the following structures: (1) Al-fired p<sup>+</sup>/p-Si contacts; (2) laser-doped n<sup>+</sup>/p-Si diodes; (3) laser-doped n<sup>+</sup>/n-Si contacts, resulting in  $\rho_c$  values  $< 5 \text{ m}\Omega \cdot \text{cm}^2$ .

<sup>6</sup> Considering a V<sub>2</sub>O<sub>x</sub> front contact, a (i/n<sup>+</sup>) a-SiC<sub>x</sub>:H passivated rear fraction ( $S_{pass} \sim 10 \text{ cm/s}$ ,  $1-f_c$ ) and (i/n<sup>+</sup>) a-SiC<sub>x</sub>:H/Ti/Al laser-doped rear fraction ( $S_{met} \sim 10^5 \text{ cm/s}$ ,  $f_c$ ).

In addition to the passivation/resistance shortcomings, the thin titanium layer (used as a high work function intermediate before Al contacting) was optically poor given its high absorption. Optical simulations showed that rear absorption losses were  $\sim 2.8 \text{ mA/cm}^2$  for the Ti/Al, in comparison to  $\sim 0.6 \text{ mA/cm}^2$  for an Al-only back reflector (with reflection losses being very similar at  $\sim 2.2 \text{ mA/cm}^2$ ). Such losses were already apparent from the steep EQE decline  $>1,000 \text{ nm}$ , an indication of excessive surface recombination and short diffusion lengths. Therefore, an alternative rear contact strategy consisting of  $(i/n^+)$  a-SiC<sub>x</sub>:H/ITO/Ag contacts (Fig. 3.1c) was implemented trying to overcome these limitations, as described in the following section.

### 5.1.7 Rear contact optimization

Fig. 5.11 shows the current-voltage response of a new set of V<sub>2</sub>O<sub>x</sub> solar cells (planar substrates) comparing the laser-doped and rear-ITO (80 nm) rearcontact strategies, also using a thinner (10 nm) front V<sub>2</sub>O<sub>x</sub> film in an attempt to increase  $J_{SC}$  values. For the  $(i/n^+)$  a-SiC<sub>x</sub>:H/ITO contact, a 160 °C N<sub>2</sub> anneal was performed before the thermal evaporation of the Ag electrode, in order to recover from a possible passivation damage. By comparing the measured  $V_{OC}$  values, it is evident that the rear-ITO strategy boosted voltage extraction by almost 60 mV, very close to the limit imposed by the V<sub>2</sub>O<sub>x</sub> ( $\sim 670 \text{ mV}$ ) and in agreement with similar reported devices [2]. Likewise,  $J_{SC}$  values increased by  $\sim 2.3 \text{ mA/cm}^2$  due to the thinner V<sub>2</sub>O<sub>x</sub> layer and the improved rear passivation. Despite the  $FF$  being lower than the previous experimental runs (attributed to  $R_{sh} \sim 300 \Omega/$  ITO films and to control issues with the sputtering equipment), an excellent conversion efficiency of 15.2% is obtained (see Table 5.3).

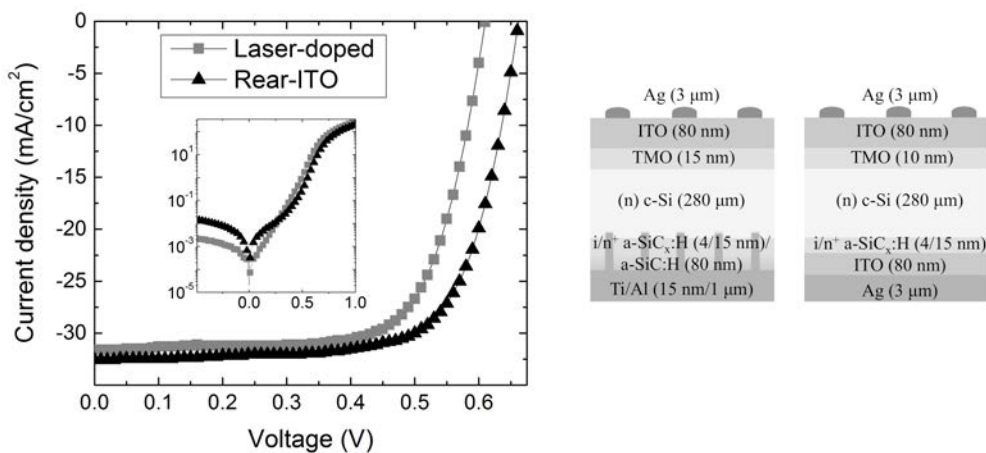


Figure 5.11 Current density-voltage response of planar V<sub>2</sub>O<sub>x</sub> (10 nm)/n-Si devices with laser-doped and ITO rear contacts (highest efficiency devices).

Table 5.3 Performance parameters for planar  $V_2O_x$  (10 nm)/n-Si devices with laser-doped and ITO rear contacts (4 device average).

$V_2O_x/n\text{-Si}$	$V_{OC}$ mV	$J_{SC}$ mA/cm <sup>2</sup>	$FF$ %	$PCE$ %
Laser-doped	606 ±7	31.2 ±0.7	70.6 ±0.4	13.3 ±0.3
Rear-ITO	661 ±4	32.1 ±0.5	70.0 ±0.6	14.9 ±0.3

The reason for the  $V_{OC}$  and  $J_{SC}$  improvement can be deduced from the analysis of the total reflectance and the internal quantum efficiency of the laser-doped and rear-ITO devices (Fig. 5.12a). As it is observed, the origin of the improvement in carrier collection is not due to changes in the  $R(\lambda)$  response (practically the same for both rear structures). Hence, a lower recombination velocity and a lower parasitic absorption at the rear contact are responsible for the enhanced passivation and current collection. This is further clarified by calculating the effective diffusion length  $L_{eff}$  from the relationship between  $1/IQE$  and the absorption coefficient  $1/\alpha$  [19]:

$$\frac{1}{IQE} = 1 + \frac{\cos(\theta)}{L_{eff}} \frac{1}{\alpha} \quad (5.4)$$

where  $\theta = 0^\circ$  is the light refraction angle at the front planar surface. The data fitting is shown in Fig. 5.12b, obtaining  $L_{eff}$  values of  $\sim 2,600$  and  $900 \mu\text{m}$  for the rear-ITO and laser-doped contacts respectively, confirming the superiority of the rear-ITO strategy.

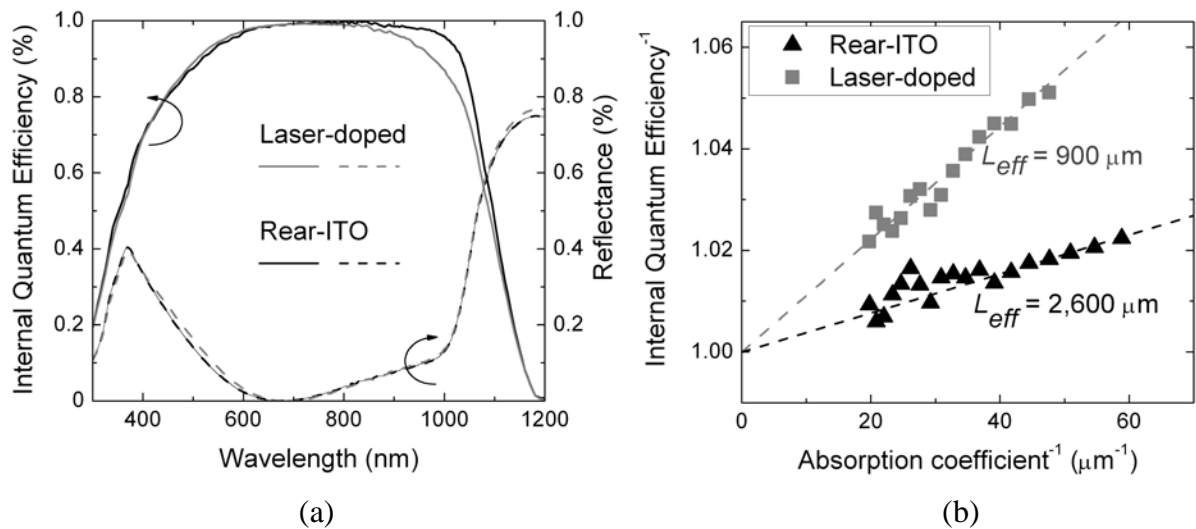


Figure 5.12 (a) Internal quantum efficiency (IQE) and total reflectance for the two rear contact strategies. (b) Inverse IQE as a function of the inverse absorption coefficient, showing the effective diffusion length extracted from the fit.

The full passivation potential of this optimized structure was made clear by measuring its  $1/C^2(V)$  characteristics (Fig. 5.13) and extracting a  $V_{bi} \sim 712$  mV [12], slightly larger than the surface potential under strong inversion conditions  $\phi_s \approx V_{bi} > 2(\frac{1}{2} E_{gap} - E_{Fn})$ . This result confirms the large potential of induced  $p^+_{II}/n$ -Si junctions for achieving  $V_{OCs} > 700$  mV, provided a good surface passivation is present.

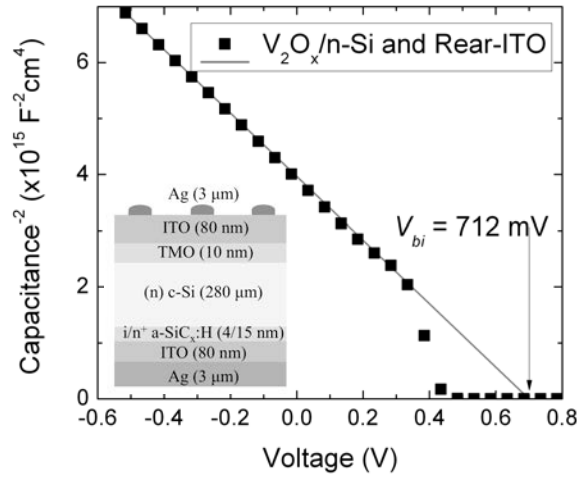


Figure 5.13 Inverse squared capacitance as a function of DC voltage for a  $V_2O_x(10 \text{ nm})/n$ -Si planar solar cell with rear ITO/Ag contact, showing the built-in voltage extracted from the x-axis extrapolation of the reverse-bias data.

Finally, the rear-ITO/Ag contact was implemented into a textured  $V_2O_x(10 \text{ nm})/n$ -Si device, obtaining a  $V_{OC} = 640 \pm 3$  mV,  $J_{SC} = 37.6 \pm 0.1$  mA/cm<sup>2</sup> and  $FF = 68.2 \pm 0.5\%$  (Fig. 5.14a). The maximum conversion efficiency of such device was 16.5%, a record efficiency value for the induced-junction solar cells presented in this thesis. One of the loss factors identified was a low  $FF < 70\%$ , attributed to either poor ideality factors ( $n_I > 1$ ) or to a large series resistance. By means of the Suns- $V_{OC}$  procedure, a pseudo- $J(V)_{\text{dark}}$  was obtained and fitted to the two-diode model, revealing a dark saturation current  $J_{0I} \sim 4,900$  fA/cm<sup>2</sup> with an ideality factor  $n_I \sim 1.1$  as well as a  $R_S \sim 2.1 \Omega \cdot \text{cm}^2$  (Fig. 5.14b), confirming that the poor  $FF$  is a result of series resistance losses at the front or rear contacts. Since ITO/Ag contacts have a minimum contact resistance  $\sim 10^{-3} \Omega \cdot \text{cm}^2$  [3], the high  $R_S$  can then be specifically attributed to the front contact, either to the ITO/ $V_2O_x/n$ -Si contact or (as is usually the case) to an insufficient ITO sheet resistance. It could also be argued that the  $\text{SiO}_x$  interlayer is limiting current transport, yet, reported  $FF$  values close to 80% indicate otherwise [2,14]. Then, considering a pseudo- $FF$  of 78.1%, the theoretical efficiency of this structure is boosted to 18.8%.



Another source of loss comes from the  $V_{OC}$ , which is lower than the  $\sim 660$  mV mark obtained in planar substrates. This is primarily due to higher recombination at the front textured surface, caused either by increased roughness (in comparison to the planar surface) or by the previously identified sputtering damage, in which case  $V_2O_x$  films thicker than 10 nm might be preferable. Moreover, the  $\tau_{eff}$  of the finished device (as calculated from Suns- $V_{OC}$  data) was decreased after the metallization step in comparison to precursor (ITO/ $V_2O_x$ /n-Si/a-SiC<sub>x</sub>:H/ITO) QSS-PC measurements (Fig. 5.15a). In brief, solving the above issues and approaching the limit  $V_{OC} \sim 660$  mV would allow for a maximum conversion efficiency of 19.4% for this type of structure.

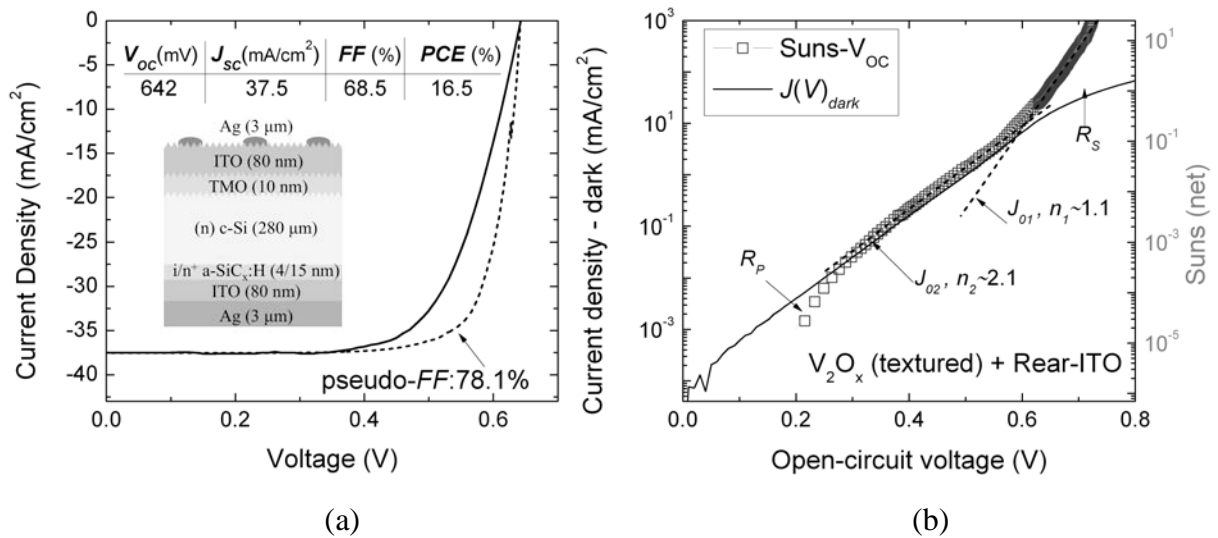


Figure 5.14 (a) Current density-voltage response of our  $V_2O_x$  (10 nm)/n-Si champion solar cell with rear ITO/Ag contact. (b) Dark current density (left axis) and illumination intensity (right axis) as measured by Suns- $V_{OC}$ .

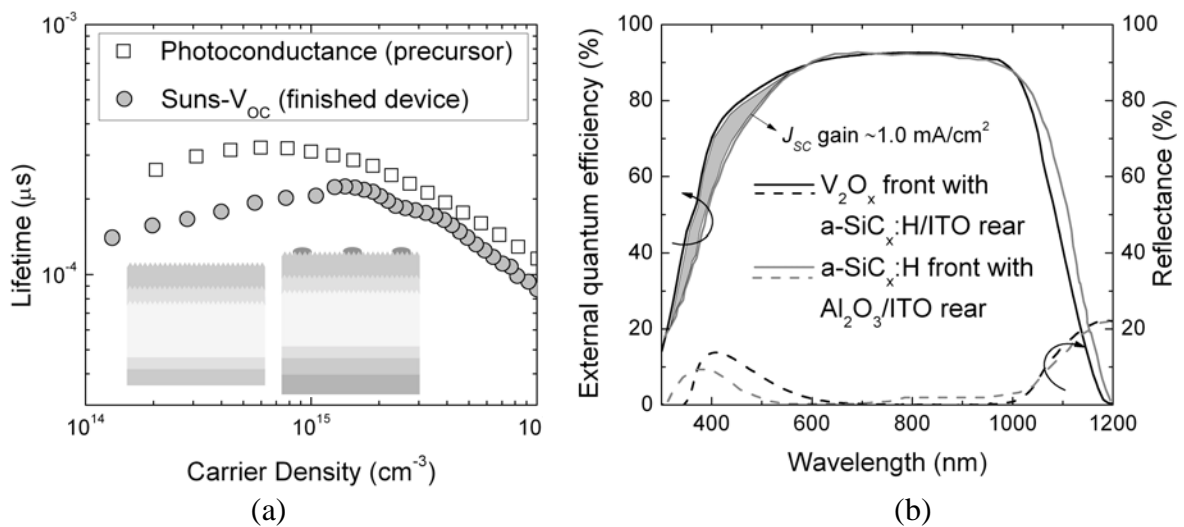


Figure 5.15 (a) Effective lifetime for the  $V_2O_x$  (10 nm) rear-ITO textured device after metallization; (b) External quantum efficiency and total reflectance. As a reference, a front (i/n<sup>+</sup>) a-SiC<sub>x</sub>:H (15 nm)/p-Si device with laser-fired  $Al_2O_3$ /ITO rear contact is also shown, with an estimated  $J_{SC}$  gain (300–600 nm range) of  $\sim 1.0$  mA/cm<sup>2</sup>.

In optical terms,  $J_{SC}$  could be improved by decreasing the parasitic absorption of the ITO layer, either by lowering its thickness (while maintaining a reasonable  $R_{sh}$ ) or by increasing its transparency, as has been reported for hydrogen-doped ITO [20] films. Regardless of this, the wider  $V_2O_x$   $E_{gap}$  (in comparison to a reference a-SiC<sub>x</sub>:H contact)<sup>7</sup> did increase photon absorption for the 300–600 nm wavelengths, resulting in  $J_{SC}$  gains of  $\sim 1$  mA/cm<sup>2</sup>, as shown in Fig. 5.15b.

## 5.2 PEDOT:PSS/n-Si solar cells performance

### 5.2.1 Current-voltage and quantum efficiency

Following the electrical characterization of the two PEDOT:PSS solutions, PH1000 and HTL Solar, it was concluded that: (1) HTL Solar provided better passivation than PH1000, resulting in higher implied open-circuit voltages ( $i-V_{OC} \sim 662$  mV); (2) HTL Solar had a much lower contact resistance ( $\rho_c \sim 30$  m $\Omega \cdot \text{cm}^2$ ) than PH1000 ( $\rho_c \sim 790$  m $\Omega \cdot \text{cm}^2$ ); and (3) both had similar transmittance ( $T > 80\%$ ) and sheet resistance values ( $R_{sh} \sim 10^1 \Omega/$ ), sufficient to substitute the ITO layer. The solar cells were fabricated on front-textured substrates, with the PEDOT:PSS layer directly contacted by the Ag grid and a rear contact consisting of (i/n<sup>+</sup>) a-SiC<sub>x</sub>:H laser-doped contacts<sup>8</sup>. The  $J(V)_{\text{light}}$  characteristics are shown in Fig. 5.16a, achieving a maximum power conversion efficiency of 11.6% and 8.5% for HTL Solar and PH1000 respectively. Despite the promising  $i-V_{OC}$  values, the measured  $V_{OC}$  for HTL Solar was 569 mV, while PH1000 also exhibited a large reduction (545 mV). The reasons for such a drop on the passivation are three-fold: (1) a poor physical contact between PEDOT:PSS and the textured surface, having observed wettability issues over the random pyramids (see Fig. 4.27); (2) the highly-recombinative rear surface, damaged by the laser-doping process; and (3) physical degradation<sup>9</sup> of the device effective lifetime after metallization.

The better performance of the HTL Solar device is also evident from its lower saturation current ( $J_0 \sim 1.4 \times 10^{-7}$  mA/cm<sup>2</sup>) and diode ideality factor ( $n_I = 1.1$ ) than PH1000 ( $J_0 \sim 3.2 \times 10^{-6}$  mA/cm<sup>2</sup>,  $n_I = 1.3$ ), as extracted from  $J(V)_{\text{dark}}$  fittings to the two-diode model (Fig. 5.15a inset). This might

<sup>7</sup> Using as reference a (i/n<sup>+</sup>) a-SiC<sub>x</sub>:H/p-Si/(p<sup>+</sup>)Al<sub>2</sub>O<sub>3</sub> laser-fired/ITO heterojunction [3].

<sup>8</sup> At a time when the intrinsic limitations of the laser-doped strategy had not been fully understood.

<sup>9</sup> Considering that PEDOT:PSS is relatively stable upon oxygen and humidity exposure [21].

be explained by a lower-quality junction between PH1000 and n-Si, as suggested by its larger contact angle (see Fig. 4.26b). Regarding the device fill factors,  $FF$ s of 61.0% and 49.6% were measured for HTL Solar and PH1000, corresponding to  $J(V)_{\text{dark}}$  series resistances of 3.4 and 6.8  $\Omega\cdot\text{cm}^2$  respectively. Such differences in  $R_S$  and  $FF$  correlate to the large disparity in contact resistances, given that their sheet resistances were very similar.

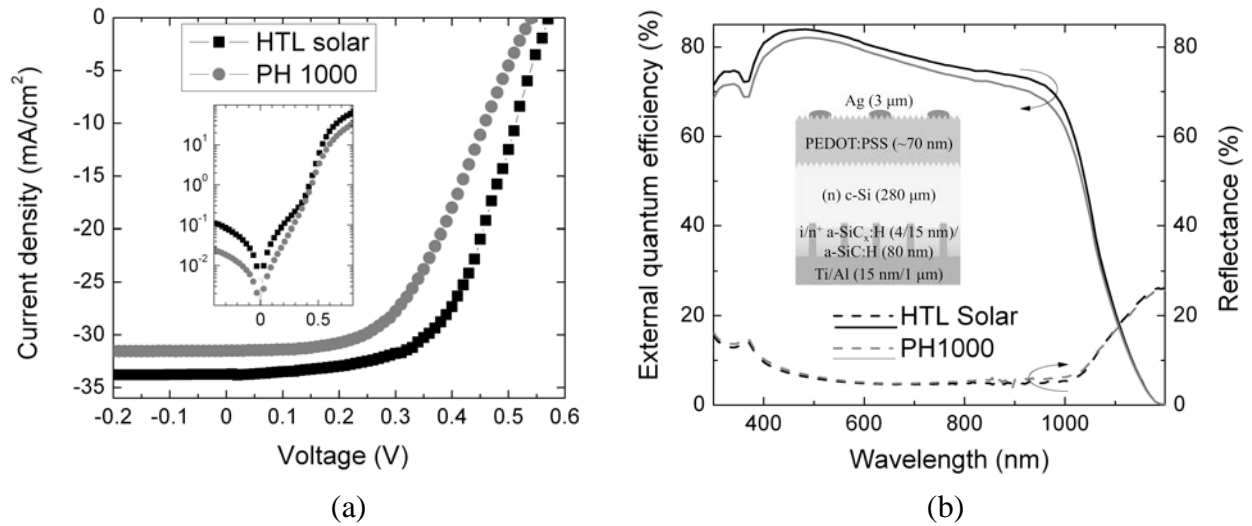


Figure 5.16 (a) Current density-voltage response of textured PEDOT:PSS/n-Si solar cells under dark (inset) and light conditions (highest efficiency devices). (b) External quantum efficiency and total reflectance.

In terms of photocurrent generation, HTL Solar achieved a  $J_{SC}$  of 33.5  $\text{mA}/\text{cm}^2$ , slightly larger than PH1000 (31.5  $\text{mA}/\text{cm}^2$ ) and confirmed by the external quantum efficiency characteristics, which follow a similar response across the whole wavelength range but vertically-shifted (Fig. 5.16b). This improvement can be partially explained by HTL Solar's higher transparency (Fig. 4.28a), although lower front recombination losses can also account for the observed vertical-shift. Table 5.4 summarizes the measured PEDOT:PSS/n-Si solar cell performance parameters.

Table 5.4 Performance parameters for PEDOT:PSS/n-Si devices on a textured substrate (4 device average).

PEDOT:PSS/n-Si	$V_{OC}$ mV	$J_{SC}$ $\text{mA}/\text{cm}^2$	$FF$ %	$PCE$ %	$J_{01}$ $\text{mA}/\text{cm}^2$	$n_1$	$R_S$ $\Omega\cdot\text{cm}^2$	$R_P$ $\text{k}\Omega\cdot\text{cm}^2$
HTL Solar	564 $\pm 6$	33.3 $\pm 0.1$	60.0 $\pm 0.9$	11.3 $\pm 0.3$	$1.4 \times 10^{-7}$	1.15	3.4	3.5
PH1000	541 $\pm 5$	31.3 $\pm 0.2$	48.2 $\pm 1.4$	8.2 $\pm 0.4$	$3.2 \times 10^{-6}$	1.3	6.8	15

---

## 5.3 References

- [1] W. Wu, J. Bao, X. Jia, Z. Liu, L. Cai, B. Liu, et al., Dopant-free back contact silicon heterojunction solar cells employing transition metal oxide emitters, *Phys. Status Solidi - Rapid Res. Lett.* **10** (2016) 662–667.
- [2] M. Bivour, J. Temmler, F. Zähringer, S. Glunz, M. Hermle, High work function metal oxides for the hole contact of silicon solar cells, in: 43rd Photovolt. Spec. Conf., IEEE, Portland, OR, USA, 2016: pp. 1–6.
- [3] A.B. Morales Vilches, Desarrollo de tecnologías de baja temperatura para la fabricación de células solares de heterounión de silicio. PhD Thesis., Universitat Politècnica de Catalunya, 2015.
- [4] M. Boccard, L. Ding, P. Koswatta, M.I. Bertoni, Z. Holman, Evaluation of metal oxides prepared by reactive sputtering as carrier-selective contacts for crystalline silicon solar cells, in: 42nd Photovoltaics Spec. Conf., IEEE, New Orleans, LA, USA, 2015: pp. 1–3.
- [5] J. Ziegler, M. Mews, K. Kaufmann, T. Schneider, A.N. Sprafke, L. Korte, et al., Plasma-enhanced atomic-layer-deposited MoOx emitters for silicon heterojunction solar cells, *Appl. Phys. A.* **120** (2015) 811–816.
- [6] M. Mews, L. Korte, B. Rech, Oxygen vacancies in tungsten oxide and their influence on tungsten oxide/silicon heterojunction solar cells, *Sol. Energy Mater. Sol. Cells.* **158** (2016) 77–83.
- [7] S.M. Sze, K.K. Ng, Physics of semiconductor devices, 3rd ed., Wiley, Hoboken, NJ, 2007.
- [8] T.F. Schulze, L. Korte, E. Conrad, M. Schmidt, B. Rech, T.F. Schulze, et al., Electrical transport mechanisms in a-Si:H/c-Si heterojunction solar cells, *J. Appl. Phys.* **107** (2010) 23711.
- [9] R. Garcia-Hernansanz, E. Garcia-Hemme, D. Montero, J. Olea Ariza, A. del Prado Millan, I. Martil de la Plaza, et al., Transport mechanisms in silicon heterojunction solar cells with molybdenum oxide as hole transport layer, *Prog. Photovoltaics Res. Appl.* (2017) Under review.
- [10] D. Pysch, A. Mette, S.W. Glunz, A review and comparison of different methods to determine the series resistance of solar cells, *Sol. Energy Mater. Sol. Cells.* **91** (2007) 1698–1706.
- [11] M.J. Kerr, A. Cuevas, R.A. Sinton, Generalized analysis of quasi-steady-state and transient decay open circuit voltage measurements, *J. Appl. Phys.* **91** (2002) 399–404.
- [12] O. Almora, L.G. Gerling, C. Voz, R. Alcubilla, J. Puigdollers, G. Garcia-Belmonte, Superior performance of V2O5 as hole selective contact over other transition metal oxides in silicon heterojunction solar cells, *Sol. Energy Mater. Sol. Cells.* **168** (2017) 221–226.
- [13] J. Geissbühler, J. Werner, S. Martin de Nicolas, L. Barraud, A. Hessler-Wyser, M. Despeisse, et al., 22.5% efficient silicon heterojunction solar cell with molybdenum oxide hole collector, *Appl. Phys. Lett.* **107** (2015) 81601.
- [14] M. Bivour, J. Temmler, H. Steinkemper, M. Hermle, Molybdenum and tungsten oxide: High work function wide band gap contact materials for hole selective contacts of silicon solar cells, *Sol. Energy Mater. Sol. Cells.* **142** (2015) 34–41.
- [15] J. Bullock, M. Hettick, J. Geissbühler, A.J. Ong, T. Allen, C.M. Sutter-Fella, et al., Efficient silicon solar cells with dopant-free asymmetric heterocontacts, *Nat. Energy.* (2016) 15031.
- [16] J. Werner, J. Geissbuhler, A. Dabirian, S. Nicolay, M. Morales Masis, S. De Wolf, et al., Parasitic absorption reduction in metal oxide-based transparent electrodes: application in perovskite solar cells, *ACS Appl. Mater. Interfaces.* **8** (2016) 17260–17267.
- [17] B. Demarex, S. De Wolf, A. Descoedres, Z. Charles Holman, C. Ballif, Damage at hydrogenated amorphous/crystalline silicon interfaces by indium tin oxide overlayer sputtering,

- Appl. Phys. Lett.* **101** (2012) 171604.
- [18] C.G. Granqvist, Handbook of inorganic electrochromic materials, 2nd ed., Elsevier, Amsterdam, Netherlands, 2002.
- [19] P.A. Basore, Extended spectral analysis of internal quantum efficiency, in: 23rd Photovolt. Spec. Conf., Louisville, KY, USA, 1993: pp. 147–152.
- [20] L. Barraud, Z.C. Holman, N. Badel, P. Reiss, A. Descoeur, C. Battaglia, et al., Hydrogen-doped indium oxide/indium tin oxide bilayers for high-efficiency silicon heterojunction solar cells, *Sol. Energy Mater. Sol. Cells.* **115** (2013) 151.
- [21] K. Sun, S. Zhang, P. Li, Y. Xia, X. Zhang, D. Du, et al., Review on application of PEDOTs and PEDOT:PSS in energy conversion and storage devices, *J. Mater. Sci. Mater. Electron.* **26** (2015) 4438–4462.

## 6 Conclusions and future outlook

*This final chapter summarizes the main findings of this thesis work, resulting in an overall understanding of the properties and working principles of TMO/n-Si heterojunctions and their application into novel solar cell devices.*

### 6.1 Conclusions

At the beginning of this thesis work, the conception of the TMO/n-Si heterojunction idea was inspired by a simplified solar cell design that incorporates a photovoltaic absorber (c-Si) and two carrier-selective contacts for the collection and extraction of electrons and one for holes. In this simple model, electron/hole separation occurs via conductivity gradients at each selective contact. Then, if all other design parameters are optimal, conversion efficiencies are completely determined by the contact resistance ( $\rho_c$ ) and the recombination current ( $J_0$ ). In light of this view, a new wave of novel passivating and/or carrier-selective materials has arisen in the past three years, achieving an equal or superior performance than their doped counterparts. These materials, which include transition metal oxides (TMOs), conductive polymers and alkaline-earth salts, have addressed some of the limitations found in conventional c-Si technologies, including energy-intensive fabrication processes, Auger-limited recombination in highly doped layers and parasitic absorption by narrow  $E_{gap}$  materials. In this thesis, these and other concerns were thoroughly investigated by use of dopant-free/wide band gap ( $E_{gap} > 3$  eV) TMO thin films, whose passivating properties and large work function values ( $\Phi_{TMO} > 5$  eV) allow their use as passivating/hole-selective contacts in n-type c-Si solar cells.

#### 6.1.1 Material characterization

First, the suitability of the three studied TMOs ( $V_2O_5$ ,  $MoO_3$  and  $WO_3$ ) as hole-selective contacts was discussed in terms of their work function, conductivity and energy band gap. From XPS analyses of thermally evaporated TMOs thin films, oxygen deficient stoichiometries of  $VO_{x-2.3}$  and  $MoO_{x-2.5}$  were determined along with moderate concentrations of reduced cation species ( $V^{+4}$ ,  $Mo^{+5}$ ), whereas  $WO_{x-3.2}$  was found to be over-stoichiometric. These oxygen vacancies, which provide the n-type semiconductive character to TMOs and may play an important role in

carrier conduction, were also inferred from the presence of mid-gap defect states located at photoelectron binding energies of  $\sim 1$  eV. In parallel, optical transmittance measurements by UV-VIS spectrophotometry showed an absorption onset at  $\sim 400$  nm for the three oxides as well as  $E_{gap}$  values of 2.5–3.1 eV, confirming that reduced absorption losses could be achieved in comparison to a-Si:H window layers (absorption onset  $\sim 600$  nm,  $E_{gap} \sim 1.7$  eV). This could translate into short-circuit current gains of  $\sim 1.6$  mA/cm<sup>2</sup> in the 400–600 nm range, as determined from ray-tracing optical simulations.

The electric characterization by TLM measurements of TMO thin films (50 nm) deposited on glass showed them to be quasi-insulating, with sheet resistance values  $R_{sh} \sim 10^{10}$   $\Omega/\square$ . Yet, 20 nm films deposited on n-Si exhibited an  $R_{sh} \sim 10, 20$  and  $1,600$  k $\Omega/\square$  for V<sub>2</sub>O<sub>x</sub>, MoO<sub>x</sub> and WO<sub>x</sub> respectively. Given that the n-Si substrate (1.2  $\Omega\cdot\text{cm}$ ) had a characteristic  $R_{sh} \sim 40$   $\Omega/\square$ , it seemed clear that carrier transport was confined to an inversion layer induced at the n-Si surface, also inferred from the large work difference  $\Phi_{TMO} - \Phi_{n-Si}$  and the resulting built-in voltage under equilibrium. This TMO-induced p<sup>+</sup>/n-Si junction can then explain the hole-selectivity in this type of heterojunctions. Likewise, the specific contact resistance  $\rho_c$  between Au/TMO/p<sup>+</sup>IL was also obtained from the TLM data, yielding  $\sim 110, \sim 370$  and  $\sim 670$  m $\Omega\cdot\text{cm}^2$  for V<sub>2</sub>O<sub>x</sub>, MoO<sub>x</sub> and WO<sub>x</sub> respectively (similar to other passivating/selective contacts reported in the literature. Another important finding was the rapid degradation of the electric properties at temperatures  $\geq 150$  °C, being incompatible with industrial annealing processes (T >400 °C).

Next, the passivation properties of TMO thin films (20 nm) on n-Si were determined from quasi-steady-state photoconductance measurements on symmetric TMO/n-Si/TMO structures (planar substrates), obtaining implied- $V_{OC}$  ( $J_0$ ) values of 671 (130), 655 (230) and 553 (3,600) mV (fA/cm<sup>2</sup>) for V<sub>2</sub>O<sub>x</sub>, MoO<sub>x</sub> and WO<sub>x</sub> respectively. Even though these values were lower than reported passivated TMO/a-Si:H/n-Si contacts ( $i-V_{OC} > 700$  mV), such level of passivation is moderately high considering the simplicity of the deposition process (thermal evaporation upon an ambient temperature substrate). Passivation was found to be independent of oxide thickness (5–80 nm range) but it showed a strong degradation under air exposure (V<sub>2</sub>O<sub>x</sub> case). Passivation was also affected by UV-luminescence from the ITO sputtering process, where the strongest degradation occurred for the thinnest films (<10 nm) and/or the more conductive ITO layers ( $R_{sh} < 110$   $\Omega/\square$ ). Additional passivating interlayers including  $\sim 4$  nm intrinsic a-SiC<sub>x</sub>:H (deposited by PECVD) and  $< 2$  nm SiO<sub>x</sub> (chemically grown by HNO<sub>3</sub>, UVO and RCA2 oxidation) were also

tested but not evident improvement in passivation was obtained. This might be due to low hydrogen content in our a-SiC<sub>x</sub>:H films (needing higher thicknesses, as with the rear 20 nm i/n<sup>+</sup> a-SiC<sub>x</sub>:H contacts), or to the absence of reduced cation species generated by charge transfer upon heterojunction formation.

In addition to transition metal oxides, two p-type polymer PEDOT:PSS solutions (HTL Solar and PH1000) were also characterized for determining their optoelectronic and passivation properties. After preconditioning treatments with surfactant and conductivity additives, TLM measurements of Ag/PEDOT:PSS on glass showed PH1000 ( $R_{sh} \sim 120 \Omega/$  ) was slightly more conductive than HTL Solar ( $R_{sh} \sim 190 \Omega/$  ), in accordance to the lower content of insulating PSS material (as determined from XPS analyses). Since both materials had a sheet resistance similar to ITO and a moderate transmittance (90% at 600 nm), they could be used as hole-selective transparent conductive electrodes in an ITO-free device. In terms of contact resistance and passivation, HTL Solar had a much lower contact resistance and a higher passivation quality ( $\rho_c \sim 0.03 \Omega \cdot \text{cm}^2$ ,  $i-V_{OC} \sim 644 \text{ mV}$  on planar substrates) than PH1000, probably related to a better wettability of the c-Si surface (as determined from contact angle measurements).

### 6.1.2 Heterojunction physics

From the above results, it was evident that V<sub>2</sub>O<sub>x</sub>/n-Si contacts (followed by MoO<sub>x</sub> and WO<sub>x</sub>) showed superior electric and passivation properties. Whereas larger conductivity values can be explained by the higher oxygen deficiency (as determined by XPS), higher  $i-V_{OC}$  values are a function of two separate contributions: (1) chemical passivation of surface dangling bonds, and (2) ‘field-effect’ passivation, characterized by large built-in potentials and highly inverted surfaces (both a function of the work function difference  $\Phi_{TMO} - \Phi_{nSi}$  and on the degree of Fermi level pinning). On the one hand, chemical passivation was inferred from HR-TEM imaging, which revealed the presence of a 1.9–2.6 nm layer in the TMO/n-Si interface, amorphous in nature and very uniform in thickness. A dynamic ToF-SIMS analysis of such interlayer showed a strong SiO<sub>x</sub> signal as well as reduced cation peaks (V<sup>+4</sup>, Mo<sup>+5</sup>, W<sup>+5</sup>), suggesting a chemical reaction had taken place between c-Si and the TMOs. This chemical reaction could be driven by thermodynamically favorable conditions (i.e. a negative Gibbs energy of reaction) in addition to electron transfer from c-Si to the TMO. Likewise, Si–H and Si–OH species were also identified from a static ToF-SIMS analysis, confirming that hydrogen species also passivate the c-Si



surface. The approximate stoichiometry of this interlayer was established at  $\text{SiO}_{x-1.5}$ , as determined from the XPS binding energy of Si  $2p^{3/2}$  peaks, whereas reduced cation species were more abundant near the reactive interface, gradually decreasing until reaching a steady bulk concentration.

On the other hand, ‘field-effect’ passivation was also deduced from chemical shifts in the XPS data. Specifically, the  $\text{Si}^0$  peak shifted to lower binding energies, a clear indication of band bending and of charge transfer occurring across the interface. Given that the large work function difference  $\Phi_{\text{TMO}} - \Phi_{\text{nSi}}$  can only be partially allocated as ionized donor charges in the n-Si bulk (up to a  $V_{bi} \sim 0.7$  V, limited by strong inversion conditions), the rest of the charge is most probably distributed in a negative interfacial dipole of magnitude  $\Delta_d = qV_{bi} - \Delta\Phi$ , as recently confirmed by other authors. In terms of carrier conduction across the  $\text{SiO}_x$  interlayer, which is thicker than the tunneling limit of  $\sim 2$  nm, it is possible that oxygen vacancies and mid-gap states facilitate carrier transport via hopping mechanisms. Similarly, carrier conduction in the n-type TMO bulk can also be explained by electron hopping between low- and high-valence cation species. Regarding the apparent paradox in hole extraction through an n-type TMO, it could be interpreted as an  $n^+/p^+$  tunneling diode, frequently used in tandem solar cells.

A compilation of the  $\rho_c$  and  $J_0$  parameters obtained for the hole-selective materials under study is presented in Fig. 6.1 (previously shown in Fig. 2.14), which shows the optimized contacted area fractions and the resulting theoretical conversion efficiency<sup>[1]</sup> for each experimental  $\rho_c$ - $J_0$  pair (white diamonds), along with the corresponding selectivity  $S_{I0} = kT/(\rho_c J_0)$ . As a reference, values reported in the literature are also shown (dark circles), including similar Pd/MoO<sub>x</sub> contacts<sup>[2]</sup> and industry-standard approaches like Al-fired BSF<sup>[3]</sup>, PH<sub>3</sub> diffusion<sup>[3]</sup> and (p) a-Si:H<sup>[4]</sup>. First, we note that V<sub>2</sub>O<sub>x</sub> had the highest selectivity ( $S_{I0} = 12.3$ ) compared to the other TMOs ( $S_{I0} = 11.5$ – $12.1$  for MoO<sub>x</sub>,  $S_{I0} = 10.0$  for WO<sub>x</sub>). As a result, a V<sub>2</sub>O<sub>x</sub>/n-Si device could reach a conversion efficiency of  $\sim 25.0\%$  for a contacted area fraction  $f_c \sim 0.4$ , a perfectly viable strategy with the current PERC/IBC technology. This is not the case for standard Al-fired BSF

<sup>[1]</sup> Simulation data obtained from the original source: J. Bullock *et al.*, Amorphous silicon enhanced metal-insulator-semiconductor contacts for silicon solar cells, *J. Appl. Phys.* **116** (2014) 163706.

<sup>[2]</sup> J. Bullock *et al.*, Molybdenum oxide MoO<sub>x</sub>: a versatile hole contact for Si solar cells, *Appl. Phys. Lett.* **105** (2014) 232109.

<sup>[3]</sup> R. Brendel, R. Peibst, Contact selectivity and efficiency in c-Si photovoltaics, *IEEE J. Photovoltaics.* **6** (2016) 1413–1420

<sup>[4]</sup> K. Yoshikawa *et al.*, Silicon heterojunction solar cell with interdigitated back contacts for a photoconversion efficiency over 26%, *Nat. Energy.* **2** (2017) 17032.

contacts, which despite their larger selectivity ( $S_{10} = 13.0$ ) they require a smaller contact fraction  $f_c \sim 0.03$  in order to achieve a similar efficiency. Also note that, until now, only a-Si:H technology is able to utilize full-area contacts and maintain a high efficiency (as in HIT solar cells), a consequence of its extremely low  $J_0 < 10 \text{ fA/cm}^2$ . It then follows that prospective TMO/n-Si devices with full-area contacts would require sufficiently lower  $J_0 < 30 \text{ fA/cm}^2$  and  $\rho_c < 0.1 \text{ } \Omega\text{-cm}^2$  values in order to surpass the 26% barrier. Regarding the HTL Solar PEDOT:PSS contact, a very good selectivity value ( $S_{10} = 12.6$ ) was obtained, with a potential maximum efficiency of 25.1% for a contact fraction  $f_c \sim 0.2$ , although recent demonstrations<sup>[5]</sup> on full-area rear contacted configurations have a similar efficiency potential.

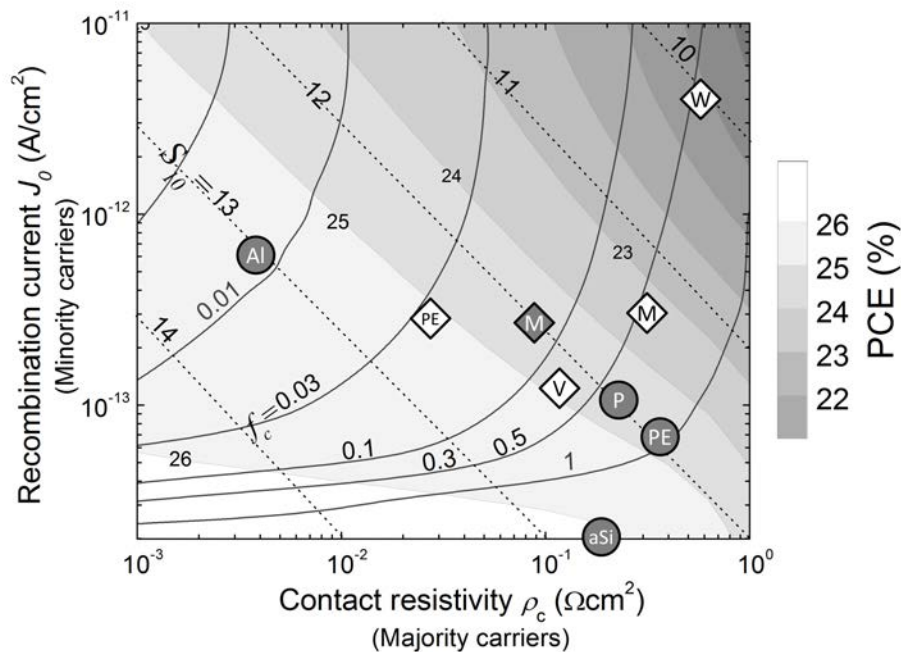


Figure 6.1 Summary of the recombination current ( $J_0$ ) and contact resistance ( $\rho_c$ ) values obtained in this thesis for the different TMO (V, M, W) and PEDOT:PSS (PE) junctions (white diamonds), showing the optimized contacted area fraction  $f_c$ , the resulting conversion efficiency and the iso-selectivity lines  $S_{10}$ . As a reference (dark circles), reported values for  $\text{MoO}_x$ , PEDOT:PSS and various standard contacts (Al BSF,  $\text{PH}_3$  diffusion and p a-Si:H) are also shown.

### 6.1.3 c-Si heterojunction solar cells

Finally, the characterized TMO/n-Si heterojunctions were implemented as hole-selective contacts in complete solar cell devices, using 15 nm TMO films contacted by 80 nm ITO transparent conductive electrodes and a Ag finger grid (4.3% shadow). As rear electron contacts, two different strategies were tested: (1) laser-doped ( $i/n^+$ ) a-SiC<sub>x</sub>:H point contacts ( $f_c = 2.4\%$ )

<sup>[5]</sup> D. Zielke *et al.*, Organic-silicon heterojunction solar cells on n-type silicon wafers: The BackPEDOT concept, *Sol. Energy Mater. Sol. Cells.* **131** (2014) 110–116.

with a-SiC:H back reflector and Ti/Al electrode; (2) full area (i/n<sup>+</sup>) a-SiC<sub>x</sub>:H contact, with ITO collector/back reflector and Ag electrode. To begin with, a comparative study was performed utilizing the laser-doped rear contact strategy, obtaining maximum conversion efficiencies of 15.7% (V<sub>2</sub>O<sub>x</sub>), 13.5% (MoO<sub>x</sub>) and 12.5% (WO<sub>x</sub>) for front-textured substrates. The main contributing factor to the measured efficiencies was the open-circuit voltage, with an average  $V_{OC}$  of 602 (V<sub>2</sub>O<sub>x</sub>), 567 (MoO<sub>x</sub>) and 554 (WO<sub>x</sub>) mV, in agreement with the implied- $V_{OC}$  values previously determined from lifetime measurements. Similarly, fill factor values were in agreement with the observed contact resistivity trend previously determined from TLM measurements, with average  $FF$ s of 73.6% (V<sub>2</sub>O<sub>x</sub>), 68.7% (MoO<sub>x</sub>) and 65.0% (WO<sub>x</sub>). Suns- $V_{OC}$  measurements yielded pseudo- $FF$  values as high as 81.1%, a proof of the excellent diode quality obtained by TMO-induced p<sup>+</sup><sub>IL</sub>/n-Si junctions. This is also confirmed by the large break-down voltages (down to -95 V) attained under large reverse bias, a rather high value considering the thinness of the p<sup>+</sup> inversion layer (<3 nm).

Regarding the short-circuit currents, average  $J_{SC}$  values of 33.9 (V<sub>2</sub>O<sub>x</sub>), 33.3 (MoO<sub>x</sub>) and 33.9 (WO<sub>x</sub>) mA/cm<sup>2</sup> were obtained. By comparing the external quantum efficiency response of each TMO/n-Si solar cell with a reference a-SiC<sub>x</sub>:H stack (20 nm), a  $J_{SC}$  gain of ~1.2 mA/cm<sup>2</sup> was calculated for the 300–550 nm wavelength range, directly attributed to the difference in optical band gaps ( $E_{gap}$  ~1.7 and >2.5 eV for a-Si:H and TMOs respectively). Despite these gains, TMOs exhibited strong sub-band gap absorption at 600 nm and above, related to the appearance of color centers after ITO sputtering. A mild annealing treatment at T = 160 °C showed a minor increase of the surface passivation (V<sub>2</sub>O<sub>x</sub> and WO<sub>x</sub> cases) but a strong degradation of the  $FF$  by a marked S-shaped  $J(V)_{light}$  curve, an indication of hole blocking behavior.

An analysis of the diffusion and recombination saturation currents ( $J_{01}$  and  $J_{02}$ ), extracted from  $J(V)_{dark}$  diode fittings in the 300–370 K range, revealed each had an activation energy  $E_{a1} \approx E_{gap}$  and  $E_{a2} \approx \frac{1}{2}E_{gap}$ , confirming that p<sup>+</sup><sub>IL</sub>/n-Si induced junctions can be described by the classic p/n junction theory, where diffusion of minority carriers is the dominant transport mechanism at forward voltages >0.4 V. This is further supported by the capacitance-voltage  $1/C^2(V)$  characteristic (as measured by impedance spectroscopy), where the typical linear response for c-Si is obtained, i.e. a slope proportional to the substrate doping and a x-axis intercept equal to the built-in voltage of the junction, with  $V_{bi}$  values of 617, 600 and 510 mV for the V<sub>2</sub>O<sub>x</sub>, MoO<sub>x</sub> and WO<sub>x</sub> textured devices.

From the obtained solar cell results, it was found that the  $V_{OC}$  (passivation) and  $J_{SC}$  (current collection) were being limited by the laser-doped rear surface, which is heavily damaged during the laser process. Therefore, solar cell devices with the alternative (i/n<sup>+</sup>) a-SiC<sub>x</sub>:H/ITO/Ag rear contact were fabricated, resulting in an immediate boost of the  $V_{OC}$  to 661 (planar) and 640 mV (textured substrate), attributed to a three-fold increase of the effective diffusion length. Likewise,  $J_{SC}$  increased to 37.6 mA/cm<sup>2</sup>, mostly due to an improved EQE response at 800 nm and above. This led to a champion conversion efficiency of 16.5% and a pseudo-efficiency of 18.8% (from Suns- $V_{OC}$  measurements). A  $1/C^2(V)$  plot confirmed a built-in voltage of  $V_{bi} \sim 712$  mV, slightly larger than the surface potential under strong inversion conditions  $\phi_s \approx V_{bi} > 2(\frac{1}{2} E_{gap} - E_{Fn})$ .

As for the PEDOT:PSS/n-Si devices, conversion efficiencies of 11.6% and 8.5% for were obtained for the HTL Solar and PH1000 solutions respectively. Despite the promising contact resistance and saturation current values previously obtained, the solar cells suffered from low  $V_{OC}$  (569–545 mV) and  $FF$  (61–50%) values, explained by an uneven coverage of the random pyramids. Also, these devices were severely limited by rear laser-doped contact, whose substitution by the rear-ITO strategy should result in large efficiency improvements.

## 6.2 Future work and scientific relevance

It is worth mentioning some unexplored aspects that could be addressed in the near future. To begin with, an unambiguous determination of the effective TMO work function on the c-Si surface is of utmost importance, as well as understanding its dependence on surface reactivity, film composition and deposition methods (for example, via ultraviolet photoelectron spectroscopy<sup>[6]</sup> or Kelvin-probe microscopy). This could also help determining the magnitude of the interfacial dipole, if it is located in the TMO or in SiO<sub>x</sub> interlayer, and possible tuning strategies to maximize the built-in potential of the heterojunction. Also, more understanding is needed on the variability of the optoelectronic properties under redox environments, exploring feasible ways to control the concentration of oxygen vacancies.

---

<sup>[6]</sup> T. Sun *et al.*, Investigation of MoOx/n-Si strong inversion layer interfaces via dopant-free heterocontact, *Phys. Status Solidi*. (2017) 1700107.

Future work should also explore the possibility of tuning the SiO<sub>x</sub> interlayer properties, during or after its formation, increasing passivation to  $V_{OC} > 700$  mV. Similarly, more work should be done on passivation interlayers other than (i) a-Si:H, focusing on ultrathin SiO<sub>2</sub> films deposited by inexpensive ambient pressure procedures and the inclusion of atomic hydrogen by H<sub>2</sub> plasma or forming gas annealings.

A frequently expressed concern is the occurrence of electrochromism in the studied TMOs, an undesired effect if intended to be used as solar cell materials with stable optics. Even though electrochromism makes use of specific chemistries and device structures (see Appendix B), no studies exist reporting this effect on TMO/c-Si devices. Also, it would be worth studying the possibility of hydrogen- or lithium-doped TMOs in order to increase their conductivity or passivation, as long as coloration and electrochromic effects are minimum. Finally, one of the attractive features of TMO materials is their deposition by solution processes amply documented in organic photovoltaics but relatively new in c-Si solar cells<sup>[7]</sup>. Then, realistic energy and cost savings could be achieved by this kind of ambient-temperature and ambient-pressure processes.

Finally, after having reviewed the main experimental results, it can be acknowledged that each of the thesis objectives stated in the introduction was successfully achieved, emphasizing four main contributions made to the photovoltaic research field:

- 1) The determination of the optoelectronic properties of V<sub>2</sub>O<sub>5</sub>, MoO<sub>3</sub> and WO<sub>3</sub> in the context of c-Si photovoltaics (passivation and contact resistance).
- 2) The elucidation of the physics behind the induced p<sup>+</sup>/n junction and its operation as a solar cell, supported by a thorough study of the TMO/c-Si interface.
- 3) The demonstration of dopant-free passivating/hole-selective contacts in heterojunction solar cells, completely fabricated at temperatures below 300 °C and with potential conversion efficiencies above 19%.
- 4) The high level of novelty and innovation, contributing to one of the most relevant research topics in c-Si photovoltaics.

---

<sup>[7]</sup> A.J. Tong *et al.*, Solution-processed Molybdenum Oxide for Hole-selective Contacts on Crystalline Silicon Solar Cells, *Appl. Surf. Sci.* 423 (2017) 139-146.

## Appendix

### A Cost and environmental assessment of c-Si solar cells

Any time a PV technology improvement is reported, as in the case of TMO/c-Si and PEDOT:PSS/c-Si heterojunctions, most of the arguments in favor go along the lines of: (1) fewer materials consumption, not only of the absorber material (as in thin-films) but also of expensive/scarce consumables (e.g. silver pastes); (2) less energy-intensive processes, with low temperature ( $T < 100$  °C) and vacuum-free steps; (3) lower environmental impact, a direct consequence of (2) but also related to toxic emissions and waste disposal; and (4) lower risk and improved safety, avoiding the use of flammable, toxic or corrosive materials.

More than often, the ultimate justification for technology changes is economical (points 1 and 2), although some other factors like product differentiation, energy consumption and environmental impact also drive technology improvements. In order to quantify these factors in a consistent manner, the following measures can be used for PV assessment:

- Production cost ( $\text{€/W}_{\text{peak}}$ ): reductions in cost are the fundamental motivation of thin-film PV, considering that c-Si wafer processing amounts for 35–50% of the final module cost [1,2] and 75% of the module production energy [3]. However, capital costs of utility scale plants are very similar for both technologies ( $\sim 0.5 \text{ €/W}_{\text{peak}}$ ) [4]. The Balance of System (BOS), which includes the inverter, mounting and cabling costs, can increase the installation cost from 0.6 to 1.2  $\text{€/W}_{\text{peak}}$ .
- Levelized Cost of Energy (LCOE): used as a measure of unit cost of electricity ( $\text{€/kWh}$ ), it accounts for the total unsubsidized costs incurred during the system lifetime ( $t$ ) divided by the total energy output ( $E_{\text{out}}$ ) under a particular solar irradiation:

$$LCOE = \sum_{t=1}^n \frac{I_t + OM_t + F_t}{(1+r)^t} \bigg/ \sum_{t=1}^n \frac{E_{\text{out}}}{(1+r)^t} \quad \text{Eq. (A1)}$$

Besides from the capital cost ( $I$ ) and interest rates ( $r$ ), PV has minimum operation/maintenance costs ( $OM$ ) and zero fuel charges ( $F$ ), leading to competitive energy prices of  $\sim 0.05$  €/kWh against coal and gas (0.05–0.21 €/kWh).

- Energy Pay-Back Time (EPBT): a measure of how many years it takes for a technology to overcome the energy consumed during its lifetime ( $E_{in}$ ):

$$EPBT = \frac{E_{in}}{E_{out}/year} \quad \text{Eq. (A2)}$$

This analysis requires a systematic calculation of the embodied energy (or cumulative energy demand) for every step of the life-cycle, including raw materials, manufacturing, installation, operation and decommissioning. For c-Si, EPBT ranges from 1.2 (multi) to 1.9 (mono) years, while for thin-film PV it ranges from 0.7 (CdTe) to 1.4 (a-Si:H) years, a consequence of lower material utilization [3].

- Carbon footprint, a similar analysis to the EPBT but in terms of CO<sub>2</sub> emissions or its equivalent. Reported carbon footprint are 50–80 g CO<sub>2</sub>-eq/kWh for c-Si and 15–45 g CO<sub>2</sub>-eq/kWh for thin films, both an order of magnitude lower than fossil fuel sources (640–1080 g CO<sub>2</sub>-eq/kWh) [3]. On the other hand, the toxicity of raw materials (Cd) or their scarcity on Earth (Ag, In) are also quantified by other environmental factors (ecotoxicity, abiotic depletion), imposing severe limitations to mass development.
- Finally, power conversion efficiencies (PCE) are of utmost importance since they determine the energy output used to evaluate the LCOE, EPBT and the carbon footprint.

In general, for equal industrialization stages and similar efficiencies at the module level, thin-film PV could have lower production and deployment costs than c-Si as a result of reduced raw materials utilization. Also, the environmental impact and EPBT are shorter for thin-film PV, especially when energy-intensive processes are avoided. However, the cumulative production of c-Si is currently 10 times larger than thin-film, resulting in very similar module prices for both technologies (see experience curve in Fig. A.1) [5]. In terms of LCOE prices, c-Si is slightly more competitive than thin-film only by a small margin ( $< 10$  ¢€/kWh) [4], while record auction prices of 0.03 €/kWh belong to c-Si (utility scale installations). With such low module and energy prices, it is no surprise that company profits (and consequently, the PV market as a whole) could become financially unsustainable [6,7].

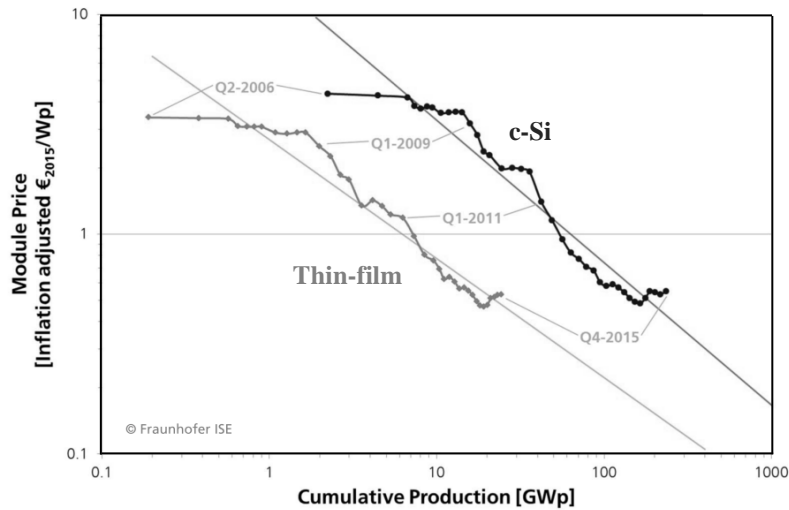


Figure A.1 Evolution of module price with global cumulative production (experience curve). Adopted from [5].

Regarding TMO/c-Si and PEDOT:PSS/c-Si heterojunctions, a reduction of the input energy during fabrication is possible if low-temperature and/or vacuum-free conditions are implemented. Although it was not possible to perform a detailed life-cycle analysis for these heterojunctions, a comparison with the thermal diffusion<sup>1</sup> and PECVD<sup>2</sup> standard processes can be done, considering an hypothetical TMO deposition processes by ALD<sup>3</sup> at ambient conditions, i.e.  $T \sim 25$  °C and atmospheric pressure [8]. In this example, changes to the cumulative energy demand (CED, in Joules/cell) will be only defined by differences in the processing conditions of the selective contacts (excluding the rest of the solar cell processing steps, i.e. texturing, ARC/TCO layers and metallization).

Table A.1 summarizes the expected contribution to the CED for each selective-contact process, as extracted/calculated from the life-cycle inventories reported in [9,10]. By looking at the energy intensity per cell (in mega-joules of primary energy MJ<sub>p</sub>), a gradual reduction is observed as the temperature/vacuum requirements decrease. For the diffusion and PECVD processes, the change in CED is not as large as expected for such a large difference in operation temperatures, mainly because PECVD operation is quite energy-intensive (e.g. pre-heating, vacuum, purging and chamber cleaning, etc.). However, when the electricity consumption related to vacuum/heating is removed, the CED drops more than 85% for the ALD process.

<sup>1</sup> Includes: thermal phosphorous diffusion at  $T \sim 900$  °C (front contact) plus contact firing at  $T \sim 500$  °C (rear contact).

<sup>2</sup> Includes: PECVD deposition of intrinsic/doped a-Si:H stacks (front and rear).

<sup>3</sup> Includes: ALD deposition of the hole-contact (e.g. MoO<sub>3</sub>) and the electron-contact (e.g. TiO<sub>2</sub>).



Table A.1 Contribution of the different selective-contact formation processes to the cumulative energy demand (CED) of a solar cell. Also included is the EPBT and carbon footprint at the module level.

Values extracted/calculated from [9,10].

Process (e and h selective)	Conditions	CED <sub>contribution</sub> <sup>(1)</sup> MJ <sub>p</sub> /cell	PCE %	EPBT <sup>(2)</sup> years	C <sub>footprint</sub> <sup>(2)</sup> gCO <sub>2</sub> -eq/kWh
Thermal diffusion P-doped (x1)/Al-fired (x1)	T ~900/500 °C P ~1 atm	2.5	20	1.4	31
PECVD i/doped stacks (x2)	T ~200 °C Mid-vacuum	2.3	24	1.2	25
ALD TMO (x2)	T ~25 °C P ~1 atm	0.3	20	1.4	29

<sup>(1)</sup> At the solar cell level, in mega-joules of primary energy (before conversion).

<sup>(2)</sup> At the module level, considering an irradiation of 1,700 kWh/m<sup>2</sup>-year and grid mix emissions of 530 gCO<sub>2</sub>-eq/kWh.

This drastic decrease in CED values is not as important when the rest of the solar cell components are considered, namely texturing (0.7), TCO sputtering (2.5) and metallization (1.6 MJ<sub>p</sub>/cell). Furthermore, the overall analysis at the module level (including Si feedstock, wafering, cell processing, module processing and balance-of-system BOS) reduces the solar cell contribution below 9%, dwarfing the effect of processing conditions. This is manifested in the relative constant EPBT and carbon footprint values, which are more sensitive to module efficiencies and solar irradiation regardless of cell processing conditions (Fig. A.2a,b). The same observation applies for the fabrication costs (€/W<sub>peak</sub>), with Si feedstock comprising ~46% and 29% of the cell and module costs respectively (Fig. A.2c). Therefore, any further reductions in c-Si costs would have to come necessarily from the utilization of thinner and/or kerfless wafers.

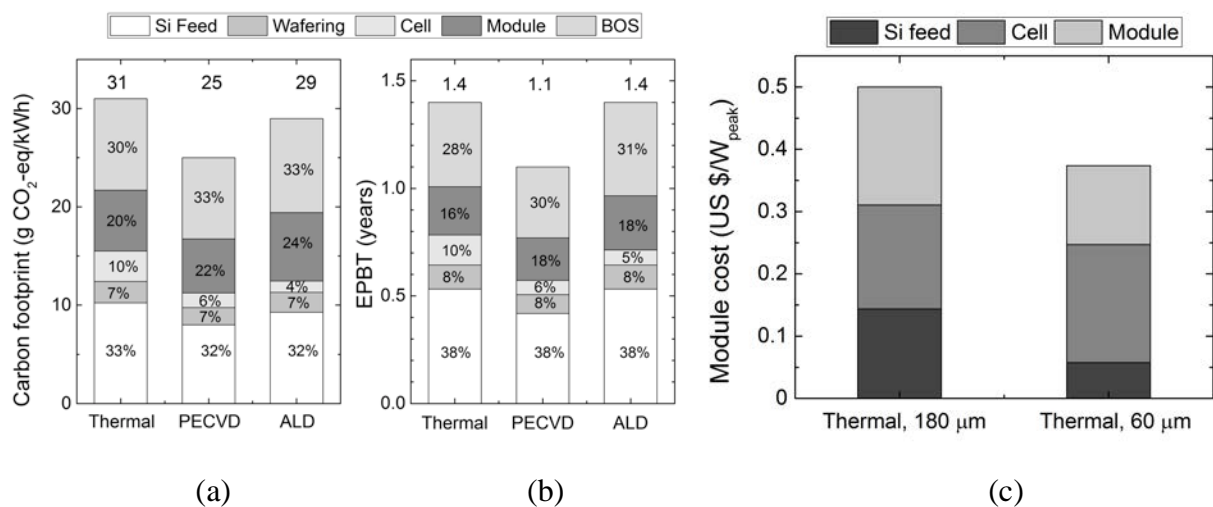


Figure A.2 (a) Energy pay-back time and (b) carbon footprint for the described selective-contact formation processes (adapted from [9]). (c) Cost components at the module level for a standard solar cell with 180 and 60 μm thick wafers (adapted from [2] for a cost of 0.5 US \$/W<sub>p</sub>).

## B Other materials tested

### B.1 NiO and ReO<sub>3</sub>

As mentioned in the main text, NiO and ReO<sub>3</sub> were partially characterized but were eventually discarded for solar cell fabrication. Beginning with ReO<sub>3</sub>, two main issues were encountered: (1) the hygroscopic nature of Re oxides led to a fast and visible degradation of the thin deposited layer, even under a N<sub>2</sub> atmosphere; (2) an unbalanced disproportionation into lower (Re<sup>+4</sup>) and higher (Re<sup>+7</sup>) valence oxides during thermal evaporation at ~400 °C [11]. This was confirmed in the XPS spectra of the Re 4*f* core level (Fig. B.1), where only the more volatile species ReO<sub>3</sub> and Re<sub>2</sub>O<sub>7</sub> were detected (the melting point of ReO<sub>2</sub> is >1,000 °C). This confirms the absence of oxygen vacancies *x* in the source material ReO<sub>3-x</sub>, while no reports exist of R<sub>2</sub>O<sub>7-x</sub> as a semiconductor material.

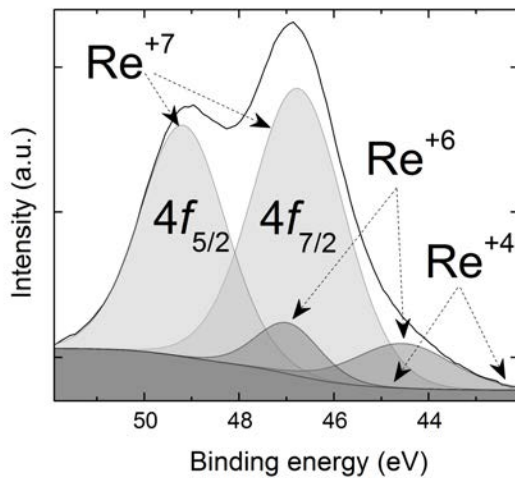


Figure B.1 XPS spectra of ReO<sub>x</sub>

Regarding NiO<sub>x</sub>, its very high melting point (1,950 °C) proved unreliable for film deposition by thermal evaporation (with other methods like sputtering and e-beam evaporation being the standard in the literature). Table B1 summarizes the cation transitions and oxygen to metal ratios as determined from the XPS spectra.

Table B.1 Binding energy (eV) of Re core levels (reflecting the M<sup>+n</sup> ↔ M<sup>-n</sup> transitions), as fitted from the XPS spectra. The relative content of M and O 1s components yield the film stoichiometry (O/M ratio).

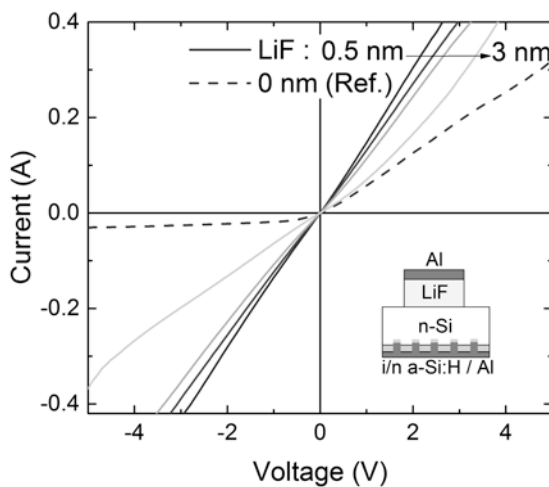
TMO	Core level peaks (eV)		Content (%)		Stoichiometry		
	Transition:	M <sup>+n</sup> ↔ M <sup>-n</sup>	M <sup>+n</sup> ↔ M <sup>-n</sup>	O 1s	O/M ratio	O content	
ReO <sub>x</sub> <sup>(1)</sup>	Re 4 <i>f</i> <sub>7/2</sub>	44.3 ( <sup>+6</sup> ) 42.5 ( <sup>+4</sup> )	0.23 0	5.95	4.5	x>>3	
	Re 4 <i>f</i> <sub>5/2</sub>	46.4 ( <sup>+7</sup> ) 44.3 ( <sup>+6</sup> )	1.13 0.23				

<sup>(1)</sup> Re<sup>+6</sup> → Re<sup>+4</sup> and Re<sup>+6</sup> → Re<sup>+7</sup>

## B.2 LiF

LiF and other similar alkali/alkaline earth compounds (MgF, KF, Cs<sub>2</sub>CO<sub>3</sub>) have recently attracted attention as electron-selective contacts for n-Si solar cells [12–15]. With an insulating nature and very large  $E_{gap}$  values >10 eV, these materials act as work function modifiers of the overlying metal (e.g. Al/LiF contact), decreasing the metal work function through the formation of an interface dipole [16]<sup>4</sup>. As a result, the Schottky barrier between c-Si and the metal is eliminated or even turned negative (i.e. an n<sup>+</sup> accumulation layer is formed), favoring electron tunneling with very low contact resistivities in the order of 10<sup>1</sup> mΩ·cm<sup>2</sup>. Similar contact qualities have also been reported for low work function alkali metals in direct contact with passivation layers, namely Mg/a-Si:H ( $\Phi_{Mg}$  ~3.7 eV) [17] and Ca/TiO<sub>2</sub> ( $\Phi_{Ca}$  ~2.9 eV) [18], indicating a similar contact-formation mechanism.

In this thesis, LiF/n-Si contacts were tested by fabricating Al/LiF/n-Si structures with variable LiF thicknesses and measuring the current-voltage response (using a laser-fired rear contact). As



seen in Fig. B.2, a Schottky-like response was obtained for the clean Al/n-Si contact, whereas a LiF film of merely 0.5 nm drastically improved the ohmic character ( $\rho_c$  ~25 mΩ·cm<sup>2</sup>) until it becomes too thick for conduction at 3 nm or more. This is in accordance with the reported optimum thickness of 0.5–1.5 nm for this kind of materials [12,13].

Figure B.2 Al/LiF/n-Si ohmic contacts for increasing LiF thickness.

In comparison to TMOs and their passivation qualities on c-Si, alkali/alkaline earth compounds do not passivate c-Si dangling bonds (see Fig. B.3a), needing additional passivation interlayers like a-Si:H [12]. In this work, the same chemical SiO<sub>x</sub> layers described in §4.4 were tested as

<sup>4</sup> In other words, these materials eliminate Fermi level pinning from the metal/Si interface, driving the index of interface behavior towards  $S_\phi \sim 1$  (Schottky limit).

passivation interlayers in Al/LiF (1 nm)/SiO<sub>x</sub>/n-Si structures, obtaining poor passivation results for all cases except for the RCA2 oxide ( $i$ - $V_{OC}$  ~600 mV). Moreover, the ohmic character of these structures was not ideal (Fig. B.3b), given the different thicknesses and stoichiometries obtained for each SiO<sub>x</sub> oxide (note for example the HNO<sub>3</sub>-grown oxide, whose high stoichiometry acts as a barrier for electron transfer).

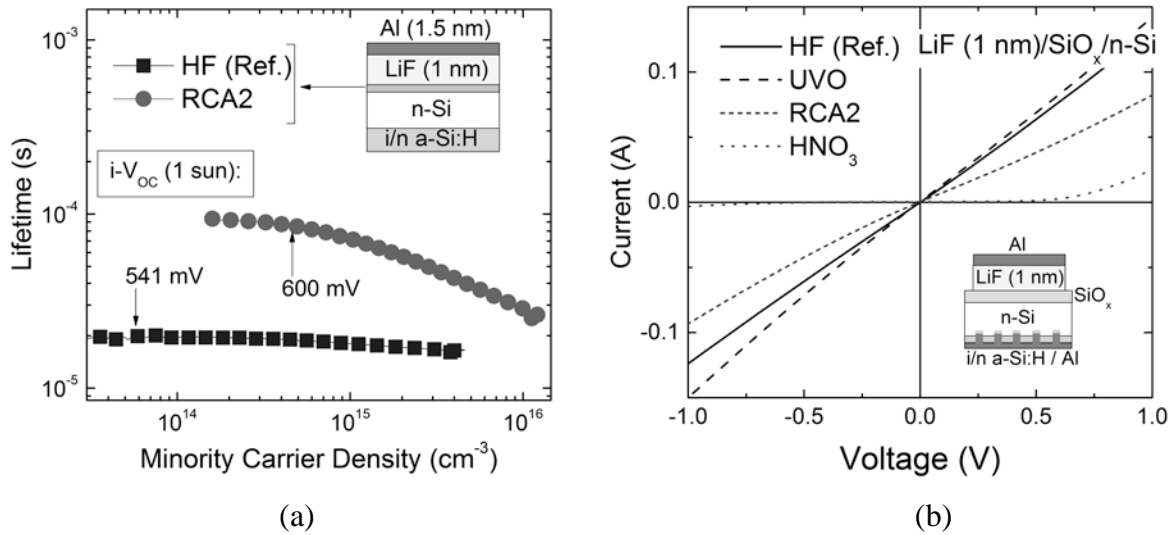


Figure B.3 (a) Lifetime measurements and (b) current-voltage response for Al/LiF (1 nm)/SiO<sub>x</sub> contacts on n-Si.

### B.3 V<sub>2</sub>O<sub>x</sub>·H<sub>2</sub>O (from solution), DBP, CuSCN and MoO<sub>3</sub> (ALD)

During the course of this thesis, additional materials and deposition processes were briefly tested as hole contacts for n-Si without significant success (based on their proven hole extraction capabilities in organic and perovskite solar cells). These materials include<sup>5</sup>: (1) V<sub>2</sub>O<sub>5</sub>·<sup>1</sup>/<sub>2</sub>H<sub>2</sub>O hydrate films deposited by spin-coating from a vanadate solution (HVO<sub>3</sub>) [19]; (2) bathocuproine (DBP) films deposited by thermal evaporation of a powder source [20]; CuSCN films deposited by spin-coating from a propylsulfide solution [21]; and (4) MoO<sub>3</sub> thin films deposited by ALD from Mo(CO)<sub>6</sub> and H<sub>2</sub>O/O<sub>3</sub> precursors at 170 °C [22]. Table B.2 summarizes the partial results obtained, where all the materials showed negligible passivation of the c-Si surface (low  $\tau_{eff}$ ) and/or poor film stability. For the case of ALD MoO<sub>3</sub>, finished devices were prepared with reasonable  $J_{SC}$  (32.8 mA/cm<sup>2</sup>) and  $FF$  (67%) values but very low  $V_{OC}$  (400 mV), in accordance with other MoO<sub>3</sub>/c-Si cells prepared by ALD [23].

<sup>5</sup> Except for DBP, cited work makes reference to the research group that deposited such materials.

Table B.2 Additional materials tested as hole-contacts for n-Si.  $\tau_{eff}$  was measured in asymmetric samples with a rear (i/n<sup>+</sup>) a-SiC<sub>x</sub>:H stack.

Material	$\tau_{eff}$ $\mu\text{s}$	Reason for failure
V <sub>2</sub> O <sub>5</sub> · 1/2H <sub>2</sub> O	<5	Uneven deposition over Si surface with 0.1% <sub>v</sub> surfactant (pinholes) Low passivation
DBP	<5	Low passivation; Degradation at 85 °C
CuSCN	~40	Marked film degradation after ITO sputtering
MoO <sub>3</sub> (ALD)	<5	Low passivation (low $V_{OC}$ ); unstable under air.

#### B.4 TMO/a-SiC<sub>x</sub>:H/n-Si contacts

As mentioned in §4.2.2, thin (~4 nm) intrinsic a-SiC<sub>x</sub>:H interlayers were implemented in TMO/a-SiC<sub>x</sub>:H/n-Si heterojunctions in pursue of additional surface passivation. Nevertheless, the overall performance of complete solar cell devices (planar substrates and rear laser-doped contacts) was worse than their TMO/n-Si counterparts, as summarized in Fig. B.4.

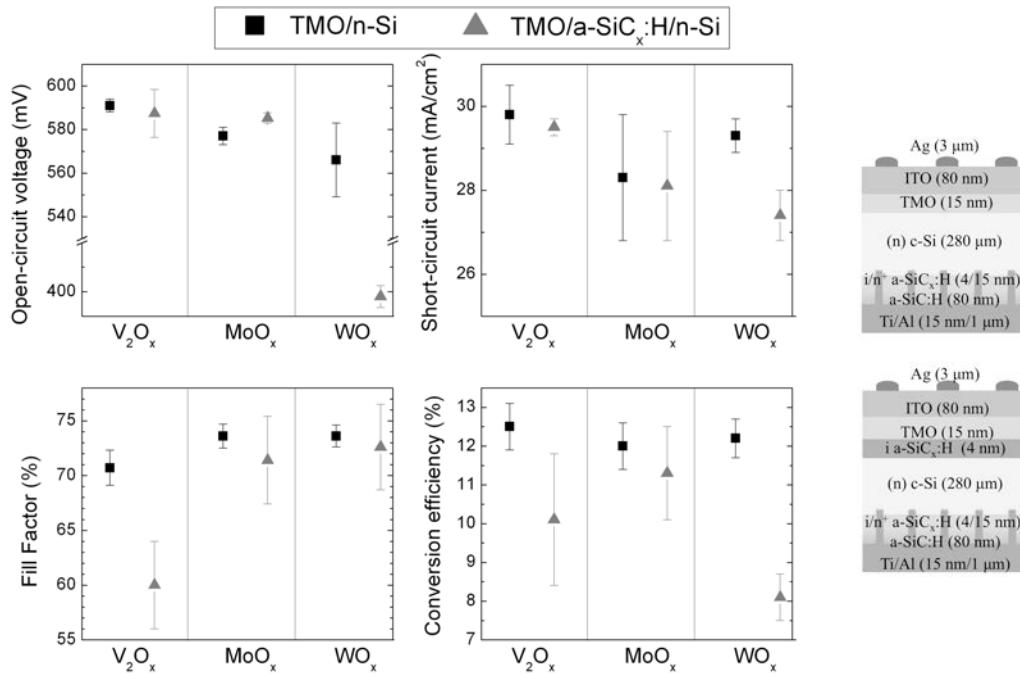


Figure B.4 Performance parameters for TMO/n-Si solar cells with and without the 4 nm a-SiC<sub>x</sub>:H interlayer (planar substrates, 4 device average).

Efficiency losses were mainly attributed to strong S-shaped  $J(V)_{light}$  curves and lower  $FF$ s, indicating a hole-blocking behavior and possible Fermi level misalignment. Measured  $J_{SC}$ s were

also slightly lower (due to parasitic absorption of the thin layer) while  $V_{OC}$  s were almost unchanged (except for the  $WO_x$  case), in agreement with lifetime measurements of device precursors. Given that (i/n<sup>+</sup>) a-SiC<sub>x</sub>:H stacks did provide good passivation, it is probable that the (i) layer alone was too thin and/or too deficient in hydrogen to effectively passivate the n-Si surface. With hopes for a  $V_{OC}$  increase, a thermal annealing treatment (160 °C, N<sub>2</sub>/H<sub>2</sub>, 15 min)

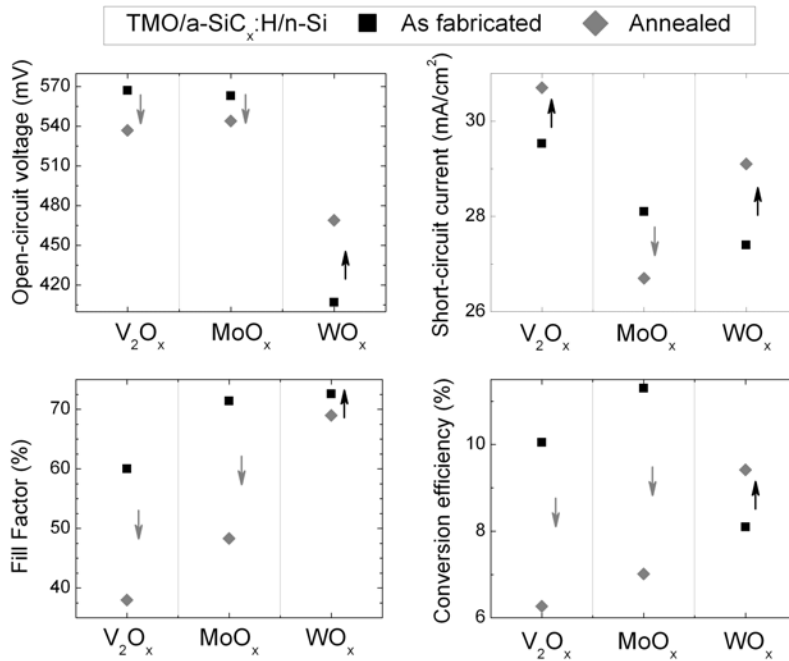


Figure B.5 Effect of temperature annealing (160°C, N<sub>2</sub>/H<sub>2</sub>, 15 min) on the performance parameters of TMO/a-SiC<sub>x</sub>:H/n-Si planar devices.

was done but no notable improvements were obtained (Fig. B.5). In fact, the overall effect of the annealing treatment was exactly the same as the one reported for TMO/n-Si devices (see Fig. 5.9), showing a substantial efficiency decrease except for the  $WO_x$ /a-SiC<sub>x</sub>:H samples. From these preliminary results, no further optimization of the a-SiC<sub>x</sub>:H interlayer was carried out, but passivation improvements cannot be fully discarded.

### B.5 Electrochromism in TMO materials

An important concern (frequently asked during conference presentations) has to do with electrochromism (EC) in transition metal oxides, an undesired phenomenon if intended to be used as window-layer materials in solar cells. EC exploits electron and ion mobility within MO<sub>6</sub> crystal structures to modulate the optical properties upon the application of minor voltages (~1 V), finding numerous applications in smart windows and electrochromic displays, of which WO<sub>3</sub> is a trademark example [24].

To address potential electrochromism in thin TMO films, we must revise a few of its working principles [24]. First, even though color and conductivity changes are already noticeable in oxygen-deficient oxides ( $\text{WO}_{3-x}$ ), an efficient coloration control requires the intercalation of hydrogen or alkali ions (Li, Na, K), forming metal oxide bronzes of the form  $\text{Li}_x\text{WO}_{3-x}$ . For the TMOs under study, absorption bands at 950 ( $\text{WO}_x$ ), 820 ( $\text{MoO}_x$ ) and 1,120 nm ( $\text{V}_2\text{O}_x$ ) can be expected. Second, noticeable transmittance changes with relevant technological applications occur only for film thicknesses above 200-400 nm. Then, thin TMO films (<20 nm) would require a radical change in structure (ion intercalation, large oxygen deficiency) to actually affect solar cell performance. Finally, and probably the most important point, is the large differentiation between EC systems and solar cells, the former involving conductive electrolytes and ion reservoirs [24]. Therefore, it can be concluded that electrochromism is not a concern in TMO/c-Si devices, at least not as important as other factors (e.g. long-term operational stability in outdoor environments).

## C List of scientific contributions<sup>6</sup>

### C.1 Journal publications

*Author:*

**L.G. Gerling**, S. Mahato, C. Voz, R. Alcubilla, J. Puigdollers, Characterization of transition metal oxide/silicon heterojunctions for solar cell applications, *Appl. Sci.* **5** (2015) 695–705.

**L.G. Gerling**, S. Mahato, A. Morales-Vilches, G. Masmitja, P. Ortega, C. Voz, R. Alcubilla, J. Puigdollers, Transition metal oxides as hole-selective contacts in silicon heterojunctions solar cells, *Sol. Energy Mater. Sol. Cells.* **145** (2016) 109–115, **Invited Paper**.

**L.G. Gerling**, C. Voz, R. Alcubilla, J. Puigdollers, Origin of passivation in hole-selective transition metal oxides for crystalline silicon heterojunction solar cells, *J. Mater. Res.* **32** (2017) 260–268, **Invited Paper**.

---

<sup>6</sup> Publications marked with an asterisk (\*) are related to the master thesis work on organic solar cells.

*Co-author:*

\*S. Galindo, M. Ahmadpour, **L.G. Gerling**, A. Marsal, C. Voz, R. Alcubilla, J. Puigdollers, Influence of the density of states on the open-circuit voltage in small-molecule solar cells, *Org. Electron.* **15** (2014) 2553–2560.

S. Mahato, **L.G. Gerling**, C. Voz, R. Alcubilla, J. Puigdollers, PEDOT:PSS as an alternative hole selective contact for ITO-free hybrid crystalline silicon solar cell, *IEEE J. Photovoltaics.* **6** (2016) 934–939.

\*M. Mariano, G. Kozyreff, **L.G. Gerling**, P. Romero-Gomez, J. Puigdollers, J. Bravo-Abad, J. Martorell, Intermittent chaos for ergodic light trapping in a photonic fiber plate, *Light Sci. Appl.* **5** (2016) e16216.

J.A. Garcia-Valenzuela, R. Rivera, A.B. Morales-Vilches, **L.G. Gerling**, A. Caballero, J.M. Asensi, C. Voz, J. Bertomeu, J. Andreu, Main properties of Al<sub>2</sub>O<sub>3</sub> thin films deposited by magnetron sputtering of an Al<sub>2</sub>O<sub>3</sub> target at different radio-frequency power and argon pressure and their passivation effect on p-type c-Si wafers, *Thin Solid Films* **619** (2016) 288–296.

S. Mahato, **L.G. Gerling**, C. Voz, R. Alcubilla, J. Puigdollers, High efficiency ITO-free hybrid solar cell using highly conductive PEDOT:PSS with co-solvent and surfactant treatments, *Mater. Lett.* **186** (2017) 165–167.

O. Almora, **L.G. Gerling**, C. Voz, R. Alcubilla, J. Puigdollers, G. Garcia-Belmonte, Superior performance of V<sub>2</sub>O<sub>5</sub> as hole selective contact over other transition metal oxides in silicon heterojunction solar cells, *Sol. Energy Mater. Sol. Cells.* **168** (2017) 221–226.

G. Masmitjà, **L.G. Gerling**, P. Ortega, J. Puigdollers, I. Martín, C. Voz, R. Alcubilla, V<sub>2</sub>O<sub>x</sub>-based hole-selective contacts for c-Si interdigitated back-contacted solar cells, *J. Mater. Chem. A.* **5** (2017) 9182–9189.

R. Garcia-Hernansanz, E. Garcia-Hemme, D. Montero, J. Olea Ariza, A. del Prado Millan, I. Martil de la Plaza, C. Voz, **L.G. Gerling**, J. Puigdollers, R. Alcubilla, Transport mechanisms in silicon heterojunction solar cells with molybdenum oxide as hole transport layer, *Prog. Photovoltaics Res. Appl.* (2017) Submitted/under review.



## C.2 Conference publications

### Author

\***L.G. Gerling**, S. Mahato, S. Galindo, C. Voz, J. Puigdollers, R. Alcubilla, J. Puigdollers, Straightforward determination of the effective mobility-lifetime product of small molecule organic solar cells, *Proc. 10th Spanish Conf. Electron Devices*, IEEE, Madrid (2015) 1–4.

**L.G. Gerling**, G. Masmitja, C. Voz, P. Ortega, J. Puigdollers, R. Alcubilla, Back junction n-type silicon heterojunction solar cells with V<sub>2</sub>O<sub>5</sub> hole-selective contact, *Energy Procedia* **92** (2016) 633–637 (From: 6th International Conference on Silicon Photovoltaics – SiliconPV).

**L.G. Gerling**, S. Mahato, C. Voz, R. Alcubilla, J. Puigdollers, Celdas solares de silicio cristalino con PEDOT:PSS y V<sub>2</sub>O<sub>5</sub> como contactos selectivos frontales y eficiencias de 11-15%, *Revista Internacional de Investigación e Innovación Tecnológica* **5** (2017) 1–11 (From: 1<sup>st</sup> Symposium on Mexican talent innovation – Innovation Match MX).

**L.G. Gerling**, G. Masmitja, P. Ortega, C. Voz, R. Alcubilla, J. Puigdollers, Passivating/hole-selective contacts based on V<sub>2</sub>O<sub>5</sub>/SiO<sub>x</sub> stacks deposited at ambient temperature, *Energy Procedia* (2017) In Print (From: 7th International Conference on Silicon Photovoltaics – SiliconPV).

### Co-author

J.A. Garcia-Valenzuela, A. Caballero, J.M. Asensi, J. Bertomeu, J. Andreu, **L.G. Gerling**, A.B. Morales-Vilches, P. Ortega, C. Voz, Intermediate amorphous silicon layer for crystalline silicon passivation with alumina, *Proc. 31st European Photovoltaic Solar Energy Conference and Exhibition (EU PVSEC)*, Hamburg (2015) 719–723.

G. Masmitjà, P. Ortega, I. Martín, J. Perez, G. Lopez-Rodríguez, E. Calle, **L.G. Gerling**, C. Voz, R. Alcubilla, Cost-effective cleaning solutions based on H<sub>2</sub>O/NH<sub>3</sub>/H<sub>2</sub>O<sub>2</sub> mixtures for ALD Al<sub>2</sub>O<sub>3</sub> passivated IBC c-Si solar cells, *Proc. 11th Spanish Conf. Electron Devices*, IEEE, Barcelona, (2017) 1–4.

### C.3 Conference presentations

#### *Oral*

\***L.G. Gerling**, Fabrication and characterization of organic solar cells, *3rd Symposium of CONACyT Scholarship Alumni*, Strasburg, France (2013).

\***L.G. Gerling**, Renewable energies in Mexico: installed capacity and regulation before the 2013 Energy Reform, *4th Symposium of CONACyT Scholarship Alumni*, Strasburg, France (2014).

**L.G. Gerling**, S. Mahato, A.B. Morales-Vilches, C. Voz, J. Puigdollers, R. Alcubilla, Characterization of transition metal oxide/Si heterojunctions for solar cell applications, *Nanotechnology for next generation photovoltaics (NextGen NanoPV)*, Menorca, Spain (2015).

**L.G. Gerling**, S. Mahato, C. Voz, R. Alcubilla, J. Puigdollers, Transition metal oxides for hole-selective contacts in Si heterojunctions solar cells, *European Material Research Society (EMRS) Spring Meeting*, Lille, France (2015).

**L.G. Gerling**, G. Masmitja, P. Ortega, C. Voz, R. Alcubilla, J. Puigdollers, Passivating carrier-selective materials for c-Si: interface reactions and passivation alternatives, *Material Research Society (MRS) Spring Meeting*, Phoenix, USA (2016).

**L.G. Gerling**, S. Mahato, C. Voz, R. Alcubilla, J. Puigdollers, Carrier-selective materials and their application to dopant-free silicon heterojunction solar cells, *1st Symposium on Mexican Talent Innovation Match MX*, Guadalajara, Mexico (2016).

L.G. Gerling, G. Masmitja, P. Ortega, I. Martin, C. Voz, J. Puigdollers, R. Alcubilla, Dopant-free carrier selective contacts: a paradigm-shift in crystalline silicon photovoltaic technology, *11th Spanish Conf. Electron Devices*, IEEE, Barcelona, (2017).

**L.G. Gerling**, G. Masmitja, P. Ortega, C. Voz, R. Alcubilla, J. Puigdollers, Passivating/hole-selective contacts based on  $V_2O_5/SiO_x$  stacks deposited at ambient temperature, *7th International Conference on Silicon Photovoltaics (SiliconPV)*, Freiburg, Germany (2017).

*Poster*

\*S. Galindo, M. Ahmadpour, **L.G. Gerling**, A. Marsal, C. Voz, J. Puigdollers, R. Alcubilla, Influence of the density of states on the open-circuit voltage in small-molecule solar cells, *Material Research Society (MRS) Spring Meeting*, San Francisco, USA (2014).

**L. G. Gerling**, A. Morales, M. Colina, C. Voz, J. Puigdollers, R. Alcubilla, Hole selective MoO<sub>3</sub> layer for heterojunction crystalline silicon solar cells, *22<sup>nd</sup> International Conference on Synthetic Metals*, Turku, Finland (2014).

**L. G. Gerling**, A. Morales, M. Colina, C. Voz, J. Puigdollers, R. Alcubilla, Novel crystalline silicon heterojunction structure based on hole selective MoO<sub>3</sub> emitter, *29th European Photovoltaic Solar Energy Conference and Exhibition (EU PVSEC)*, Amsterdam, Netherlands (2014).

**L.G. Gerling**, S. Mahato, C. Voz, J. Puigdollers, R. Alcubilla, Silicon heterojunction solar cells with hole-selective-layers based on transition metal oxides, *26<sup>th</sup> International Conference on Amorphous and Nanocrystalline Semiconductors (ICANS)*, Aachen, Germany (2015). – **Young Researcher Award**

**L.G. Gerling**, G. Masmitja, C. Voz, P. Ortega, J. Puigdollers, R. Alcubilla, Back junction n-type silicon heterojunction solar cells with V<sub>2</sub>O<sub>5</sub> hole-selective contact, *6th International Conference on Silicon Photovoltaics (SiliconPV)*, Chambéry, France (2016).

**L.G. Gerling**, C. Voz, P. Ortega, J. Puigdollers, R. Alcubilla, V<sub>2</sub>O<sub>5</sub> as a hole-selective contact for novel heterojunction solar cells based on n-type crystalline silicon, *Material Research Society (MRS) Fall Meeting*, Boston, USA (2016).

## Appendix references

- [1] ITRPV, International Technology Roadmap for Photovoltaic, Frankfurt am Main, Germany, 2016. [www.itrpv.net](http://www.itrpv.net).
- [2] A. Goodrich, P. Hacke, Q. Wang, B. Sopori, R. Margolis, T.L. James, et al., A wafer-based monocrystalline silicon photovoltaics road map: Utilizing known technology improvement opportunities for further reductions in manufacturing costs, *Sol. Energy Mater. Sol. Cells*. **114** (2013) 110–135.
- [3] M.J. De Wild-Scholten, Energy payback time and carbon footprint of commercial photovoltaic systems, *Sol. Energy Mater. Sol. Cells*. **119** (2013) 296–305.
- [4] LAZARD, Levelized cost of energy analysis - version 9.0, 2015.
- [5] Fraunhofer Institute for Solar Energy Systems, Photovoltaics report, Freiburg, Germany, 2016. [www.ise.fraunhofer.de](http://www.ise.fraunhofer.de).
- [6] Michael Lynch, Negative electricity prices are not a sign of renewable success, (2016). <https://www.forbes.com/sites/michaelyllynch/2016/02/19/negative-electricity-prices-are-not-a-sign-of-renewable-success/#4928dbe43806> (accessed June 7, 2017).
- [7] Bloomberg New Energy Finance, Solar panels now so cheap manufacturers probably selling at loss, (2016). <https://about.newenergyfinance.com/about/blog/solar-panels-now-so-cheap-manufacturers-probably-selling-at-loss> (accessed June 7, 2017).
- [8] D.H. Levy, D. Freeman, S.F. Nelson, P.J. Cowdery-Corvan, L.M. Irving, Stable ZnO thin film transistors by fast open air atomic layer deposition, *Appl. Phys. Lett.* **92** (2008) 192101.
- [9] A. Louwen, W.G.J.H.M. van Sark, R.E.I. Schropp, W.C. Turkenburg, A.P.C. Faaij, Life-cycle greenhouse gas emissions and energy payback time of current and prospective silicon heterojunction solar cell designs, *Prog. Photovolt Res. Appl.* **23** (2015) 1406–1428.
- [10] C. Olson, M. de Wild-Scholten, M. Scherff, P.-J. Ribeyron, Life cycle assessment of heterojunction solar cells and modules, in: 26th Eur. Photovolt. Sol. Energy Conf., Hamburg, 2011: pp. 3–6.
- [11] G. Glemser, Handbook of preparative inorganic chemistry, 2nd Ed., Academic Press, New York, USA, 1963.
- [12] J. Bullock, M. Hettick, J. Geissbühler, A.J. Ong, T. Allen, C.M. Sutter-Fella, et al., Efficient silicon solar cells with dopant-free asymmetric heterocontacts, *Nat. Energy*. (2016) 15031.
- [13] Y. Wan, C. Samundsett, J. Bullock, T. Allen, M. Hettick, D. Yan, et al., Magnesium fluoride electron-selective contacts for crystalline silicon solar cells, *ACS Appl. Mater. Interfaces*. **8** (2016) 14671.
- [14] Y. Zhang, W. Cui, Y. Zhu, F. Zu, L. Liao, S.-T. Lee, et al., High efficiency hybrid PEDOT:PSS/nanostructured silicon Schottky junction solar cells by doping-free rear contact, *Energy Environ. Sci.* **8** (2015) 297–302.
- [15] H.D. Um, N. Kim, K. Lee, I. Hwang, J.H. Seo, K. Seo, Dopant-free all-back-contact Si nanohole solar cells using MoOx and LiF films, *Nano Lett.* **16** (2016) 981–987.
- [16] D. Xu, X. Yu, L. Zuo, D. Yang, Interface engineering and efficiency improvement of monolayer graphene-silicon solar cells by inserting an ultra-thin LiF interlayer, *RSC Adv.* **5** (2015) 46480–46484.
- [17] Y. Wan, C. Samundsett, D. Yan, T. Allen, J. Peng, J. Cui, et al., A magnesium/amorphous silicon passivating contact for n-type crystalline silicon solar cells, *Appl. Phys. Lett.* **109** (2016) 113901.

- [18] T.G. Allen, J. Bullock, Q. Jeangros, C. Samundsett, Y. Wan, J. Cui, et al., A low resistance calcium/reduced titania passivated contact for high efficiency crystalline silicon solar cells, *Adv. Energy Mater.* (2017) 1602606.
- [19] G. Teran-Escobar, J. Pampel, J.M.C. A, M. Lira-Cantu, Low-temperature, solution-processed, layered V<sub>2</sub>O<sub>5</sub> hydrate as the hole-transport layer for stable organic solar cells, *Energy Environ. Sci.* **6** (2013) 3088–3098.
- [20] D. Fujishima, H. Kanno, T. Kinoshita, E. Maruyama, M. Tanaka, M. Shirakawa, et al., Organic thin-film solar cell employing a novel electron-donor material, *Sol. Energy Mater. Sol. Cells.* **93** (2009) 1029–1032.
- [21] S. Chavhan, O. Miguel, H.-J. Grande, V. Gonzalez-Pedro, R.S. Sánchez, E.M. Barea, et al., Organo-metal halide perovskite-based solar cells with CuSCN as the inorganic hole selective contact, *J. Mater. Chem. A.* **2** (2014) 12754.
- [22] P. Sippola, Z. Zhu, B. Oy, T. Sajavaara, H. Savin, H. Lipsanen, Growth behaviour and stability of atomic layer deposited MoO<sub>3</sub> by Mo(CO)<sub>6</sub> and H<sub>2</sub>O/O<sub>3</sub> precursors, in: 17th Int. Conf. At. Layer Depos., Denver, CO, USA, 2017.
- [23] M. Bivour, B. Macco, J. Temmler, W.M.M. Kessels, M. Hermle, Atomic layer deposited molybdenum oxide for the hole-selective contact of silicon solar cells, *Energy Procedia.* **92** (2016) 443–449.
- [24] C.G. Granqvist, Handbook of inorganic electrochromic materials, 2nd ed., Elsevier, Amsterdam, Netherlands, 2002.